# MULTISCALE THERMAL AND MECHANICAL ANALYSIS OF DAMAGE DEVELOPMENT IN CEMENTITIOUS COMPOSITES

by

**Hadi Shagerdi Esmaeeli**

**A Dissertation**

*Submitted to the Faculty of Purdue University*

*In Partial Fulfillment of the Requirements for the degree of*

**Doctor of Philosophy**


Lyles School of Civil Engineering

West Lafayette, Indiana

August 2020

## THE PURDUE UNIVERSITY GRADUATE SCHOOL
## STATEMENT OF COMMITTEE APPROVAL

**Dr. Pablo D. Zavattieri, Chair**
Lyles School of Civil Engineering

**Dr. Na Lu**
Lyles School of Civil Engineering

**Dr. Jan Olek**
Lyles School of Civil Engineering

**Dr. Amir Yaghoob Farnam**
Civil, Architectural and Environmental Engineering

**Dr. W. Jason Weiss**
Civil and Construction Engineering

**Approved by:**
Dr. Dulcy Abraham

To my beloved wife

*Helia*

to my parents

*Mohammadali* and *Fahimeh*

And to my brother

*Hamed*

# ACKNOWLEDGMENTS

First, I would like to offer my sincere gratitude to my mentor, advisor, and friend Professor Pablo Zavattieri. Over the last years, I have been benefited from his knowledge and wisdom immensely. Professor Zavattieri provided me with invaluable guidance while educating me to be an independent researcher. One simply cannot wish for a better advisor.

I would like to appreciate my examination committee members, Professor Luna Lu, Professor Jan Olek, Professor Amir Yaghoob Farnam, and Professor Jason Weiss, for their constant support and invaluable guidance and comments during my Ph.D. studies that have made this thesis more philosophical.

Multiple funding sources supported this research. Of those, the generous financial supports provided by Federal Aviation Administration through the PEGASAS center as Heated Airport Pavement project (Task 1-C), Indiana Department of Transportation (Grant No. SPR-3905), National Science Foundation (Grant No. CMMI 1449358), Purdue Graduate School (Bilsland Fellowship), and Department of Energy under the ARPA-E program are gratefully acknowledged. I would like to thank Professor Jeffrey Youngblood, Professor Alexander Wei, Professor John Haddock, Professor Bernard Tao, Professor Kendra Erk, and Professor Erik Kvam for their friendship and advice. I have been very fortunate to have the opportunity to collaborate with them. The friends that I made during this time made this journey very enjoyable. I would like to thank Mohammadreza Moini, Mehdi Shishehbor, Robert Spragg, Raikhan Tokpateyeva, Federico Antico, Fernando Cordisco, Nobphadon Suksangpanya, Enrique Escobar de Obaldia, David Restrepo, Nicolas Guarin, Tim Barrett, Albert Miller, Nathan Todd, Catherine Lucero, Heather Todak, Yunlan Zhang, Di Wang, Adwait Trikanad, Chunyu Qiao, Adwait Trikanad, HyunGu Jeong, and Amir Yaghoob Farnam.

This thesis has not been completed without the support of my parents. The emotional and technical support of my father for eight years has always been the source of enthusiasm. There are not enough words to express how thankful I am. My mother, who I thank her for her unconditional love and devotion during all these years. She has introduced me to the definition of “motivation” with all the sacrifices that she has made to help me reach my professional achievements. I would also like to thank my older brother for being the role model in my personal life.

Lastly, I offer my deepest gratitude to my beloved wife, Helia. She has always been caring and loving during the last two years. I cannot express how thankful I am for all these years, for being compassionate, and for helping deal with crucial times.

# TABLE OF CONTENTS

# LIST OF TABLES

# LIST OF FIGURES

# ABSTRACT

The exceptional long-term performance of concrete is a primary reason that this material represents a significant portion of the construction industry. However, a portion of this construction material is prone to premature deterioration for multi-physical durability issues such as internal frost damage, restrained shrinkage damage, and aggregate susceptibility to fracture. Since each durability issue is associated with a unique damage mechanism, this study aims at investigating the underlying physical mechanisms individually by characterizing the mechanical and thermal properties development and indicating how each unique damage mechanism may compromise the properties development over the design life of the material.

The first contribution of this work is on the characterization of thermal behavior of porous media (e.g., cement-based material) with a complex solid-fluid coupling subject to thermal cycling. By combining Young-Kelvin-Laplace equation with a computational heat transfer approach, we can calculate the contributions of (i) pore pressure development associated with solidification and melting of pore fluid, (ii) pore size distribution, and (iii) equilibrium phase diagram of multiple phase change materials, to the thermal response of porous mortar and concrete during freezing/thawing cycles. Our first finding indicates that the impact of pore size (and curvature) on freezing is relatively insignificant, while the effect of pore size is much more significant during melting. The fluid inside pores smaller than 5 nm (i.e., gel pores) has a relatively small contribution in the macroscopic freeze-thaw behavior of mortar specimens within the temperature range used in this study (i.e., +24 °C to -35 °C). Our second finding shows that porous cementitious composites containing lightweight aggregates (LWAs) impregnated with an organic phase change material (PCM) as thermal energy storage (TES) agents have the significant capability of improving the freeze-thaw performance. We also find that the phase transitions associated with the freezing/melting of PCM occur gradually over a narrow temperature range (rather than an instantaneous event). The pore size effect of LWA on freezing and melting behavior of PCM is found to be relatively small. Through validation of simulation results with lab-scale experimental data, we then employ the model to investigate the effectiveness of PCMs with various transition temperatures on reducing the impact of freeze-thaw cycling within concrete pavements located in different regions of United States.

The second contribution of this work is on quantification of mechanical properties development of cementitious composites across multiple length scales, and two damage mechanisms associated with aggregate fracture and restrained shrinkage cracking that lead to compromising the long-term durability of the material. The former issue is addressed by combining finite element method-based numerical tools, computational homogenization techniques, and analytical methods, where we observe a competing fracture mechanism for early-age cracking at two length scales of mortar (meso-level) and concrete (macro-level). When the tensile strength of the cement paste is lower than the tensile strength of the aggregate phase, the crack propagates across the paste. When the tensile strength of the cement paste exceeds that of the aggregate, the cracks begin to deflect and propagate through the aggregates. As such, a critical degree of hydration (associated with a particular time) exists below which the cement paste phase is weaker than the aggregate phase at the onset of hydration. This has implications on the inference of kinetic based parameters from mechanical testing (e.g., activation energy). Next, we focus on digital fabrication of a cement paste structure with controlled architecture to allow for mitigating the intrinsic damage induced by inherent shrinkage behavior followed by extrinsic damage exerted by external loading. Our findings show that the interfaces between the printed filaments tend to behave as the first layer of protection by enabling the structure to accommodate the damage by deflecting the microcrack propagation into the stable configuration of interfaces fabricated between the filaments of first and second layers. This fracture behavior promotes the damage localization within the first layer (i.e., sacrificial layer), without sacrificing the overall strength of specimen by inhibiting the microcrack advancement into the neighboring layers, promoting a novel damage localization mechanism. This study is undertaken to characterize the shrinkage-induced internal damage in 7-day 3D-printed and cast specimens qualitatively using X-ray microtomography (μCT) technique in conjunction with multiple mechanical testing, and finite element numerical modeling. As the final step, the second layer of protection is introduced by offering an enhanced damage resistance property through employing bioinspired Bouligand architectures, promoting a damage delocalization mechanism throughout the specimen. This novel integration of damage localization-delocalization mechanisms allows the material to enhance its flaw tolerant properties and long-term durability characteristics, where the reduction in the modulus of rupture (MOR) of hardened cement paste (hcp) elements with restrained shrinkage

cracking has been significantly improved by ~ 25% when compared to their conventionally cast hcp counterparts.

# 1. INTRODUCTION

## 1.1 Literature Review

Cementitious composite materials are made of cement, water, and aggregate of various sizes. These materials are known for their exceptional performance over their designed service life. However, a considerable portion of the infrastructures made by these materials undergoes premature deterioration. According to the Department of Transportation, $231.4 billion per year is needed just to maintain the existing concrete pavement network, which has fallen into the backlog of roads in poor condition, in a good and operable condition. These durability-related issues are simultaneously governed by multiple complex damage mechanisms, depending on multiple primary factors, including intrinsic dynamic chemical reaction in concrete as well as extrinsic environmental conditions. It is noteworthy to mention that at a certain age of the specimen, a few specific mechanisms are responsible for being the primary reasons for premature deterioration, classifying this performance problem into two distinct categories of short-term and long-term durability issues. To this end, this study intends to provide a comprehensive multi-physical experimental-numerical framework to find the driving reasons that contribute to lowering the intrinsic resistance of cementitious materials over their service life period. The durability-related issues examined in this work are visually displayed in Figure 1-1.

Cementitious composites exhibit a homogeneous continuum structure at the macro level; However, when these materials are scanned at lower length scales (across nano- to meso-level), they have a complex heterogeneous structure with phases of different physical properties. The primary goal of this study is to examine the principle components that play an important role in governing a specific durability issue.

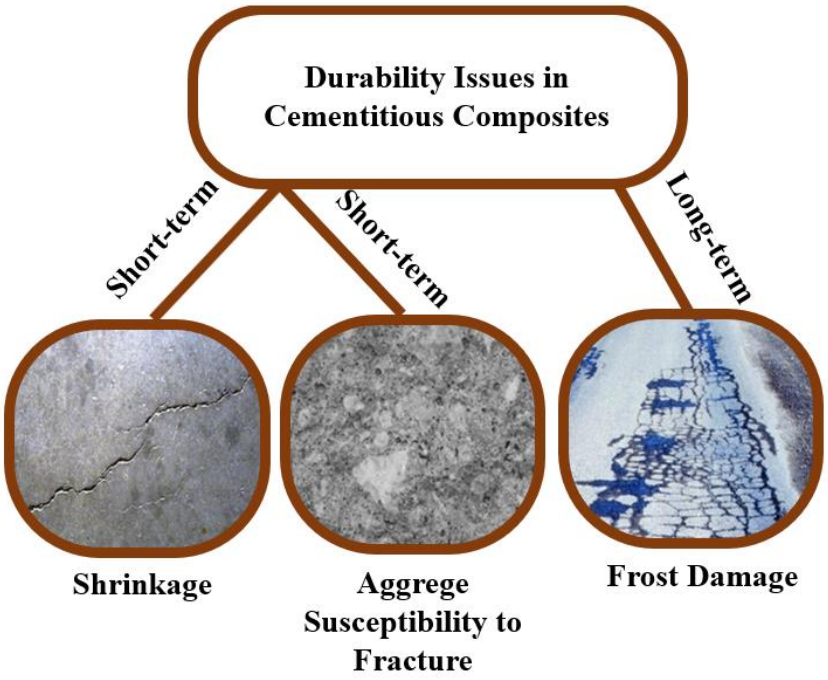


Figure 1-1. Diagram of the three common durability issues observed in cementitious systems.

Probing the nano- and micro-levels, this study investigates the contribution of heterogeneities in governing the macroscopic physical behavior of cementitious systems across these length scales. Depending on the water/cement, type of aggregates, the addition of different admixtures, as well as environmental conditions (e.g., temperature and humidity), the rate of the chemical reaction between water and cement for making cement paste is determined. During the hydration process, the two phases of calcium silicate hydrate (C-S-H) and calcium hydroxide (CH) constitute the majority of products during cement hydration, where comprise about 50~60% and 20-25% of the products in volume, respectively. The CH phase contributes to mainly control the pH of the solution at the level of 12.5. In contrast, the formation of C-S-H gel particles divided by thin layers of water (gel pores network) is mainly responsible for the gradual development of mechanical properties of cement-based materials. In simple words, the hardened cement paste is considered to include four main phases of unreacted cement clinker, CH, C-S-H gel (and its gel pores), and capillary pores. Figure 1-2 depicts these four main components.

Due to a net decrease of solid product volume during hydration and water consumption, a portion of space of originally water-filled space between (cement) particles remains unfilled, known as capillary pore space. The disjoining pressure of solution in a capillary pore, arising from

dissimilar surface tensions of the solution and cement particle, leads to shrinking the C-S-H gel products, which causes a common type of durability-related issue in cementitious systems. In conjunction with the shrinkage issue, the internal frost damage is also a primary durability-related issue takes place from nanograins level to the mesoscale, where the phase transition of available solution entrapped within the pores of various sizes (e.g., gel pores, capillary pores, and air voids) leads to multiple degradation mechanisms.

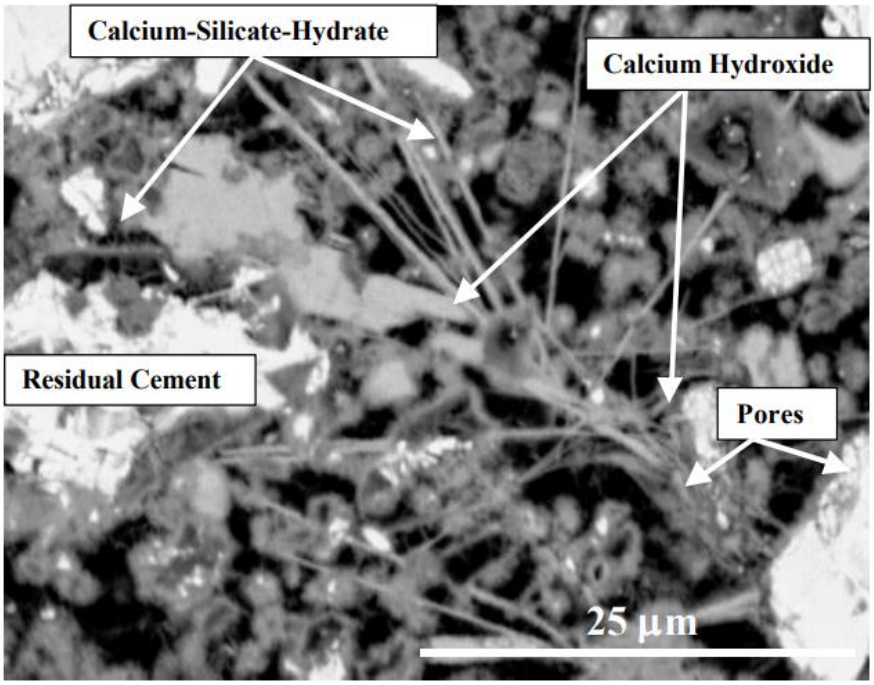


Figure 1-2. Backscattered electron imaging of the hardened cement pastes at 1 day. Visualization of hydration productions of Calcium-Silicate-Hydrate (C-S-H), Calcium Hydroxide (CH), unhydrated residual cement particles, and pores of various sizes (adapted from Stutzman(Stutzman, 2000).

Cementitious composites, such as mortar and concrete, have complex structures where damage and failure mechanisms can occur across different length scales. The mechanical response of these materials is frequently predicted by considering the material structure as a homogeneous continuum at the macro-level. However, when these materials are viewed at the meso-level, they have heterogeneous structures in which concrete is composed of coarse aggregate inclusions surrounded by a mortar matrix formed by cement paste and fine aggregate inclusions (Folker H. Wittmann, 1983), shown in Figure 1-3. The key mesostructure morphological (i.e., size, shape,

volume fraction, and spatial distribution of aggregates), as well as mechanical properties (stiffness, strength, and fracture energy), play an important role in the observable mechanical macroscopic behavior. Prior meso-level numerical models were developed to analyze the heterogeneous and anisotropic behavior of concrete to obtain knowledge on the basic mechanisms underlying the observed macroscopic behavior (Du & Jin, 2014; Huang et al., 2015; López et al., 2008a; Ren et al., 2015; B. Sun et al., 2015; X. Wang et al., 2015; X. F. Wang et al., 2015; A. Yin et al., 2015). While these mesomechanical modelings qualitatively investigated the overall mechanical response as well as fracture process in the mesostructure constituents including matrix, aggregate inclusions, and the interface transition zone between them (ITZ), little is known about the interplay between the evolution of hydrating cement paste phase at early ages, the morphological and the mechanical properties of aggregate phase, and how this combination affects the likelihood of early-age cracking in cementitious composites.

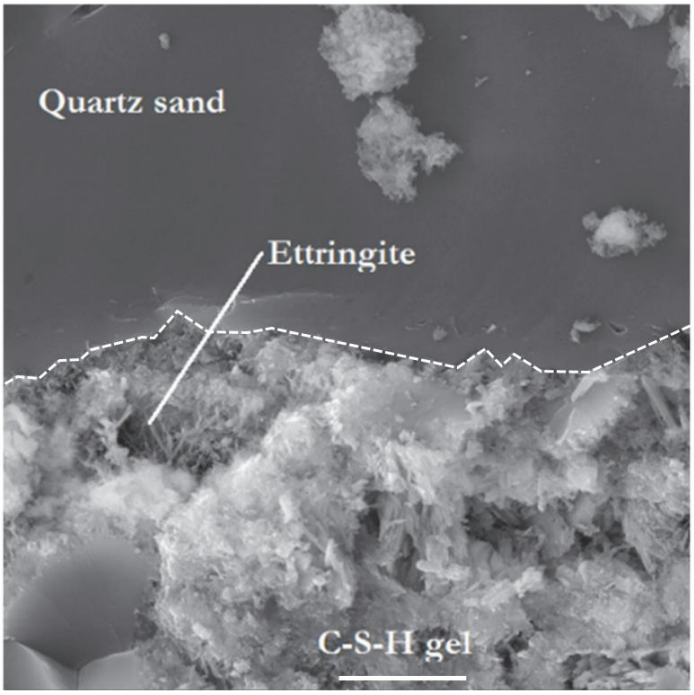


Figure 1-3. Microstructure of the interfacial region between cement paste and fine aggregate known as interfacial transition zone (ITZ), adapted from (Simonova et al., 2017). The scale bar indicates a length of 5 μm.

### 1.1.1 Internal Frost Damage

Cementitious composites are prone to cracking internally when they experience thermal cycling that enables freezing and thawing actions. The damage mechanisms associated with freeze-thaw actions include (1) the hydraulic pressure (i.e., negative tensile stress) attributed to the crystallization of in-pore solution which was firstly proposed by Powers (Powers, 1949), (2) the osmotic pressure induced by cryo-suction effect where initially frozen water in larger pores tend to absorb excess water from adjacent smaller unfrozen pores (Coussy & Monteiro, 2008; Powers et al., 1953), and (3) the ice crystallization pressure exerted by a thin layer of water between ice crystals formed in the pore and the pore wall (L. Liu et al., 2011). All these mechanisms are factually governed by the effect of the role of curvature (also known as pore size effect, or Gibbs-Thomson effect). The general idea is that as the temperature goes below freezing point, pore solution solidification begins inside the pores of larger size. Sun and Scherer (Z. Sun & Scherer, 2010a) have performed extensive research to understand better the role of air voids (which have the largest size) on the physical behavior of mortar specimens experiencing internal frost damage. They measured the volume change of mortar under one freezing cycle, the amount of ice produced at specific stages of the freezing process, and the physical properties of frozen specimens for strain and stress calculations. In frozen saturated specimens without air-entrainment, the experiment observations showed that the hydraulic pressure is the primary mechanism responsible for damage.

In contrast, ice crystallization pressure exerted to the mesopore walls was responsible for damage in air-entrained saturated specimens through transporting the considerable amount of solution from the mesopores to the air voids. Liu et al. (L. Liu et al., 2011) have carried out thermodynamic- and fracture-based simulations to explain the role of crystallization pressure as the primary source of frost damage in saturated cement paste at a micro-level. Similar to results reported by Sun and Scherer, these results confirmed the direct relation between volumetric dilation and an increasing number of microcracks with decreasing the temperature below the freezing point. Coussy and Monteiro (Coussy & Monteiro, 2008) provided a novel poromechanical approach to investigate the role of pore size distribution and suggested a theoretical formula for a spacing factor between the air voids connected through pore network channel for frost damage mitigation. This model, however, was incapable of capturing the micro-crack development since a homogenization scheme was employed to convert the pore pressure associated with freezing to the effective stress tensor. In order to accommodate this issue, Zhou et al. (T. Zhou et al., 2019)

developed a novel framework based on the distribution of pore solution and stress field at the nanograin level to indicate that the largest freezing-induced pressure is associated with the capillary forces concentrated at the interface between large capillary pores and gel pores. Consequently, a homogenized length scale for the representative volume element (RVE) was obtained for upscaling the physical behavior from nano- to macro-level.

Based on various internal and external conditions, including the degree of saturation of specimen, mixture proportioning, rate of thermal loading, and size of the specimen, there are plenty of competing mechanisms to account for simulation of the physical behavior of cementitious composites with a complex liquid-solid coupling. Nevertheless, there is little known about at which temperature the ice nucleation begins to take place, the size range of freezing pores, and the volume of freezing pores at the freezing onset. Li et al. (W. Li et al., 2012) used a passive acoustic emission technique to monitor the progress of internal frost damage of mortar specimens with 13% air content and 96% degree of saturation. After performing two consecutive thermal cycles, a significant number of acoustic events were observed once the temperature dropped below -8$^{o}$C, highlighting the high density of microcrack formation due to frost damage. Farnam et al. (Yaghoob Farnam, Bentz, Sakulich, et al., 2014) have provided sufficient evidence on both thermal and mechanical behavior of partially and fully saturated mortar specimens with air entrainment. However, there is still little known about the influence of the role of curvature and associated capillary pressure on the macroscopic physical behavior of porous cementitious systems.

### 1.1.2 Frost Resistance Improvement Using Sustainable Organic Materials

After analyzing the role of curvature on the pore solution solidification at the microscopic scale and assess the validity of resulting macroscopic thermal behavior of frozen mortar specimens with experimental data, we leverage from these earlier findings to investigate the effectiveness of sustainable green materials incorporated into cementitious composites on enhancing their internal frost resistance. A research study by Riayzi et al. (Riyazi et al., 2017) emphasized the use of superabsorbent polymers (SAPs) for synthetic air void manufacturing that leads to frost resistance enhancement of concrete. Organic (green) phase change materials (PCMs) can be used as substitutes to inorganic admixtures for thermal energy storage (TES) purposes, since these materials are capable of recurrently storing and releasing latent heat energy upon solidification and melting, respectively. Owing to their significant thermal mass, PCMs with a high transition

temperature (about 40 ~ 50 $^{o}$C) were incorporated into concrete pavements to mitigate the thermal cracking by diminishing the interior temperature rise in early-age concrete (Dale P. Bentz & Turpin, 2007; Fernandes et al., 2014). Bentz and Turpin also developed a computer simulation to highlight the effectiveness of PCM use on frost damage mitigation in bridge structures. Sakulich and Bentz (Aaron R. Sakulich & Bentz, 2012) provided evidence on the feasibility of low-temperature PCM addition for service-life extension of bridge decks in various climates located throughout the United States.

To (i) incorporate and retain the PCMs in the cementitious composites, (ii) indulge any potential chemical reactions between the fresh cement paste and PCM, and (iii) maximize the thermal efficiency of cementitious composites by optimizing the distribution of PCMs, two practical methods of micro-encapsulation and lightweight aggregate (LWA) impregnation were used. Two recent research studies by Yeon and Kim (Yeon & Kim, 2018) and Urgessa et al. (Urgessa et al., 2019) have proven the effectiveness of low-temperature PCMs (with a characteristic freezing point of 4.5 $^{o}$C) microencapsulated with melamine-formaldehyde resin in improving the frost resistance of mortar and concrete specimens. Farnam et al. (Yaghoob Farnam et al., 2017) and Li et al. (W. Li et al., 2019) have demonstrated the significant heat storage capacity of PCM-LWA composite on melting surface ice and snow and delaying internal ice formation, respectively. In the conventional method of concrete casting, it is unlikely to control the distribution of particulates during the mixing process as these inclusions were randomly distributed. While there is no carefully designed spatial pattern of PCM capsulate distribution, the literature falls short of addressing how to govern the temporal distribution of latent heat release and storage rate during freezing and thawing cycles. Leveraging from our findings on the role of curvature effect on the thermal behavior of freezing saturated mortar specimens, prudently robust design of PCM-LWA composite allows us to maintain the internal temperature of the specimen above the freezing point of the solution by (1) selecting PCMs with two favorable physical properties of *latent heat energy* and *thermal diffusivity*, in conjunction with (2) selecting a porous LWA particulate with a pore size range similar to that for cementitious composite.

### 1.1.3 Aggregate-matrix composite effect on the mesoscale fracture of early-age cementitious composites

The prediction of early-age physical properties development of cementitious composites is of importance in various infrastructures, such as bridges and pavements. To this end, an empirical approach of *maturity method* is used to establish a direct relationship between strength development of material, cement hydration progress, and environmental conditions, including ambient moisture and curing temperature (Carino, 1991). The prediction accuracy of this method, however, is subjected to debate due to a lack of deep understanding of the relationship between hydration kinetics, microstructure development, maturity, and physical properties development (Jieying Zhang et al., 2008). As a result, Zhang et al. (Jieying Zhang et al., 2008) proposed a mathematical methodology to back-calculate the maturity control variable (i.e., activation energy) by lessening the error between empirical and experimental data. While this research highlighted that there is no unique value of activation energy for every physical property of concrete, we question the validity of this research finding as the activation energy merely depends on the mixture proportioning of the cementitious material and is independent of the type of external loading.

On the other hand, this method analyzes the structure mortar and concrete as a homogeneous continuum, where the role of mesostructure phases of aggregate inclusions and ITZ on resulting physical properties is neglected. Based on the concept of structure-property, there is a strong effect of existing heterogeneous characteristics of mesostructure (both morphological and physical) on the resulting homogenized physical response of cementitious composites (i.e., size effect) (Eliáš et al., 2015). Outstanding works by Carpinteri (Carpinteri, 1986), and Bazant (Bažant, 1997) have suggested a bottom-up approach for fracture simulation, explicitly considering a heterogeneous mesostructure.

Previous investigations demonstrated the role that aggregates played in the early-age flexural strength development, highlighting a common short-term durability issue of concrete pavements (Barde et al., 2005). The aggregate volume content and the type of aggregate were varied to illustrate that the aggregates play an important role in strength development. Figure 1-4(a) shows a linear relationship between the flexural strength ($f_r$) development and non-evaporable water ($w_{nevap}$) (i.e., assumed to be directly proportional to the quantity of chemically bound water) for cement paste specimen (0% aggregate). In comparison, the mortar (paste and 55% fine

aggregate by volume) and concrete (paste, 34% of fine aggregate and 38% of coarse aggregate by volume) show a bilinear response where aggregates are present. Also, two concrete specimens containing only 30% of a single size coarse aggregate were tested. Figure 1-4(b) illustrates how the failure strength is influenced by the aggregate type (e.g., limestone is weaker than granite) after the *knee point*, which implied that the strength of aggregate may influence the maturity prediction.

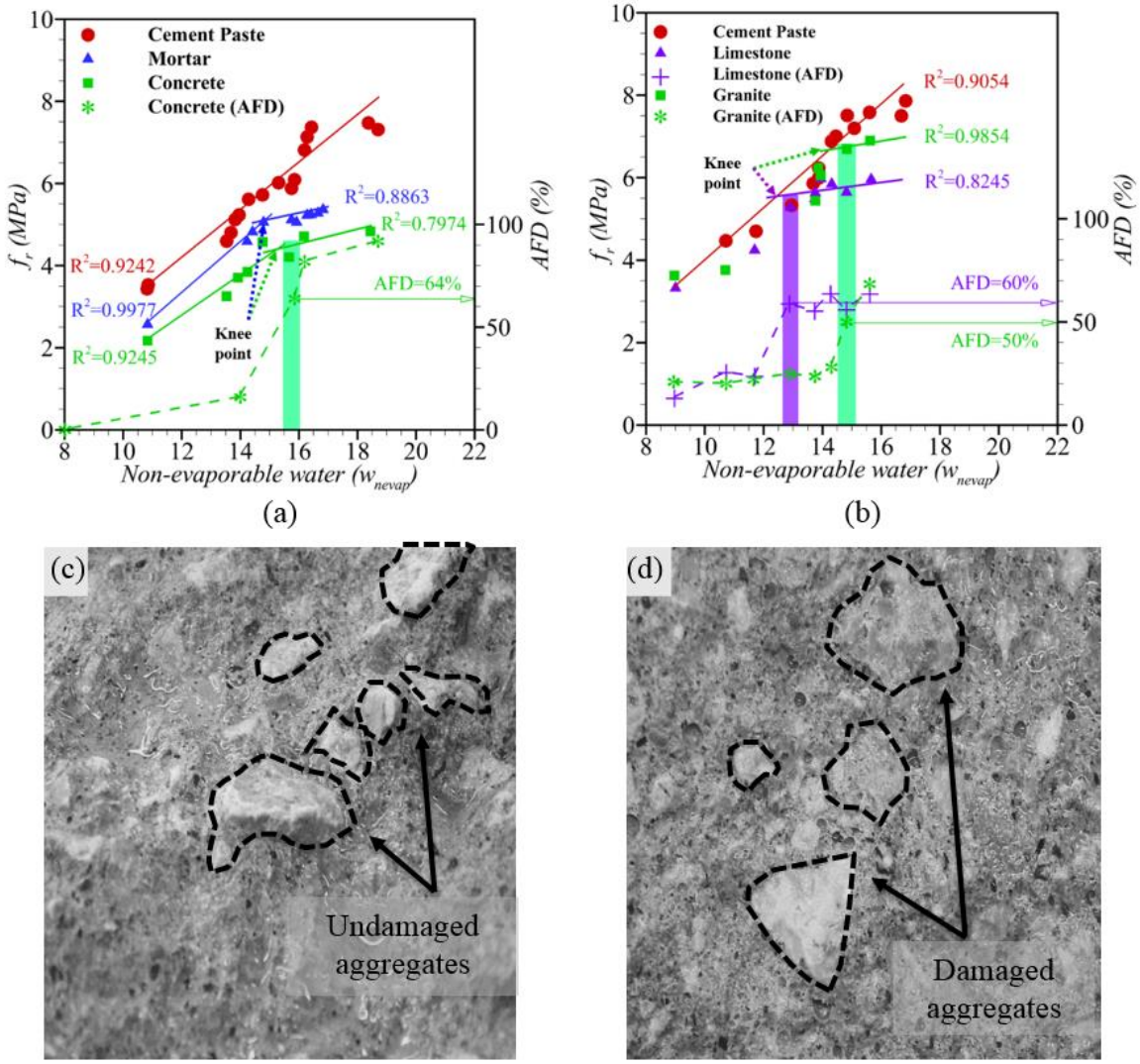


Figure 1-4. Experimental measurement of (a) effect of aggregate content on early age flexural strength development of cementitious composites, (b) effect of aggregate strength on flexural strength development of concrete, and photos of fractured surfaces of concrete specimens (c) at $t$ = 12 $h$, and (d) $t$ = 72 $h$ (Barde et al., 2005).

The knee point is determined through a two-step process: first, the data points are clustered into two groups that will define the two linear rate of strength development. This is attained by maximizing each coefficient of determination ($R^2$). Then the knee point is selected as the interception between the two linear regression functions. Barde et al. (Barde et al., 2005) also observed that the ratio of the number of fractured aggregates to the total number of aggregates in the fractured surface, defined as aggregate fracture density (*AFD*), significantly increased after the knee point of the bilinear behavior, illustrated by dashed lines in Figure 1-4(a) and (b). These findings imply that aggregate fracture strongly influences the knee point. Figure 1-4(c) and (d) show an example of two fractured surfaces of concrete beams subjected to four-point flexural test at a very early age of $t = 12\ h$ (corresponding to $w_{nevap} = 14$) and a later age of $t = 72\ h$ (corresponding to $w_{nevap} = 16.05$), respectively. Figure 1-4(c) shows that the majority of coarse aggregates remained undamaged "and pulled out of the matrix," and the crack propagates around the aggregates (before the knee-point). After the knee point, however, the aggregate fracture density suggests that the cracks have more tendency to propagate across the aggregates, shown in Figure 1-4(d).

### 1.1.4 Mitigation of Shrinkage Cracking Through Digital Fabrication Approach

Shrinkage of cementitious composites is an inevitable major durability issue which is caused due to the migration of water from the interior structure (i.e., higher water concentration) to the outer surface of the specimen (i.e., lower water concentration), and the net decrease of solid products volume during the hydration process. A variety of factors, including mixture proportioning, ambient conditions, curing age, the specimen size, and the restraint degree, are the key factors that determine the development of residual tensile stresses (S. Shah et al., 1998). When there is significant shrinkage, the cementitious composite undergoes a high density of microcracking development, which results in reducing the mechanical capacity of the specimen. Therefore, shrinkage-induced damage occurs at very early ages, and thus may significantly compromise the durability and service-life span of the cementitious composites (Holt & Leivo, 2004).

Five major shrinkage mechanisms are responsible for the volume reduction of cementitious composites: 1) *chemical shrinkage* occurs in a fresh mixture before hardening stage when the rate of water evaporation exceeds that of the bleeding water moving towards the surface of specimen,

2) *drying shrinkage* that refers to the capillary tension induced by in-pore condensed solution at the pore wall during moisture exchange with environment, causing some dimensional change of solid structure (Dale P Bentz et al., 1998), 3) *autogenous shrinkage* represents the volume contraction of cementitious composters in isothermal and sealed condition due to self-desiccation (generating empty pores within cement paste structure during hydration), 4) *thermal shrinkage* which corresponds to the volume contraction of massive structures due to significant rate of hydration and associated temperature development in hardening cementitious composites, and 5) *carbonation shrinkage* happens as a reaction between CH dissolution and ambient carbon dioxide on the surface of specimen and has no contribution in internal microcrack development. While thermal and carbonation shrinkage mechanisms can occur in concrete structures, these two shrinkage mechanisms have an insignificant impact on internal microcrack development in thin structures (such as pavements and bridges). Conversely, three mechanisms of plastic, autogenous, and drying shrinkage are the primary cause of early-age shrinkage in fresh and hardening cement-based materials (D. P. Bentz & Jensen, 2004; Cohen et al., 1990; Ghourchian et al., 2019; Lura et al., 2003), which all highlight the effect of water movement in volumetric contraction in conventional cast specimens.

The current literature has surveyed multiple solutions for reducing the effect of shrinkage cracking on microcrack development and resulting macroscopic behavior of cementitious composites manufactured by conventional casting techniques. Weiss and Shah (W. J. Weiss & Shah, 2002) have shown the effectiveness of shrinkage reducing admixtures (SRAs) in reducing the early-age drying shrinkage by lowering the surface tension of the solution. Ghourchian et al. (Ghourchian et al., 2018a) provided a comprehensive understanding of the effect of chemical admixture incorporation on plastic shrinkage mitigation by modifying the material property rather than altering environment conditions (i.e., evaporation rate). Among various SRA (stabilizer), viscosity modifying admixture (VMA) (stabilizer), and C-S-H seeds, SRA was found to be the most efficient admixture by adjourning the capillary pressure rise. At the same time, no substantial impact on mechanical properties development during early stages of hydration was observed (no retarding effect). Radlinska et al. (Radlinska et al., 2008) clarified that SRA is a desirable admixture for shrinkage mitigation in a sealed system. In contrast, lightweight aggregate (LWA) incorporation lowers the shrinkage by providing sufficient amount of water distributed throughout the specimen volumetrically.

While the academic community has extensively explored several shrinkage mitigation strategies for the traditionally cast specimens, little research has been conducted on the capacity of digitally fabricated (i.e., 3D printed) cementitious composites on compensating the cracking associated with shrinkage. Buswell et al. (Buswell et al., 2018) have anticipated that the 3D printed concrete specimens are more likely to be susceptible to premature cracking due to significant autogenous shrinkage and greater exposed surface area when exposed to a dry environment. Marchon et al. (Marchon et al., 2018) have introduced the plastic shrinkage mechanism as the primary source of cracking development, wherein the absence of framework, excessive water loss may retard the hydration and resulting physical properties gain. Similarly, De Schutter et al. (De Schutter et al., 2018) observed the severe shrinkage cracking in a showcase of 3D printed cement mortar at an early age. To accommodate for creation of early-age cracks associated with drying and plastic shrinkage, Kazemian et al. (Kazemian et al., 2017) have used Polypropylene fiber as a reinforcement mechanism, given that the incorporation of this fiber of high tensile strength can significantly improve the tensile cracking resistance of a printed structure. Slavcheva (Slavcheva, 2019) has provided quantitative evidence on increased deformability of fabricated cement paste structure using a 3D printing technique compared to that measured in the conventional casting technique. As a result, the magnitude of internal tensile stress in 3D printed hardened cement paste (hcp) elements may substantially increase as the drying shrinkage mechanisms is of the primary source of development of residual stresses under cyclic wetting-drying conditions. However, prior studies have failed to quantitatively investigate the adverse impact of shrinkage cracking on physical properties of 3D printed hcp elements and compare the results with those for traditionally cast hcp elements.

## 1.2 Motivations for this study

While cementitious composites interact with their surrounding environment, they frequently experience extensive physical changes that are likely to have a substantial adverse influence on their intrinsic properties. Thus, the durability of cementitious composites and their constituent phases at multiple length scales have received extensive consideration; however, several short- and long-term durability issues are of important concern that yet remained to be fully addressed. The level of complexity of these issues becomes more immense when the onset of each deterioration may begin at an unsightly lower length scale, which makes it more difficult to

understand the underlying physical damage mechanisms. This study will, first, focus on the role of curvature of pores of nano- to millimeter size on macroscopic freeze-thaw behavior of a cementitious composite with a complex fluid-solid coupling.

*Motivation 1*: To understand the effect of the role of curvature on macroscopic freeze-thaw behavior of air-entrained cementitious composites under thermal loading.

Prior research has thoroughly investigated various thermodynamic- and physical-based mechanisms that are responsible for phase transition of the in-pore solution, solution transport within the porous network, and resulting volumetric change at the local and global scale. These studies proffered the damage onset associated with the freezing of solution within air voids in fully saturated cementitious composites, following the Gibbs-Thomson effect (Z. Sun & Scherer, 2010a). However, little research has been conducted to identify a synergistic effect between the phase transition of the in-pore solution and the undercooling effect before ice formation onset. Owing to the undercooling phenomenon, in-pore ice crystals nucleate at a temperature lower than the characteristic freezing point of unconfined pore solution. The onset of freezing action, thus, may occur within multiple pore-length scales, including capillary pores (>5 *nm* of radius size) and air voids (>5 $\mu m$). We, then, hypothesize that an instantaneous freezing action takes place in a broad range of pore sizes which promotes the contribution of capillary pores into frost damage onset, as observed using passive acoustic emission experiments performed by Farnam et al. (Yaghoob Farnam, Bentz, Sakulich, et al., 2014).

*Motivation 2*: To understand the effect of sustainable phase change materials as thermal energy storage (TES) agent on macroscopic freeze-thaw behavior of cementitious composites.

Deicing salts are often used to melt the ice or snow from the surface of concrete sidewalks and pavements to reduce the risk of injuries for the traveling public (W. Li et al., 2012). The water-salt solution that is produced during melting can infiltrate into the concrete and cause frost damage as the temperature drops below the freezing point of the solution in the pores (Yaghoob Farnam, Dick, et al., 2015; Yaghoob Farnam, Wiese, et al., 2015; Litvan, 1976; Powers, 1945; G. W. Scherer & Valenza, 2005; Z. Sun & Scherer, 2010c). Phase change materials (PCMs) are green-sustainable substances with a high enthalpy of fusion, $\Delta H_f$, that can be used to increase the thermal inertia of pavements(Cabeza et al., 2011). Hence, PCMs can be incorporated as alternatives to

deicing salts in some applications to reduce the number of freeze-thaw cycles experienced by pavements (Dale P. Bentz & Turpin, 2007; Yaghoob Farnam et al., 2017). Reducing freeze-thaw cycles is important as this may improve the mechanical response of pavement, thereby reducing the cracking. The presence of cracks can exacerbate reinforcing steel corrosion by providing aggressive media easy access to the steel and amplifying the amount of damage caused by successive freeze-thaw cycles (Kan et al., 2010).

The main characteristic of a PCM is to release a considerable amount of thermal energy during the exothermic solidification reaction that occurs when the concrete pavement temperature drops to the freezing temperature of PCM. If the solidification reaction occurs at a slightly higher temperature than the freezing point of pore solution in concrete, it can delay the freezing of the pore solution (Yaghoob Farnam, Krafcik, et al., 2015; Aaron R. Sakulich & Bentz, 2012). The released heat maintains the surrounding pore solution at the freezing temperature of PCM, where the length of time that this temperature can be maintained is dictated by $\Delta H_f$ of PCM(Baetens et al., 2010). Many PCMs have high $\Delta H_f$ and associated narrow temperature range for releasing and absorbing the thermal energy from exothermic solidification or endothermic melting reactions, respectively(He et al., 2004). This range corresponds to the phase transition temperature of the PCM. While the effectiveness of using PCM to delay or prevent freeze-thaw cycling is recognized as a promising technology, previous research has failed to investigate the contribution of the rate of $\Delta H_f$ and associated temperature range.

Given the fact that LWA represents a porous aggregate material containing an internal porous network with a significant capacity of liquid absorption (Balapour & Farnam, 2018; Castro, Keiser, et al., 2011), we leverage our findings of a robust analysis on the pore size effect on the macroscopic thermal behavior of freezing and melting cementitious composite, to include two important thermodynamic-based effects of pore size distribution inside LWAs in conjunction with $\Delta H_f$-temperature relationship obtained from equilibrium phase diagram of PCM.

*Motivation 3*: To understand the intertwined effect between maturity method and composite nature of cementitious composites on their early-age fracture behavior.

In the transportation environment, one primary factor of short-term durability issue is the premature failure of concrete pavements before reaching their designed physical properties (e.g., strength). The maturity method is used as an empirical concept that establishes an early-age

relationship between maturity index (i.e., degree of hydration which represents the fraction of cement that has chemically reacted with water) and strength of concrete (Carino, 1991). However, the contradicting field observations of premature deterioration of concrete pavements, particularly observed in high-performance concrete (HPC) pavements, highlights that the maturity method falls short in the prediction of accurate early-age properties. Therefore, more research is needed to understand better the competing fracture mechanism, which governs the resulting physical properties and time of cracking.

One of the major drawbacks of the maturity method is modeling of cementitious composites as homogeneous isotropic materials, and merely considers the effects of ambient conditions on hydration process and properties development of cement paste. However, when these materials are viewed at one length scale lower than macro-level (i.e., meso-level), they exhibit heterogeneous structures where concrete is comprised of aggregates of larger sizes bounded by a mortar matrix which is developed by mixture of aggregates of smaller sizes and cement paste matrix (Folker H. Wittmann, 1983). While previous mesomechanical numerical tools examined the effect of mesostructure morphological properties as well mechanical properties on fracture behavior in the heterogeneous mortar and concrete, prior research has disregarded the strong interaction between the progress of cement paste hydration in conjunction with the morphological and mechanical properties of aggregates, and the effect of this combination on the probability of premature cracking in cementitious composites.

*Motivation 4*: To gain insight into the synergistic effect between heterogeneous (macro-)structure, provided by the interface, and carefully designed architecture inspired by nature on shrinkage-induced damage in additively manufactured cement-based materials.

As discussed in motivation 3, precise estimation of early-age physical properties of HPC is imperative in many structural applications such as concrete pavements, slabs, and bridges (W. J. Weiss et al., 2000). Besides the incorrect application of maturity method, a primary short-term durability issue of these thin (i.e., low thickness-to-width and low thickness-to-length ratios) structures with low w/c are premature cracking associated with multiple shrinkage mechanisms. Three water-related shrinkage mechanisms of plastic, autogenous, and drying are most likely to be responsible for the development of in-pore tensile stresses, which leads to detrimental early-age micro- and macro-cracking. Given the fact that prior research has extensively explored the

underlying physical mechanisms responsible for shrinkage cracking (Cohen et al., 1990; Ghourchian et al., 2018b; Lura et al., 2003; William Jason Weiss, 1999), and thus provided mitigation strategies for alleviating the corresponding detrimental effect on short-term durability of traditionally concrete cast specimens (D. P. Bentz & Jensen, 2004; Ghourchian et al., 2018a; Radlinska et al., 2008), the rise of novel processing technique of digital fabrication (also known as additive manufacturing and 3D printing) allows for controlling the architecture and associated anisotropy behavior of extrudable cementitious composites (Biernacki et al., 2017; Gosselin et al., 2016; Lim et al., 2012; Perrot & Amziane, 2019; Sanjayan & Nematollahi, 2019). As a result, the fabrication of 3D printed specimens creates a unique opportunity by utilizing the creation of interface regions between filament layers and thus the creation of an extra level of anisotropy, which leads to arresting the shrinkage associated microcrack development and preventing their adverse effect on the mechanical performance of specimen. In simple words, while printed filament behaves identical to their cast counterparts under shrinkage loading, the creation of interface regions as "cold spots" for shrinkage-induced microcrack growth results in localizing the progressive damage. The claim of this novel proposal is in contrary with the current literature, as it is considered that fast rate of shrinkage deformation in filament layers, combined with mechanical properties dissimilarity of neighboring printed filaments can result in significant deformation and causing damage in the 3D printed specimen, ultimately causing a quicker premature failure compared to cast specimens.

## 1.3 Objectives of this study

This study aims at establishing a fundamental understanding of complex physical behavior of cementitious composites at multiple length scales, and extending our knowledge to (1) develop novel sustainable infrastructure materials that exhibit paradigm-shifting properties, (2) provide robust guidelines on enhancing their service life through combining the state-of-the-art computational and experimental findings to distinguish the primary physical mechanisms that lead to a specific durability issue. As a result of a comprehensive analysis of the physical behavior of damaged specimens, appropriate solutions to reducing the risk of premature cracking are proposed. The sub-objectives are found below:

1) To identify factors that affect the internal frost damage in porous cementitious composites with inherent fluid-solid coupling.

2) To harness the incorporation of phase change material for alleviating the frost damage in porous cementitious composites.
3) To understand the primary competing fracture mechanism in cementitious composites at multiple length scales, and its effect on the prediction of tensile mechanical properties by maturity (empirical) method.
4) To learn about an intertwined relationship between the presence of heterogeneous interfaces fabricated by additive manufacturing, and novel bio-inspired architecture, how these two structural features promote a novel and complex localization-delocalization damage mechanism.

## 1.4 Organization of Thesis

This thesis contains five chapters. Its layout is addressed as follows:

- Chapter 1: Introduction
- Chapter 2: Computational heat transfer modeling of wet cement mortar: the role of curvature effect
- Chapter 3: Enhancing the freeze-thaw performance of cementitious composites through the incorporation of phase change material (PCM)
- Chapter 4: A two-step multiscale model to predict early-age strength development of cementitious composites considering competing fracture mechanisms
- Chapter 5: Toward fabrication of enhancing damage-tolerant architecture cement-based material
- Chapter 6: Conclusion

In the first chapter, the literature review, motivations, and objectives of this work are described thoroughly. Besides, the structure and organization are deliberated in the first chapter. In the second chapter, the interplay between the role of curvature and associated capillary pressure, and the undercooling phenomenon on the macroscopic thermal response of air-entrained mortar is investigated. This chapter simulates the heat flow and associated phase transformation events during thermal cycling in partially and fully saturated mortar specimens. This chapter was used to

develop a paper published in 2017 titled “Numerical simulation of the freeze-thaw behavior of mortar containing deicing salt solution” (Hadi S. Esmaeeli et al., 2017); and the contributions of Prof. Amir Yaghoob Farnam, Mr. Dale Bentz, Prof. Pablo Zavattieri, and Prof. Jason Weiss are greatly acknowledged.

In the third chapter, the thermal performance of organic paraffin oil as a substitute for deicing salt on reducing the number of thermal cycles and thus improving the freeze-thaw performance of a small-scale mortar specimen and a large-scale concrete specimen is analyzed. Next, the effectiveness of multiple phase change materials with various characteristic transition temperatures was examined. This chapter was used to develop a paper published in 2018 titled “Numerical analysis of the freeze-thaw performance of cementitious composites that contain phase change material (PCM)” (Hadi S. Esmaeeli et al., 2018). The contributions of Prof. Amir Yaghoob Farnam, Prof. John Haddock, Prof. Pablo Zavattieri, and Prof. Jason Weiss are greatly acknowledged.

In chapter four, a mesoscopic mechanistic approach was used to investigate the composite effect of cementitious composites on the development of early-age mechanical properties. We developed a two-step homogenization numerical framework to enable the upscaling of the physical properties of heterogenous mortar. This chapter was used to develop a paper published in 2019 titled “A two-step multiscale model to predict early-age strength development of cementitious composites considering competing fracture mechanisms” (Hadi S Esmaeeli et al., 2019); and the contributions of Dr. Mehdi Shishehbor, Prof. Jason Weiss, and Prof. Pablo Zavattieri are greatly acknowledged.

Chapter five describes a novel damage mechanism in the cementitious system by modification of hcp elements at the architectural scale. We manifested the role of weaker interfacial regions on localizing the cracking induced by shrinkage loading followed by delocalizing the cracking exerted by mechanical loading, which yields to enhancing the mechanical properties of the hcp element. This chapter will be used to develop a paper, and the contributions of Dr. Mohammadreza Moini, Prof. Jan Olek, and Prof. Jason Weiss, and Prof. Pablo Zavattieri are greatly acknowledged.

In chapter six, the results obtained throughout the research are summarized, and the summary of the conclusion of the research is provided.

# 2. COMPUTATIONAL HEAT TRANSFER MODELING OF WET CEMENT MORTAR: THE ROLE OF CURVATURE EFFECT

This chapter contains work that was originally published in Springer Nature as "Hadi S. Esmaeeli, Yaghoob Farnam, Dale P. Bentz, Pablo D. Zavattieri, W. Jason Weiss. Numerical simulation of the freeze–thaw behavior of mortar containing deicing salt solution. In Journal of Materials and Structures. Volume 50., pp. 1-20. Springer, Cham, 2017." The original article has been used with permission as stated below.



## 2.1 Introduction

Prediction of phase transformation within the pores requires an understanding of heat flow within a mortar during a freezing/thawing cycle (Han et al., 2006; Radjy, 1968). For this discussion, the term "latent heat" is used to denote the amount of energy released or absorbed during a phase transformation (formation or melting of ice or eutectic solid). The latent heat produced by the phase transformation of the pore solution can be used to quantify the amount of pore solution in concrete that freezes (Powers, 1945). Two main phenomena affect the freezing of pore solution in a mortar/concrete: (1) its pore size distribution and (2) undercooling. The former influences its freezing. Concrete pores are typically categorized into three main classes: 1) gel pores with a radius smaller than 5 nm that is associated with the formation of cement (binder) hydration products, 2) capillary pores that are the remnants of the original water-filled space between (cement) particles and commonly range from 5 nm to 5 µm in radius, and 3) pores (voids) associated with entrained or entrapped air that range from 5 µm to 10 mm (Castro, Bentz, et al., 2011; Kumar & Bhattacharjee, 2003; Whiting & Nagi, 1998; Young, 1988). The size of the pores in the concrete can influence the temperature at which freezing occurs. This is described using the Gibbs-Thomson equation (Z. Sun & Scherer, 2010a). A large fraction of water associated with pore sizes greater than 5 nm (i.e., capillary pores or pores associated with entrained or entrapped air) is susceptible to freezing at a temperature above -10 °C (Cai & Liu, 1998; Yaghoob Farnam, Bentz, Sakulich, et al., 2014; W. Li et al., 2012). According to the Gibbs-Thomson equation, the water absorbed in the gel pores will not begin to freeze until the temperature of the specimen drops to

about -13 °C (Cai & Liu, 1998; W. Li et al., 2011; Z. Sun & Scherer, 2010b). It is also worth mentioning that the solution inside concrete pores (i.e., pore solution) contains different ionic species (such as $Na^+$, $K^+$, $Ca^{++}$, and $OH^-$) (Andersson et al., 1989) that depress its freezing temperature (Mehta, P. K. and Monteiro, 2006). The absorption of salt solution into the pores can further depress the freezing temperature of this pore solution, due to the presence of additional ions such as $Cl^-$ (Beddoe & Setzer, 1988; Pigeon & Pleau, 2010; G. Scherer, 1999).

Undercooling also influences freezing in concrete. While it is expected that a solution freezes at its characteristic melting point temperature, $T_m$, freezing usually occurs at a temperature (i.e., $T_f$) lower than $T_m$. This reduction in freezing temperature is known as undercooling (Askeland & Pradeep, 2003; Debenedetti, 2003; Wilding, 1992) and is primarily since solidification (in most cases) requires the presence of or formation of nuclei that can trigger the freezing action. Once the heterogeneous nuclei are present in the liquid phase, ice crystals begin to nucleate/grow. Consequently, the latent heat of fusion is released into the undercooled liquid, increasing the temperature of the liquid toward $T_m$. The growth of ice continues until the temperature of the liquid reaches $T_m$ (Askeland & Pradeep, 2003). Afterward, the temperature of the liquid remains at $T_m$ until the entire liquid solidifies; this is known as thermal arrest (Askeland & Pradeep, 2003). After thermal arrest, the amount of ice increases gradually as the further temperature decreases. Melting, however, occurs gradually in the pores as the temperature of each pore reaches its $T_m$ value (Yaghoob Farnam, Bentz, Sakulich, et al., 2014; Qian et al., 2014; Z. Sun & Scherer, 2010b). The amount of ice transformed to solution increases gradually as each set of larger pores, in turn, reaches the associated $T_m$ (according to the Gibbs-Thomson equation) (Z. Sun & Scherer, 2010b, 2010c).

These two phenomena (i.e., pore size and undercooling) affect the freezing behavior of pore solution simultaneously in the mortar specimen and it may be essential to consider both in the simulation during freezing. In melting, however, only pore size influences the thawing behavior. Numerically, it is feasible to develop a theoretical model based on the heat transfer formulation to predict and simulate phase transformation and heat transfer in materials (L. C. Thomas, n.d.; Velraj et al., 1999). One-dimensional finite difference (D. Bentz, 2000; Dale P. Bentz & Turpin, 2007; Costa et al., 1998; Lecomte & Mayer, 1985; Velraj et al., 1999), the two-dimensional finite difference (Dale P. Bentz & Turpin, 2007; Costa et al., 1998; Ismail & Abugderah, 2000; Velraj et al., 1999; Zivkovic & Fujii, 2001), control volume (Fukai et al., 2003; Hamada et al., 2003;

Ismail & Da Silva, 2003; Voller & Swaminathan, 1993), and finite element (Gong & Mujumdar, 1997; Rubinsky & Cravahlo, 1981; Yoo & Rubinsky, 2007) based methods all have been used to simulate such heat transfer problems. In this paper, a one-dimensional finite-difference model is used. In particular, this numerical method approximates the complex solid-liquid interactions in the porous mortar using a fixed grid method (Hibbert et al., 1988; Shamsundar & Sparrow, 1975). The computational model is applied to estimate the thermal behavior of mortar containing in-pore water under freeze-thaw cycles. The formation of ice is quantified by calculating the volume fraction of ice that is produced (Callister & Rethwisch, 2009; Smith & Hashemi, 2006). As the ice grows, the liquid to solid phase transformation releases latent heat, $\Delta H_f$ , that increases the temperature of the material locally and slows down the ice growth. An empirical approach is used to account for the sudden latent heat release produced by undercooling. This model is also used to describe, analyze and interpret the experimental data obtained from low-temperature longitudinal guarded comparative calorimeter (LGCC) tests (Yaghoob Farnam, Bentz, Hampton, et al., 2014; Yaghoob Farnam, Bentz, Sakulich, et al., 2014).

### 2.2 Numerical Simulation of Heat Transfer Coupled with Phase Transformation

The main objective of this study is to predict the thermal response of a mortar (considered at a macroscopic scale) that is experiencing phase transformations during a reduction and subsequent increase in specimen temperature (i.e., a freezing and thawing cycle). The goal of the simulations is to quantify the fraction of pore solution that can freeze in an undercooled mortar specimen. The temperature of the specimen can be tracked by solving the heat (energy balance) equation and considering the frozen fraction of the pore solution. The governing equation for the heat transfer within a mortar specimen can be described using the energy balance equation 2-1 (Incropera et al., 2007).

$$\frac{\partial}{\partial x}\left[k_m(T)\cdot\frac{\partial T(x,t)}{\partial x}\right]+q_{gen}-q_{loss}=\rho_m(T)\cdot C_m^p(T)\cdot\frac{\partial T(x,t)}{\partial t} \qquad 2\text{-}1$$

where $T(x,t)$ is the temperature at location $x(mm)$ and time $t(\sec)$, $k_m(T)$ is the thermal conductivity of the mortar specimen $[W/(m\cdot K)]$ at temperature $T$, $\rho_m(T)$ is the density of the mortar specimen $\left(kg/m^3\right)$ at temperature $T$, $C_m^p$ is its specific heat capacity $[J/(kg\cdot K)]$ at

temperature $T$, $q_{gen}$ is the rate of generated or consumed heat from any phase change of the pore solution $\left[J/\left(m^3 \cdot \sec\right)\right]$, and $q_{loss}$ is the rate of heat dissipation (to the environment) in the experiment $\left[J/\left(m^3 \cdot \sec\right)\right]$.

In Equation 2-2a, the incorporation of a released/absorbed latent heat term, $q_{gen}$ associated with the freezing/melting of the pore solution within a mortar specimen is described. A heat sink term $q_{loss}$ is also included, as shown in equation 2-2b, to calculate the rate of heat dissipation to the environment (even though insulation is present). This heat term is considered as a fraction of the rate of generated latent heat to simulate the significant heat exchange between the mortar specimen and its surroundings in the lateral directions.

$$q_{gen} = \Delta H_f \cdot \rho_{sol} \cdot v_P \cdot \frac{\partial[v_F(T) \cdot \xi(T)]}{\partial t} \qquad 2\text{-}2a$$

$$q_{loss} = \Delta H_f \cdot h_{loss} \cdot \rho_{sol} \cdot v_P \cdot \frac{\partial[v_F(T) \cdot \xi(T)]}{\partial t} \qquad 2\text{-}2b$$

$$q_{gen} - q_{loss} = \Delta H^m{}_f \cdot \rho_{sol} \cdot v_P \cdot \frac{\partial[v_F(T) \cdot \xi(T)]}{\partial t} \qquad 2\text{-}2c$$

where $\Delta H_f$ is the latent heat of fusion $\left(kJ/kg\right)$, $\rho_{sol}$ is the density of pore solution $\left(kg/m^3\right)$, $v_p$ is the total volume fraction of pores within the mortar specimen (0 to 1), $v_F\left(T\right)$ is the volume fraction of the pore solution that can freeze at temperature $T$ (0 to 1), $\xi\left(T\right)$ is the frozen volume fraction of freezable pore solution with salt at temperature $T$ (0 to 1), $h_{loss}$ is the heat dissipation coefficient (< 1), and $\Delta H_f^m = \Delta H_f \cdot \left(1 - h_{loss}\right)$ is the apparent latent heat measured considering heat dissipation during phase transformation in the system (< $\Delta H_f$).

### 2.3 Frozen fraction of pore solution without salt, $v_F(T)$

The mortar specimens contain a pore structure with a broad range of sizes. The pore size can alter the freezing temperature of water (Beddoe & Setzer, 1988; Kaufmann, 2000; Mehta, P. K. and Monteiro, 2006; G. Scherer, 1999). To determine the pore size distribution in the mortar

specimen and thus to calculate $v_F(T)$, a desorption isotherm was obtained for the mortar using a dynamic vapor sorption analyzer (TA Q5000). The vacuum saturation method is used to fully saturate the mortar specimen (i.e., $D_S$ = 100 %). Therefore, all of the pores, including air voids, are filled with water, to investigate the role of curvature of the pores on the thermal behavior of the mortar. For melting, the pore size distribution obtained from an absorption isotherm is used (Litvan, 1972). Figure 2-1 provides the desorption-absorption isotherm for the mortar specimen, and it correlates the degree of saturation $(D_S)$ to the relative humidity $(RH)$, which is the amount of water vapor present in the specimen expressed as a percentage of the amount needed for saturation at the same temperature (Villani et al., 2015). A characteristic hysteresis is observed in the absorption/desorption isotherm in Figure 2-1, at least partially due to the presence of "ink-bottle" pores.

To calculate $v_F(T)$, two approaches were evaluated in this study: (1) a model with explicit consideration of a continuous pore size distribution, and (2) a phenomenological model with consideration of only a discrete pore size distribution. The first approach considers the effect of all pore sizes on the freezing process and $v_F(T)$ varies continuously as the temperature changes. In the second approach, the effect of a discrete pore size distribution on ice formation inside the mortar specimen is simplified. A phenomenological model is adapted to simulate the freezing process of water inside the mortar specimen (it considers only two classes of pores- large pores that include all pores except gel pores (the capillary and air-entrained/entrapped pores) and small pores (known as gel pores)).

In the phenomenological model, $v_F(T)$ is considered to be a constant value based on three main classes of pores: 1) gel pores, 2) capillary pores, and 3) water-filled pores associated with entrained or entrapped air. To investigate the accuracy of these two approaches, the LGCC test conducted by Farnam et al. (Yaghoob Farnam, Bentz, Hampton, et al., 2014; Yaghoob Farnam, Bentz, Sakulich, et al., 2014) was simulated using these two models with consideration of continuous and discrete pore sizes, respectively. Also, the thermal behavior of the mortar specimens saturated with water was compared with experimental results obtained in a temperature range between 24 °C and -35 °C.

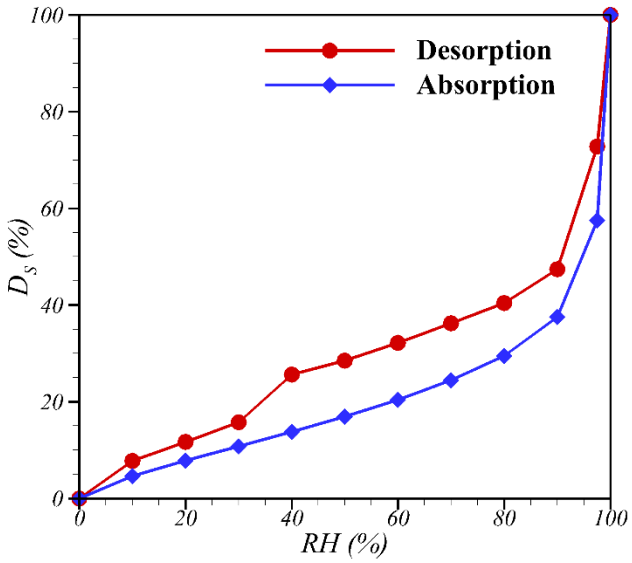

Figure 2-1. Desorption-absorption isotherms of mortar specimen.

### 2.3.1 A model with consideration of a continuous pore size distribution

Equation 2-3 describes the Gibbs-Thomson equation that relates the freezing temperature of a liquid inside a porous material to the pore radius.

$$\frac{2\gamma_{CL}}{r^*} \approx \left(\frac{S_L - S_C}{V_L}\right)\left(T_m - T_f\left(r^*\right)\right) \qquad 2\text{-}3$$

where $\gamma_{CL}$ is the crystal/liquid interfacial energy $\left(J/m^2\right)$, $r^*$ is the radius of the pore for homogeneous nucleation $(m)$, $S_L$ and $S_C$ are the molar entropies of the liquid and crystalline phases $[J/(mol\cdot K)]$, $V_L$ is the molar volume of the liquid $\left(m^3/mol\right)$, $T_m$ is the melting temperature $(K)$, and $T_f$ is the freezing temperature as a function of pore radius $(K)$(Brun et al., 1977; Z. Sun & Scherer, 2010b). Therefore, the temperature at which ice begins to form can be predicted as a function of the critical pore radius $r^*$ by solving Equation 2-3 for $T_f$ (Z. Sun & Scherer, 2010a, 2010b, 2010c).

Figure 2-2 displays the relationship between the size of the pore and the temperature that is needed to freeze water inside the pore $T_f\left(r^*\right)$. At a temperature above $T_f\left(r^*\right)$, no phase

transformation occurs inside the pores with a radius less than $r^*$. Once the temperature reaches the associated freezing temperature, ice begins to form inside the pores with radii $r^*$. Afterward, ice propagates into the smaller pores, but only as the temperature drops further. This process is reversed during melting.

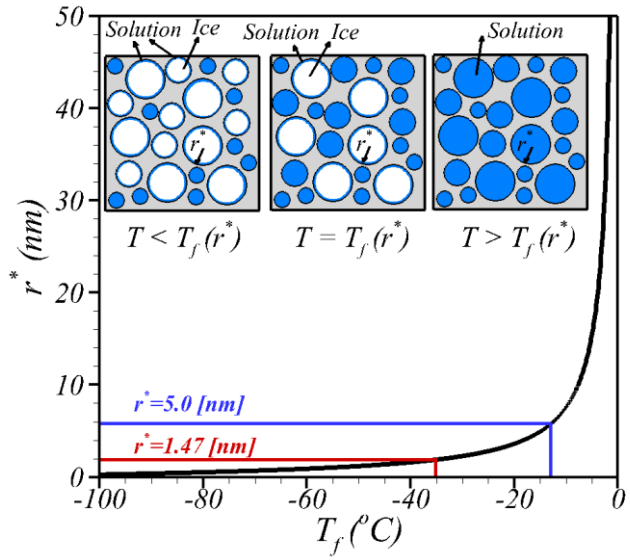


Figure 2-2. The effect of pore size on the freezing temperature of the water using the Gibbs-Thomson equation, including a schematic of ice formation in a porous material (inset).

The Kelvin-Young-Laplace equation can be used to correlate the pore radius to the relative humidity $(RH)$ in a water-filled pore as described in Equation 2-4 (Henkensiefken et al., 2009; Radlinska et al., 2008).

$$r^* = \left(\frac{2\gamma}{\ln(RH)}\right)\cdot\left(\frac{V_m}{RT}\right) \qquad 2\text{-}4$$

In this study, the Kelvin-Young-Laplace equation (Equation 2-4) was used alongside the Gibbs-Thomson equation (Equation 2-3) to obtain the relationship between $v_F(T)$ and pore size in the mortar specimen based on its measured desorption isotherm (Figure 2-1). At a temperature of -35 °C, solution absorbed into the mortar pores with sizes greater than 1.47 nm is susceptible to freezing, as shown in Figure 2-2. Figure 2-2 also displays the process of ice formation in a porous material, as the ice forms inside the larger pores initially. Ice invades into the smaller pores

progressively as the temperature drops. Figure 2-3 shows that 72 % of the solution absorbed in the pores by volume can freeze between 0 °C and -35 °C. For the case of melting, the formed ice in the pores is similarly considered to melt gradually according to the Gibbs-Thomson equation (Equation 2-3). In this work, it is assumed that $1 = v_{air} + (D_S/100)$ and $(D_s/100) = v_w(r < r^*) + v_F(r > r^*)$ where $v_{air}$ and $v_w$ are the volume fraction of air and non-freezable pore solution in the total pores (0 to 1), respectively. To investigate the role of pore sizes, all of the pores with various sizes are assumed to be filled with water in this section, i.e., $v_{air} = 0$. It should be mentioned that the LGCC test was conducted within a temperature range between 24 °C and -35 °C.

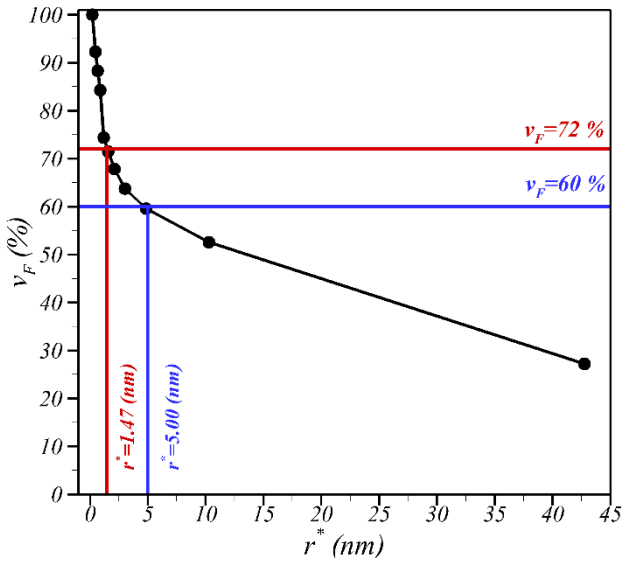


Figure 2-3**.** Volume fraction of pore solution that can freeze as a function of the critical nucleus (pore) size.

### 2.3.2 A phenomenological model with consideration of a discrete pore size distribution

Although the continuous pore size distribution can be estimated to determine the volume fraction of the freezable pore solution, this measurement is generally not available for field/commercial concretes. In this paper, a phenomenological model is developed to use in practice, when knowledge of the continuous pore size distribution is not available. Since the freezing and thawing responses of most cementitious systems are dominated by the category of relatively large pores (i.e., capillary, air-entrained, and air-entrapped pores), a discrete pore size of

5 nm (a pre-defined critical pore size as the division between gel and capillary pores) can be utilized as a criterion to differentiate the freezable and non-freezable pore solution (W. Li et al., 2012; Z. Yang et al., 2006; Young, 1988). For a mortar specimen saturated with deionized water, this critical pore radius corresponds to a relative humidity $(RH)$ equal to 81 %. At this point, all of the gel pores are filled by a solution (Radlinska et al., 2008).

The corresponding freezing temperature of water in pores with a size of 5 nm is about -13 $^{o}$C according to the Gibbs-Thomson equation as displayed in Figure 2-2. Figure 2-3 displays the relation between derived volume fraction of freezable pore solution, $v_F$ from associated relative humidity measured in experiments, and pore radius, $r^*$, using Equation 2-4. The corresponding volume fraction of freezable pore solution, $v_F$, in pores with size greater than 5 nm is measured to be 60 % concerning the total volume fraction of pores displayed in this figure. Consequently, the volume of freezable pore solution in the phenomenological model is underestimated by about 16 % concerning the model with direct consideration of pore size distribution, assuming pure water to be the solution in the pores. This implies that 60 % of the total solution by volume, corresponding to the solution that is absorbed into large pores (i.e., capillary pores, air-entrained pores, and air-entrapped pores) begins to transform to ice instantaneously. The gradual process of ice formation in the remainder of the freezable pores (i.e., smaller pores, containing a lower volume fraction) will be neglected. Therefore, the radius of curvature (pore size) would have a relatively small impact on the macroscopic freezing response of the air-entrained mortar specimen, and the approach of a discrete pore size distribution will be implemented in the numerical model to investigate the thermal behavior of mortar specimens containing NaCl solutions.

To develop a reliable numerical simulation at the macro-scale, it is essential to define the material properties accurately. For detailed information on the utilization of homogenization techniques for calculation of the thermal properties of the mortar specimen, the readers are suggested to read my master's thesis (Hadi Shagerdi Esmaeeli, 2015).

### 2.4 Configuration of numerical simulation and boundary conditions

Following the work by Farnam et al. (Yaghoob Farnam, Bentz, Sakulich, et al., 2014), the LGCC test was simulated to quantify heat flow and predict the temperature profiles of the mortar specimens. Two types of experimental data are used: 1) fully saturated mortar specimens (i.e., 100 %

degree of saturation) with solutions containing 0 %, 5 %, 10 %, and 23.3 % NaCl (by mass), and 2) specimens saturated partially with water (i.e., no NaCl involved in the solution) at degrees of saturation equal to 75 %, 85 %, 95 %, and 100 %. The procedures used for the preparation of fully saturated and partially saturated mortar specimens were addressed in previous experimental works (Yaghoob Farnam, Bentz, Sakulich, et al., 2014; Yaghoob Farnam, Esmaeeli, et al., 2015; Yaghoob Farnam, Todak, et al., 2015).

The experimental conditions of one-dimensional heat transfer were provided in the LGCC experiment by using a heat sink at the bottom, longitudinal insulation on the sides, and foam as thermal insulation around the system to minimize the heat dissipation from the experimental apparatus (Figure 2-4a). However, a difference between the measured released heat in an LGCC experiment and the associated enthalpy of fusion of phase change materials (i.e., Methyl Laurate and Paraffin Oil), likely due to experimental imperfections (thermal bridges, heat leaks, etc.), was observed. Therefore, $h_{loss}$, a heat loss coefficient, is employed to simulate the energy dissipation in the experimental system, which is estimated as a 40 % to 60 % heat loss (Yaghoob Farnam, Krafcik, et al., 2015). It is worth mentioning that the advection of heat to simulate the water transport occurring during the freeze/thaw cycle is neglected in this numerical investigation.

Two references (meter) bars made of Pyroceram code 9606[1] with known thermal properties were used to measure the heat flow passing through the mortar specimen in the experiment (see Figure 2-4a.

[1] Certain commercial products are identified in this paper to specify the materials used and procedures employed. In no case does such identification imply endorsement or recommendation by the National Institute of Standards and Technology or Purdue University, nor does it indicate that the products are necessarily the best available for the purpose.

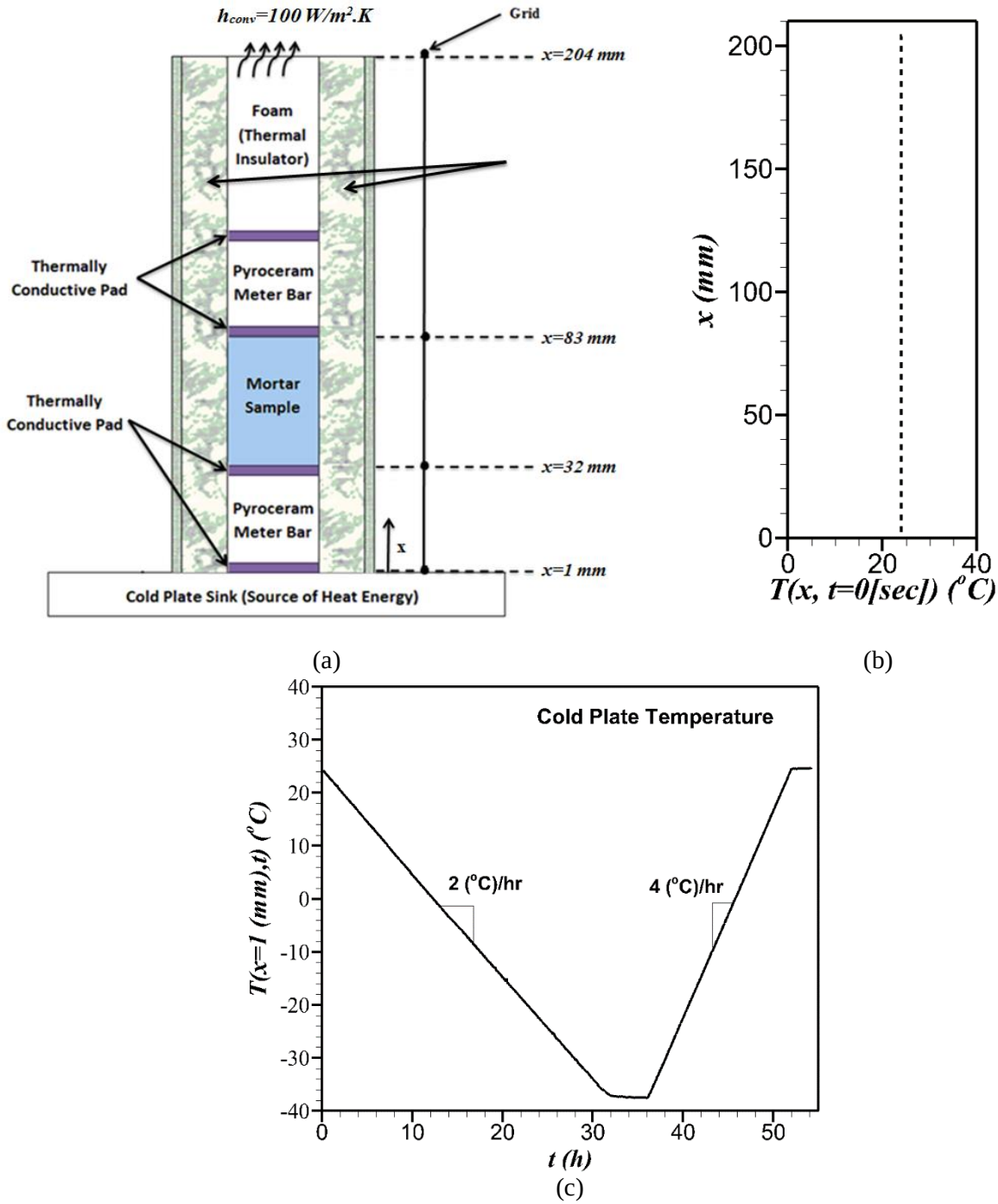


Figure 2-4. (a) Schematic view of LGCC experiment with adapted finite-difference nodes; (b) initial temperature of finite difference simulation, i.e., T (x,t = 0); and (c) temperature at the bottom of the LGCC experiment, i.e., T (x = 1,t), as a function of time.

Table 2-1. Thermal properties of the thermally conductive pad, foam and Pyroceram code 9606

| Material | $k$ *(W/(m·K))* | ρ *(kg/m$^3$)* | $C^p$ *(kJ/(kg·K))* |
|---|---|---|---|
| Thermal Pad | 3.0 | 309 | 850 |
| Foam (Williams & Aldao, 1983) | 0.03 | 20 | 1340 |
| Pyroceram Code 9606 (Yaghoob Farnam, Bentz, Sakulich, et al., 2014) | * | 2600 | 900 |

Note: *The thermal conductivity of Pyroceram code 9606 as a meter bar material was calculated as a function of temperature (Yaghoob Farnam, Bentz, Sakulich, et al., 2014).

The first step in the numerical approach was to discretize the experimental setup by a finite difference method using an appropriate grid spacing size, $\Delta x$ of 1 (mm) and time step, $\Delta t$ of 0.05 (sec). The initial temperature of the entire experimental setup was set equal to the ambient temperature $T\ (x, t=0)$ = 24 (°C), as displayed in Figure 2-4b. The temperature at the bottom of the LGCC experiment, $T\ (x = 1\ mm,\ t)$ (see Figure 2-4a), varied in the numerical simulation as a function of time according to the LGCC experimental protocol (Figure 2-4c). A heat convection coefficient $h_{conv}$ = 100 W/(m$^2$·K) is employed to simulate the heat transfer between the air and the foam on the top (Incropera et al., 2007). Even though the insulating foam has quite a small thermal diffusivity parameter, significant heat energy is still transferred to the environment, resulting in a slight temperature differential between the top of the foam and the ambient environment. The relevant thermal properties of the thermally conductive pad, foam, and Pyroceram code 9606 used in the modeling are listed in Table 2-1.

Figure 2-5 displays a flow chart of the one-dimensional explicit finite difference method adopted to simulate the saturated mortar specimen containing de-ionized water and NaCl solution with various concentrations. First, the thermal properties of components of the mortar specimen, temporal and spatial step sizes, and thermal initial and boundary conditions are determined. All of the discretized layers (i.e., x = 1 mm to x = 204 mm) are employed to simulate the heat transfer for the LGCC experiment; however, only the finite layers of the mortar specimen (i.e., x = 32 mm to x = 83 mm) are investigated in this figure. During phase transformation of the pore solution in the mortar specimen filled with de-ionized water, two approaches of consideration of either a discrete pore size distribution or a continuous pore size distribution were employed. The approach

of using a distribution of continuous pore sizes introduces a progressive ice formation/melting in the pores that are simulated using equations 2-3 and 2-4 and Figure 2-1; however, the volume fraction of pores with the size greater than 5 nm ($v_F$ = 60 %) is considered to simulate the instantaneous ice formation/melting occurring in the approach of using discrete pore sizes. Additionally, the progressive fraction of produced/melting ice is calculated using the lever rule.

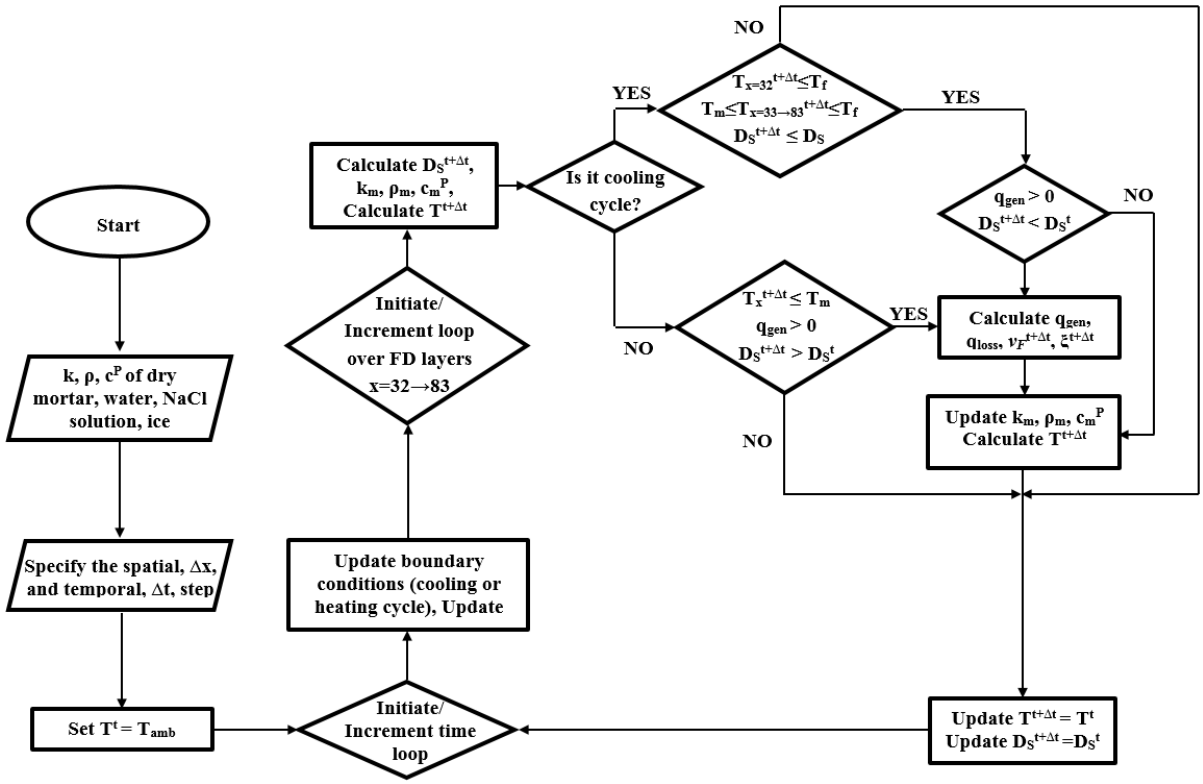


Figure 2-5**.** Numerical algorithm of finite difference strategy using heat transfer equation to simulate the thermal behavior of a saturated mortar specimen.

## 2.5 Results and discussion

In this section, mortar specimens saturated with water at 75 %, 85 %, 95 %, and 100 % degrees of saturation ($D_S$) and the effect of pore size distribution are numerically investigated.

### 2.5.1 Fully saturated mortar specimen

Two numerical models, with either a continuous or discrete pore size distribution, are investigated in this section. Figure 2-6 shows the experimental and numerical results for the

thermal behavior of mortar specimens that were saturated (i.e., $D_S = 100$ %) with water. The heat loss coefficient, $h_{loss}$ is assumed to be a constant value of 60 % in this figure. The model with a discrete pore size distribution only considers the instantaneous freezing of the pore solution that can freeze ($v_F = 60\,\%$). In contrast, the model with the continuous pore size distribution also considers an additional process of gradual freezing of the pore solution ($v_F = 72\,\%$), as displayed in Figure 2-6(c). Figure 2-6(a) indicates the numerical and experimental temperature profile for the saturated mortar specimen at the bottom layer in the LGCC experiment setup (i.e., $x = 32$ mm). A nearly instantaneous temperature rise that occurred at the moment of freezing can be observed, demonstrating the instantaneous freezing due to the temperature of the first finite difference layer of the mortar specimen (i.e., $x = 32$ mm) reaching the freezing temperature of (undercooled) water in the mortar specimen ($T_f = -6.1$ °C). However, the model with a continuous pore size distribution considers that the remaining amount of unfrozen water in the pores transforms to ice gradually until the temperature reaches $-35$ °C.

The model with a discrete pore size distribution considers the ice melting to occur by absorbing sufficient heat at the melting temperature of the large frozen pores observed in the experiment ($T_m = 0$ °C). In the model with a continuous pore size distribution included, the ice formed in the pores is considered to melt gradually starting at $-35\,^{o}$C (Z. Sun & Scherer, 2010b), based on the measured absorption isotherm for the mortar.

The heat flow is obtained using the numerical simulation to evaluate the role of pore size distribution and compared to the experimental data shown in Figure 2-6(b). The formation of ice in the pore solution results in an exothermic peak, which is representative of the latent heat released during a freezing cycle**.** In the model with a discrete pore size distribution, the exothermic peak is considered to occur at $T_f$. Subsequently, it ceases when the entire amount of latent heat has been emitted to the surroundings. The endothermic peak begins as a gradual process at 0 °C until all of the previously formed ice melts inside the frozen pores.

Conversely, the exothermic peak is extended to the end of the freezing cycle ($-35$ °C) due to gradual ice nucleation inside the smaller pores in the model with a continuous pore size distribution. For the case of melting, the endothermic peak is considered to occur gradually as a function of temperature and the pore size.

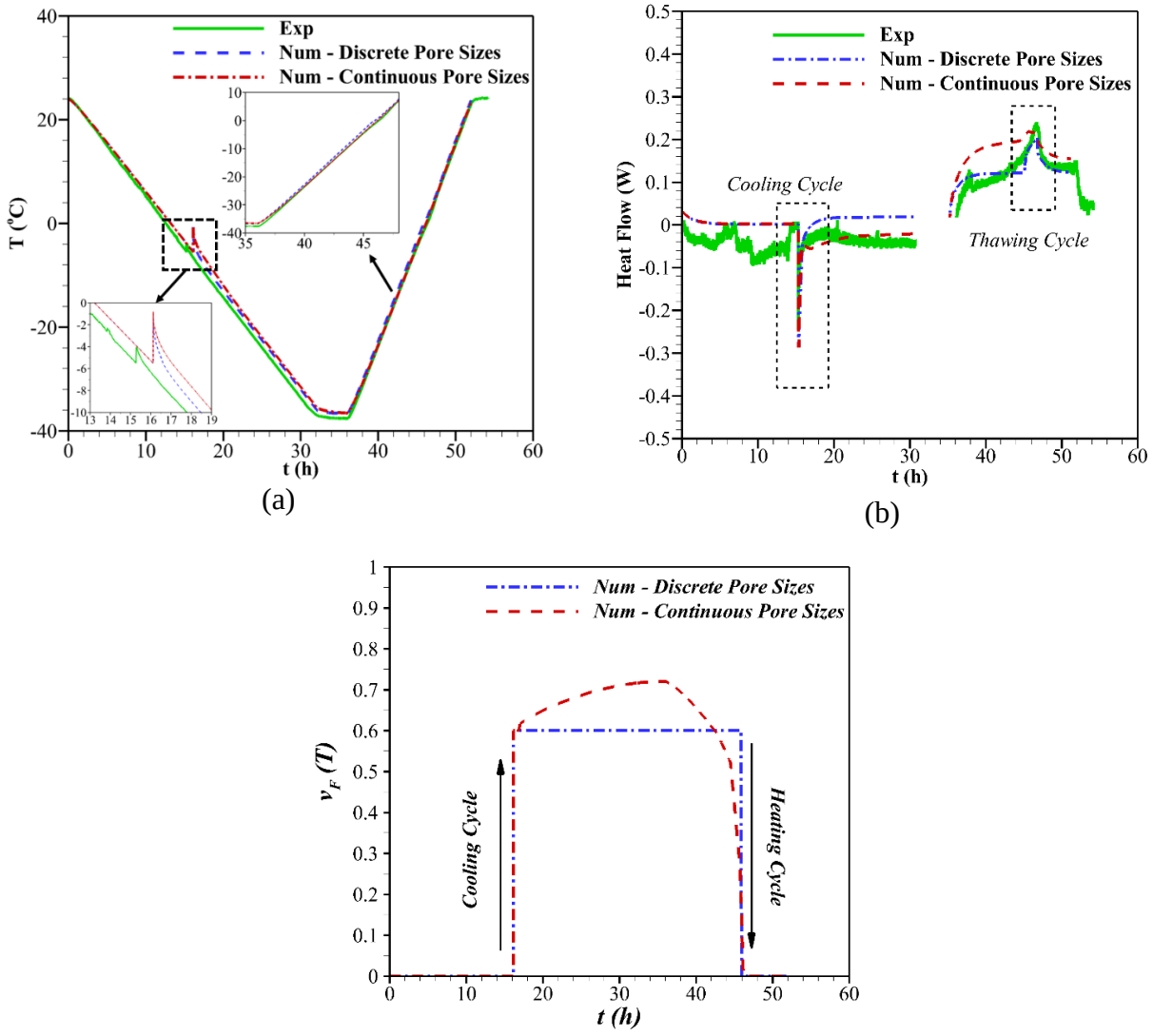


Figure 2-6. Experimental and numerical results for mortar specimen fully saturated with water (a) temperature profiles at $x$ = 32 mm (see Figure 2-1 for the definition of $x$); (b) predicted heat flow; (c) volume of pore solution undergoes a phase transformation at the bottom surface of the mortar specimen.

Therefore, the melting curve extends progressively to 0 °C, owing to the broad range of pore sizes in the model with a continuous pore size distribution. It is concluded that the consideration of pore size distribution can reasonably be neglected during the freezing process due to undercooling. In contrast, the melting of formed ice indicated a gradual process as the temperature increases in both the experimental data and the model with a continuous pore size distribution.

#### 2.5.1.1 **Partially saturated mortar specimen**

The amount of heat released during freezing $\left(\Delta H_m^F\right)$ was obtained using the numerical simulation for mortar specimens saturated at different degrees of saturation with the discrete pore size distribution model and is compared with experimental results in Figure 2-7. For partially saturated specimens, the value of $v_F$ was calculated using $v_F=D_S-v_w$, where $v_w$ is the volume fraction of pores with a size of less than 5 nm ($v_w$ = 40 %). The results for these partially saturated mortar specimens are the experimental investigation of this work, whereas the experimental data of the fully saturated mortar specimen was already published (Yaghoob Farnam, Bentz, Sakulich, et al., 2014). Two heat dissipation coefficients of 40 % and 60 % are considered. The coefficient of variation for the experimental results is obtained at 8.6 %. The numerical simulation predicts greater heat release than that obtained in the experiment due to further experimental imperfections.

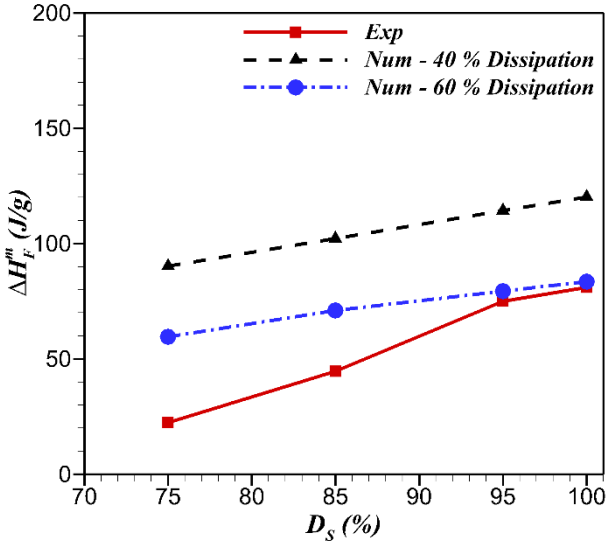


Figure 2-7. The amount of heat released during freezing ($\Delta H_m^F$) for the mortar specimen saturated at different degrees of saturation ($D_S$).

The amount of heat released during freezing ($\Delta H_m^F$) was obtained using the numerical simulation for mortar specimens saturated at different degrees of saturation with the discrete pore size distribution model and is compared with experimental results in Figure 2-7. For partially saturated specimens, the value of $v_F$ was calculated using $v_F=D_S-v_w$, where $v_w$ is the volume fraction of pores with a size of less than 5 nm ($v_w$ = 40 %). The results for these partially saturated mortar

specimens are the experimental investigation of this work, whereas the experimental data of the fully saturated mortar specimen was already published (Yaghoob Farnam, Bentz, Sakulich, et al., 2014). Two heat dissipation coefficients of 40 % and 60 % are considered. The coefficient of variation for the experimental results is obtained at 8.6 %. The numerical simulation predicts greater heat release than that obtained in the experiment due to further experimental imperfections.

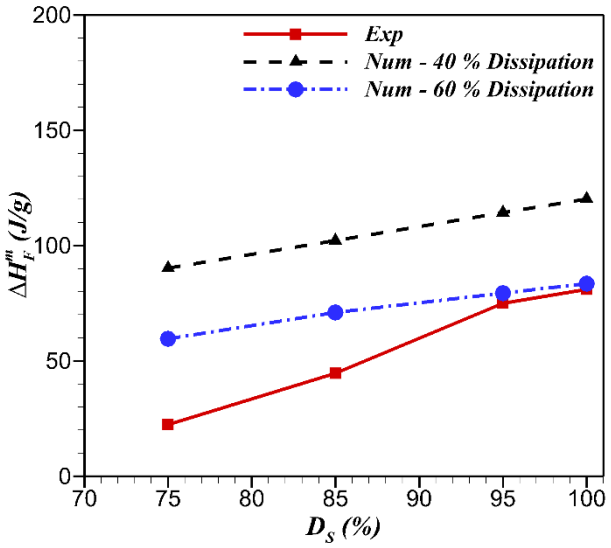


Figure 2-8 The amount of heat released during freezing ($\Delta H_m^F$) for the mortar specimen saturated at different degrees of saturation ($D_S$).

## 2.6 Summary and conclusion

In this paper, a one-dimensional finite difference numerical model was used to predict the macroscopic freeze-thaw behavior of air-entrained mortar specimens. The effective thermal properties of the composite mortar were estimated using homogenization techniques. The role of curvature, owing to a broad range of pore sizes, was considered in calculating the volume fraction of freezable pore solution exposed to freezing/thawing cycles using measured absorption-desorption isotherms. It was concluded that the role of pore size (or curvature) on the macroscopic behavior of the air-entrained mortar specimen was negligible during freezing due to the quantity of larger pore sizes in realistic mixtures and undercooling. In contrast, the role of curvature had a considerable impact on the macroscopic behavior of the frozen mortar specimen during melting. The lever rule approach, derived from a phase diagram of the NaCl-water solution, and

undercooling were adopted in the numerical model. It was concluded that this model can simulate the freezing and thawing process of mortar specimens saturated with water or various NaCl solutions to predict the thermal behavior of mortar specimens at various degrees of saturation or saturated with various concentrations of NaCl solutions.

The computational results were compared to the experimental ones obtained for mortar specimens saturated with NaCl solution using a low-temperature longitudinal guarded comparative calorimeter (LGCC). A lower amount of heat release (or freezable fraction of pore solutions) was observed in the experiment than the theoretical value predicted based on the measured desorption isotherm. The difference may be mainly due to experimental conditions allowing significant heat dissipation within the LGCC experiment. To justify the experimental under-estimation of heat release, two heat loss coefficients of 40 % and 60 % were evaluated to validate the numerical results. Accordingly, a better agreement was exhibited between the numerical results and the experimental data.

# 3. ENHANCING FREEZE-THAW PERFORMANCE OF CEMENTITIOUS COMPOSITES THROUGH INCORPORATION OF PHASE CHANGE MATERIAL (PCM)

This chapter contains work that was originally published in Elsevier as "Hadi S. Esmaeeli, Yaghoob Farnam, John E. Haddock, Pablo D. Zavattieri, W. Jason Weiss. Numerical analysis of the freeze-thaw performance of cementitious composites that contain phase change material (PCM). In Journal of Materials and Design. Volume 145., pp. 74-87. Elsevier, 2018." The original article has been used with permission as stated below.



## 3.1 Introduction

Two main factors affect the freezing and melting behavior of PCM impregnated within LWA: (1) the rate of heat release or absorption of bulk PCM, and (2) pore size distribution inside LWA. Low-temperature differential scanning calorimeter (LT-DSC) is a standard method to analyze the thermal energy storage capacity of PCM and to determine the thermal properties of PCM, including the transition temperature range and $\Delta H_f$-temperature relationship (Castellón et al., 2008). According to the Gibbs-Thomson equation, the pore size causes a capillary pressure in the solution inside the pore, which leads to depressing the freezing temperature of PCM, depending on the pore size (Z. Sun & Scherer, 2010b). Therefore, the size of pores in the LWA can alter the freezing temperature of PCM and the corresponding $\Delta H_f$-temperature relationship. In this work, we employ paraffin oil as the PCM. However, it is worth mentioning that undercooling does not occur to a significant extent for this particular PCM, as paraffin is chemically stable with a low vapor pressure (C. Liu et al., 2010).

Improving the freeze-thaw performance of concrete pavements would have significant economic impacts. The American Society of Civil Engineers issued a grade of "D" to America's road infrastructure, as some $67 billion was spent annually on the repair of damaged roads in 2013 (Herrmann, 2013). It is believed that PCM incorporation can be used as an effective method to increase the thermal energy storage capacity by reducing the depth and time of freezing that a concrete pavement can experience, thus minimizing concrete pavement damage. A finite-difference approach is implemented to simulate the concrete pavement considering realistic

thermal (environmental) boundary conditions. PCMs with three transition temperatures, which are all designed above the freezing point of pore solution, are considered. Year-long simulations throughout the United States are performed to demonstrate the impacts of transition temperatures and $\Delta H_f$-temperature relationship of PCMs on reducing the time and depth of freezing within the pavements. The outcomes provide new insights that are needed to ascertain the optimal PCM characteristics that mitigate the risk of freeze-thaw cycling in concrete pavements.

### 3.2 Numerical modeling

This study aims to determine the thermal behavior of cementitious composites such as mortar and concrete specimens in which the incorporated PCM undergoes phase transition during cooling and heating cycles. The heat release/absorption is determined as well as the corresponding fraction of PCM that can freeze/melt within the LWA pores. Consequently, the temperature profile and associated heat flow within the specimen can be calculated by solving the heat transfer equation shown in equation 3-1 (Hadi S. Esmaeeli et al., 2017).

$$k_c(T)\cdot\left[\frac{\partial^2 T(x,t)}{\partial x^2}\right]+\dot{q}_{latent-gen}-\dot{q}_{latent-loss}-\dot{q}_{conv}=\rho_c(T)\cdot C_c^p(T)\cdot\left[\frac{\partial T(x,t)}{\partial t}\right] \qquad 3\text{-}1$$

where $T(x,t)$ is the temperature of the specimen at the location of $x$ *(mm)* and time of $t$ *(sec)* ($^oC$), $k_c$ is the thermal conductivity of specimen at temperature $T$ [$W/(m.K)$], $\rho_c$ is the density of the specimen at temperature $T$ ($kg/m^3$), $C_c^p$ is the heat capacity of the specimen at temperature $T$ [$J/(kg.K)$], $\dot{q}_{latent-gen}$ is the rate of heat release or absorption associated with freezing or melting of PCM, as described in equation 3-2a [$J/(m^3.sec)$], $\dot{q}_{latent-loss}$ considers the rate of heat dissipation during phase transition of PCM (to the environment), as described in equation 3-2b [$J/(m^3.sec)$], and $\dot{q}_{conv}$ is the rate of heat dissipation throughout the experiment due to the temperature gradient between the specimen and surroundings (or vice versa) through convection as described in equation 3-2c [$J/(m^3.sec)$]. The heat sink term representing the heat dissipation during phase transition of PCM is a fraction of heat release/absorption $\dot{q}_{latent-loss}=\dot{q}_{latent-gen}\cdot h_{latent-loss}$ which is

determined using the dissipation coefficient of $h_{latent\text{-}loss}$ (<1) obtained from experiments (Hadi S. Esmaeeli et al., 2017; Yaghoob Farnam et al., 2017; Yaghoob Farnam, Krafcik, et al., 2015). Equation 3-2c describes a convection heat term that represents the heat dissipation to the surrounding using the convection coefficient, $h_{conv\text{-}diss}$ which is also obtained empirically (Yaghoob Farnam et al., 2017; Yaghoob Farnam, Krafcik, et al., 2015).

$$\dot{q}_{latent-gen} = \Delta H_f \cdot \rho_{PCM} \cdot v_{PCM} \cdot \frac{\partial v_F(T)}{\partial t} \quad \text{3-2a}$$

$$\dot{q}_{latent-loss} = \Delta H_f \cdot h_{latent-loss} \cdot \rho_{PCM} \cdot v_{PCM} \cdot \frac{\partial v_F(T)}{\partial t} \quad \text{3-2b}$$

$$\dot{q}_{conv} = h_{conv-diss} \cdot \left[ \frac{\partial T(x,t)}{\partial x} \right] \quad \text{3-2c}$$

where $\rho_{PCM}$ is the density of phase change materials (PCM or pore solution) within the specimen in this study (PCM or pore solution) ($kg/m^3$), $v_{PCM}$ is the volume fraction of phase change materials (PCM or pore solution), $v_F$ is the volume fraction of phase change materials (PCM or pore solution) that can freeze or melt at temperature ($T$). The variable $v_F$ is calculated by normalizing the amount of heat release/absorption at the temperature $T$ respect to the total amount of heat that PCM can release or absorb.

In this study, two phase change materials, (1) water solution absorbed within the pore structure of mortar and concrete specimens, and (2) PCM absorbed within the pore structure of LWAs, each with distinct thermal properties, are studied in two small-scale longitudinal guarded comparative calorimeter (LGCC) and large-scale (slab) tests. PCM is designed to experience phase transition at a temperature above the freezing point of pore solution, where the freezing of pore solution depends on the thermal (environmental) and saturation conditions of specimens. An LGCC test was conducted on a mortar specimen, which was prepared using LWAs fully saturated with PCM and then maintained in a chamber with a controlled relative humidity of 50 ± 1 % (Yaghoob Farnam, Krafcik, et al., 2015). A slab test was performed on a concrete specimen, which was prepared using LWAs fully saturated with PCM, then moist cured for 14 days and air-cured until the testing time (Yaghoob Farnam et al., 2017). Under these conditions, the internal relative humidity of the slab was reduced to 81 % (Jun Zhang et al., 2012). Esmaeeli et al. (Hadi S.

Esmaeeli et al., 2017) predicted that the impact of the solution inside the pores smaller than 5 *nm* (corresponding to a relative humidity less than 80 %) on freezing was relatively insignificant. It can be concluded that the pore solution inside the mortar and concrete is less likely to experience phase transition, thus considering the PCM as the only phase change material in this study. This prediction is consistent with the experimental results of the LGCC and slab tests where no phase transition events associated with freezing of pore solution were observed (Y. Farnam et al., 2015; Yaghoob Farnam et al., 2017).

### 3.3 Numerical methodology and applied boundary conditions

An in-house one-dimensional explicit finite difference code has been developed using a C programming language to predict the thermal response of cementitious composites with and without freeze-thaw cycling applied to the PCM. Depending on the test (e.g., LGCC or slab test), the experimental setup is discretized spatially and temporally using a convergent grid spacing size, $\Delta x$, and time step, $\Delta t$. The cementitious composites had effective thermal properties $k_c(T)$, $\rho_c(T)$, $C_c^p(T)$ and experienced a local rate of heat release/absorption per unit volume within each finite-difference grid $\dot{q}_{latent-gen}$. In the LGCC test, the bottom surface is exposed to heat conduction with a heat sink term. In the slab test, the top surface of the pavement was exposed to convection with the ambient temperature with convective coefficient $h_{conv\text{-}diss}$. At time $t = 0\ sec$, the temperature in the cementitious composites is considered to be uniform and equal to ambient temperature, $T_{amb}$, as described in equation 3-3.

$$T(x, t=0) = T_{amb} \qquad 3\text{-}3$$

Further details on the simulation methodology can be found in (Hadi S. Esmaeeli et al., 2017).

### 3.4 Freezable fraction of PCM, $v_F$ (T)

Paraffin oil ($C_{14}$-$C_{16}$) is used as a commercially available PCM in this study, which is a petroleum-based material with a specific density of 0.77 and a vapor pressure less than 0.01 mmHg. Figure 3-1 shows the thermal energy storage analysis to characterize the thermal properties of bulk PCM, including transition temperature range and the associated $\Delta H_f$. A TA instrument Q2000 LT-DSC instrument with temperature range varied between -40 $^oC$ to +24 $^oC$ with a cooling rate of

+2 ($^oC/h$) and heating rate of +4 ($^oC/h$) (identical to the LGCC experiment protocol) is used. The paraffin oil specimens with a mass of 10 ± 2 mg are weighed into a T-zero stainless-steel high-volume pan (with 100 $\mu L$ volume capacity) and sealed hermetically. Dry nitrogen is used as the specimen purge gas and cooling gas with the flow rate regulated at 50 ($mL.min^{-1}$). Figure 3-1(a) shows the DSC thermogram of PCM, where the heat flow of PCM is plotted as a function of temperature. In the DSC thermogram, the main exothermic peak labeled as "A" represents solid-liquid phase transition associated with freezing of PCM at the temperature of +4 $^oC$. In comparison, minor peak labeled as "B" corresponds to the solid-solid phase transition of PCM at a temperature of -27.5 $^oC$.

On the other hand, minor endothermic peak labeled as "C" represents the phase transition associated with solid-solid of PCM at a temperature of -28.4 $^oC$. In contrast, major peak labeled as "D" corresponds to solid-liquid phase transition associated with the melting of PCM at temperatures of +5.1 $^oC$. The heat released during the cooling cycle and heat absorption during the heating cycle are calculated and shown in Figure 3-1(b). For this study, only the phase transition of PCM at the "A" and "D" peaks are considered since (1) a PCM with an initial freezing temperature somewhat above the initial transition temperature of pore solution (assumed 0 $^oC$ in this study) has good performance in ice and snow melting/removal applications (Yaghoob Farnam et al., 2017; Yaghoob Farnam, Krafcik, et al., 2015) and also leads to improvement in freeze-thaw performance of cementitious materials (Dale P. Bentz & Turpin, 2007; T.-C. Ling & Poon, 2013; A.R. Sakulich & Bentz, 2012); and (2) $\Delta H_f$ measured at these two peaks are significantly higher comparing to $\Delta H_f$ measured at the "B" and "C" peaks. Hence, a modified version of fusion of enthalpy "$\Delta H_f^m$" is defined as a function of temperature for freezing and melting processes, as shown in Figure 3-1(b). For the freezing process, it is observed that $\Delta H_f^m$ begins to release once temperature reduces to +4 $^oC$ (i.e., the initial freezing temperature of PCM, $T_F^i$) and increases gradually until temperature reduces, to approximately -10 $^oC$ (i.e., the final freezing temperature of PCM, $T_F^f$). As the temperature drops below -10 $^oC$, no considerable change in $\Delta H_f^m$ is observed. For the melting process, no change in $\Delta H_f^m$ is detected until temperature increases to -8 $^oC$ (i.e., the initial melting temperature of PCM, $T_M^i$). At this temperature, $\Delta H_f^m$ begins to retrieve the

released heat gradually until the total heat is absorbed at a temperature of +5.1 $^oC$ (i.e., the final melting temperature of PCM, $T_M^f$). On the other hand, the manufacturer of this particular PCM has reported a freezing temperature of 1.7 $^oC$ and a melting temperature of 4.5 $^oC$. It is necessary to note that the difference between the experimental and reported transition temperatures may be caused as the DSC results highly depend on the cooling and heating rates (Watson et al., 1988). Although the slower cooling and heating rates more evenly affect the specimen which can lead to reduce the calculated $T_F^i$ and $T_M^f$ to the reported freezing and melting temperatures. The cooling and heating rates employed in the LT-DSC test is consistent with the LGCC experiment protocol which enables us to validate the numerical model by comparing the numerical results with experimental data obtained for mortar specimen containing PCM subjected to freeze-thaw cycles.

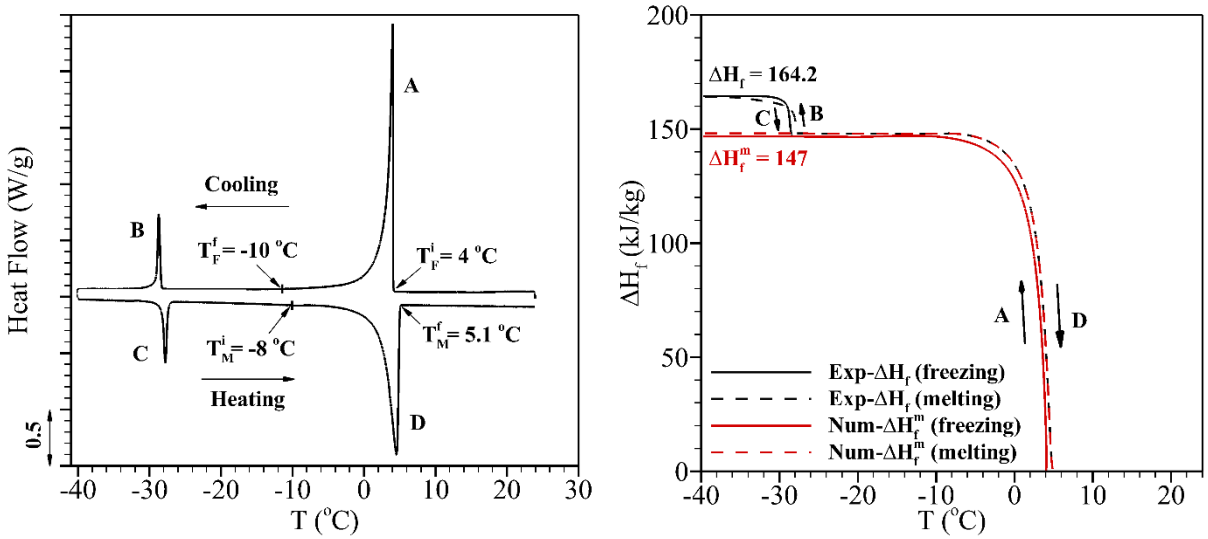


Figure 3-1. (a) Thermal storage analysis of PCM using an LT-DSC device, (b) the amount of released and absorbed heat, $\Delta H_f$, calculated at exothermic peaks of "A-B" and endothermic peaks of "C-D" using LT-DSC result, and the amount of released and absorbed modified heat, $\Delta H_f^m$, used in the numerical analysis.

The pore size distribution of LWA is also a primary factor that can impact the freezing and melting processes of PCM. The LWAs contain a pore structure with a broad range of sizes, which can alter the freezing temperature of liquid PCM (Yaghoob Farnam, Krafcik, et al., 2015). The

Gibbs-Thomson equation can be used to correlate the freezing temperatures of a liquid PCM inside an LWA pore to the pore size, as shown in equation 3-4.

$$T_F = T_M - 2T_M \cdot \frac{\gamma_{L/S} \cdot v_L}{\Delta h_{L/S} \cdot r} \qquad 3\text{-}4$$

where $\gamma_{L/S}$is the energy of the liquid/solid PCM interface (≈ 0.0488 ($J/m^2$)) (Davies, 2012), $r$ is the pore radius (size), $v_L$ is the molar volume of the liquid PCM (≈ 0.0002761 ($m^2/mol$)) (Huggins, 1941), $\Delta h_{L/S}$ is the molar enthalpy of melting of PCM (≈ 3850 ($J/mol$) (Jackson & McKenna, 1990), $T_F$ is the freezing temperature of PCM inside pore size $r$, and $T_M^f$ is the final melting temperature of an infinitely large solid PCM ($T_M^f$ is obtained from LT-DSC analysis) (Parks & Todd, 1929). Figure 3-2(a) displays the correlation between the pore size and the temperature at which PCM inside the LWA pore freezes, $T_f$ ($r$). Once the temperature reaches the associated freezing temperature, solid PCM begins to form inside the pore with radii of $r$. This process is reversed during melting.

Figure 3-2(b) illustrates the relationship between $v_F$ and $r$ obtained from the empirical measurement of the size distribution of LWA pores (Castro, Keiser, et al., 2011). It is observed that 84 % of the total PCM by volume absorbed in the LWA pores with sizes larger than 29 *nm* can freeze once the temperature drops to +4 $^oC$ ($T_F^i$). In comparison, 99 % of liquid PCM by volume absorbed in the LWA pores with sizes larger than 2.13 *nm* can freeze as the temperature drops further to -10 $^oC$ ($T_F^f$ ). Consequently, the volume of freezable PCM determined without considering the effect of the size distribution of LWA pores is underestimated by about 15 %, compared to the approach where the size distribution effect of LWA pores is considered. Esmaeeli et al. observed that the approximate 16 % underestimation of the volume of freezable pore solution absorbed inside the mortar has a negligible impact on the macroscopic freezing response of specimen (Hadi S. Esmaeeli et al., 2017). Consequently, the work reported in this paper considers the pore size of LWA to have a negligible contribution to the macroscopic thermal behavior of cementitious materials containing PCM.

To calculate $v_F$, two approaches are evaluated in this study: (1) a model considering the instantaneous phase transition of PCM and (2) a model considering a gradual phase transition of

PCM. The first approach only considers the instantaneous freezing or melting of PCM at temperatures of $T_F^i$ or $T_M^f$, respectively, whereas the second approach considers a gradual process of phase transition of PCM. In a second approach, the freezing process is considered to initiate $T_F^i$ and gradually continues until the total heat is released $T_F^f$. In contrast, the melting process is considered to initiate $T_M^i$ and continues gradually until the total released heat is absorbed at $T_M^f$, as shown in Figure 3-1(b).

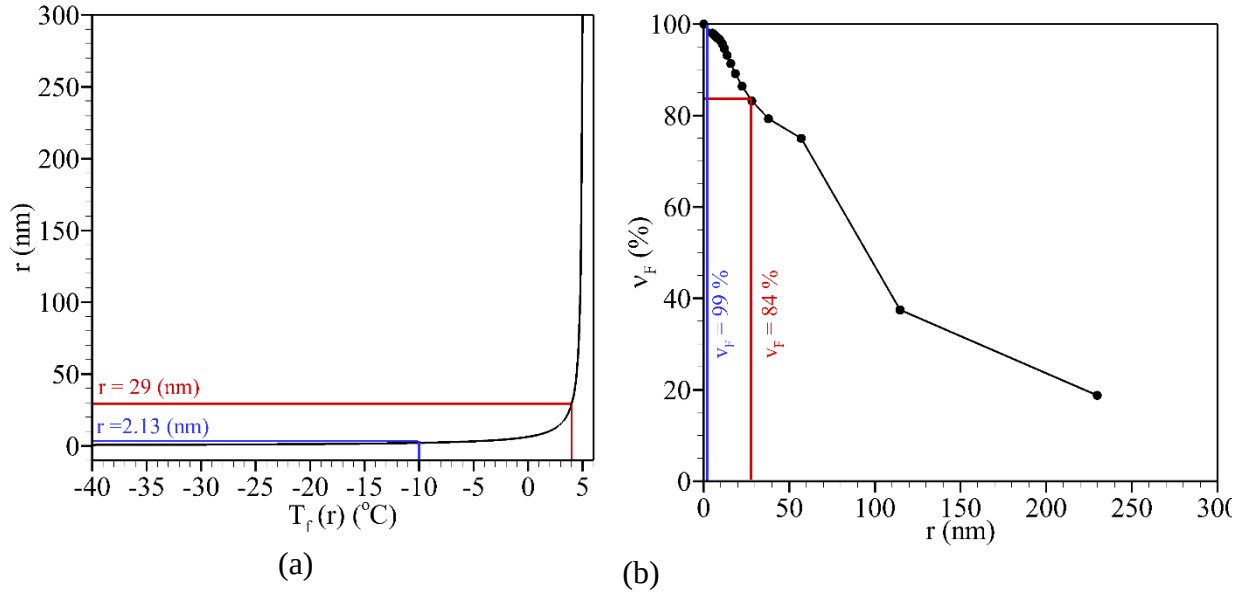


(a) (b)

Figure 3-2. (a) The effect of pore size ($r$) on the freezing temperature of liquid PCM using the Gibbs-Thomson equation, (b) volume fraction of liquid PCM that can freeze ($v_F$) as a function of pore size ($r$).

### 3.5 Homogenization of the thermal properties of cementitious composites

This section discusses how the thermal properties of a mortar or concrete specimen composed of three constituents with distinct thermal properties (i.e., dry mortar or concrete, water solution absorbed within the pores of the specimen, and PCM incorporated within the LWA pores) can be determined using homogenization techniques such that they can be used in the finite difference approach.

Depending on the saturation state and temperature of the specimen, pores may contain various constituents, including air, pore solution, liquid PCM, or solid PCM. The amount of

solution and air in the specimen depends on its degree of saturation ($D_S$), where the amount of liquid and solid PCM depends on the temperature of the specimen. Two PCM dosages of 145 ($kg/m^3$) and 170 ($kg/m^3$) are used to make mortar and concrete specimens tested in the LGCC and slab tests, respectively. Subsequently, the change in the amount of air, pore solution, liquid PCM, or solid PCM can substantially alter the effective thermal properties of the specimen due to considerable differences between the thermal properties of constituents, as outlined in Table 3-1.

### 3.5.1 Thermal conductivity, $k_c$

The rule of the mixture is used to determine the effective thermal properties of pores, $k_p$, as a function of the volume fractions of each constituent (i.e., $k_{air}$, $k_w$, $k_{LP}$, and $k_{SP}$), which is outlined in equation 3-6. Afterward, the effective medium theory (EMT) can be used to determine the thermal conductivity of a cementitious composite, $k_c$, composed of the dry cementitious composite as matrix and pores as inclusions of composite and using equation 3-5 (Levy & Stroud, 1997).

$$k_P = k_{air}.v_{air} \cdot v_c^P + k_w.v_w \cdot v_c^P + k_{LP}.\left(v_{LWA}^P - v_F\right) + k_{SP}.v_F \qquad 3\text{-}5$$

$$k_c = k_{dry} \cdot \frac{2\left(1 - v_c^P - v_{LWA}^P\right)\cdot k_{dry} + \left(1 + 2v_c^P + 2v_{LWA}^P\right)\cdot k_P}{\left(2 + v_c^P + v_{LWA}^P\right)\cdot k_{dry} + \left(1 - v_c^P - v_{LWA}^P\right)\cdot k_P} \qquad 3\text{-}6$$

where $k_{dry}$ is the thermal conductivity of dry cementitious material [$W/(m.K)$], $v_c^P$ is the volume fraction of pores in the cementitious material respect to the total volume of pores $\left(v_c^P + v_{LWA}^P\right)$, $v_{LWA}^P$ is the volume fraction of pores in the LWAs respect to the total volume of pores $\left(v_c^P + v_{LWA}^P\right)$, $k_{air}$ is the thermal conductivity of air [$W/(m.K)$], $v_{air}$=1-$v_w$ is the volume fraction of pores of cementitious material filled with air respect to the total volume of pores in the cementitious material ($v_c^P$), $k_w$ is the thermal conductivity of water solution [$W/(m.K)$], $v_w$ is the volume fraction of pores of cementitious material filled with water solution concerning the total

volume of pores in the cementitious material ($v_c^P$), $k_{LP}$ is the thermal conductivity of liquid paraffin [$W/(m.K)$], and $k_{SP}$ is the thermal conductivity of solid paraffin [$W/(m.K)$].

Table 3-1. Thermal properties of constituents of mortar and concrete composites containing water solution and PCM

| Material | $k$ ($W/m.K$) | $\rho$ ($kg/m^3$) | $c^p$ [$KJ/(kg.K$] |
|---|---|---|---|
| Air | 0.023 | 1.35 | 1.005 |
| Dry mortar | 1.78 ± 0.3 | 2162 ± 150 | 950 ± 100 |
| Dry concrete | 1.7 ± 0.1 | 2200 ± 100 | 880 ± 70 |
| Water solution | 0.52 ± 0.018 | 998 ± 5 | 4183 ± 5 |
| Liquid paraffin | 3.1 ± 0.7 | 766 ± 340 | 2981 ± 190 |
| Solid paraffin | 3.2 ± 0.7 | 865 ± 148 | 2604 ± 248 |

### 3.5.2 Density, $\rho_c$, and specific heat capacity, $C_c^p$

The law of mixtures is employed to predict the effective density and heat capacity of the cementitious composite, $\rho_c$ and $C_c^p$. The effective density is estimated using equation 3-7.

$$\rho_c = \rho_{dry} \cdot (1 - v_P) + \rho_P \cdot v_P \qquad 3\text{-}7$$

where $\rho_{dry}$ is the density of dry cementitious composite ($kg/m^3$), $\rho_P$ is the density of the materials inside the pores (i.e., pore solution and PCM) ($kg/m^3$), which is calculated using equation 3-8.

$$\rho_P = \rho_{air}.v_{air} \cdot v_c^P + \rho_w.v_w \cdot v_c^P + \rho_{LP}.(v_{LWA}^P - v_F) + \rho_{SP}.v_F \qquad 3\text{-}8$$

where $\rho_{air}$ is the effective density of air ($kg/m^3$), $\rho_w$ is the density of water solution ($kg/m^3$), $\rho_{LP}$ is the density of liquid paraffin ($kg/m^3$), and $\rho_{SP}$ is the density of solid paraffin ($kg/m^3$).

The process of determining an effective heat capacity is conceptually similar to determining an effective density (Hadi S. Esmaeeli et al., 2017; L.-P. Zhou et al., 2010). The effective heat capacity for a cementitious composite is calculated using equation 3-9.

$$C_c^p \cdot \rho_c = C_{dry}^p \cdot \rho_{dry} \cdot (1 - v_P) + C_P^p \cdot \rho_P \cdot v_P \quad \text{3-9}$$

where $C_{dry}^p$ is the heat capacity of the dry composite [*J/*(*kg.K*)] and $C_P^p$ is the effective heat capacity of the materials inside the pores, where $C_P^p$ is calculated using equation 3-10.

$$C_P^p \cdot \rho_P = C_{air}^p . \rho_{air} \cdot v_{air} \cdot v_c^P + C_w^p . \rho_w \cdot v_w \cdot v_c^P + C_{LP}^p . \rho_{LP} . (v_{LWA}^P - v_F) + C_{SP}^p . \rho_{SP} . v_F \quad \text{3-10}$$

where $C_{air}^p$ is the heat capacity of air [*J/*(*kg.K*)], $C_w^p$ is the heat capacity of water solution [*J/*(*kg.K*)], $C_{LP}^p$ is the heat capacity of liquid paraffin [*J/*(*kg.K*)], and $C_{SP}^p$ is the heat capacity of solid paraffin [*J/*(*kg.K*)].

## 3.6 Simulation results

### 3.6.1 Sensitivity analysis

Table 3-1 outlined the input variables representing the thermal properties of individual constituents of cementitious composites that contain PCM. The range of input variables indicates an uncertainty that may influence the thermal behavior of the specimen as the output variable. Hence, a sensitivity analysis is required to investigate how the uncertainty in the output variable can be apportioned to different sources of uncertainty in the input variables. In this analysis, the numerical analysis of the LGCC test is used to study the sensitivity of the input variables by employing the minimum and maximum values for input variables to quantify the heat flow response of a mortar (i.e., output variable). Following the experimental work by Farnam et al. (Y. Farnam et al., 2015), the LGCC test was designed to quantify the temperature profile and corresponding heat flow within a mortar specimen. More information on the mixture proportioning, specimen preparation, and conditioning of the mortar can be found in (Y. Farnam et al., 2015). Figure 3-3(a) displays the LGCC test setup, where a one-dimensional heat transfer is conducted by providing a heat sink at the bottom, longitudinal thermal insulation on the sides and the top, and foam insulation around the specimen to minimize the specimen/environment heat transfer.

The first step in the numerical approach is to employ the finite difference method using an appropriate grid spacing size, $\Delta x$ of 1 *mm*, and time step, $\Delta t$ of 0.05 *sec*. Figure 3-3(b) shows the temperature at the bottom of the LGCC test, $T$ ($x$ = 1 *mm*, $t$) that imposes one thermal cycle by varying the temperature as a function of time within the range of +24 $^oC$ to -35 $^oC$, according to the LGCC test protocol. At $x$ = *2 mm*, the temperature in the first finite-difference grid of pad is determined by imposing a heat flux boundary condition to include the effect of conductive heat transfer, as described in equation 3-11.

$$k_{pad}\frac{\partial^2 T(x,t)}{\partial x^2}=\rho_{pad}\cdot C_{pad}^{p}\cdot\frac{\partial T(x,t)}{\partial t} \qquad 3\text{-}11$$

The heat convection coefficient at the top surface ($x$ = *204 mm*) is considered to be approximately $h_{conv\text{-}diss}\approx 100$ [$W/(m^2.K)$] to simulate the heat transfer between the air and the foam on the top (Incropera et al., 2007). At $x$ = *203 mm*, the temperature in the top finite-difference grid of foam is determined by imposing a heat flux boundary condition to include the effect of convective heat transfer occurring between foam and environment, as described in equation 3-12.

$$-k_{foam}\frac{\partial T(x,t)}{\partial x}=h_{conv-diss}\cdot\left[T_{amb}(t)-T(x,t)\right] \qquad 3\text{-}12$$

A considerable temperature difference between the specimen and surroundings throughout the experiment, where a heat flux boundary condition can be taken into account through the lateral side of the experimental setup, as described in equation 3-13.

$$-k(x)\cdot\frac{\partial T(x,t)}{\partial x}=h_{conv-diss}\cdot\left[T_{amb}(t)-T(x,t)\right] \qquad 3\text{-}13$$

Additionally, a difference between the measured heat released in the experiment and the associated $\Delta H_f$ of incorporated PCMs was observed (Hadi S. Esmaeeli et al., 2017; Yaghoob Farnam, Bentz, Sakulich, et al., 2014; Yaghoob Farnam, Krafcik, et al., 2015). Volume fractions of PCM ($v_{LWA}^{P}$), pore solution ($v_w$), and air ($v_{air}$) concerning the total volume of the pores ($v_{LWA}^{P}+v_{LWA}^{P}$) are calculated as 42 %, 23 %, and 35 % in the LGCC test, respectively (Yaghoob Farnam, Krafcik, et al., 2015).

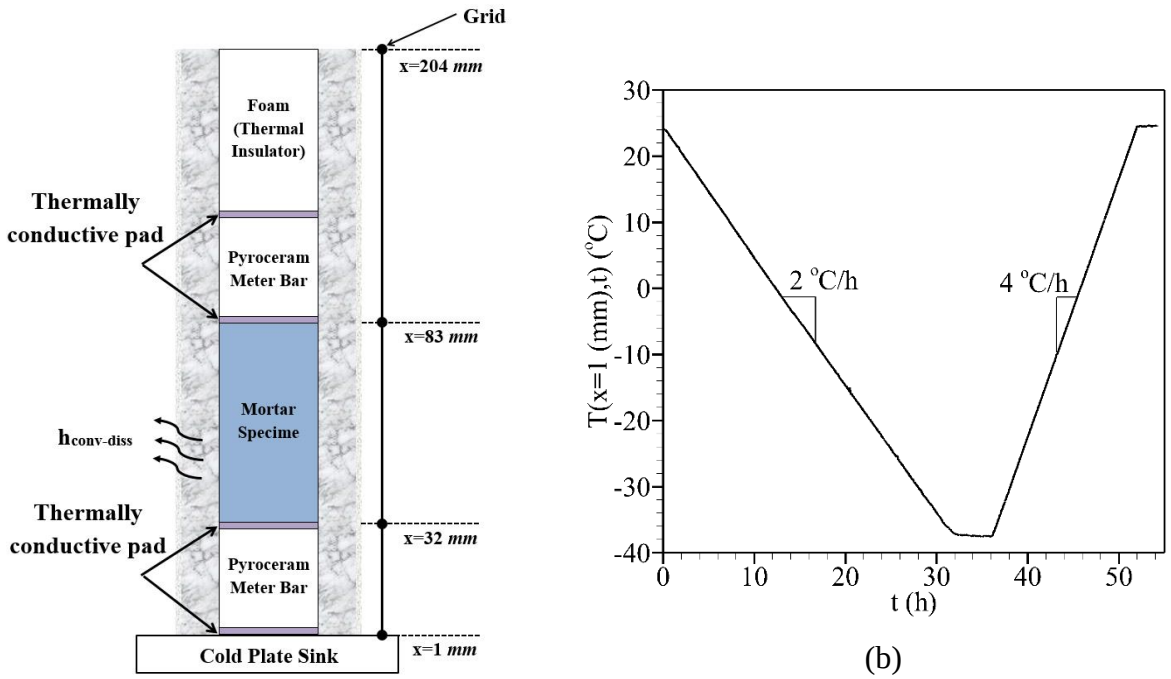


Figure 3-3. (a) Schematic presentation of the LGCC experiment with imposed finite-difference nodes at certain levels, (b) temperature profile at the bottom of LGCC test, i.e., $T$ (x = 1 *mm*, *t*), adapted from (Hadi S. Esmaeeli et al., 2017).

Figure 3-4 shows the heat flow response of mortar in the LGCC test, where eight parameters $S_{C1}$, $S_{C2}$, $S_{H1}$, $S_{H2}$, $L_{PT1}$, $L_{PT2}$, $H_{PT1}$, and $H_{PT2}$ are introduced to characterize heat flow. For the cooling cycle, two parameters $S_{C1}$ and $S_{C2}$ control the slope of the curve before initiation and after completion of the freezing process of PCM. In comparison, two parameters $H_{PT1}$ and $L_{PT1}$ control the maximum heat flow and exothermic peak time during the freezing process of PCM. For the heating cycle, the two parameters $S_{H1}$ and $S_{H2}$ control the slope of curve initiation and after completion of the melting process of PCM. In contrast, the parameters $H_{PT2}$ and $L_{PT2}$ control the maximum heat flow and exothermic peak time during the melting process of PCM.

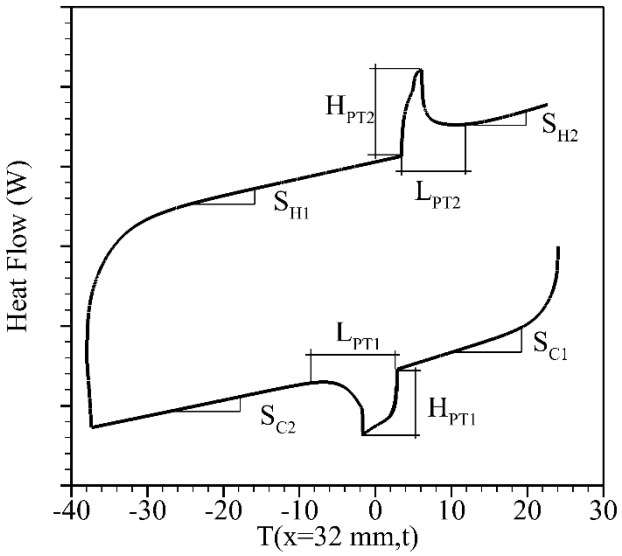


Figure 3-4. The categorization of heat flow response of mortar into six parts of (*C1*) cooling before phase transition of PCM, (*PT1*) cooling during phase transition of PCM, (*C2*) cooling after a phase transition of PCM, (*H1*) heating before phase transition of PCM, (*PT2*) heating during phase transition of PCM, and (*H2*) heating after a phase transition of PCM.

Figure 3-5 shows the results for sensitivity analysis of seven input variables, $k_{dry}$, $\rho_{dry}$, $C^{p}_{dry}$ $k_{LP}$, $k_{SP}$, $h_{latent\text{-}loss,}$ and $h_{conv\text{-}diss}$. For simplicity, this analysis considers the approach of the instantaneous phase transition of PCM to simulate the freezing and melting processes. It is also necessary to mention that the water transport occurring during the freeze-thaw cycling is neglected as no phase transition associated with ice formation inside the pores is expected (G. W. Scherer & Valenza, 2005).

The coefficient $h_{conv\text{-}diss}$ can describe the heat energy transferred between specimens and the environment through convection (Incropera et al., 2007). The typical convection coefficient between air and objects is considered in the range of 1-25 [$W/(m^2.K)$] [37, 38]. As two layers of foam and longitudinal insulators are placed on the sides of the LGCC apparatus to minimize the heat transfer to the environment, $h_{conv\text{-}diss}$ can be considered much less than 1 [$W/(m^2.K)$]. The increase of $h_{conv\text{-}diss}$ would increase the temperature gradient within the specimen, thereby increasing the amount of heat flow. Figure 3-5(a) also shows that a slight change in $h_{conv\text{-}diss}$ from 0 to 1 [$W/(m^2.K)$] significantly increases the four slope parameters $S_{C1}$, $S_{C2}$, $S_{H1}$, and $S_{H2}$.

The variation and the range of $k_{dry}$ $\rho_{dry}$ and $C_{dry}^{P}$ are respectively shown in Figure 3-5(b), Figure 3-5(c), and Figure 3-5(d). The increase of $k_{dry}$ would either (1) decrease the temperature gradient within the specimen, which may decrease the heat flow, or (2) increase the effective thermal conductivity of specimen, which may increase the heat flow. The sensitivity analysis result shows that the increase of $k_{dry}$ from 1.5 to 2.1 [$W/(m.K)$] results in an increase of heat flow, and therefore the slope parameters $S_{C1}$, $S_{C2}$, $S_{H1}$, and $S_{H2}$ are decreased; this change has a relatively smaller impact than does the variation of $h_{conv\text{-}diss}$. Furthermore, parameters $H_{PT1}$ and $H_{PT2}$ decrease, whereas parameters $L_{PT1}$ and $L_{PT2}$ increase. Conversely, the increase of $\rho_{dry}$ from 2012 to 2312 ($kg/m^3$) and $C_{dry}^{p}$ from 850 to 1050 [$J/(kg.K)$] would result in a decrease of a temperature gradient within the specimen and therefore decrease the heat flow throughout the experiment except during the phase transition of PCM. As such, the increase of $\rho_{dry}$ and $C_{dry}^{p}$ tend to decrease the slope parameters $S_{C1}$, $S_{C2}$, $S_{H1}$, and $S_{H2}$.

Figure 3-5(e) and Figure 3-5(f) show how the variation of thermal conductivities of liquid and solid PCM ($k_{LP}$ and $k_{SP}$) can influence heat flow. The density and heat capacity of liquid and solid PCM ($\rho_{LP}, C_{LP}^{p}$ $\rho_{SP} C_{SP}^{p}$) have a negligible influence on heat flow due to a relatively low volume of cementitious composites occupied by PCM. The sensitivity analysis results show that an increase of $k_{LP}$ from 0.21 to 0.30 [$W/(m.K)$] increases the heat flow before initiation of freezing or after completion of the melting of PCM. On the other hand, an increase of $k_{SP}$ from 0.21 to 0.30 [$W/(m.K)$] increases the heat flow after completion of freezing or before initiation of the melting of PCM. Therefore, the increase of $k_{LP}$ only decreases two slope parameters $S_{C1}$ and $S_{H2}$, while the increase of $k_{SP}$ only decreases two slope parameters $S_{C2}$ and $S_{H1}$.

Figure 3-5(g) shows how the input variable $h_{latent\text{-}loss}$ associated with the heat energy dissipation during the phase transition of PCM significantly influences the heat flow. The sensitivity analysis result indicates that the variation of $h_{latent\text{-}loss}$ from 40 % to 60 % would result in a significant decrease of the area under the exothermic and endothermic curves, and therefore decrease the slope parameters $H_{PT1}$, $L_{PT1}$, $H_{PT2}$, and $L_{PT2}$. Table 3-2 summarizes the list of effective input variables indicated by sensitivity analyses on the corresponding heat flow parameters.

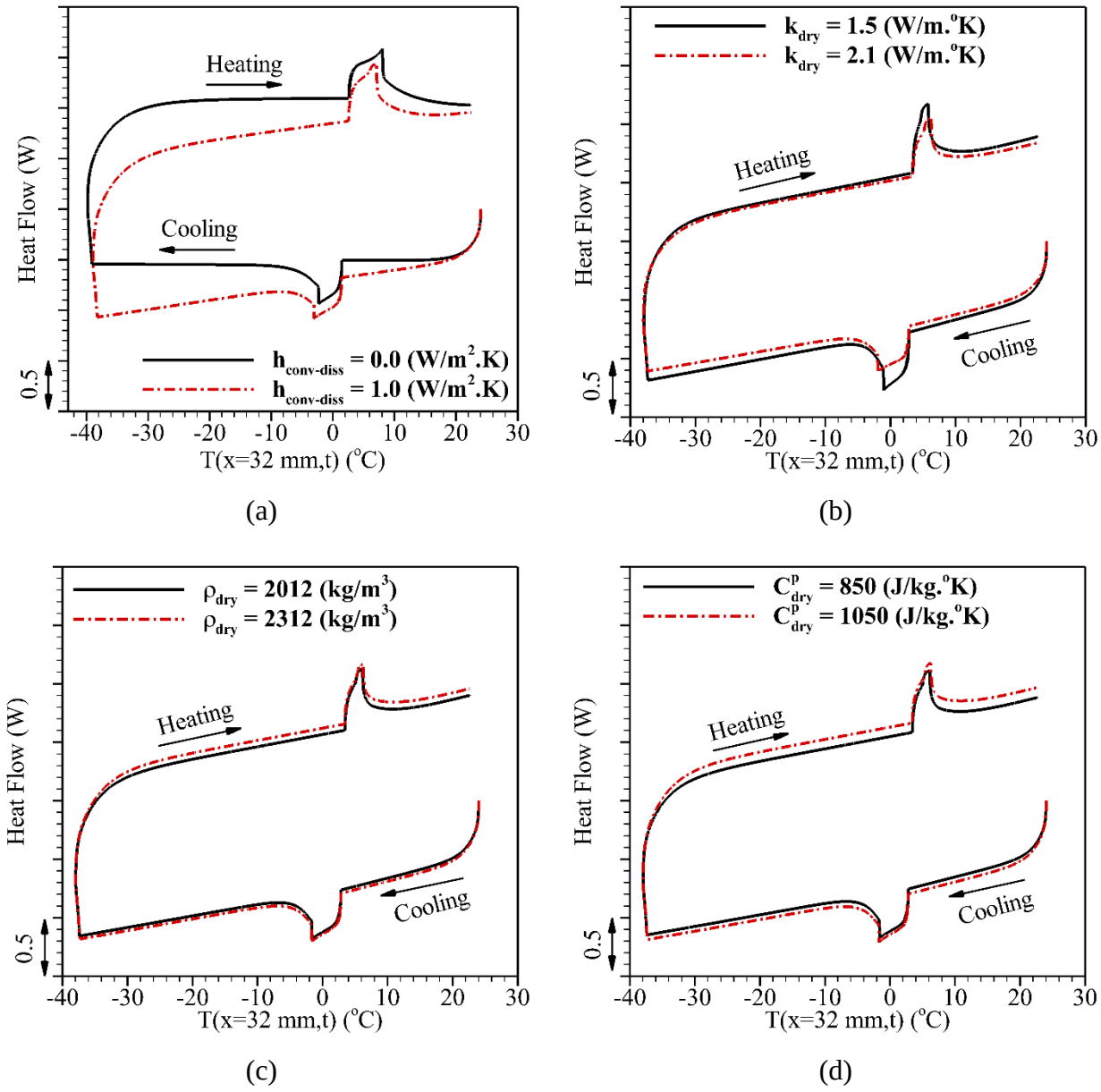


Figure 3-5. Assessment of the uncertainty of the input variables (a) convection dissipation coefficient, (b) thermal conductivity of dry mortar, (c) density of dry mortar, (d) heat capacity of dry mortar, (e) thermal conductivity of liquid PCM, (f) thermal conductivity of solid PCM, and (g) dissipation coefficient during phase transition of PCM, on the output variable (e.g., heat flow) of mortar specimen in the LGCC test.

Figure 3-5 continued

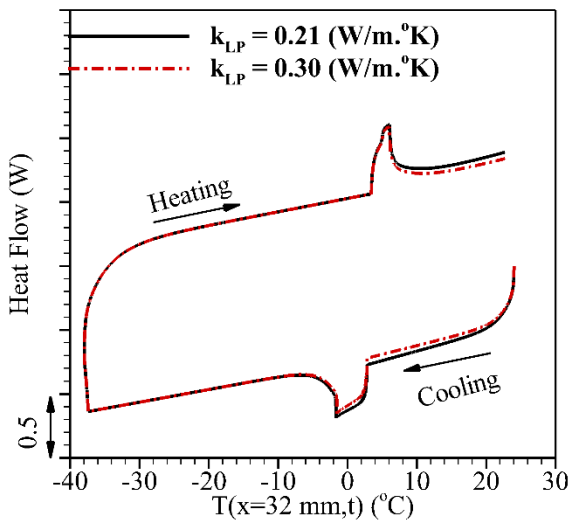


(e)

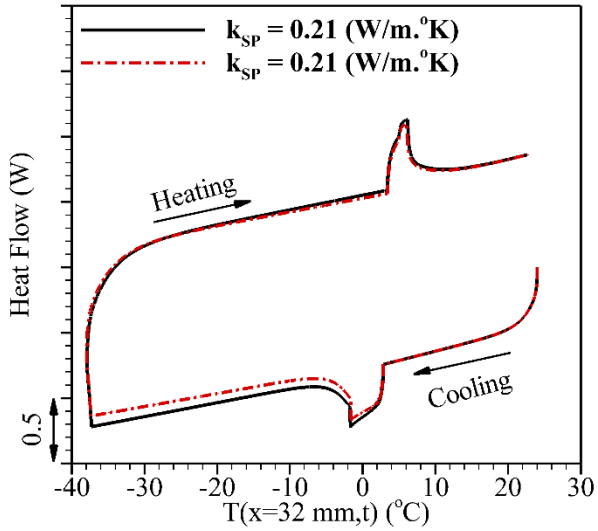


(f)

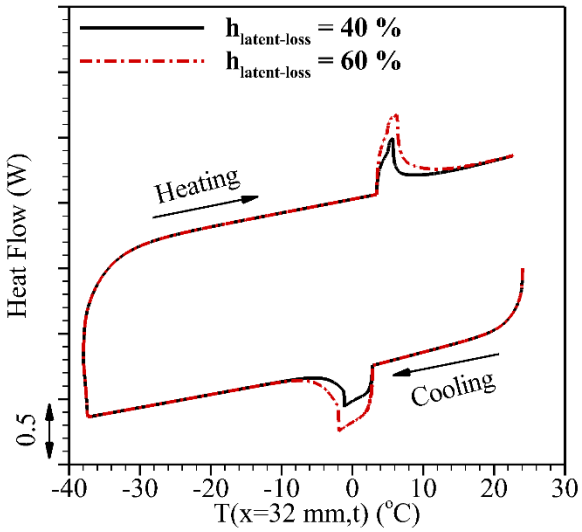


(g)

Table 3-2. The influencing input variables on the heat flow parameters of mortar composite containing PCM in the LGCC test.

| Parameters | $S_{C1}$ | $S_{C2}$ | $H_{PT1}$ | $L_{PT1}$ | $S_{H1}$ | $S_{H2}$ | $H_{PT2}$ | $L_{PT2}$ |
|---|---|---|---|---|---|---|---|---|
| Input variables | $h_{conv\text{-}diss}$ | $h_{conv\text{-}diss}$ | $k_{dry}$ | $k_{dry}$ | $h_{conv\text{-}diss}$ | $h_{conv\text{-}diss}$ | $k_{dry}$ | $k_{dry}$ |
| | $k_{dry}$ | $k_{dry}$ | $h_{latent\text{-}loss}$ | $h_{latent\text{-}loss}$ | $k_{dry}$ | $k_{dry}$ | $h_{latent\text{-}loss}$ | $h_{latent\text{-}loss}$ |
| | $\rho_{dry}$ | $\rho_{dry}$ | | | $\rho_{dry}$ | $\rho_{dry}$ | | |
| | $C^{p}_{dry}$ | $C^{p}_{dry}$ | | | $C^{p}_{dry}$ | $C^{p}_{dry}$ | | |
| | $k_{LP}$ | $k_{SP}$ | | | $k_{SP}$ | $k_{LP}$ | | |

### 3.6.2 Small-scale LGCC test

The numerical results for heat flow response of a mortar specimen containing PCM (incorporated within LWA) with dimensions of 25.4 *mm* × 25.4 *mm* × 50.8 *mm* tested in the LGCC test are compared to experimental data, as shown Figure 3-6(a). Two distinct numerical approaches, a model considering of instantaneous PCM phase transition and a model considering gradual PCM phase transition, are employed to investigate the impact of the transition temperature range of PCM on heat flow response. Table 3-3 shows the values for the thermal properties of mortar specimen constituents obtained from sensitivity analyses. The two dissipation coefficients $h_{conv\text{-}diss}$ and $h_{latent\text{-}loss}$ are also adjusted to be 0.7 [$W/(m^2.K)$], and 50 % for the LGCC test, respectively.

Figure 3-6 (b) shows the freezing process of PCM results in an exothermic peak due to significant heat release during a thermal cycle. In the approach with instantaneous PCM freezing, the exothermic peak is considered to occur at $T_F^i$ and subsequently ceases when the total amount of heat has been released to the surroundings. Conversely, the approach with gradual PCM freezing considers the exothermic peak to be extended $T_F^f$ due to a gradual process of solid PCM formation, as shown in Figure 3-6(b). For the case of instantaneous PCM melting, the endothermic peak is considered to occur at $T_M^f$ and subsequently ceases when the total amount of heat has been absorbed from the surroundings. In contrast, the endothermic peak is considered to be extended to $T_M^i$ as the previously formed solid PCM melts, as shown in Figure 3-6(c). The promising agreement between the experimental data and numerical results illustrates that

consideration of gradual freezing or melting of PCM over a narrow temperature range can reasonably simulate the thermal response of mortar specimens containing PCM exposed to one thermal cycle.

### 3.6.3 Large-scale slab experiment

A large-scale test with dimensions of 350 *mm* × 350 *mm* × 215 *mm* is simulated to assess the freeze-thaw performance of concrete slabs with and without PCM. A gradual phase transition of the PCM over a narrow temperature range is considered (see Figure 3-1(b)). The materials and mixture proportioning for making the concrete slabs are explained in Appendix 1. More information on the mixture proportioning, specimen preparation, and conditioning of the concrete slabs can be found in (Yaghoob Farnam et al., 2017). Figure 3-7(a) displays the slab test setup, where a one-dimensional heat transfer is conducted by providing a heat sink at the top, thermal insulation foam and wood frame with relatively low thermal conductivities of 0.03 [*W/*(*m.K*)] and 0.12 [*W/*(*m.K*)], respectively, placed on the sides and bottom of the specimen (Sears et al., 1982; Williams & Aldao, 1983). The specimen domain is discretized spatially and temporally using layer size and a time step of 1 *mm* and 0.1 *sec* to obtain convergence in results, respectively. Therefore, this study considers 215 and 25 layers for the concrete specimen and base thermal insulator, respectively. Figure 3-7(b) shows the temperature at the top of the slab test, $T\,(x = 1\ mm, t)$ that imposes one thermal cycle by varying the temperature as a function of time within the range of +10 $^oC$ to -10 $^oC$, according to the slab test protocol. Volume fractions of PCM $(v_{LWA}^P)$, water solution ($v_w$), and air ($v_{air}$) concerning the total volume of the pores $(v_c^P + v_{LWA}^P)$ are estimated to be 46 %, 45 %, and 9 % in the slab test, respectively (Yaghoob Farnam et al., 2017).

Table 3-3. Thermal properties of constituents of mortar specimen in the LGCC test

| Material | $k$ ($W/m{\cdot}K$) | $\rho$ ($kg/m^3$) | $C^p$ $[kJ/kg{\cdot}K]$ |
|---|---|---|---|
| Dry mortar | 1.92 | 2080 | 870 |
| Liquid paraffin | 0.21 | 670 | 3071 |
| Solid paraffin | 0.21 | 800 | 2461 |

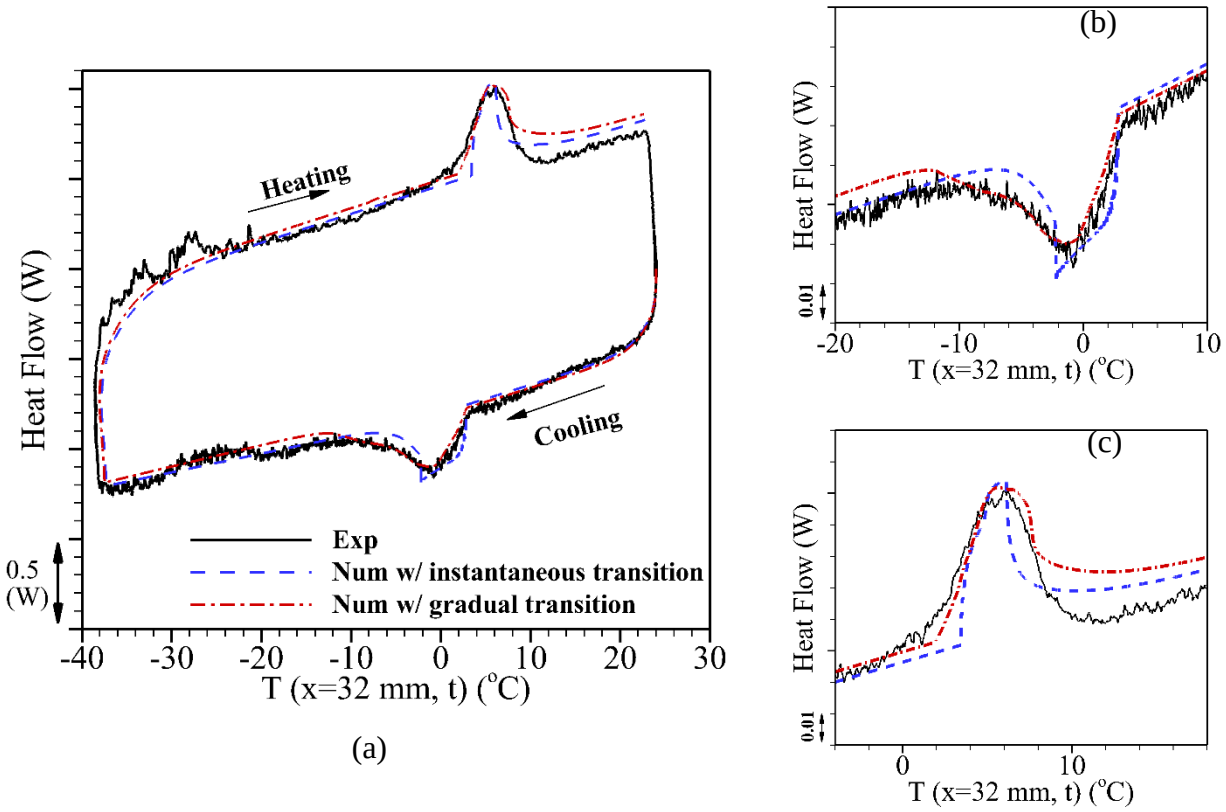


Figure 3-6. Comparison of experimental and numerical results of (a) heat flow of concrete specimen containing paraffin oil (PCM) in the LGCC experiment, (b) exothermic peak representing the heat release of PCM during the solidification process, (c) endothermic peak representing the heat absorption of PCM during the melting process.

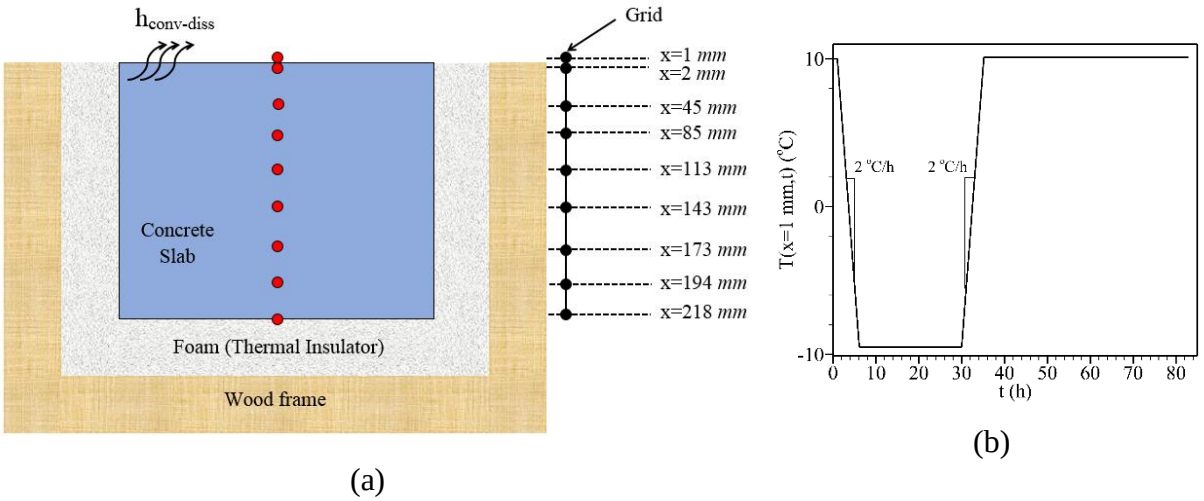


Figure 3-7 (a) Schematic configuration of the slab tests with adapted finite-difference grids, and (b) temperature profile at the top of the slab test, *T (x=1, t)*.

The nature of heat transfer between the top of the slab and the environment can be classified as forced convection as the heat flow is caused by the external means of a fan to change the temperature of the environment. The heat transfer coefficient for forced convection using air is recommended to be within the range of 10 and 250 [$W/(m^2 \cdot K)$] (Incropera et al., 2007; Rohsenow et al., 1998). Therefore, a heat flux boundary condition is imposed on the top surface of the slab ($x = 2\ mm$) to include the effects of convective heat transfer, as described in equation 3-14.

$$-k_c(T)\frac{\partial T(x,t)}{\partial x} = h_{conv-diss} \cdot \left[T(x = 1mm, t) - T(x,t)\right] \qquad 3\text{-}14$$

Similar to the LGCC test, a difference between the measured heat release during solid PCM formation and the associated enthalpy of fusion of paraffin oil due to experimental imperfection conditions (thermal bridges, heat leaks, etc.) is observed (Hadi S. Esmaeeli et al., 2017). Hence, a sensitivity analysis is conducted for the slab test to obtain the optimal values of input variables; while the thermal properties of liquid and solid PCM used in the LGCC and slab tests are assumed to be identical, as outlined in Table 3-4. The dissipation coefficients $h_{conv\text{-}diss}$ and $h_{latent\text{-}loss}$ are adjusted to be 20 [$W/(m^2 \cdot K)$] and 60 %, respectively.

Table 3-4. Thermal properties of constituents of mortar specimen in the slab test

| Material | $k$ [$W/(m \cdot K)$] | $\rho$ ($kg/m^3$) | $C^p$ [$KJ/(kg \cdot K$] |
|---|---|---|---|
| Dry concrete | 1.75 | 2250 | 850 |
| Liquid paraffin | 0.21 | 670 | 3071 |
| Solid paraffin | 0.21 | 800 | 2461 |

The numerical result for temperature profile within a concrete slab without PCM, the 'reference' slab, exposed to a thermal cycle is compared to the experimental data, as shown in Figure 3-8. The profile for ambient temperature is shown in Figure 3-8(a) (similar to Figure 3-7(b)) to display the cooling and heating moments in the concrete slab. Once the cooling cycle ceases, the ambient temperature remains unchanged at -10 $^oC$ for 24 $h$ to allow the slab to reach thermal equilibrium before the heating cycle begins. Similarly, the ambient temperature remains unchanged at +10 $^oC$ for 48 $h$ once the heating cycle is completed.

Figure 3-8(b) and Figure 3-8(c) illustrate the temperature contour within the slab obtained from experimental data and numerical results by interpolation of recorded and predicted

temperature values at the eight locations within the slab, respectively. In these figures, the white color represents the locations within the slab in which the temperature drops below 0 $^oC$. Numerical results predict that the temperature within the slab decreases or increases very rapidly and is associated with the decrease or increase of ambient temperature in the absence of PCM, which is consistent with the experimental results. The absolute temperature difference between the predicted numerical results and experimental data is quantitatively calculated at two locations of $x$ = 85 *mm*, and $x$ = 113 *mm*. It is observed that this difference remains below 1 $^oC$ at the location of $x$ = 85 *mm* throughout the thermal cycle. For the location of $x$ = 113 *mm*, this difference exceeds 1.2 $^oC$ only for a very short period (less than 6 *min*) and remains below 1 $^oC$ for the remainder of the thermal cycle. The numerical model also indicates that the temperature within the concrete slab without PCM remains below 0 $^oC$ for an average time of 25 *h*.

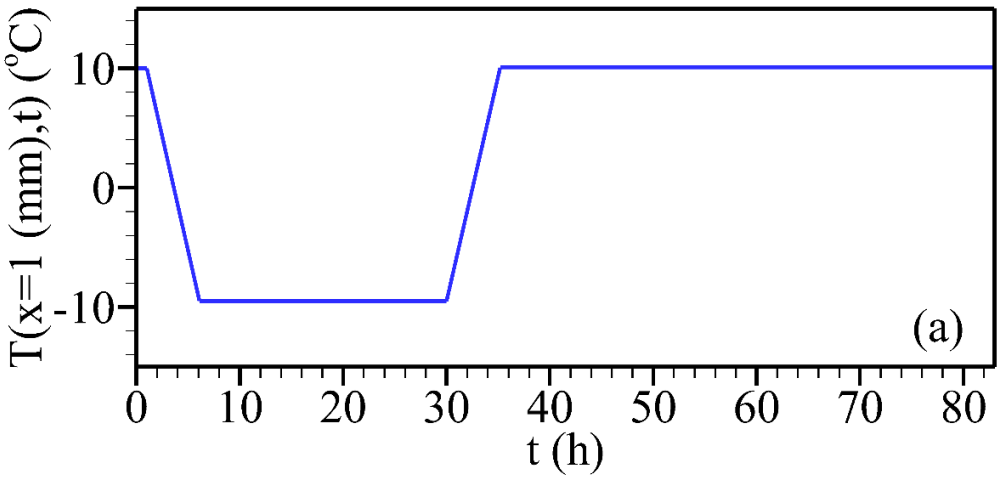


(a)

Figure 3-8. Thermal analysis of the concrete slab without PCM (a) ambient temperature applied to the slab as one thermal cycle, (b) experimental results for temperature contour within the slab as a function of time, and (c) numerical results for temperature contour within the slab as a function of time.

Figure 3-8 continued

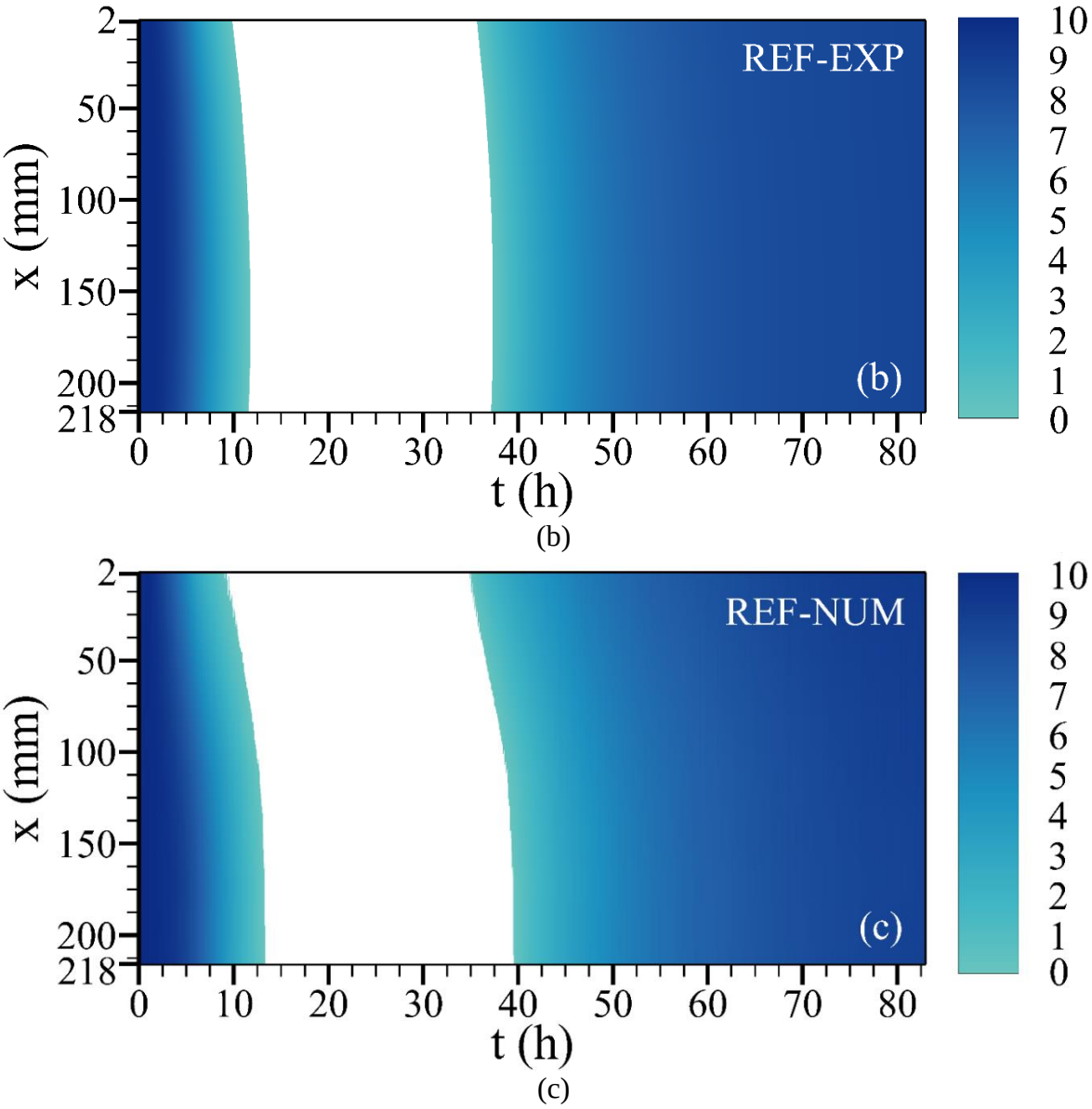


Figure 3-9 shows the experimental data and numerical results for temperature profile within a concrete slab containing PCM exposed to a thermal cycle. The profile for ambient temperature is shown in Figure 3-9(a) (similar to Figure 3-7(b)) to display the cooling and heating moments in the concrete slab. Figure 3-9(b) and Figure 3-9(c) illustrate the temperature contour within the slab obtained from experimental data and numerical results by interpolation of recorded and predicted temperature values at the eight locations within the slab, respectively. The analysis of experimental data and numerical results shows a relatively slow variation of temperature as the gradual heat release during freezing of PCM, or gradual heat absorption during melting of PCM

keeps the temperature within slab above 0 $^oC$, for a longer time compared to the temperature within reference slab. It is concluded that the gradual heat release or absorption can compensate for the heat loss or gain in the slab as the ambient temperature varies. The numerical model implies that the slab with PCM remains "warmer" for a longer period; the time at which the temperature is kept above 0 $^oC$ is reduced to 15 *h*. Although no ice formation within concrete pores in the slab test was considered, the slab would be subjected to freeze-thaw cycling at a temperature below 0 $^oC$, if the slab was fully saturated with water solution (i.e., $v_w$ = 100 %) and no undercooling would occur. Therefore, the incorporation of PCM would reduce the freeze-thaw time by 9 *h*, and thus improve the freeze-thaw performance of the slab.

Similar to the analysis of reference slab, the absolute temperature difference between the predicted numerical results and experimental data is quantitatively calculated at two locations of $x$ = 85 *mm*, and $x$ = 113 *mm*. It is observed that this difference always remains below 1 $^oC$ at these two locations throughout the thermal cycle. It is concluded that the numerical model reasonably predicts the thermal behavior of concrete slabs with and without PCM exposed to one thermal cycle.

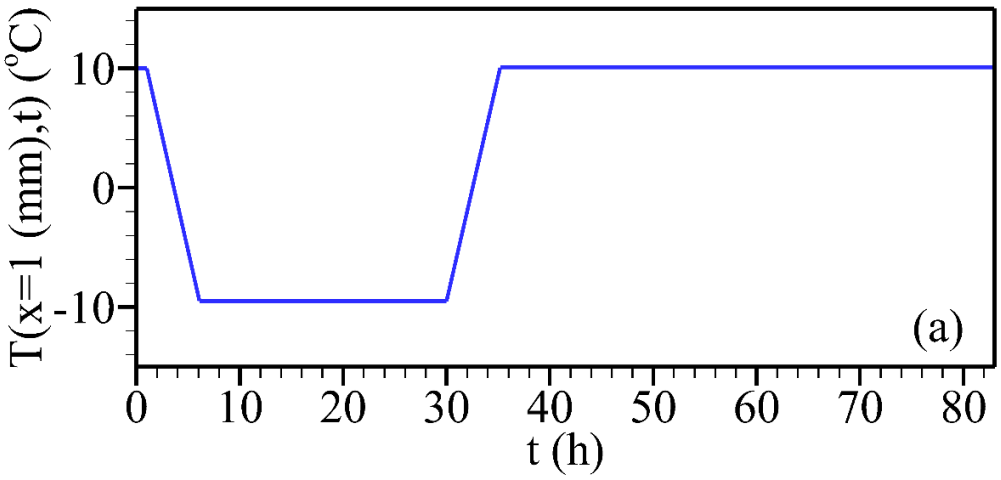


(a)

Figure 3-9. Thermal analysis of the concrete slab with PCM (a) ambient temperature applied to the slab as one thermal cycle, (b) experimental results for temperature contour within the slab as a function of time, and (c) numerical results for temperature contour within the slab as a function of time.

Figure 3-9 continued

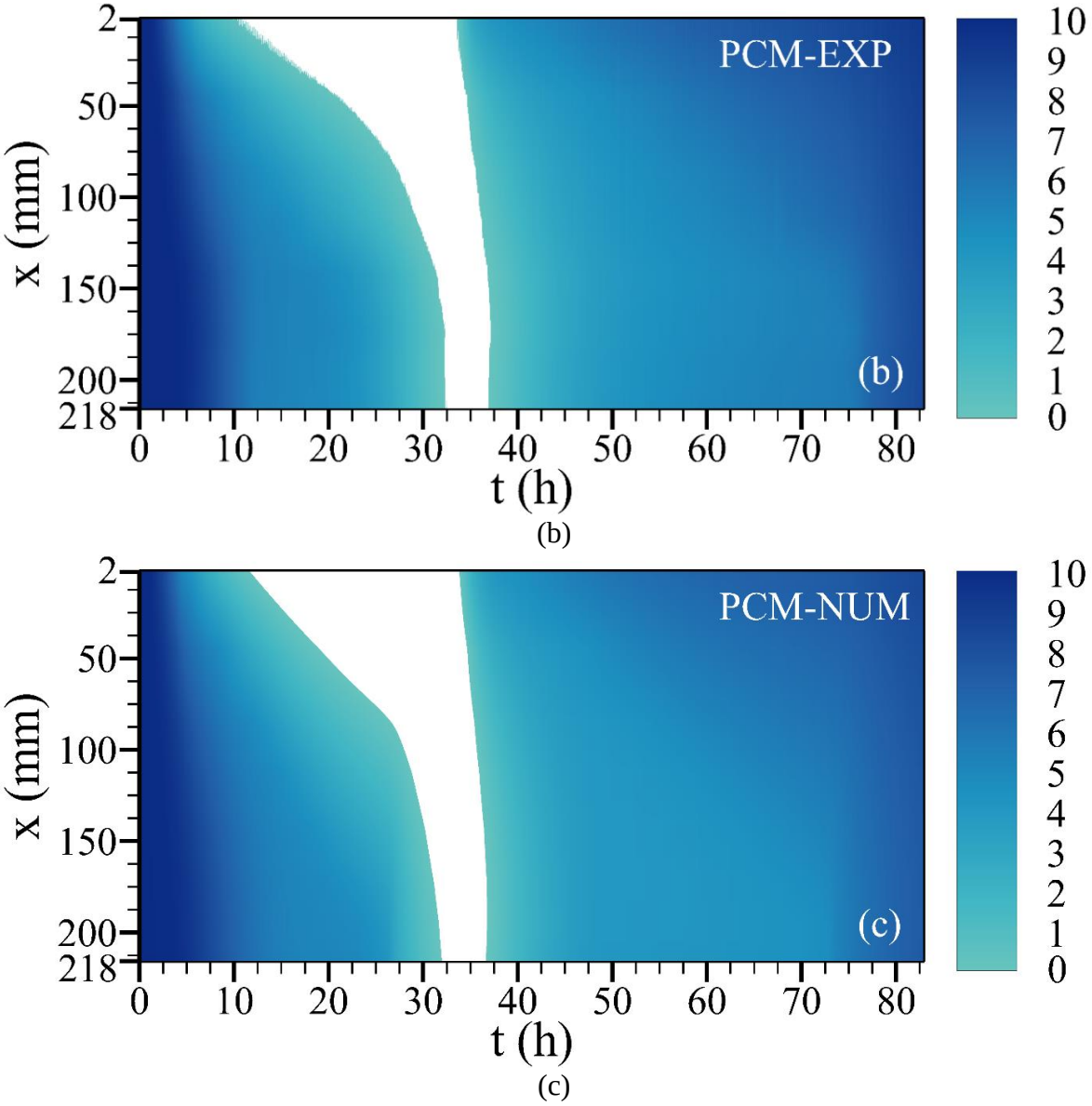


(b)

(c)

### 3.6.4 Field application

Although the thermal diffusivity (i.e., thermal conductivity divided by heat capacity) of PCM incorporated within the concrete infrastructure, such as bridge decks, was determined to be an important property governing the effectiveness of PCM at improving the freeze-thaw performance (A.R. Sakulich & Bentz, 2012), little is known about the contribution of the PCM transition temperature. According to the modeling, the comparison of temperature contours within

the concrete slabs with and without PCM indicated that incorporation of PCM with an initial freezing temperature above 0 $^oC$ significantly reduces the time at which the slab experiences a temperature below 0 $^oC$. It is believed that a slight change in the transition temperatures (i.e., the rate of heat release or absorption over the transition temperature range) of PCM would significantly impact the thermal behavior of the concrete slab exposed to thermal cycles. Therefore, three different PCMs are proposed to be used: a paraffin oil, FT4-MT5, and two modified paraffin oils, FT0-MT1, and FT2-MT3. FT4-MT5 represents the paraffin oil used in the LGCC and slab tests, while initial freezing and melting temperatures of FT0-MT1 and FT2-MT3 PCM are modified, as outlined in Table 3-5.

Table 3-5. Transition temperatures and effectiveness of three PCMs used in field application study.

| PCM | FT0-MT1 | FT2-MT3 | FT2-MT3 |
|---|---|---|---|
| $T_F^i$ ($^oC$) | 0 | -10 | -8 |
| $T_F^f$ ($^oC$) | 2 | -10 | -8 |
| $T_M^i$ ($^oC$) | 4 | -10 | -8 |
| $T_M^f$ ($^oC$) | 1.1 | 3.1 | 5.1 |
| Locations where effective more than 10 % and less than 20 % (#) | 28 | 61 | 62 |
| Locations where effective more than 20 % and less than 30 % (#) | 37 | 43 | 14 |
| Locations where effective more than 30 % | 57 | 5 | 2 |

Figure 3-10(a) shows the correlation between $\Delta H_f^m$ and freezing temperature for the three PCMs used in the numerical model to simulate the gradual heat release due to PCM solidification. Figure 3-10(b) shows the correlation between $\Delta H_f^m$ and melting temperature for the three PCMs used in the numerical model to simulate the gradual heat absorption due to PCM melting.

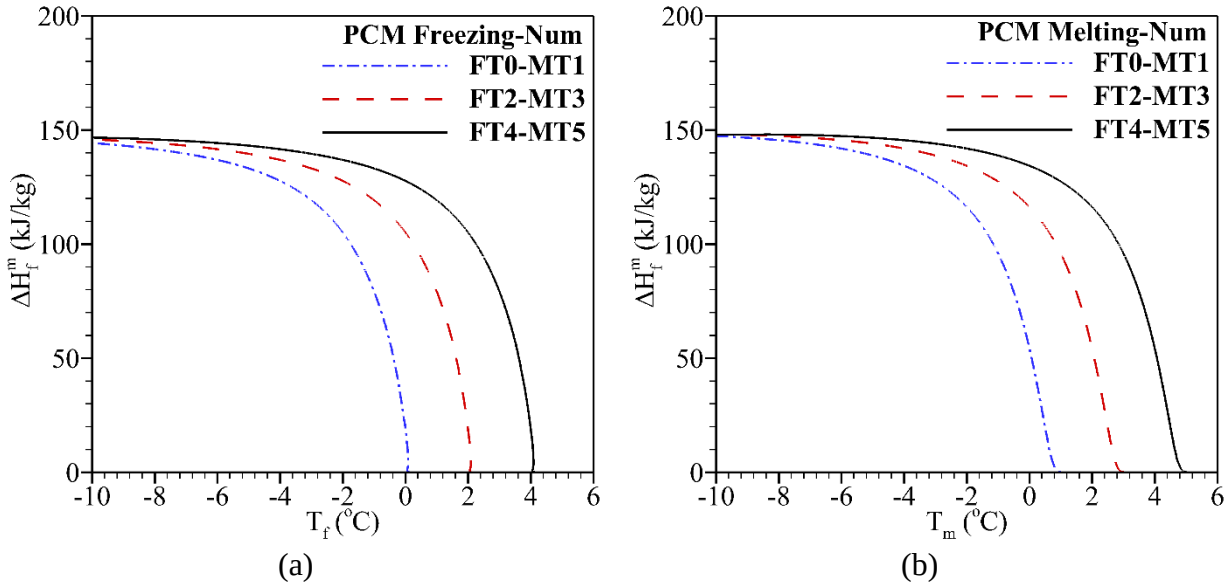


Figure 3-10. The calculation of modified fusion of enthalpy, $\Delta H_f^m$ as a function of temperature during (a) freezing of PCM in the cooling cycle, and (b) melting of PCM in the heating cycle.

The numerical model is used to predict the thermal behavior of reference pavement, and pavements with PCMs incorporated with a dosage of 170 ($kg/m^3$) at 210 different cities throughout the United States. The concrete pavements are subjected to arbitrary realistic climate data, including hourly averages of temperature for one year from August 2016 through August 2017 (obtained from the national climate database (*Https://Www.Wunderground.Com/*, n.d.)) for each location. The year-long temperature data is used to simulate the thermal cycling condition imposed on the top surface of the pavement to estimate the PCM effectiveness in determining the long-term response of the pavement concerning reducing the number of freeze-thaw cycles. For this analysis, the only one-year analysis was done. Similar to the thermal conditions imposed in the slab test, these pavements are assumed as semi-infinite media in which: (i) one-dimensional heat conduction determines the temperature profile through the depth of the pavement, (ii) all the thermal properties become temperature-dependent when PCM experiences phase transition, (iii) the convection coefficient *h*, at the top surface of pavement remains constant, (iv) radiation exchange between the pavement and sky is considered to be obstructed by cloud-covered condition, (v) no precipitation event is considered to occur. Therefore, the pavement surface conditions used in the model have been restricted to those found in the slab test, which includes a dry surface (i.e., free of snow, ice and rain), totally cloud-covered, and windy surface. It is necessary to note that the equivalent

temperature of radiation of the sky is logically close to the ambient temperature under cloud-covered conditions (Mammeri et al., 2015; Walker & Anderson, 2016).

These locations are assumed to be fully saturated with water solution; thus, it is subjected to freeze-thaw cycling at a temperature below 0 $^oC$. However, the freezing of water solution inside the concrete pores occurs at a temperature between ~ -3 to -6 $^oC$ (W. Li et al., 2012) due to the presence of ions in the pore solution. For the sake of simplicity, this study assumes that the concrete pavements experience one freeze-thaw cycle once the pavement temperature reduces to 0 $^oC$. The temperature profile within a pavement section is predicted based on the assumed environmental inputs on the ambient and the concrete material properties; the numerical model predicts the concrete surface temperature (see equation 3-14)) (Antaki, 1997; D. Wang & Roesler, 2012). The temperature of the surface of concrete, however, may be different than the air temperature due to different factors such as solar radiation, wind velocity, and earth thermal effect that can be the objectives of future research. Two criteria are thus defined to determine the PCM effectiveness at improving the freeze-thaw performance by comparing the pavement containing PCM with reference pavement. These two criteria are: (1) the percentage difference of maximum depth within the pavement that experience temperature below 0 $^oC$ as shown in equation (3-15a), and (2) the percentage difference of time within the pavement that experience temperature below 0 $^oC$ as shown in equation (3-15b).

$$X_{PCM-eff}(\%) = \frac{\max(X_{ref}[T<0(^oC),t]) - \max(X_{PCM}[T<0(^oC),t])}{\max(X_{ref}[T<0(^oC),t])} \times 100 \quad (3\text{-}15a)$$

$$t_{PCM-eff}(\%) = \frac{t_{ref}[T<0(^oC), x=2mm] - t_{PCM}[T<0(^oC), x=2mm]}{t_{ref}[T<0(^oC), x=2mm]} \times 100 \quad (3\text{-}15b)$$

where $X_{PCM\text{-}eff}$ is the percentage difference of maximum depth within the pavement (%), $t_{PCM\text{-}eff}$ is the percentage difference of time within the pavement (%), $X_{ref}$ is the depth of reference pavement which experiences a freeze-thaw cycle at time $t$, $X_{PCM}$ is the depth of pavement with PCM which experiences a freeze-thaw cycle at time $t$, $t_{ref}$ is the number hours that reference pavement experiences a freeze-thaw cycle on the top surface ($x$ = 2 $mm$), $t_{PCM}$ is the number hours that pavement with PCM experiences a freeze-thaw cycle on the top surface ($x$ = 2 $mm$).

Modeling of reference pavement shows that there is a total of 44 locations where PCM effectiveness is less than 10 %, as these locations are either warm enough that freezing cycles rarely occur (located primarily in the Southwest, Southeast and along the Gulf Coast), or cold enough that the temperature of the pavement generally remains below 0 $^{o}C$ (located primarily in the North and the Northeast). Figure 3-11 and Table 3-5 show the effectiveness of the three PCMs on the freezing time and depth of concrete pavements throughout the United States. It is observed that all three PCMs are effective in regions with milder weather (i.e., the majority of cities located in the East, Central, and Northwest regions). In a total of 78 cities, one of the three PCMs reduces both freezing time and depth of pavement by at least 10 percent. Sakulich et al. also predicted that the incorporation of two PCMs with transition temperatures of 4 $^{o}C$ and 6 $^{o}C$ within concrete mixtures was effective in these regions, where at least 48 of the 100 most populous American cities are located (A.R. Sakulich & Bentz, 2012).

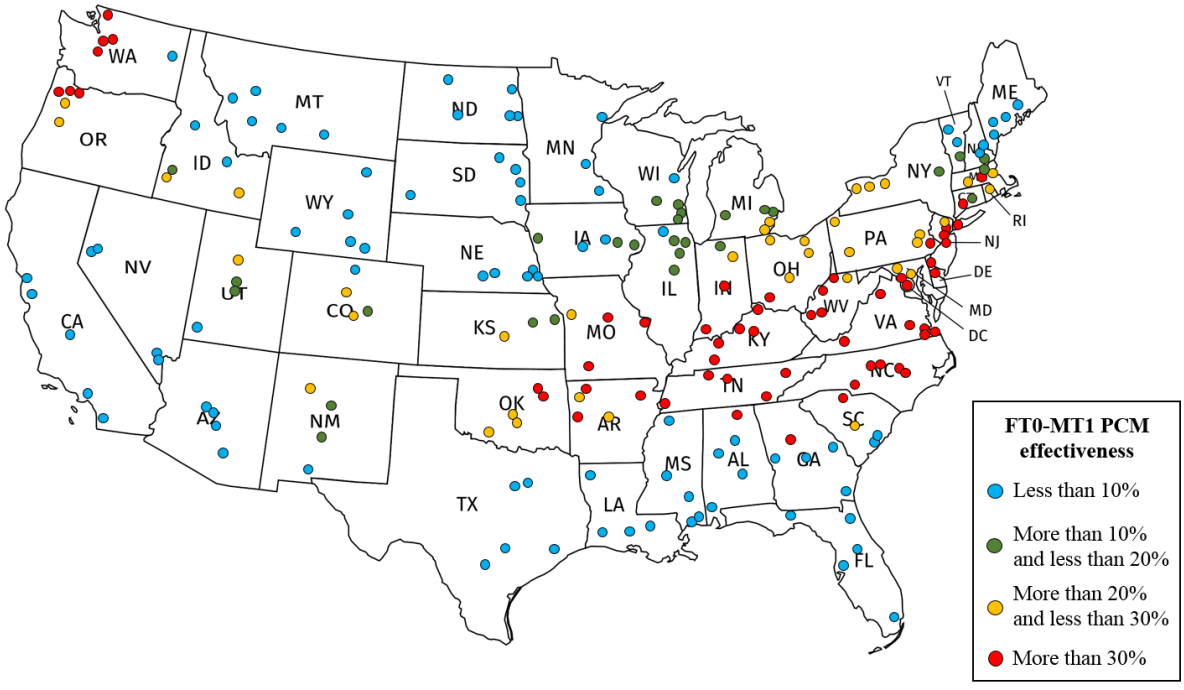


(a)

Figure 3-11. Map of cities in which the concrete pavements incorporating three PCMs investigated here decrease the time and depth of freezing. The types of PCM used in pavements are (a) FT0-MT1, (b) FT2-MT3, and (c) FT4-MT5. Point color indicates what percentage the time and depth of freezing within concrete pavement decreased, by quartile: blue indicates PCM effectiveness less 10 %, green indicates PCM effectiveness between 10 % and 20 %, orange indicates PCM effectiveness between 20 % and 30 %, and red indicates PCM effectiveness more than 30 %.

Figure 3-11 continued

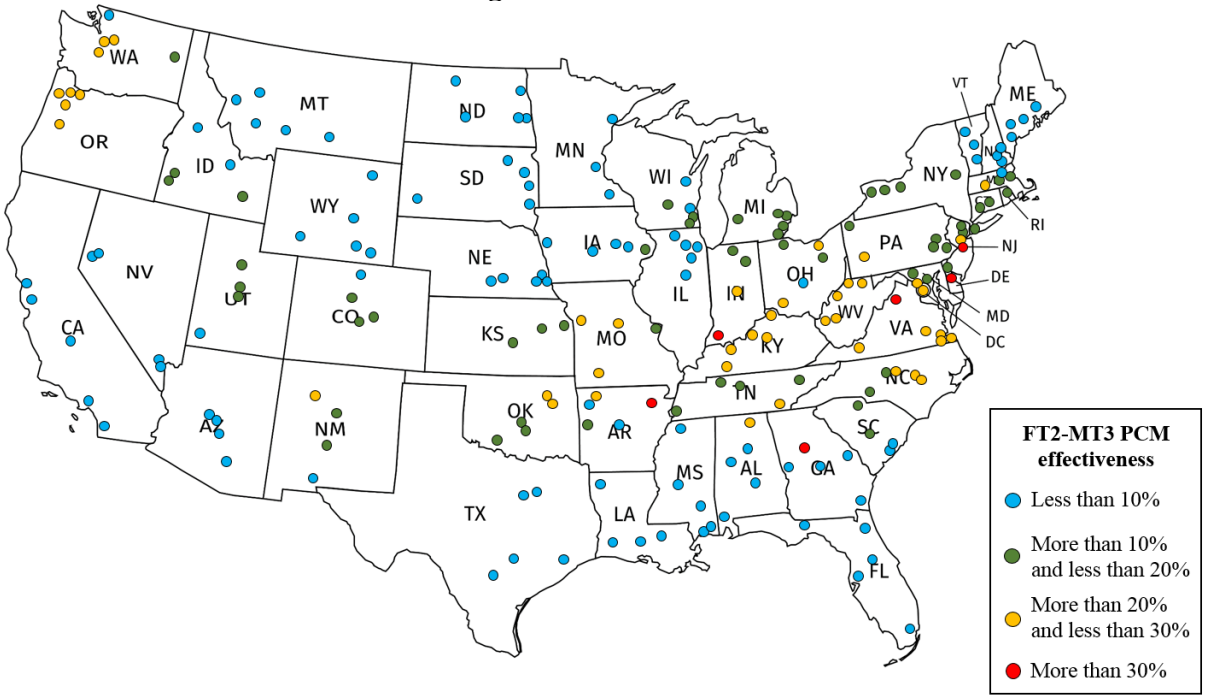


(b)

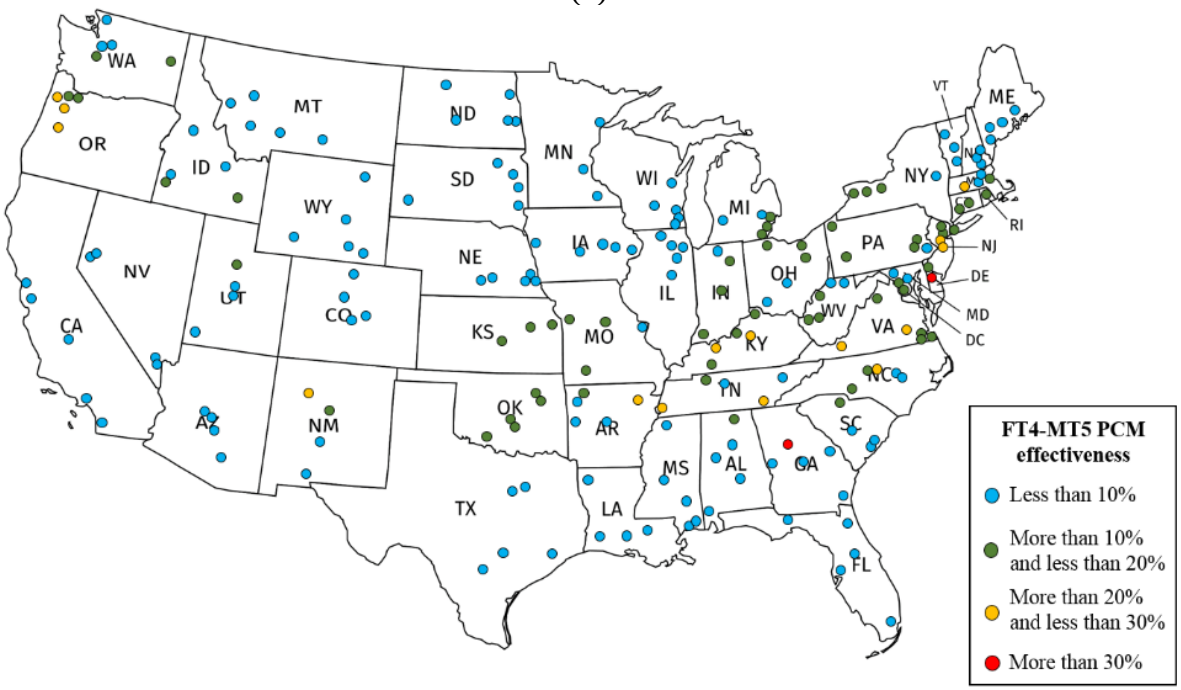


(c)

In this study, the numerical model predicts that PCM incorporation is more effective at preventing freeze-thaw cycling, as the freezing and melting temperatures are decreased toward 0 $^{o}C$ for FT0-MT1 and FT2-MT3 PCMs. Figure 3-11(a) shows that the FT0-MT1 PCM is relatively more

effective in reducing the freezing time and depth in states with milder weather compared to the effectiveness of FT2-MT3 and FT4-MT5 PCMs, as displayed in Figure 3-11(b) and Figure 3-11(c), respectively. It is concluded that the incorporation of a PCM with relatively low $T_F^i$ would lead to release a considerable amount of heat inside the pavement right before the ice formation within concrete pores and prevent localization of freeze-thaw damage. Conversely, a lower $T_M^f$ would cause the solid PCM to melt completely to retrieve the heat right before a subsequent cooling cycle, thereby decreasing the localized damage due to freeze-thaw cycles.

### 3.7 Conclusions and summary

This paper investigated the development of a computer simulation tool that used a one-dimensional finite difference method and homogenization techniques to assess the thermal behavior of cementitious materials containing PCM exposed to thermal cycling. The computational results were compared to the experimental data for mortar specimen tested in the LGCC (small-scale) test with a temperature range of -40 $^oC$ to +24 $^oC$ and concrete slabs (large-scale) tested with a temperature range of -10 $^oC$ to +10 $^oC$. The numerical model was validated by measured data from LGCC experimental data where it was concluded that the consideration of a gradual phase transition of PCM with a narrow range of transition temperature better predicted the thermal response (temperature profile and associated heat flow) of the specimen, while the LWA pore sizes had a negligible effect. Analysis of the slab test also showed that the time of freezing at which temperature reduced below 0 $^oC$ was decreased roughly by 9 $h$ when compared to a slab without PCM, which implied the improvement in the freeze-thaw performance of slab.

The numerical model was also used to investigate the PCM effectiveness on reducing the impact of freeze-thaw cycling within concrete pavements located in different regions of the United States. It was observed that the transition temperatures of PCM during freezing and melting events are important properties that govern the effectiveness of PCM at reducing the impact of freeze-thaw cycles. In other words, they help control how quickly the temperature of the pavement drops below the freezing point of pore solution within concrete pores. In 122 out of 210 cities investigated, a dose of 170 ($kg/m^3$) of FT0-MT1 PCM would reduce the freezing time and depth of concrete pavement by at least 10 %, primarily throughout the East, the Central, and Pacific Northwest regions. The model results also showed that low transition temperatures were more

effective, where pavements located in an additional 13 and 44 experienced a reduction in freezing time and depth of pavements by at least 10 %. These preliminary results suggested that the use of PCM-LWA composites as a thermal energy storage system shows promise in improving the freeze-thaw performance of concrete pavements and merits further, more detailed investigations.

# 4. A TWO-STEP MULTISCALE MODEL TO PREDICT EARLY AGE STRENGTH DEVELOPMENT OF CEMENTITIOUS COMPOSITES CONSIDERING COMPETING FRACTURE MECHANISMS

This chapter contains work that was originally published in Elsevier as "Hadi S. Esmaeeli, Mehdi Shishehbor, W. Jason Weiss, and Pablo D. Zavattieri. A two-step multiscale model to predict early age strength development of cementitious composites considering competing fracture mechanisms. In Journal of Construction and Building Materials. Volume 208., pp. 577-600. Elsevier, 2019." The original article has been used with permission as stated below.

Reprinted by permission from Elsevier, in: Journal of Construction and Building Materials. "A two-step multiscale model to predict early age strength development of cementitious composites considering competing fracture mechanisms." Hadi S. Esmaeeli, Mehdi Shishehbor, W. Jason Weiss, and Pablo D. Zavattieri, COPYRIGHT (2019).

## 4.1 Introduction

Mesomechanical models have recently gained prominence in the analysis of damage and failure mechanism of concrete (Benedetto et al., 2018; Dutta & Chandra Kishen, 2018; Eliáš et al., 2015; Zhichao Liu & Hansen, 2016; López et al., 2008b; R. Zhou & Lu, 2018). A well-recognized approach to fracture for concrete is to use the cohesive zone model which enables the crack to propagate through zero-thickness interfaces equipped with a normal-shear traction-separation law representing non-linear fracture process (Feng & Wu, 2018; Toyama et al., 2018; X. Xu & Needleman, 1995). Several FEM-based models in the literature have dealt with cracking in heterogeneous materials via computational models, such as continuum damage mechanics (CDM) (Kim & Abu Al-Rub, 2011), extended finite element method (XFEM) (Ng & Dai, 2011) and cohesive zone model (CZM) (W. Gao et al., 2015). CDM model cannot model the initiation, and propagation of explicitly, as cracks occur continuously. In the XFEM approach, additional degrees of freedom are considered in the standard finite element using local enrichment functions, where further external criteria are required to anticipate the cracking (Sukumar et al., 2000). A major drawback of this method is the complexity of problems involving pervasive fracture and fragmentation (i.e., interaction of many cracks which is of interest in this paper). On the other hand, the cohesive element approach is consisted in inserting interface (cohesive) elements along the surfaces of the two- or three-dimensional continuum elements correspondingly (Camacho & Ortiz, 1996; M. Ortiz & Pandolfi, 1999; Rimoli & Rojas, 2015; X.-P. Xu & Needleman, 1996). Finite element method (FEM) based models have been beneficial to analyze the mesostructure and the

effects of local properties on the macroscopic behavior of concrete. For instance, Wang et al. (X. Wang et al., 2015) and Lopez et al. (López et al., 2008a) employed a mesomechanical model to systematically study by considering constant cohesive properties (strength and fracture energy per unit area) of mortar and $ITZ^c$ phases and morphological properties (arrangement, size, and volume fraction) of coarse aggregate phases. The mechanical response was calculated to consider microcracking coalescence, localization, and macroscopic crack formation. While they did not consider the aging effect for the cement paste and local failure of aggregate phase on early-age mechanical response of concrete, their model provided information on how cohesive properties of concrete constituents have direct effect on the resulting strength, softening behavior, and crack morphology.

This paper proposes a computational approach to assess the competing mechanisms occurring under remote predominantly mode-I failure for early-age mortar and concrete. The study analyzes the evolution of the mechanical properties for the cement paste and ITZ phases, along with constant mechanical properties for the aggregate phase to simulate the crack propagation through the potential phases to complete fracture. We hypothesize that the knee point is primarily controlled by the competition between the fracture of the cement that change over time at early ages and the fracture of the aggregate phase at later ages. This work aims to develop a holistic numerical framework to understand the role played by the aggregate phase on limiting the early-age mechanical response and resulting alteration in the cracking pattern of cementitious composites.

The multiscale approach consists of a two-step homogenization model where (1) the material properties of the cement paste, fine aggregate, and $ITZ^m$ ("m" denotes mortar) phases are utilized to analyze the homogenized properties and associated failure mechanisms for heterogeneous mortar using a coupled continuous and discontinuous homogenization scheme (De Borst, 2008; Geers et al., 2010; Nguyen, Stroeven, et al., 2011; Phu Nguyen et al., 2010; Verhoosel et al., 2010), and compares to the experimental observations, and afterward (2) the homogenized mechanical properties of mortar obtained from the first step are upscaled to be utilized along with the mechanical and morphological properties of coarse aggregates to quantify the mechanical response and crack propagation within mesostructure of concrete via continuous homogenization scheme and contrast them with experimental counterparts.

The proposed multiscale approach considers three representative structures of cementitious composites, outlined in Figure 4-1 (Bernard et al., 2003; Constantinides & Ulm, 2004):

Level I ($10^{-6}$-$10^{-4}$ $m$): The microstructure of paste material with the characteristic length of $l_p$ is composed of large calcium hydroxide (CH) crystals (<200 $\mu m$), reacted aluminate phase (A-phase), pore space, and calcium silicate hydrate (C-S-H) (Bernard et al., 2003; Constantinides & Ulm, 2004). The structure of paste develops during the hydration process, which leads to reducing the porosity and increasing the strength (J. J. Thomas & Jennings, 2006). The size of homogeneous phases is the order of magnitudes smaller than the sizes of mortar and concrete specimens used in four-point flexural tests (Barde et al., 2005); thus, the paste material is treated as a homogeneous and brittle phase in this study.

Level II ($10^{-3}$-$10^{-2}$ $m$): The mortar material is treated as a three-phase composite with the characteristic length of $l_m$ that is composed of homogeneous phases of paste as the matrix, and fine aggregate particles as inclusions (<4.75 $mm$), and $ITZ^m$ embedded between cement paste and fine aggregate. This level has been the focus of previous mesomechanical models, both numerically (G. Li et al., 1999) and analytically (Garboczi, 1993). In this work, Level II is considered as the starting point for the computational homogenization approach.

Level III ($10^{-1}$-$10^{1}$ $m$): The concrete material is considered as a three-phase composite with the characteristic length of $l_c$ that is composed of homogeneous phases of mortar as the matrix, coarse aggregate as the inclusion (4.75 $mm$< <25 mm), and $ITZ^c$ (“c” denotes concrete) embedded between the mortar and coarse aggregate particles (Garboczi, 1993; G. Li et al., 1999).

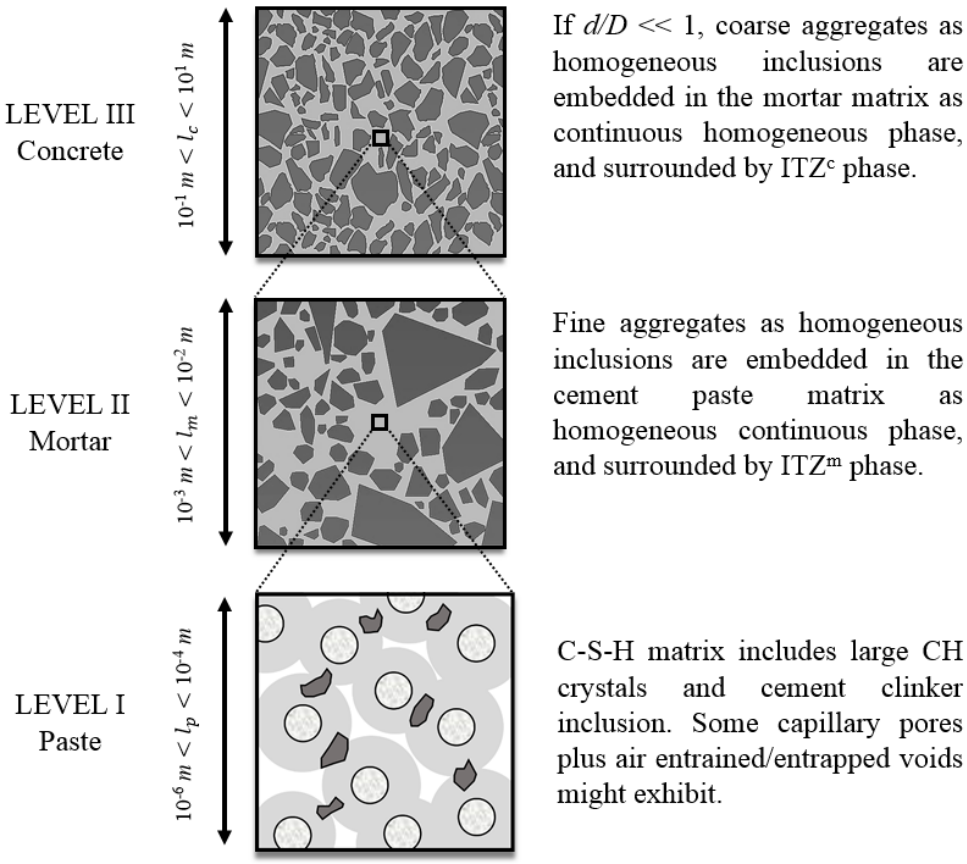


Figure 4-1. The three-level representative structures of cementitious composites, adapted from (Bernard et al., 2003; Constantinides & Ulm, 2004).

## 4.2 A two-step homogenization mesomechanical model

A mesomechanical model has been developed to understand better the composite effect on the early-age mechanical response of cementitious composites under mode-I loading. This includes the prediction of tensile stiffness and strength gain, as well as damage mechanism through micro-crack propagation and coalescence, macro-crack pattern, and fracture energy. Finite element method (FEM) based models have been beneficial to analyze the mesostructure and the effects of local properties on the macroscopic behavior of concrete. For instance, Wang et al. (X. Wang et al., 2015) and Lopez et al. (López et al., 2008a) employed a mesomechanical model to systematically study by considering constant cohesive properties (strength and fracture energy per unit area) of mortar and ITZ$^c$ phases and morphological properties (arrangement, size, and volume fraction) of coarse aggregate phases. The mechanical response was calculated to consider microcracking coalescence, localization, and macroscopic crack formation. While they did not

consider the aging effect for the cement paste and local failure of the aggregate phase on early-age mechanical response of concrete, their model provided information on how cohesive properties of concrete constituents have a direct effect on the resulting strength, softening behavior, and crack morphology.

This work develops a two-dimensional FEM-based mesomechanical model that accounts for the evolution of tensile stiffness and strength of cement paste (and ITZ) in time, and the differences between the strengths of constituents. This study also investigates the effects of Poisson's ratio and fracture energy development of cement paste (and ITZ) on elastic and fracture properties of cementitious composites. To test the validity of the hypothesis developed in the previous section, the mesostructures of mortar and concrete are modeled under uniaxial tension and four-point flexural tests. Prior experimental observations illustrate that different failure mechanisms are at work as the hydration of cement paste progresses. We hypothesize that the effects of cement paste strength versus aggregate strength compete in the hydration process: before knee point, the tensile strength of cement paste phase seems to have a stronger influence than the tensile strength of aggregate phase on the evolution of the composite strength of cementitious composites, and after knee point, it is the inverse. As the cement paste gains strength, it also becomes more brittle, which forces the cement paste to fail primarily in tension. The failure mechanism is observed to be dictated by crack propagation around the aggregates at a low degree of hydration. At the same time, the knee point in the bilinear mortar and concrete curves represents a transition to aggregate fracture.

To provide insights into the mechanical properties of mesostructure constituents and how different phases fail during mode-I loading, we explicitly consider the competition of the crack propagation of each phase in our mesomechanical model. The contribution of the aggregate phase of different sizes to the macroscopic mechanical response and cracking patterns occurs at two length scales. The two levels that particularly distinguish the contribution of fine aggregates at Level II from the contribution of coarse aggregates at Level III indicates a two-step homogenization scheme, as shown in Figure 4-2. The homogenization procedure is used as a computational tool to alleviate the burden of material properties characterization, in which the properties can be homogenized as a function of key morphological and mechanical properties such as the structural composition, aggregate morphology, and the mechanical properties of constituents.

Figure 4-2(a-c) illustrates a continuum-based finite element modeling framework that considers the individual mechanical properties of the mortar constituents (e.g., cement paste and fine aggregate) to homogenize the elastic and cohesive properties of Level II mortar to replace the heterogeneous mortar by an identical homogeneous mortar in Level III concrete. To this end, we employ continuous and discontinuous computational homogenization schemes. Figure 4-2(a) shows an arbitrary mesostructure of heterogeneous mortar. To characterize the linear elastic region of mortar, the developing tensile stiffness of cement paste $E^p(t)$ over early ages were obtained from experimental measurements (Yoshitake et al., 2012; Zhao et al., 2014) along with constant tensile stiffness of fine aggregate ($E^{fa}$), as displayed in Figure 4-2(b). The inset in Figure 4-2(b) shows the evolution of $E^p$ as a function of $t$ (e.g., $E^p_{t_2} > E^p_{t_2}$ where $t_2 > t_1$), and a constant $E^{fa}$ which is determined experimentally by Esmaeeli et al. (Hadi Shagerdi Esmaeeli, 2015) based on mechanical analysis of limestone beams under three-point flexural test. Afterward, the tensile strength development of mortar $f_t^m(t)$ is determined by specifying the cohesive properties (tensile strength and fracture energy) of the interface elements embedded within cement paste ($f_t^p(t)$ and $G_{Ic}^p$), fine aggregates ($f_t^{fa}$ and $G_{Ic}^{fa}$), and ITZ$^m$ ($f_t^p(t)$ and $G_{Ic}^p$) continuum elements, as illustrated in Figure 4-2(c). We formulate the traction-separation law ($T$-$u$ curve) for early-age mortar at each discrete time ($f_t^m(t)$ and $G_{Ic}^m$) to capture the nonlinear pre-peak region governed by tensile micro-cracking and post-peak region dominated by micro-crack coalescence, macro-crack formation, and corresponding shear failure development. The interpretation of this $T$-$u$ curve is demonstrated in the inset in Figure 4-2(c). $T$-$u$ curve for cement paste evolves as its tensile strength develops (e.g., $f^p_{t,t_2} > f^p_{t,t_1}$ where $t_2 > t_1$) acquired from experimental data (Barde et al., 2005), while $G_{Ic}^p$ is considered to remain constant. For fine aggregate, $T$-$u$ curve is characterized by constant $f_t^{fa}$ and $G_{Ic}^p$ obtained from experimental results (Hadi Shagerdi Esmaeeli, 2015). We will get back to this nonlinear fracture approach associated with a bilinear traction-separation law.

The second homogenization step is composed of connecting from Level II to Level III, where the continuous homogenization scheme is used to quantify the macroscopic tensile stiffness and strength of early-age concrete ($f_t^c(t)$ and $E^c(t)$). Figure 4-2(d) shows an arbitrary mesostructure of heterogeneous concrete composed of the mortar matrix resulting from the first homogenization step and coarse aggregate particles. Similar to the modelling of Level II mortar, we adopt a continuum FEM-based model to characterize the linear elastic region of Level III concrete by

utilization of developing tensile stiffness of mortar at discrete ages ($E^m_{t_2} > E^m_{t_2}$ where $t_2 > t_1$) along with constant tensile stiffness of coarse aggregate ($E^{ca}$), displayed in Figure 4-2(e). Unlike Level II, here we employ the values for properties $E^m(t)$, $f_t^m(t)$, and $G_{Ic}^m$ taken from first homogenization step, while the properties $E^{ca}$, $f_t^{fa}$, and $G_{Ic}^{ca}$ are obtained from experimental measurements. Similar to Level II, Figure 4-2(f) depicts the evolution of *T-u* curves for mortar at early ages as $f_{t,t_2}^m > f_{t,t_1}^m$ where $t_2 > t_1$, while $G_{Ic}^m$ remains constant. The mixture proportioning and specimen preparation procedures for making the mortar and concrete specimens are explained in Appendix A. It is necessary to note that the viscoelastic phenomenon of cement paste is neglected in this study, as the mortar and concrete specimens are tested at fast loading rate. A few mesoscopic models have systematically investigated the effects of temperature and moisture variations on the mechanism of shrinkage cracking in cementitious composites (Neubauer et al., 1996; Tang et al., 2013, 2016). This study, however, is focused on well cured and unrestrained mortar and concrete specimens, where the effect of shrinkage attributed to moisture diffusion due to external drying does not contribute to the cracking. Future work will focus on better determining and quantifying if moisture diffusion results in the development of stress and early-age cracking.

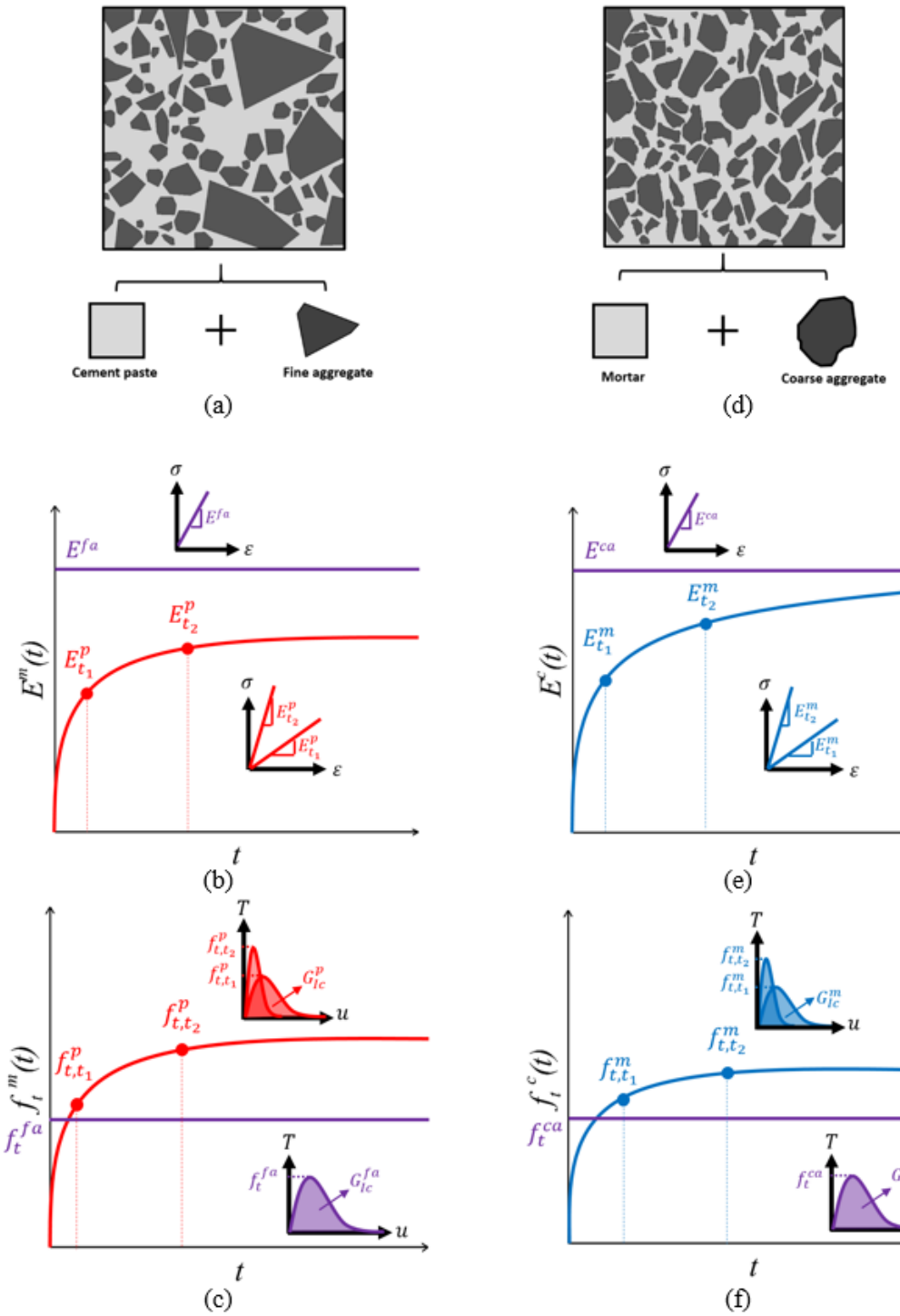


Figure 4-2. Numerical framework representing a two-step multiscale modeling the mechanical response development of (a) a heterogeneous Level II mortar, knowing (b) the tensile stiffness of paste and fine aggregate ($E^p(t)$ and $E^{fa}$), and (c) the tensile strength ($f_t^p(t)$ and $f_t^{fa}$) and fracture energy ($G_{Ic}^p$and $G_{Ic}^{fa}$) of paste and fine aggregate; afterwards modeling the mechanical response development of (d) a heterogeneous Level III concrete, knowing (e) the tensile stiffness of mortar and coarse aggregate ($E^m(t)$ and $E^{ca}$), and (f) the tensile strength ($f_t^m(t)$ and $f_t^{ca}$) and fracture energy ($G_{Ic}^m$and $G_{Ic}^{ca}$) of mortar and coarse aggregate.

After finite element meshing of mesostructures of cementitious composites[2], 4-node zero-thickness cohesive interface elements are pre-inserted between existing 3-node bulk elements by developing an in-house code in C programming language. We employed an explicit finite element approach enhanced with a central difference time integration scheme to predict the behavior of heterogeneous mesostructures in transient dynamics applications using finite element package FEAP (Taylor, 2008). To calculate the field variables at respective nodes, the requirement for small time steps for stability reason is met.

### 4.2.1 Mesomechanical representation

#### 4.2.1.1 Representative volume element (RVE)

Homogenization methods have been used to estimate the macroscopic material properties by averaging the response of a representative volume element (RVE) with a determined size where the mesostructure is specifically analyzed (Nguyen, Stroeven, et al., 2011). For materials having a random mesostructure, this RVE has been used for the description of composition and heterogeneity of the internal structure of the material system (see Figure 4-2(a)). The RVE describes the different phases of mesostructure with their specific structural geometry, in which the spatial distribution of material properties has been addressed. Considering the development of mechanical properties of matrix and ITZ phases at an early age, we incorporate these time-dependent properties into separate RVEs to perform the simulations at discrete ages. It is worth mentioning that an RVE represents a mesoscopic specimen statistically when (1) the homogenized properties do not alter considerably as the size of specimen increases, and (2) the homogenized properties do not depend on the mesostructural randomness as the size of the specimen is large enough (Nguyen, Lloberas-Valls, et al., 2011).

#### 4.2.1.2 Fracture-based interface cohesive law

A mesomechanical model has been developed to assess the roles of elastic deformation of continuum elements coupled with the damage and failure of the material on the mechanical behavior of heterogeneous RVEs selected for cementitious composites. The existence of phases with dissimilar properties requires the establishment of an approach to fracture, where the

[2] *Commercial FE package ABAQUS is used to generate triangular bulk elements with random sizes and orientations.*

contribution of geometrical and mechanical properties of heterogeneities on the overall mechanical behavior of cementitious composites is determined. While previous FEM-based models were beneficial to quantify the stress distribution and local material failure in the mortar and interface between mortar and coarse aggregates (ITZc) (Mirzabozorg & Ghaemian, 2005; Skrikerud & Bachmann, 1986), not many have addressed the influence of mechanical properties of hydrating cement paste and aggregates resulting in potential cracking in the aggregates. By inserting interface elements between continuum elements, these elements represent the potential crack paths that allow the cracks to propagate through them. Several FEM-based models in the literature have dealt with cracking in heterogeneous materials via computational models, such as continuum damage mechanics (CDM) (Kim & Abu Al-Rub, 2011), extended finite element method (XFEM) (Ng & Dai, 2011), and cohesive zone model (CZM) (W. Gao et al., 2015). CDM model cannot model the initiation, and propagation of explicitly, as cracks occur continuously. In the XFEM approach, additional degrees of freedom are considered in the standard finite element using local enrichment functions, where further external criteria are required to anticipate the cracking (Sukumar et al., 2000). A major drawback of this method is the complexity of problems involving pervasive fracture and fragmentation (i.e., interaction of many cracks which is of interest in this paper). On the other hand, the cohesive element approach is consisted of inserting interface (cohesive) elements along the surfaces of the two- or three-dimensional continuum elements correspondingly. This approach suits for the analysis of problems which include pre-defined crack paths; however, several recognized issues have effects on its accuracy when modeling the problems with random crack directions, i.e., (i) artificial flexibility resulting in alteration of propagation of stress wave speed, (ii) spurious crack tip speed, and (iii) mesh size and orientation effects. Regardless of these widely definite constraints, this approach is one of the most robust methods for fracture analysis. Therefore, we employ a non-linear fracture analysis in which the zero-thickness interface elements enhanced with a traction-separation cohesive law embedded as intra-phase (aggregate-aggregate and matrix-matrix) and inter-phase (aggregate-matrix) elements.

It is assumed that the interface elements carry forces that oppose separation and shear between two surfaces until failure, where the magnitude of these forces is a function of the relative separation and shear displacement between the two surfaces. Note that the intrinsic strength and fracture toughness of cementitious composites are much larger in pure mode-II than those in pure mode-I. Therefore, the tensile stresses at the intra- and inter-phase elements have a significant

influence on the load capacity and fracture behavior of these materials subjected to remote mode-I loading condition. In contrast, the contribution of shear tractions at these interface elements to the overall mechanical behavior is negligible. The formulation of a cohesive element approach as a function of traction (rather than strain) and $G_c$ regularizes unstable behavior during crack nucleation occurring on the weak interface element. The continuum elements are commonly considered to show a linear elastic behavior. For instance, let us consider a 2D Level II mortar RVE discretized with linear triangular elements, shown in Figure 4-3(a), with prescribed displacement, $\bar{u}$ on the Dirichlet boundary condition $\Gamma^u$. Schematics of three sets of interface elements with different cohesive laws inserted within fine aggregate particles ($f_a$-$f_a$), cement paste matrix (p-p), and their interface ($ITZ^m$) is shown in Figure 4-3(b). While characterizing the fracture properties of ITZ phase at two levels of II ($ITZ^m$ in the mortar) and III ($ITZ^c$ in concrete) can be useful to understand the onset of cracking as a displacement discontinuity between matrix and particles with dissimilar properties may exist, we take an approach in this study where the cohesive properties of both ITZ phases are explicitly considered to be identical to their associated matrix.

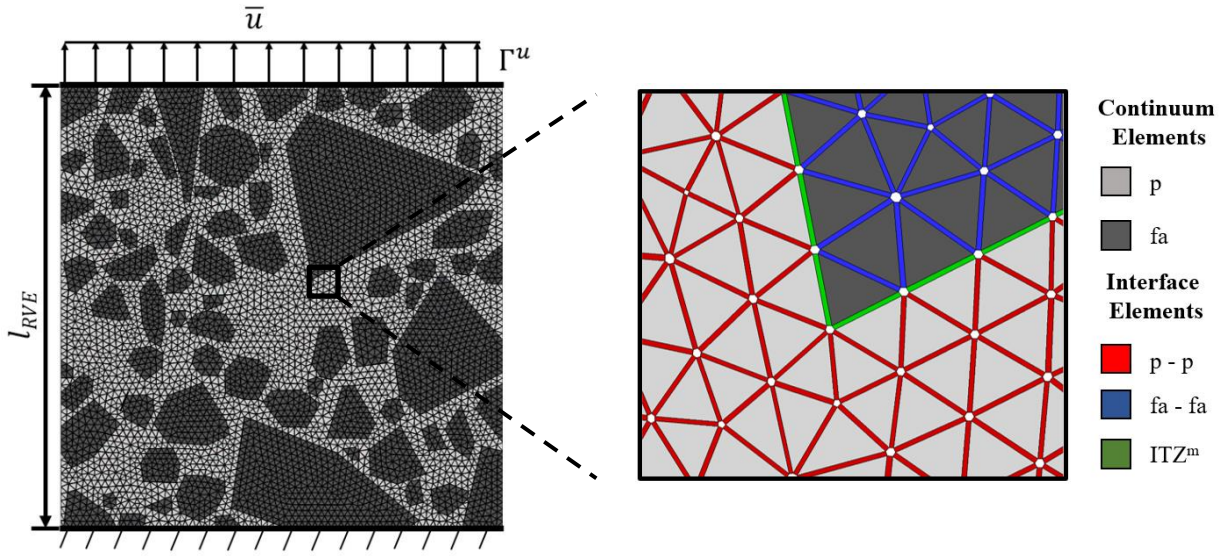


(a) (b)

Figure 4-3. (a) Fracture analysis of an RVE for Level II mortar RVE subjected to mode-I loading containing (b) continuum elements for two phases of the matrix, and aggregate as well as three interface elements inserted between paste-paste (p-p), fine aggregate-fine aggregate (fa-fa), and paste-fine aggregate ($ITZ^m$), with a cohesive law defined in (c) opening mode, and (d) shear mode.

Figure 4-3 continued

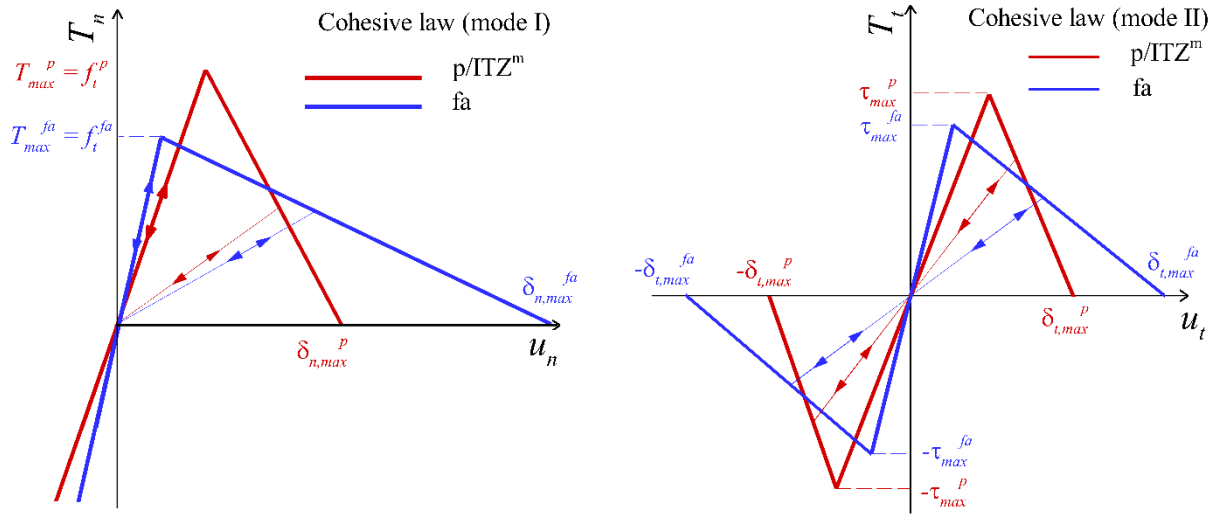


(c) (d)

The cohesive law for interface elements is formulated in terms of normal and shear components of stresses $\sigma = (T_n, T_t)$ on the interface element and corresponding relative displacements $u = (u_n, u_t)$. We employ a bi-linear cohesive law in opening and shear mode implemented as a user-subroutine in the finite element package FEAP. The non-dimensional displacement jump, $\lambda = \sqrt{\left(\frac{u_n}{\delta_n}\right)^2 + \left(\frac{u_t}{\delta_t}\right)^2}$ is defined to describe the degradation of interface element by normalizing the evolution of $u_n$ and $u_t$ parameters respect to the maximum normal and shear displacement values to reach failure ($\delta_n$, $\delta_t$).

The mechanical behavior of the interface elements is primarily governed by two fracture energy parameters $G_{Ic}$ (associated with opening mode) and $G_{IIc}$ (associated with shear mode). Two traction components describe the resistance to separate the interface elements in normal ($T_n(t) = \frac{1-\lambda^*}{\lambda^*}\left(\frac{u_n}{\delta_n}\right)\frac{T_{max}(t)}{1-\lambda_{cr}}$) and tangential directions ($T_t(t) = \frac{1-\lambda^*}{\lambda^*}\left(\frac{u_t}{\delta_t}\right)\frac{\tau_{max}(t)}{1-\lambda_{cr}}$), where $T_{max}$ and $\tau_{max}$ are nominal tensile and shear strength. The value of $\lambda^*$ monotonically increases given by $\lambda^*$= max ($\lambda^*$, $\lambda$), where $\lambda_{max} = \lambda_{cr}$ initially and $\lambda_{max} = \lambda$ if $\lambda_{max} > \lambda$. It should be noted that the normal and tangential tractions reach their maximum value at $\lambda = \lambda_{cr}$. The cohesive law in opening and shear modes is identified in Figure 4-3(c) and (d), respectively. It should be noted that the initial stiffness of cohesive law is selected with care to avoid the addition of compliance due to the presence of

interface elements if compared with the compliance of continuum elements. Therefore, at this initial stage, the continuum elements remain intact.

The area under the traction-separation curves corresponds to fracture energy in the opening ($G_{Ic}$=0.5$T_{max}$.$\delta_n$) and shear modes ($G_{IIc}$=0.5$\tau_{max}$.$\delta_t$) required to create new discontinuous surfaces (i.e., cracks). When displacement initially increases in the linear-elastic portion of the traction–separation response, the interface element inserted around the crack tip quickly raises to its strength and progresses to the softening portion of the response. Once $\lambda^* \geq \lambda_{cr}$, the interface element initiates to degrade, thus dissipating energy. Further increasing the tip displacement, elements adjacent to the crack tip also undergo reversible deformation, in which the characteristic length of these elements is defined as cohesive zone length, $l_{cz} \approx EG_{Ic}/T_{max}^2$. Any unloading during degradation follows the irreversible path illustrated in Figure 4-3(c) and (d). The onset of cracking in the interface element initiates while $\lambda_{max}$=1 (i.e., $T_n$=$T_t$=0).

### 4.2.2 A coupled multiscale approach for cohesive crack homogenization

Figure 4-5 presents the fundamental concept of continuous and discontinuous homogenization schemes for cohesive crack modeling. For quasi-brittle materials such as cementitious composites subjected to a simple uniaxial tension, the averaged stress-strain response ($\sigma$–$\varepsilon$) can be separated into two regions of pre-peak hardening and post-peak softening, as shown in Figure 4-5(a). The early part of the hardening region of $\sigma$–$\varepsilon$ curve (highlighted with a lighter color in Figure 4-5(a) determines the elastic properties ($E$) and Poisson's ratio ($\upsilon$) utilizing continuous homogenization scheme. The continuous homogenization calculates a homogenized macroscopic $\sigma$–$\varepsilon$ response governing the bulk behavior before strain localization (Geers et al., 2010; Smit et al., 1998). For completeness, this computational homogenization scheme is described here.

The behavior of bulk material at a macro level is determined through the continuous computational homogenization as described in (Zohdi & Wriggers, 2008). For completeness, this homogenization scheme is briefly described as follows. The homogenized stresses and strains of an RVE are determined as the volume averages of its element constituents using equation 4-1.

$$\sigma = \frac{1}{|\Omega_e|}\int_{\Omega_e} \sigma_e \, d\Omega = \frac{1}{|\Omega_e|}\int_{\Gamma_e} t_i^e x_j^e \, d\Gamma, \qquad 4\text{-}1$$

$$\varepsilon = \frac{1}{|\Omega_e|}\int_{\Omega_e} \varepsilon_e \, d\Omega = \frac{1}{|\Omega_e|}\int_{\Gamma_e} \left(u_i^e n_j^e + u_j^e n_i^e\right) d\Gamma$$

where $\Omega_e$ denotes the RVE domain, $|\Omega_e|$ is the area of RVE, $\Gamma_e$ is the boundary of RVE, $\sigma_e$ and $\varepsilon_e$ are the stress and strain tensors at bulk Gauss points, respectively, $t^e$ represents the traction vector while $x^e$ is the position vector and $n^e$ is the unit outward normal to $\Gamma_e$. Therefore, the homogenized tensile stiffness, $D_0$ is determined using the analytical expression $\sigma = (D_0.\varepsilon)$.

For modeling cohesive cracks in random heterogeneous quasi-brittle materials, a discontinuous homogenization scheme is employed as a regularization technique for the continuous homogenization to extract the localized deformation from the state of deformation of RVE though failure zone averaging technique. Therefore, we define the homogenized stresses ($T_n$) and strains ($\varepsilon_{dam}$) as the volume averages of the stress and strains of RVE elements within $\Omega_d$ rather than over $\Omega_e$ using equation 4-2.

$$T_n = \frac{1}{|\Omega_d|}\int_{\Omega_d} \sigma_e \, d\Omega_e, \; \varepsilon_{dam} = \frac{1}{|\Omega_d|}\int_{\Omega_d} \varepsilon_e \, d\Omega_d \qquad 4\text{-}2$$

The above integrals are calculated directly using numerical quadrature as they cannot be converted to surface integrals. We, thus, define $u_n$ as the damage opening $\hat{u}_{dam}$ shifted to the left by $u_{dam}$ to obtain the homogenized traction-separation relations using equation 4-3.

$$u_n = \hat{u}_{dam} - u_{dam}, \; \hat{u}_{dam} = \varepsilon_{dam} \cdot (l_b n) \qquad 4\text{-}3$$

where $n$ denotes the cohesive crack normal vector.

To determine the existence of an RVE for softening mortar when using continuous and discontinuous homogenization scheme, let us consider the example shown in Figure 4-4. Table 4-1 outlines the material properties for continuum elements as well as interface elements at two early ages of 16 *h* and 96 *h*. The equilibrium path is determined through applying a uniaxial displacement control with a fixed increment of $2\times10^{-5}$ *mm*. A plane strain condition is assumed. The behavior of bulk mortar can be calculated a priori using the continuous homogenization scheme. Given the application of the prescribed displacement field on the RVE, the mesoscopic boundary value problem (BVP) is computed to quantify the macroscopic stress through the calculation of the mesoscopic stress field in the pre-peak region. Furthermore, the discontinuous homogenization scheme is considered as an effective complementary method to the continuous homogenization scheme to homogenize the cohesive law in random heterogeneous RVEs, thus define a unique RVE for softening materials. To validate the objectiveness of a unique RVE for mortar w.r.t its size, the response of five mortar RVEs with $l_m$ of 6 mm to 15 mm subjected to

uniaxial tension is homogenized through discontinuous homogenization scheme, displayed in Figure 4-4. It is necessary to note that, although the $l_{cz}$ parameter of interface elements inserted along aggregate-aggregate continuum elements is very large respect to the RVE size, it is suggested to consider the optimum size of the RVE about three times larger than the fine aggregate size (Z. Bazant & Oh, 1983). The convergence of $T_n$-$u_n$ relation upon increasing the size of RVE verifies the existence of an RVE.

Table 4-1. Material parameters of continuum and interface elements within mortar RVE.

| Mechanical Property | Unit | $t$ = 16 $h$ | | $t$ = 96 $h$ | | fa |
|---|---|---|---|---|---|---|
| | | p | $ITZ^m$ | p | $ITZ^m$ | |
| $E$ | $[GPa]$ | 6.162 | - | 16.342 | - | 31.074 |
| $\upsilon$ | [-] | 0.2 | - | 0.2 | - | 0.15 |
| $G_{Ic}$ | $[J/m^2]$ | 41 | 41 | 41 | 41 | 43.4 |
| $G_{IIc}$ | $[J/m^2]$ | 410 | 410 | 410 | 410 | 434 |
| $T_{max}$ | $[MPa]$ | 1.68 | 1.68 | 5.862 | 5.862 | 3.8 |
| $\tau_{max}$ | $[MPa]$ | 2.35 | 2.35 | 8.8 | 8.8 | 5.7 |
| $\delta_n$ | $[mm]$ | 0.0488 | 0.0488 | 0.013 | 0.013 | 0.0013 |
| $\delta_t$ | $[mm]$ | 0.349 | 0.349 | 0.0931 | 0.0931 | 0.015 |
| $l_{cz}$ | $[mm]$ | 89.51 | 89.51 | 19.49 | 19.49 | 38.103 |

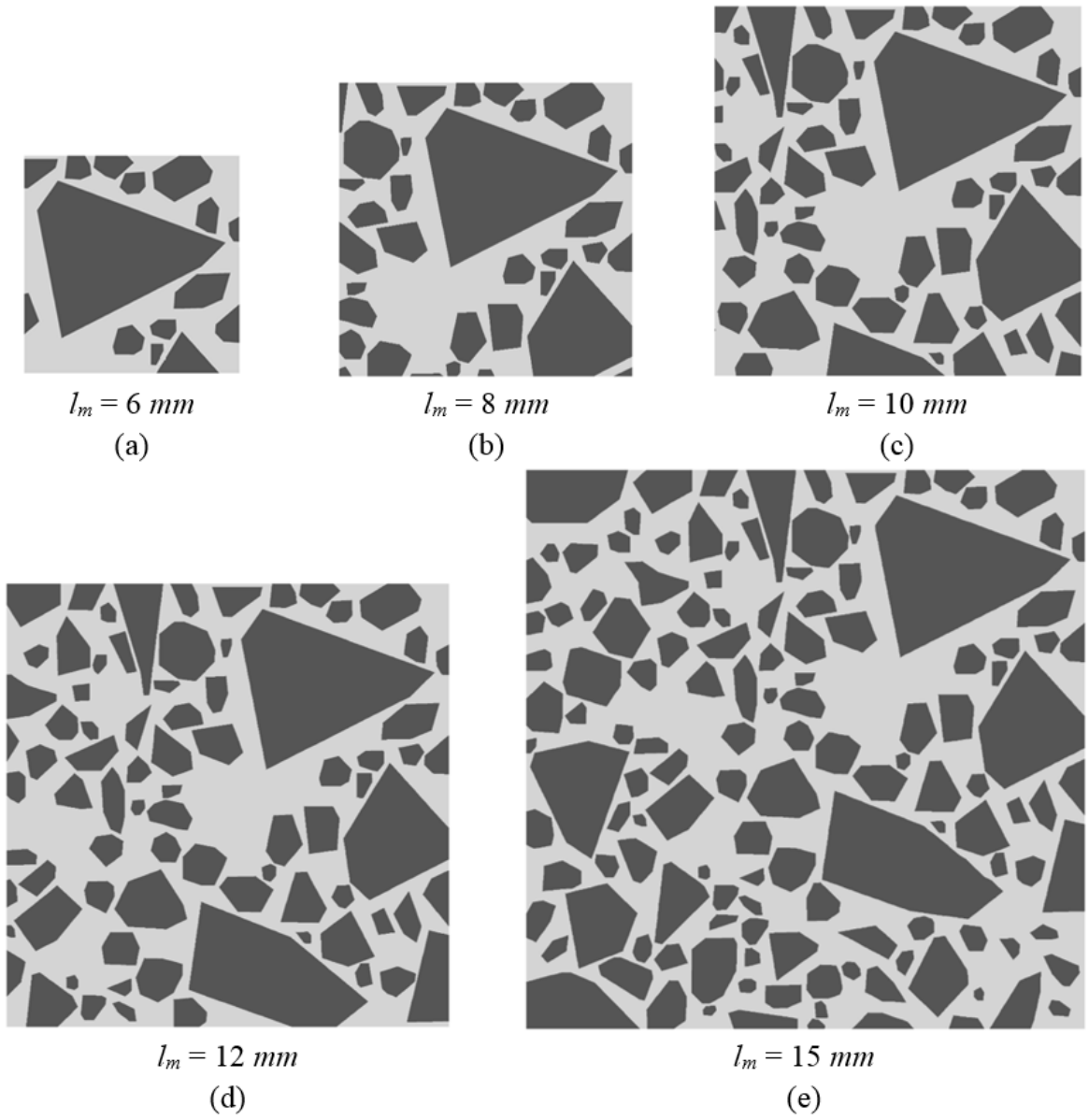


Figure 4-4. Mortar RVEs for the case of 55% fine aggregate by volume with sizes of (a) $l_m$ = 6mm, (b) $l_m$ = 8mm, (c) $l_m$ = 10mm, (d) $l_m$ = 12mm, and (e) $l_m$ = 15mm.

When strain localizes within the RVE, the homogenized $\sigma$–$\varepsilon$ response exhibits a local strain-softening behavior. Subsequently, the response obtained with this homogenization approach depends on the size of the RVE, the homogenized response becomes more brittle for larger sizes of the RVE (e.g. $l_{m_2} > l_{m_1}$), shown in Figure 4-5(a) (Gitman et al., 2007).

While a unique RVE cannot be found using continuous homogenization scheme, as the material does not maintain its statistical representativeness at the onset of strain localization,

Nguyen et al. (Phu Nguyen et al., 2010) introduced a novel approach utilizing the failure zone averaging technique to develop a discontinuous homogenization scheme, in which the cohesive law has been homogenized. Using the failure zone averaging approach, the discontinuous homogenization scheme explicitly considers the averaging over a localization domain, denoted as $\Omega_d$. Therefore, a cohesive law is upscaled by extracting only the localized deformation using the discontinuous homogenization scheme. There is no necessity to calculate the bulk stresses outside the localization domain as the material is considered to undergo a linear elastic behavior. It should be noted that this model assumes the nonlinear part of the pre-peak response (indicated by the darker region) to be insignificant.

The total deformation for RVE $\Delta$ can be described using the following homogenization relation:

$$\Delta = [l_m - l_b] \cdot D_0^{-1} \cdot T_n + u_{dam} + u_n \qquad 4\text{-}4$$

where $\Delta$ is the displacement over the entire domain of RVE, the first RHS term demonstrates the linear displacement over the domain $\Omega_e$, $u_{dam}$ represents the deformation quantified at the onset of crack localization in $\Omega_d$, and $u_n$ is the separation at one cohesive integration point, as shown in Figure 4-5(b). In equation 4-4, $l_b$ is the width of the localization band, the matrix $D_0$ is the homogenized tensile stiffness quantified over the domain $\Omega_e$, and $T_n$ is the corresponding traction at given $u_n$. Computation of $L_b$ and $u_{dam}$ is performed using the failure zone averaging approach. The reader is suggested to refer to the work of Nguyen et al. (Nguyen et al., 2012b) for further detailed information on the formulation and computer implementation.

By comparison of responses obtained from discontinuous homogenization scheme for various RVE sizes, we observe a small discrepancy between the peak stress and post-peak responses which are associated with the deviation in the hardening response (i.e., the darker region in Figure 4-5(a)) which are not considered in the discontinuous homogenization scheme (i.e., the pre-peak region is considered to exhibit a linear behavior). Herein, we use five mesostructures with randomly distributed fine aggregates for a certain size of RVE to compensate for this discrepancy by quantifying the mean value and standard deviation of $T_{max}$. Nguyen et al. (Nguyen et al., 2012b) also demonstrated that both continuous and discontinuous homogenization schemes yield the same value of peak stress; Therefore, we consider that $T_{max}$ can also be obtained using continuous homogenization scheme.

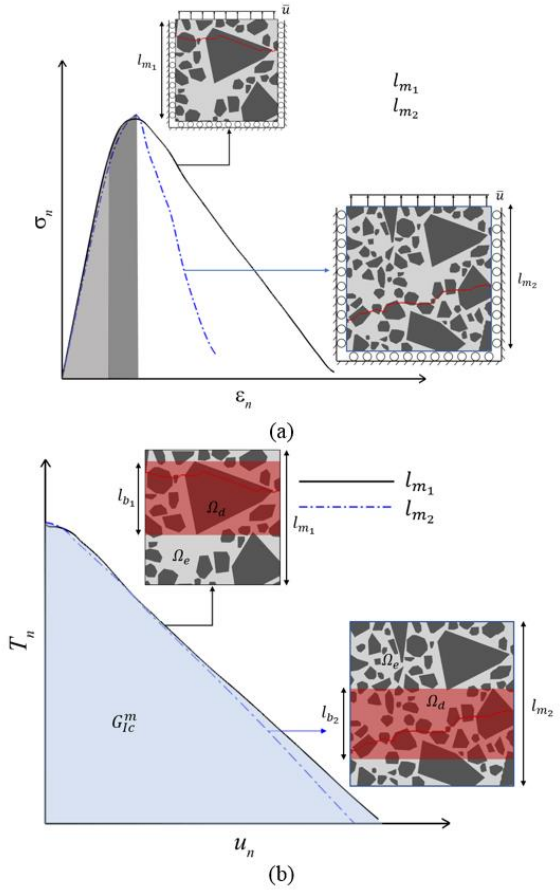


Figure 4-5. Using continuous and discontinuous homogenization schemes to couple macro-and meso level models. (a) Altering homogenized $\sigma$-$\varepsilon$ relations obtained with continuous homogenization scheme, and (b) unique homogenized $T_n$-$u_n$ relations obtained with discontinuous homogenization scheme.

The principle of separation of scales is defined by assuming the RVE size at the meso level be significantly smaller than the macro-scale over which the loading is applied (Nguyen et al., 2012a). As a result, the stress and strain fields at the macro level are uniform over the RVE. It is necessary to mention that the minimum distance between coarse aggregates in the RVE of Level III concrete is most likely to be small compared to the size of the RVE of Level II mortar. In this work, this issue has been resolved as the numerical solutions will demonstrate a good quantitative agreement in contrast with experimental observations. It is also worth mentioning that, in the case of material discontinuity during the crack initiation, the size of the interface elements should be small compared to the $l_{cz}$ parameter to obtain a homogenized cohesive law.

## 4.3 Results and discussion

### 4.3.1 Step 1: Mortar composite at Level II

The mortar material at the meso level is considered as a three-phase composite, in which the fine aggregate phase with a relatively high stiffness plays the role of inclusion surrounded by a weaker $ITZ^m$ embedded in a paste matrix with relatively low stiffness. From a geometrical standpoint, it is indicated that the precise geometry of the inclusions is less likely to considerably affect the homogenized elastic properties when the inclusions have a relatively higher stiffness than the matrix (Simeonov & Ahmad, 1995). However, the exact geometry of the inclusions is of importance to quantify the mechanical and cracking responses. Therefore, 2D mortar RVEs digitized from realistic images of mortar are generated using computed tomography (Lavergne et al., 2015). The first step is composed of the application of continuous and discontinuous homogenization schemes to Level II mortar RVE with a characteristic length of $l_m = 6 - 15\ mm$. The mechanical properties account for the effect of porosity (capillary and air-entrained pores of sizes smaller than 100 $\mu m$), of hydrated products (< 1 $\mu m$), and of unhydrated cement particles (< 100 $\mu m$) present at smaller scales. The RVE is considered to be composed of three phases: (i) cement paste of volume $V_p$, (ii) fine aggregate of volume $V_{fa}$, and (iii) the ITZ of zero thickness and volume (VITZm = 0). The volume fractions of these phases are described in Equation 4-5.

$$f_{fa} = V_{fa}/V_m\ ;\ f_p = V_p/V_m = 1 - f_{fa} \qquad 4\text{-}5$$

where $f_p$ and $f_{fa}$ parameters represent the volume fractions of cement paste and fine aggregate phases. It is worth mentioning that the average width of ITZ is of the order of 15 µm around each aggregate particle (Scrivener et al., 2004), which is 1/7th of average element size used in mortar RVE. Considering a constant non-zero width for ITZ may lead to computationally expensive models; thus, we assume an ITZ phase with zero width.

The early-age elastic properties of the three phases in the mortar and the cohesive properties of the interface elements are defined as follows:

- Regarding the Level I paste, the development of tensile stiffness, $E^p(t)$ is obtained from the experimental works of Yoshitake et al. (Yoshitake et al., 2012) and Zhao et al. (Zhao et al., 2014). The development of $T_{max}$ for cement paste is acquired from the experimental

work of Barde et al. (Barde et al., 2005). While it is known that the progress in hydration of cement paste may lead to alteration of Poisson's ratio $\upsilon^p$, $G_{Ic}^p$ and $G_{IIc}^p$ parameters with respect to time, we explicitly consider these parameters remain unchanged our numerical analysis indicates that the evolution of $\upsilon^p$ has a negligible effect on $\nu_m$ and $E_m$ development. Since the relative size of the fracture process zone, $l_{cz}$ is relatively larger than the size of mortar RVEs (e.g., mortar RVE with characteristic length $l_m$<15 mm), the mode-I failure is dominated by $T_{max}^p$ rather than $G_{Ic}^p$ (Z. P. Bazant & Planas, 1997; S. S. P. S. Shah et al., 1995). Based on previous mechanical analysis of the early-age cement paste, the two parameters $\upsilon$ = 0.18 (Kupfer & Hilsdorf, 1969), and $G_{Ic}$ = 41$\pm$4 (J/m2) (Hoover & Ulm, 2015) are used in this work. Therefore, the damage model accounts for the time-dependent behavior of $T_{max}^p$ to address its impact on damage initiation and growth, while $G_{Ic}^p$ is kept constant at 410 (J/m2). Previous mechanical analysis of the early-age cement paste found the development of $G_{Ic}^p$ to be in the range of 410$\pm$40 (J/m2) (Hoover & Ulm, 2015).

- The elastic and cohesive properties of aggregate used in the experiment (Indiana limestone) phase is obtained from our previous experimental study as follows (Hadi Shagerdi Esmaeeli, 2015): $E^{fa}$ = 31.07 ± 3.87 MPa, $\upsilon^{fa}$ = 0.15, $T_{max}$ = 3.8 ± 0.748 MPa, and $G_{Ic}^{fa}$ = 43.4 ± 16.9 (J/m$^2$).
- The shear components of cohesive law capture an accurate nonlinear pre-peak (dominated by crack initiation) and post-peak behavior (dominated by crack coalescence and corresponding shear failure development). To this end, the intrinsic mechanisms of opening and shear modes are assumed to yield to two relations of $G_{IIc} \approx 10.G_{Ic}$ (López et al., 2008a), and $\tau_{max} \approx 1.4.T_{max}$ (Eldin & Senouci, 1993).
- The development of $\delta_n$ and $\delta_t$ parameters for cement paste, ITZ$^m$ phases along with constant $\delta_n$ and $\delta_t$ parameters for the fine aggregate phase are determined using the cohesive bilinear law ($\delta_n = 2G_{Ic}/T_{max}$ and $\delta_t = 2G_{IIc}/\tau_{max}$).

It is necessary to mention that these two phases are considered to exhibit a homogenous brittle behavior, as the size of heterogeneities is the order of magnitudes smaller than the size of cement paste and fine aggregate elements; thus the cement paste and fine aggregate phases are treated as homogeneous and brittle materials.

#### 4.3.1.1 **Effect of $T_{max}^{p}$ development at early ages**

For evaluation of the existence of a unique RVE for mortar (softening material) via continuous and discontinuous homogenization schemes, we study the mechanical response of five sizes of mortar RVEs to evaluate the resulting mechanical properties along with crack patterns under uniaxial tension at two ages: early age of $t$ = 16 $h$ and a later age of $t$ = 96 $h$. The RVEs has a 45% volume fraction of fine aggregates of a maximum size of 4.75 $mm$. Five RVEs of size $l_m$ = 6 $mm$, 8 $mm$, 10 $mm$, 12 $mm$, and 15$mm$ are investigated. The mortar RVEs are tested under static load, under a displacement control and a plane strain condition. The domain of mortar RVE is meshed with triangular continuum elements with quadrilateral interface elements, with element size as small as 0.01 $mm$ inserted between fine aggregates. The convergence of averaged $\sigma$–$\varepsilon$ response by increasing the size of the RVE verifies the existence of an RVE. Average strain ($\varepsilon$) is calculated through dividing the prescribed displacement by the size of RVE, while the average stress ($\sigma$) is similarly obtained through dividing the total reaction force (at the bottom edge of RVE) by the size of RVE.

Figure 4-6 plots the $\sigma$-$\varepsilon$ curves and corresponding homogenized $T_n$-$u_n$ curves, as well as localized strain patterns (crack pattern) at the final stages of loading obtained for five sizes at an early age. Using the continuous homogenization, the homogenized response becomes more brittle for larger specimens, as the averaged stresses and strains are calculated over the entire domain of the RVE, shown in Figure 4-6(a). As a result, the RVE size is scaled with the region outside the localization band. However, the slope of the linear region of pre-peak response ($E^m$), and the peak response itself ($T_{max}^{m}$) make convergence as the RVE size increases. In order to evaluate the effect of $v^p$ development on homogenized $E^m$ and $v^m$ at $t$ = 16 $h$, two values of $v^p$ = 0.15 (based on experimental measurement at very early ages (Byfors, 1980)) and an assumed constant value of $v^p$ = 0.2 are used. The results indicate that the differences remain less than 3 %, implying that a constant value of $v^p$ = 0.2 can be considered at a very early age. It is necessary to note that the solution of $l_m$ = 6 $mm$ specimen diverges considerably from the solutions of the larger specimens, and thus we conclude that this specimen is too small to represent the RVE statistically. Using a discontinuous homogenization scheme, Figure 4-6(b) shows that the obtained homogenized cohesive laws are independent of the size of the RVE. The averaging is performed only over the localization band ($L_b$), which essentially takes a constant width. Figure 4-6(c) depicts the crack pattern in the five RVEs. We observe that the cracks have more tendency to propagate around fine

aggregates and across the cement paste and ITZ$^m$ leading to complex crack patterns with more crack zig-zag mechanism. This is due to the fact of $T_{max}^{p} < T_{max}^{fa}$ at $t$ = 16 $h$ which corresponds to an age of cement paste before the knee point.

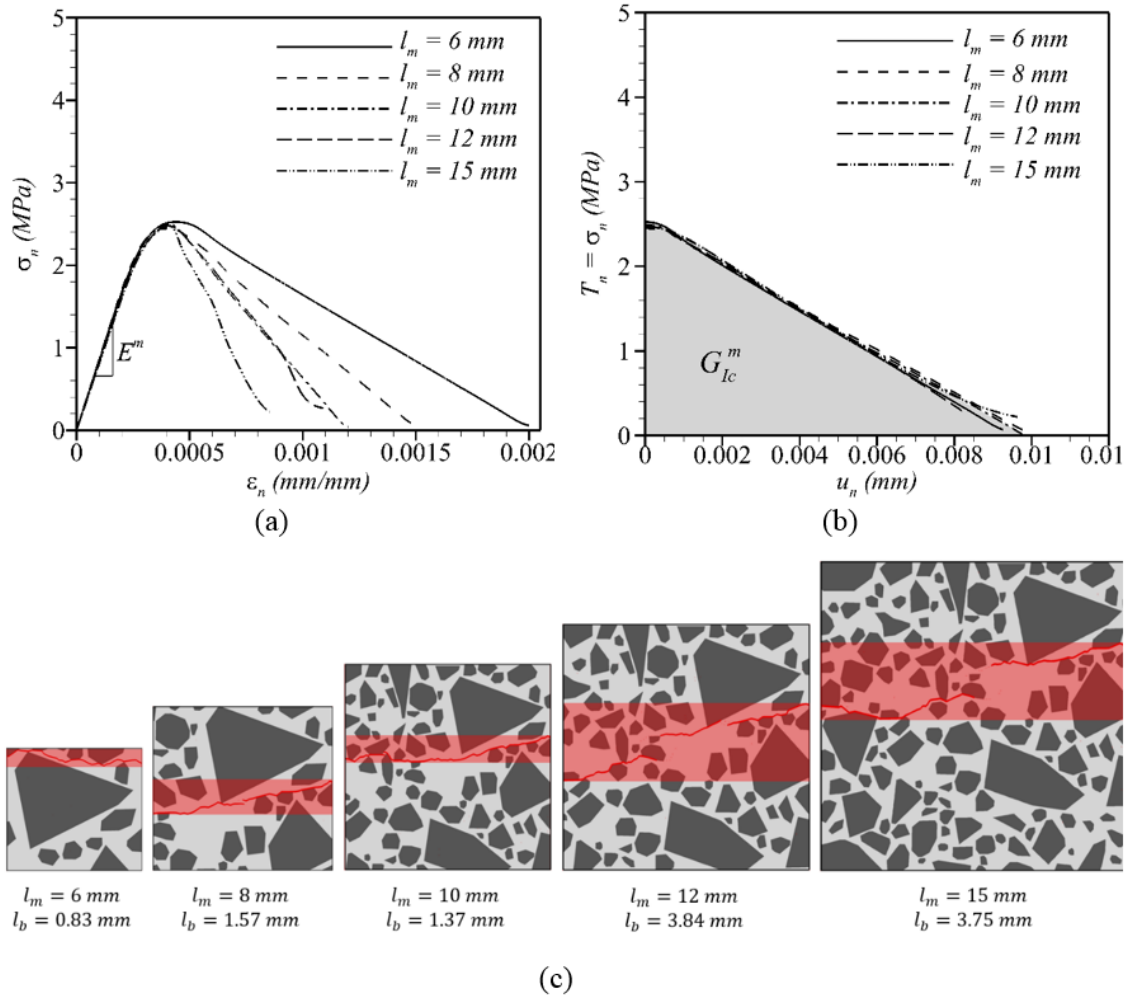


Figure 4-6. Existence of a unique RVE for heterogeneous mortar RVEs at an early age of $t$ = 16 $h$: (a) altering homogenized $\sigma$-$\varepsilon$ relations obtained with continuous homogenization scheme versus (b) homogenized $T_n$-$u_n$ relations obtained with discontinuous homogenization scheme, and (c) localized strain patterns.

To investigate the effect of mesh size on the mechanical response of mortar at t = 16 h, the range of mesh size studied goes from 0.1 mm to 0.3 mm. In the analyzed range, it is observed that the error in $E^m$ is less than 5%, in $T_{max}^{m}$ is less than 6%, and in $G_{Ic}^{m}$ is less than 5%. For this range of mesh sizes, we observe no changes in the crack pattern and number of fractured aggregates. Finally, we adopted an optimum mesh size of 0.15 mm that enables the best compromise between

the mechanical properties and the computational time. The current model has 10707 nodes with two degrees of freedom per node. For an explicit scheme, the time step is chosen to be $10^{-6}$ *secs* to satisfy the stability criterion. The computations are carried out to a total of 0.316 *mm* in displacement (until loads drop due to failure) with a total number of time steps of 326,000.

Figure 4-7 analyzes the mechanical response of mortar RVEs at a later age of 96 h, including the homogenized $\sigma$–$\varepsilon$ and $T_n$-$u_n$ responses as well as the crack pattern at the final stages of loading. The averaged $\sigma$-$\varepsilon$ curves for five RVE sizes are given in Figure 4-7(a), while the homogenized $T_n$-$u_n$ curves are shown in Figure 4-7(b). Similar to the analysis of mortar at an early age, the result depicts that the linear elastic responses are independent of the RVE size using continuous homogenization scheme (since the elastic slope and maximum tensile stress in the $\sigma$-$\varepsilon$ curves is $E^m$ and $T_{max}^m$ in one dimension, respectively). The comparison of difference of results between the experimental measurement of $\nu^p = 0.25$ (Byfors, 1980) and an assumed constant value of $\nu^p = 0.2$ indicates that the differences in terms of $E^m$ and $\nu^m$ remain less than 5 %, implying that a constant value of $\nu^p = 0.2$ can be considered at later age of $t = 96\ h$. However, the softening responses are not objective w.r.t the RVE size. Deriving $T_n$-$u_n$ curves independent of the RVE size consecutively implies that a unique RVE exists for mortar using the discontinuous homogenization scheme, shown in Figure 4-7(b). Upon the convergence of $T_n$-$u_n$ curves, we quantify a unique value for $G_{Ic}^m$ (i.e., the area under this curve) that leads to characterization of a homogenized cohesive law for mortar. Figure 4-7(c) depicts the crack pattern in the RVEs of five sizes. We observe that the cracking pattern takes straighter paths through aggregate particles with the less zig-zag mechanism as $T_{max}^p > T_{max}^{fa}$ at $t = 96\ h$ which corresponds to an age of cement paste before the knee point.

The change in cracking patterns in early-age mortar highlights the competition between two mechanisms, which is an important finding in this study. Comparing the values of $T_{max}^p$, $T_{max}^{ITZ^m}$ (=$T_{max}^p$), and $T_{max}^{fa}$, the results indicated that the increase of $T_{max}^p$ and $T_{max}^{ITZ^m}$ leads to a significant increase in load capacity of mortar as the hydration of cement paste progresses; however, the ratio of two tensile strengths ($T_{max}^p/T_{max}^{fa}$) primarily governs the crack propagation. Knowing the fact that the $ITZ^m$ phase is weak relative to aggregates and cement paste, this phase becomes preferred crack paths. At very early age $t = 16\ h$, the crack impinging on the $ITZ^m$ is likely to be deflected into the cement paste matrix as the condition for crack propagation in the cement

paste will be met at a lower load than for penetration across the fine aggregates (i.e., $T_{max}^{p}/T_{max}^{fa} < 1$). Conversely, at a later age $t$ = 96, the crack will tend to penetrate through fine aggregates when the inequality is reversed. In this study, we assess the role of $T_{max}$ considering constant values of $G_{Ic}^{p} = G_{Ic}^{ITZ^m} = 410\ (J/m^2)$ and $G_{Ic}^{fa} = 43.4\ (J/m^2)$.

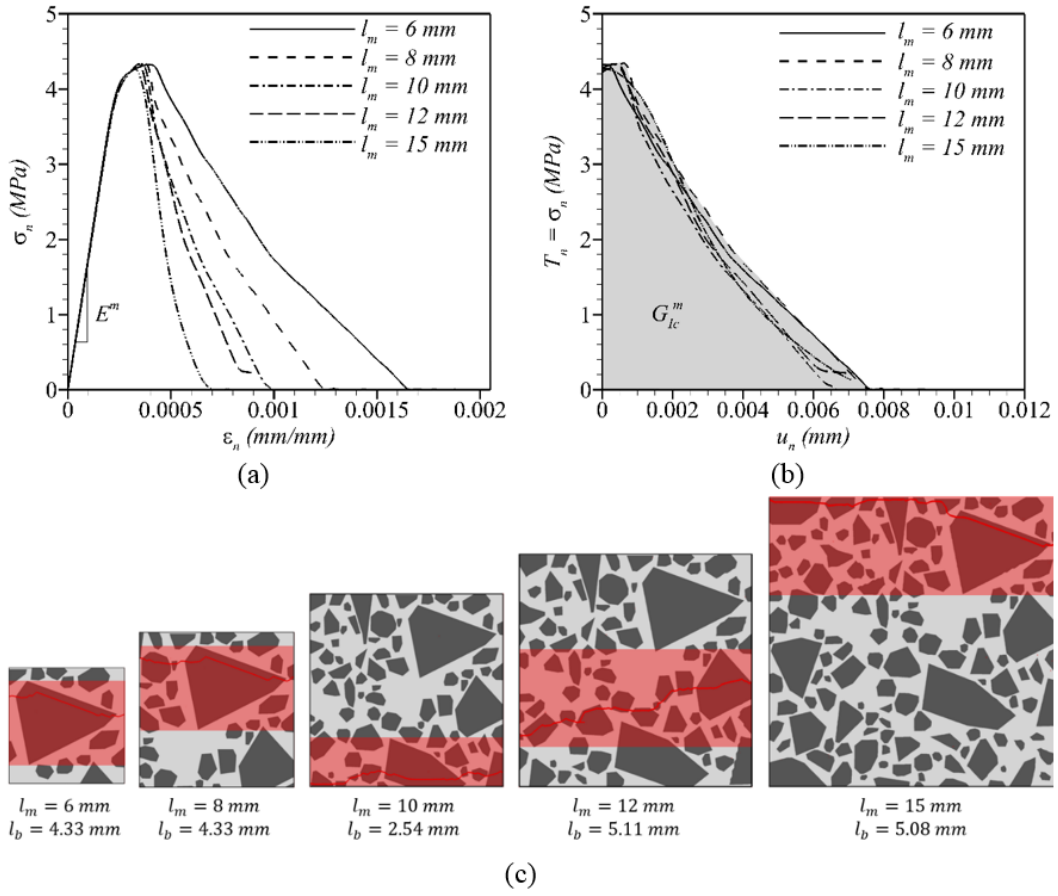


Figure 4-7. Existence of a unique RVE for heterogeneous mortar RVEs at an early age of $t$ = 96 $h$: (a) altering homogenized $\sigma$-$\varepsilon$ relations obtained with continuous homogenization scheme versus (b) homogenized $T_n$-$u_n$ relations obtained with discontinuous homogenization scheme, and (c) localized strain patterns.

#### 4.3.1.2 **Determination of $\mathbf{E^m(t)}$, $\mathbf{T_{max}^m(t)}$, and $\mathbf{G_{Ic}^m}$**

While experiments are useful to quantify the tensile stiffness ($E$) and strength ($T_{max}$), they provide no knowledge on the onset of failure. To this end, we employ our developed numerical

methodology considering the mortar as a heterogeneous composite with interfaces to interpret the experimental results. This model allows us to look at how the knee point in the bilinear mortar curves (point of change in slope) is related to variable $T_{max}^{p}/T_{max}^{fa}$ and the distribution of stress respect to the degree of hydration of cement paste, which cannot be explicitly quantified from experiments. Therefore, we use the experimental $E^p$ and $T_{max}^{p}$ values for early-age cement paste by Zhao et al. (Zhao et al., 2014) and Barde et al. (Barde et al., 2005), respectively, along with $E^{fa}$ and $T_{max}^{fa}$ values for aggregate (Indiana limestone used in this study) by Esmaeeli (Hadi Shagerdi Esmaeeli, 2015), as shown in Figure 4-8, to evaluate the role of $E$ and $T_{max}$ of mortar constituents on the early-age mechanical response of mortar. These results obtained numerically for mortar are compared to experimental observations of the flexural behavior of cement paste and mortar beams (performed by Barde et al. (Barde et al., 2005)). As previously mentioned, we consider that the tensile strength development of $ITZ^m$ used in this study is identical to that of the paste due to a lack of experimental data on the early-age tensile strength development of $ITZ^m$. However, to assess any effect of the strength of $ITZ^m$ on the overall properties of the material we carried out a conservative analysis considering that the tensile strength development of $ITZ^m$ is reduced to 50% of the paste (as experimentally determined by Hsu et al. [67] for later ages). The numerical results indicate that the tensile strength of mortar is reduced by 12.5% and 7% at $t$ = 16 $h$ and $t$ = 96 $h$, respectively. However, we found that the number of fracture aggregates and the general crack pattern did not change significantly. While this model can easily incorporate more experimental data as it becomes available, it does not change the main observations discussed in this paper.

Figure 4-8(a) illustrates the variation in $E^p$ and $E^m$ as a function of cement paste age (i.e., proportional to the degree of hydration). The slopes between $E^p$ as well as $E^m$ and $t$ resemble each other where the curve representing the variation of $E^m$ is shifted to higher value respect to $E^p$ curve, due to the presence of fine aggregates in the mortar. Note that $E$ depends on the behavior of the specimen under very low levels of loading (i.e., the slope of σ-ε curve in the linear elastic region). At these low load levels, mortar does not develop significant damage, and therefore the aggregates have not fractured, and as such, it is assumed not to influence the $E^m$ development. Comparing the numerical results and experimental data, it is observed that the percentage difference becomes less than 10% calculated at 16 discrete ages, except at two very early ages of 10 $h$ (25%) and 13 $h$ (27%), which implies a good agreement.

The next step is to predict the development of $T_{max}^{m}$ as a function of cement paste age, and to contrast the numerical results with experimental observation performed by Barde et al. (Barde et al., 2005). Given $T_{max}^{p}$ and $T_{max}^{fa}$, a bilinear relationship is observed for development of $T_{max}^{m}$as a function of cement paste age while paste shows a linear response, shown in Figure 4-8(b). We observe that the general trend between the strength and age is similar at early ages (i.e., before 25 hours) for paste and mortar (i.e., $T_{max}^{p}/T_{max}^{fa} < 1$). However, this trend significantly deviates for mortar once $T_{max}^{p}$ (and $T_{max}^{ITZ^m}$ ) exceeds the $T_{max}^{fa}$ (i.e., $T_{max}^{p}/T_{max}^{fa} > 1$ ), highlighting the considerable role of aggregate on prediction of strength development of mortar under mode-I loading. Figure 4-8(b) shows that the comparison shows that the deviation between numerical and experimental results is less than 5%, except at two very early ages of 10 hours and 16 hours, where the deviation is 47% and 8.25%. With discontinuous homogenization scheme, the fracture energy associated with the amount of energy dissipation over the localized band has been estimated to be approximately $G_{Ic}^{m}$ =15.7 ± 3.4 ($J/m^2$). Comparing the elastic and cohesive properties quantified with the numerical model and experimental data, it is concluded that the employed continuous and discontinuous homogenization schemes can reasonably predict the mechanical properties of mesoscopic mortar.

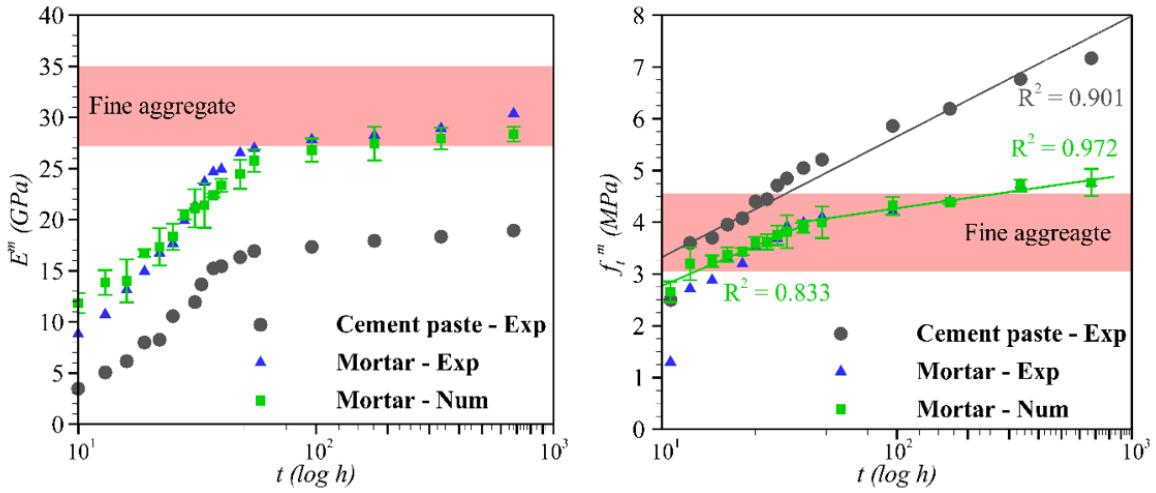


Figure 4-8. (a) Numerical and experimental results for early-age mechanical properties development of mortar in terms of (a) $E^m$, and (b) $f_t^m$.

### 4.3.2 Step 2: Toward concrete composite at Level III

This study considers the concrete material as a three-phase composite that contains coarse aggregate particles, surrounded by a transition zone ($ITZ^c$) phase, and embedded in the homogenized Level II mortar. Similar to mortar, we consider a zero width for ITZ in concrete RVE to avoid the expensive computational cost, as the average width of ITZ is $1/40^{th}$ of the average element size. Figure 4-8(a) indicates that the tensile stiffness of early-age mortar is most likely to approach the tensile stiffness of coarse aggregate as the hydration of cement paste progresses at an early age (i.e., $E^m \approx E^{ca}$). Constantinides et al. (Constantinides & Ulm, 2004) suggested that the key morphological parameters of inclusions including the size gradation, spatial distribution, and specific fraction, play important roles in the determination of local stress distribution, micro-crack initiation and coalescence resulting in the macroscopic failure of concrete (Wriggers & Moftah, 2006). Hence, the initial step to developing a suitable input for this mesomechanical model is to acquire appropriate parameters mentioned above for coarse aggregates within the concrete RVE. To this end, 3D mesostructures of concrete with randomly distributed coarse aggregates of spherical shape are generated, where the fraction and size distribution of aggregates is controlled.

Prior experimental (F. H. Wittmann et al., 1988) and numerical studies (López et al., 2008a) have shown that volume fraction has the most pronounced influence on the mode-I fracture behavior such as load capacity (i.e., tensile strength), cracking tendency, or fracture energy. Here, we develop an in-house composite material generator program composed of spherical aggregate generation and packing where the specific size distribution and the specific fraction of aggregates ($f_{ca}$ = 38%) are determined experimentally by Barde et al. (Barde et al., 2005) based on the mixture proportioning for concrete. To place a spherical aggregate at an arbitrary position within the mesostructure, three requirements should be met: (1) the whole sphere needs to be placed within the boundaries of the mesostructure with no intersection; (2) no overlap with previously placed spheres should occur; and (3) A limitation on two minimum distances between the edge of a sphere and the boundaries of the mesostructure, as well as the gap width between two adjacent spheres should be set. Figure 4-9 depicts the flowchart of processes of packing of aggregate, including "input," "taking," and "placing" (X. Wang et al., 2015). The "input" process examines the prominent parameters, including specimen size, aggregate size gradation, and aggregate volume fraction, for generating an RVE with randomly distributed aggregates. According to the random size description, the "taking" process produces a single aggregate particle. Next, the aggregate

placement into the predefined location in an arbitrary fashion is determined through the "placing" process, in which prescribed physical constraints (intersection and overlap checking) are implemented. Three following conditions need to be considered to check even if there is any intersect or overlap among randomly distributed aggregates: (1) the entire domain of aggregate particle must be fully embedded within the box, (2) no overlap should exist with previously embedded aggregate particles, and (3) the minimum gap width between the surface of an aggregate and the edge of the box as well as the minimum distance between two neighboring aggregate particles should be set.

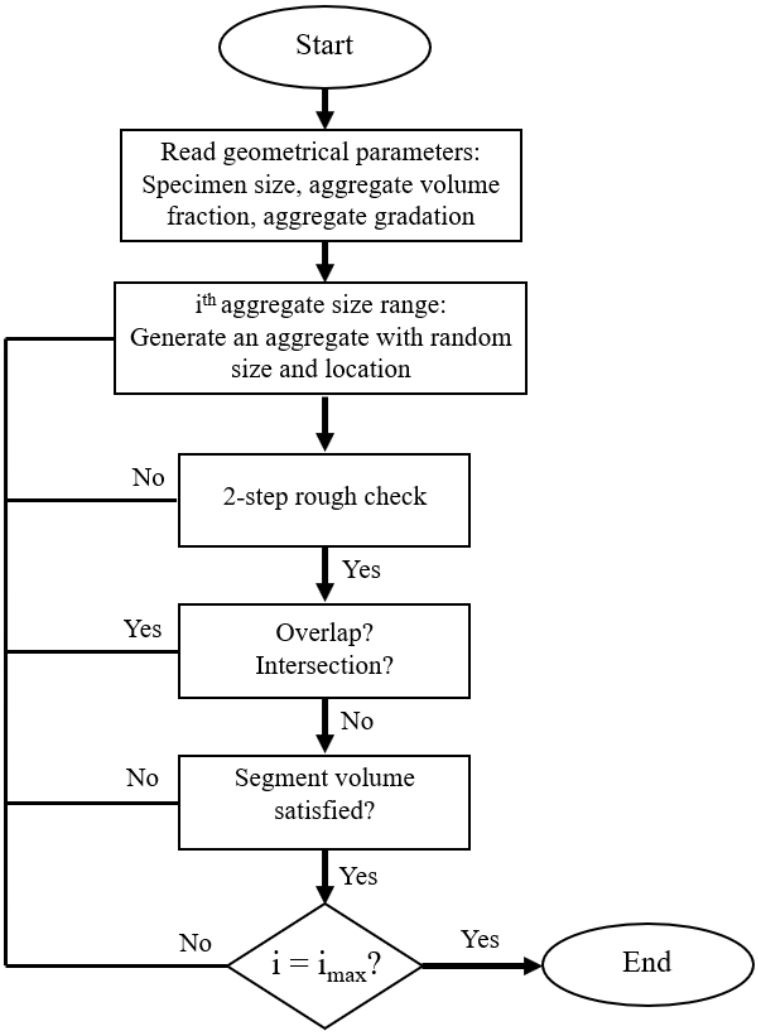


Figure 4-9. Flowchart of RVE generation with random aggregate distribution, adapted from (X. Wang et al., 2015).

#### 4.3.2.1 **The representative fraction of aggregates**

Afterward, 2D planar slices are extracted from 3D mesostructures to obtain a specific fraction of aggregates in 2D mesostructures statistically. The statistical analysis indicates that a skewed normal distribution can well describe the fraction distribution of aggregates with a mean value $f_{ca}$ = 45% and a standard deviation of 3% for a 2D mesostructure. Afterward, 2D mesostructures with the specific fraction of coarse aggregates acquired from statistical analysis are extracted from the 3D mesostructures of concrete with randomly distributed coarse aggregates of polyhedral (realistic) shape. The newly generated 2D and 3D mesostructures are tested under uniaxial tension to assess the validity of numerical results by contrasting the mechanical response of the 2D model with the 3D model, along with experimental and analytical results. The need for statistical analysis is since assumption of an identical fraction of coarse aggregates for 2D and 3D specimens is a crude approximation as the 2D model does not capture the constraint effect in the thickness direction that may bring significant underestimation of pre-peak and post-peak responses. We also assume that the failure of mortar and coarse aggregate phases obey Weibull statistics. It means that they contain uniformly distributed defects using Weibull distribution in which their strength is determined based on the number of defects subjected to tensile stresses with high values.

Prior experimental and numerical studies have shown that volume fraction has the most pronounced influence on the mode-I fracture behavior such as load capacity (i.e., tensile strength), cracking tendency, or fracture energy. Here, we develop an in-house composite material generator program composed of spherical aggregate generation and packing where the specific size distribution and the specific fraction of aggregates ($f_{ca}$ = 38%) are determined experimentally based on the mixture proportioning for concrete. To place a spherical aggregate at an arbitrary position within the mesostructure, three requirements should be met: (1) the whole sphere needs to be placed within the boundaries of the mesostructure with no intersection; (2) no overlap with previously placed spheres should occur; and (3) A limitation on two minimum distances between the edge of a sphere and the boundaries of the mesostructure, as well as the gap width between two adjacent spheres should be set. More information on a comprehensive procedure for the generation of 3D mesostructure of concrete with spatially distributed spherical aggregates. Based on the developed procedure, a series of 3D mesostructures ($50 \times 50 \times 50\ mm^3$) consisting of mortar and spherical aggregates are generated and shown in Figure 4-10(a). The inset in this figure displays a typical size distribution of coarse aggregates obtained from INDOT specification [67].

Afterward, 2D planar slices from each one of 100 constructed mesostructures are extracted every 1 *mm* along with x, y, and z axes. Note that the first slices extracted from each side of the 3D mesostructure are neglected in our analysis due to the limited space between the edge of the coarse aggregate and the boundary of the mesostructure (i.e., a total number of 14100 2D slices are extracted). The fraction distribution of aggregates can be well described by a skewed normal distribution with a mean value of 45% and a standard deviation of 3% for a 2D mesostructure), as shown in Figure 4-10(b).

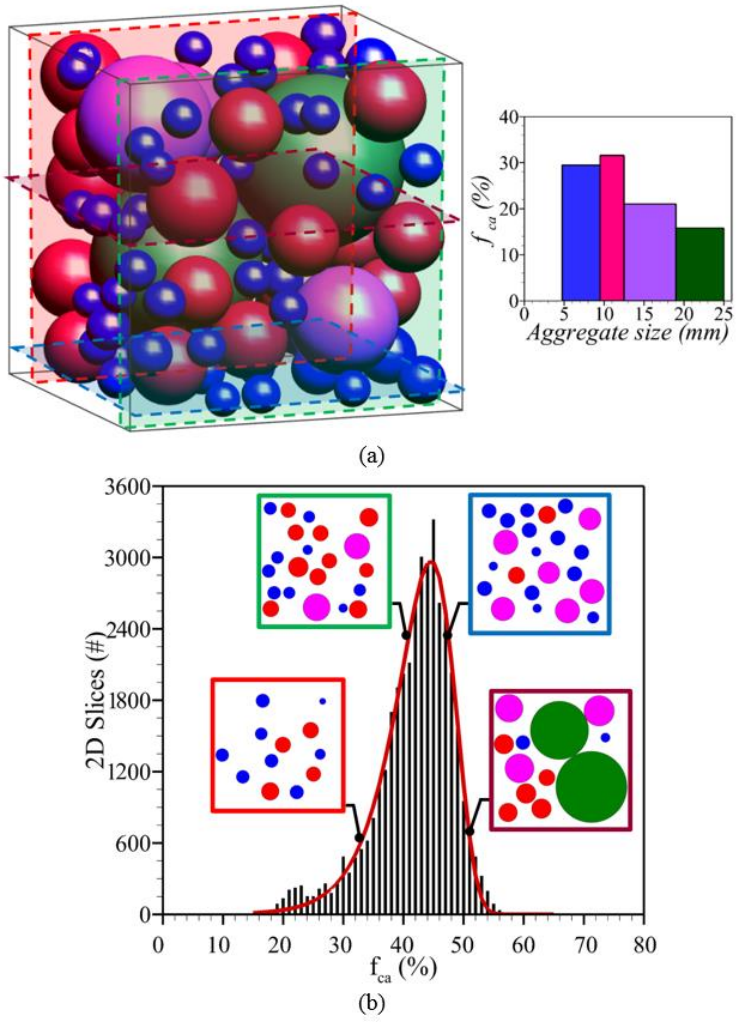


Figure 4-10. (a) 3D mesostructure of concrete consisting of mortar and spherical aggregates with a specific fraction $f_{ca}$ = 38% spatially distributed, (b) statistical analysis of the highest probability of occurrence of aggregate fraction in a 2D mesostructure extracted from 3D mesostructure of concrete. It is observed that a skewed normal distribution (fitted red curve) describes the distribution of aggregate fraction with a mean value $f_{ca}$ = 45% in 2D mesostructures extracted from 3D mesostructure.

#### 4.3.2.2 **Generation of 2D and 3D concrete mesostructures**

To investigate the validity of the proposed representative area fraction of aggregate, the mechanical response of 2D and 3D concrete RVEs under pure tension are assessed. To this end, a series of cubic 3D concrete RVEs ($50 \times 50 \times 50$ $mm^3$) containing arbitrarily distributed coarse aggregates of realistic (polyhedron) shape with a volume fraction of 38% and maximum aggregate size of 25 mm is generated, shown in Figure 4-11. The generated convex polyhedrons are made via the digitization of real crushed coarse aggregates with nominal sizes between 5 *mm* and 25 *mm* (in accordance with ASTM C-33 [68]). The main idea is to generate polyhedron aggregates with arbitrary orientations in a random arrangement until the target fraction of aggregates is reached. For this case, the geometrically arranged aggregates being placed within the concrete RVE need to satisfy two conditions: (1) despite the procedure of placement of spherical aggregates, there is no distance between the surface of a polyhedral aggregate and the edge of the concrete specimen to avoid the decrease of aggregate volume fraction on the boundaries; (2) if an aggregate crosses through the boundary of concrete RVE, the volume of the portion of aggregate being placed will be considered for calculation of aggregate fraction; (3) the minimum distance between any two aggregates are considered to be 0.2 *mm*. Figure 4-11(a) shows an example of 3D concrete RVE. Similar to the previous section, 2D planar slices with aggregate area fractions of 45%, shown in Figure 4-11(b) and (c), and 38%, as shown in Figure 4-11(d) and (e), are extracted from the 3D RVE to assess the validity of proposed representative aggregate area fraction.

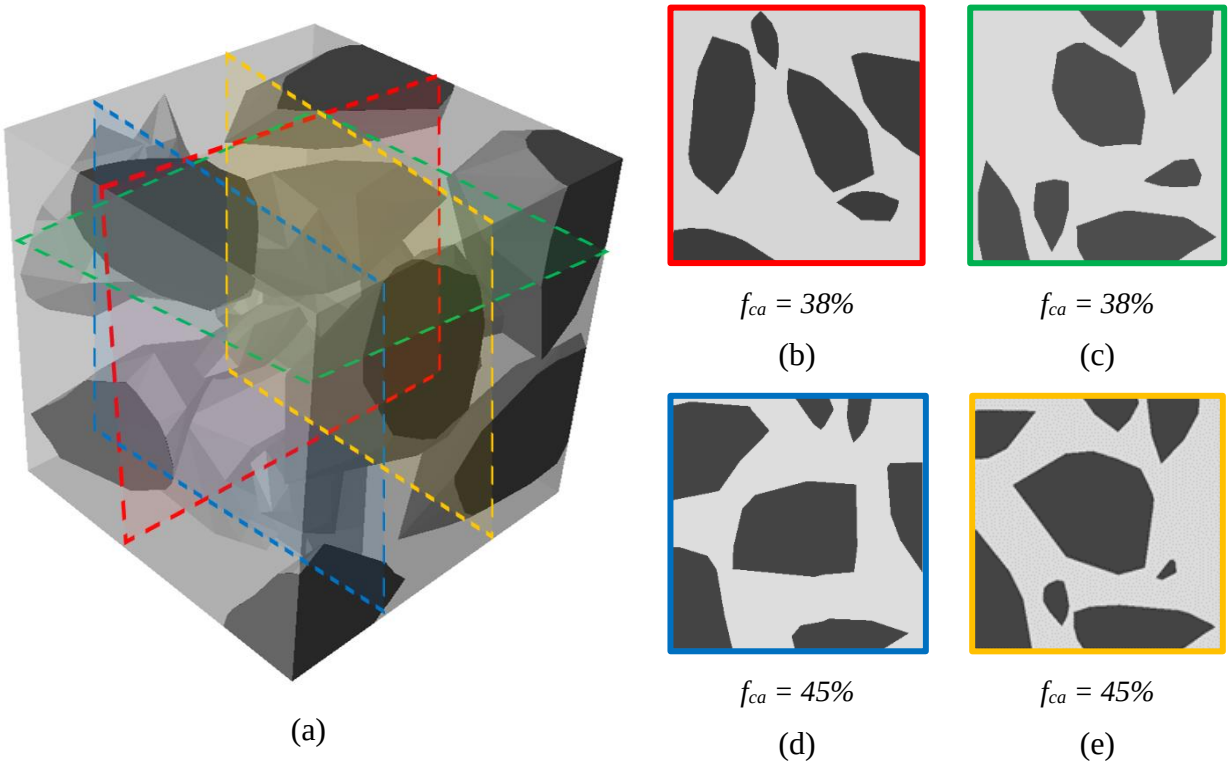


Figure 4-11. (a) A three-dimensional RVE of concrete containing irregular shape of coarse aggregates with $f_{ca}$ = 38%; two-dimensional slices extracted from three-dimensional concrete RVE containing aggregates with (b, c) $f_{ca}$ = 38%; (d, e) $f_{ca}$ = 45%.

To account for the effect of pre-existing cracks in the mortar, coarse aggregate, and ITZ[c] phases (these materials contain voids with dimensions up to a few millimeters) on the resulting peak stress, a Weibull distribution of strength for concrete constituents is employed [69-71]. Theoretically, this statistical approach enables the definition of strength distribution of concrete material considering a large variability in tensile strength of concrete constituents (mortar and aggregate) due to the variability in the distribution of crack size, shape, and orientation concerning the loading direction. It should be noted that ductile materials exhibit a very narrow strength distribution curve, which can be represented by *Gaussian* or *normal distribution*. In contrast, brittle and quasi-brittle materials exhibit a fairly broad strength distribution which can be described by Weibull distribution. This study considers a spatial distribution of strength, $T_{max}$ for interface elements as fracture energy per area, $G_{Ic}$ is assumed to remain unchanged. Zhou et al. (F. Zhou & Molinari, 2004) described that the strength of the interface element ($T_{max}$) strongly depends on the local length scale, namely an interface element volume ($V$). Therefore, Weibull distribution

enables the characterization of the strength of mortar and ITZ$^c$ from the numerical results, as well as the strength of coarse aggregate from the flexural experiment, and the use of this information to predict the peak stress and the onset of failure in the mesostructure of concrete. Considering a volume $V$ consisted of equivalent reference volume $V_0$ and a reference tensile strength $f_t$, the strength distribution for interface elements within concrete constituents is described by equation 4-6:

$$f(T_{max}) = \frac{m(\sigma)^{m-1}}{(T_{max})^m} exp\left(-\frac{V}{V_0}\left(\frac{\sigma}{T_{max}}\right)^m\right) \quad 4\text{-}6$$

where $m$ is the Weibull modulus that controls the shape of the distribution, the exponent $m$ specifies how the strength is distributed around the average strength $T_{max}$. The shape parameter generally takes on a value between 5 and 20 for the case of brittle materials, including mortar and aggregate materials. Within our model, $m$ = 20 describes a practical defect-free material, while $m$ = 5 determines a thoroughly heterogeneous material. We have two values of $m$ = 5 and $m$ = 7 for mortar (ITZ$^c$) and aggregate phases to capture the influence of two various defect distributions on the resulting strength and crack patterns.

Equation 4-6 indicates that an interface element with a smaller $V$ compared to $V_0$ exhibits a lower probability of failing subjected to given tensile stress as it is less probable to have defects (i.e., $T_{max} \propto f_t \cdot \left(\frac{V}{V_0}\right)^{1/m}$). In order to obtain the material parameters used in equation 4-6, we first assess the influence of length scale on $T_{max}$ of mortar, ITZ$^c$, and coarse aggregate in the concrete mesostructure. Because $T_{max}$ of mortar is acquired from numerical simulation of Level II mortar RVE with an average interface element size of 1.5 mm, then we adopt $V_0$ = 1.5 $mm^2$ (simulations are performed under plane strain condition). Considering an average finite element size in 2D mesostructure of concrete to be 5 $mm$ (i.e., $V$ = 5 $mm^3$) and $m$ = 5, $T_{max}^{m,ITZ^c}$ is set to be equal to $f_t^{m,ITZ^c}$ as $\left(\frac{V}{V_0}\right)^{1/m} \approx 1$. For coarse aggregate, the higher values of tensile stress occur over a region in which the typical size of material inhomogeneities, known as, fracture process zone (FPZ) is characterized. Bazant et al. (Z. P. Bazant & Planas, 1997) suggested that large specimens tend to fail in a brittle manner when FPZ size << specimen dimension. Therefore, we simply assume that the problem of size effect for coarse aggregate phase can be neglected (i.e., $\left(\frac{V}{V_0}\right)^{1/m} \approx 1$) as

the length of FPZ (= 38 *mm*) is significantly smaller than the specimen size tested in a four-point flexural experiment (152.4 × 152.4 × 457.2 $mm^3$).

The effect of *m* parameter, for instance, on the spatial distribution of strength within concrete mesostructure, is shown in Figure 4-12. The left and right insets show the strength variation and spatial distribution within a random region of concrete RVE for selected shape parameters *m* = 5 and *m* = 7 for mortar and aggregate phases, respectively (blue color associates with lower strength values, and red color associates with higher strength values).

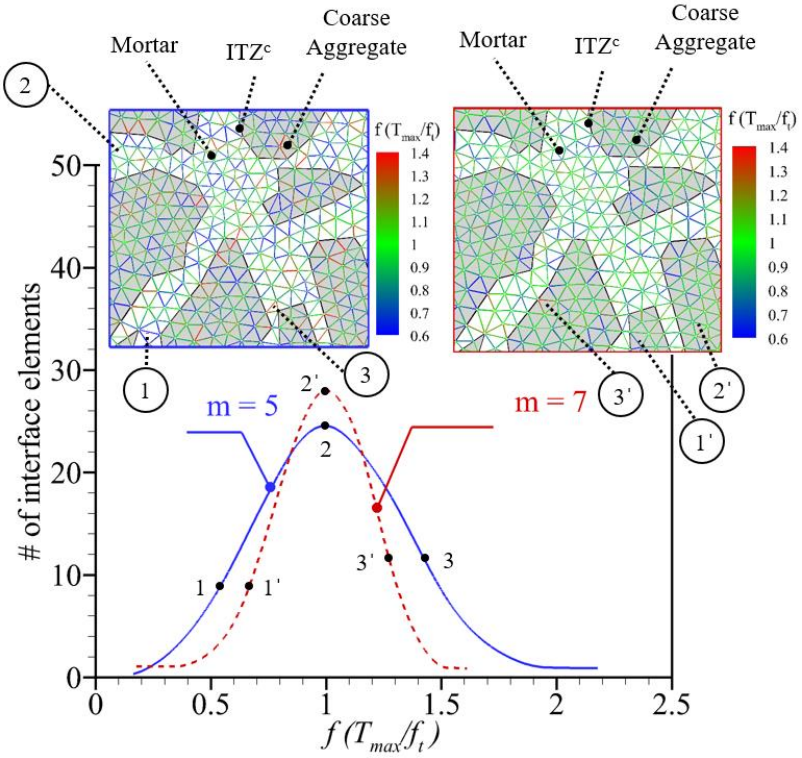


Figure 4-12. A plot of two Weibull distributions of tensile strength with shape parameters of m = 5 and m = 7 within concrete RVE. Histogram for $T_{max}$; the color map presents the ratio of the tensile strength of interface elements respect to constant tensile strength, $T_{max}$.

The early-age elastic properties of the three phases in concrete and the cohesive properties of the interface elements are defined as follows:

- Regarding the Level III concrete (and $ITZ^c$), the development of $E^m(t)$ and $T_{max}^m(t)$ as well as constant Poisson's ratio, $v^m$ and $G_{Ic}^m$ are obtained from the homogenization of the mechanical response of Level II mortar. The elastic and cohesive properties of coarse

aggregate are identical to the properties determined for fine aggregate, as shown in Table 1. Similarly, the relations for shear components of cohesive law for concrete constituents are identical to the relations defined for mortar constituents.

- The development of $\delta_n$ and $\delta_t$ parameters for mortar, ITZ$^c$ phases along with constant $\delta_n$ and $\delta_t$ parameters for the coarse aggregate phase are determined using the bilinear cohesive law ($\delta_n = 2G_{Ic}/T_{max}$ and $\delta_t = 2G_{IIc}/\tau_{max}$).

#### 4.3.2.3 Effect of the aggregate fraction on the mechanical response of concrete mesostructure

To evaluate the effect of $f_{ca}$ on the tensile mechanical response of concrete including $E^c$ and $T^c_{max}$ at a very early age, $t$ = 16 $h$, numerical results for 2D mesostructures with statistically representative $f_{ca}$ = 45%, and 2D/3D mesostructures with $f_{ca}$ = 38% are analyzed under uniaxial tension and contrasted with analytical and experimental solutions, shown in Figure 4-13. Three mesostructures of 2D concrete with $f_{ca}$ = 38%, 2D concrete with $f_{ca}$ = 45%, and 3D concrete with $f_{ca}$ = 38% are investigated. The material parameters of the mesostructural constituents can be found in Table 4-2.

Table 4-2. Material parameters of the continuum and interface elements within concrete RVE.

| Mechanical Property | Unit | $t$ = 16 $h$ | | $t$ = 96 $h$ | | ca |
|---|---|---|---|---|---|---|
| | | m | ITZ$^c$ | m | ITZ$^c$ | |
| $E$ | [$GPa$] | 14.02 | - | 36.81 | - | 31.074 |
| $\upsilon$ | [-] | 0.18 | - | 0.18 | - | 0.18 |
| $G_{Ic}$ | [$J/m^2$] | 15.7 | 15.7 | 15.7 | 15.7 | 43.4 |
| $G_{IIc}$ | [$J/m^2$] | 157.0 | 157.0 | 157.0 | 157.0 | 434 |
| $T_{max}$ | [$MPa$] | 3.24 | 3.24 | 5.862 | 5.862 | 3.8 |
| $\tau_{max}$ | [$MPa$] | 4.53 | 4.53 | 8.8 | 8.8 | 5.7 |
| $\delta_n$ | [$mm$] | 0.0096 | 0.0096 | 0.0053 | 0.0053 | 0.0013 |
| $\delta_t$ | [$mm$] | 0.069 | 0.069 | 0.035 | 0.035 | 0.015 |
| $l_{cz}$ | [$mm$] | 20.96 | 20.96 | 16.82 | 16.82 | 38.103 |

While numerical simulations widely quantify tensile stiffness of heterogeneous composites containing inclusions with complex geometries, two analytical solutions of Mori-Tanaka (MT) and self-consistent method (SCM) were proposed based on mean-field homogenization schemes (R. Christensen et al., 1992; Hori & Nemat-Nasser, 1994). These two analytical methods were established based on the linear elasticity theory that estimates the effective tensile stiffness of composite using elasticity solution of Eshelby's for inclusions placed in an infinite matrix. These two models are best suited for the given homogenization problem, as their predictive capabilities are effective when (1) the composite contains a high fraction of inclusions, and (2) the matrix has a relatively low stiffness compared to inclusions (R. M. Christensen, 1990). This allows us to compare $E^c$ of concrete mesostructures with that of idealized elastic two-phase solid, showing how the numerical model not only gives logical results but is also capable of fitting analytical solution and proper experimental data (Antico et al., 2015), as shown in Figure 4-13(a). It is observed that the mean value of $E^c$ predicted by 2D and 3D mesostructures with $f_{ca}$ = 38% are 16.2 and 19.1 *GPa*, respectively (i.e., the relatively more realistic 3D specimen predicts 15.1 % higher $E^c$ value). This significant difference can be alleviated to a relatively negligible difference of less than 5% by increasing $f_{ca}$ of 2D mesostructures to 45%. Also, the simulated $E^c$ of 2D mesostructures with $f_{ca}$ = 45% is following MT and SCM solutions for a heterogeneous composite with an inclusion volume fraction of 45%, as well as experimental measurements.

Next, we evaluate the capability of the 2D mesostructure with $f_{ca}$ = 45% on the prediction of $T^c_{max}$ as well as damage mechanisms. We then carried out numerical simulations with two values of *m* varied between 5 and 7. The mean peak stresses from 2D and 3D modeling against $f_{ca}$ are presented in Figure 4-13(b). The mean peak stresses obtained from the analysis of 2D and 3D mesostructures with $f_{ca}$ = 38% are 1.57 and 1.65 *MPa*, respectively, i.e., the relatively more realistic 3D mesostructure estimates 4.8 % higher peak stress. It is concluded that the rise in the peak stress in the 3D model compared to the 2D model with identical $f_{ca}$ is associated with the constraint effect through-thickness direction considered in 3D modeling, not accounted by the 2D model. Liu et al. (L. Liu et al., 2016) also confirmed that this effect yields a uniform distribution of pre-peak meso-cracks in 2D, as the spatial distribution of aggregates may have a lesser influence on the pre-peak response in the 3D model. To alleviate the 2D effect, we analyze the peak response of 2D mesostructures with $f_{ca}$ = 45% (rather than $f_{ca}$ = 38%), where the difference between the mean peak stresses of 2D and 3D models reduces to less than 4 %. One typical macro-crack pattern

with only one dominant crack propagated across ITZ[c] and mortar phases is observed from 2D and 3D simulations and illustrated in the inset of Figure 4-13(b). Afterward, the peak stresses obtained from 2D mesostructure with $f_{ca}$ = 45% and 3D mesostructure with $f_{ca}$ = 38% are contrasted with experimental observation (Barde et al., 2005). The experimental work investigated the mechanical response of concrete beams subjected to a four-point flexural loading, where a constant bending moment is induced between the inner two loadings with no effect of shear stress. As a result, the local stress and strain fields on the bottom surface between two loadings are subjected to equivalent tensile stress which implies that failure mechanism is dominated by mode-I once maximum principal stress exceeds $T^c_{max}$. Compared to experimental observations, the 2D and 3D modellings demonstrate a prediction of mean peak stress with a difference of 2% and 6%, respectively, i.e. a better agreement is suggested between 2D model with $f_{ca}$ = 45% and experiment.

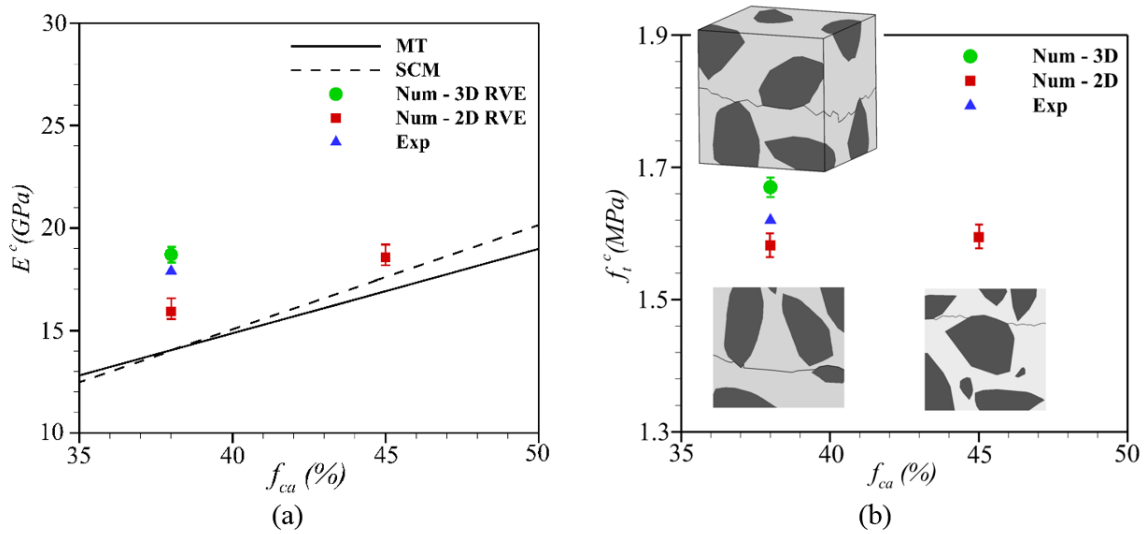


Figure 4-13. (a) Analytical, numerical and experimental results for homogenized $E^c$ parameter of concrete at $t$ = 16 $h$. A 2D model with $f_{ca}$ = 45% produces a negligible uncertainty of 5% in prediction of $E^c$ parameter contrasted with the experimental measurement; (b) Comparison of numerical and experimental results for homogenized $f_t$ parameter of concrete at $t$ = 16 $h$. Similar to the prediction of the E parameter, the difference between the mean peak stress predicted by 2D with $f_{ca}$ = 45% (rather than 38%) becomes less than 4 %.

#### 4.3.2.4 **Development of mechanical properties of concrete**

In this section, the mechanical contribution of constituents on mechanical properties development of composite concrete is analyzed. To this end, we extend the numerical results, illustrated in Figure 4-13, to include the aging effect of mortar along with the mechanical contribution of coarse aggregate using the same continuous homogenization scheme. To verify the validity of the numerical model, the development of mechanical properties of concrete including $E^c$ and $f_t^c$ are quantified at early ages (16 discrete ages), and then contrasted with proper experimental observations (Antico et al., 2015) and (Barde et al., 2005), respectively. Following the experimental protocol (Barde et al., 2005), the four-point flexural loading is simulated using 4 rigid rollers having frictionless contact between the rollers and the concrete beam (508 × 152.4 $mm^2$), displayed in Figure 4-14(a). The images from the cross-section of the concrete beam tested in the experiment are used to obtain the real 2D RVEs of concrete using a computed tomography approach (Hadi Shagerdi Esmaeeli, 2015). To reduce the computational expense, only one RVE is embedded on the midspan of the beam, which consists of continuum elements of different phases (e.g., mortar and aggregate) along with interfacial elements inserted between them. For the elements outside the RVE, continuum elements with homogenized elastic properties of $E$ and $\upsilon$ are obtained from the response of RVEs with no interface elements tested under uniaxial tension. The elastic properties of the continuum elements are obtained from performing separate simulations of concrete RVE, where the development of $E^c$ is illustrated in Figure 4-14(a) and the constant Poisson's ratio $v^c$ is determined to be equal to 0.17. It is also observed that the micro-crack coalescence begins from the bottom edge approaching to the top edge of RVE, while the resulting response is still in the pre-peak region. In order to avoid this boundary effect on the fracture process, RVEs of sizes $l_c$ = 60 *mm*, 80 *mm*, 100 *mm*, and 120 *mm* with $f_{ca}$ = 45% and maximum aggregate size of 25 mm are investigated. The elastic and cohesive properties of mortar (and $ITZ^c$) phases are acquired from homogenization of Level II mortar as well as the coarse aggregate properties are obtained from our previous experimental investigation (Hadi Shagerdi Esmaeeli, 2015). The concrete beam is loaded under displacement-controlled plane strain condition.

To verify the existence of an RVE, the mechanical response of concrete beams in terms of load-midspan displacement (P-δ) relations (measured through the contact between rollers and beam located at the top edge) with increasing the size of the RVEs are investigated at an early age

of $t$ = 16 $h$ and a later age of $t$ = 96 $h$. Figure 4-14(b) and Figure 4-14(c) show that macroscopic load-displacement curves converge as the size of the RVE increases. It should be considered that the 60 × 60 $mm^2$ specimen is too small to statistically represent the mesostructure as its solution diverges considerably from the solutions of the larger specimens. The comparison of results shows that the pre-peak response of the 80 × 80 $mm^2$, 100 × 100 $mm^2$, and 120 × 120 $mm^2$ specimens are not on top of each other or very closed to each other due to considering only one realization for a certain size. Therefore, the macroscopic pre-peak responses for these three specimens begin to converge upon increasing the mesostructure size. Thus the 80 × 80 $mm^2$ specimens will be considered as the representative 2D RVE for concrete in the following simulations.

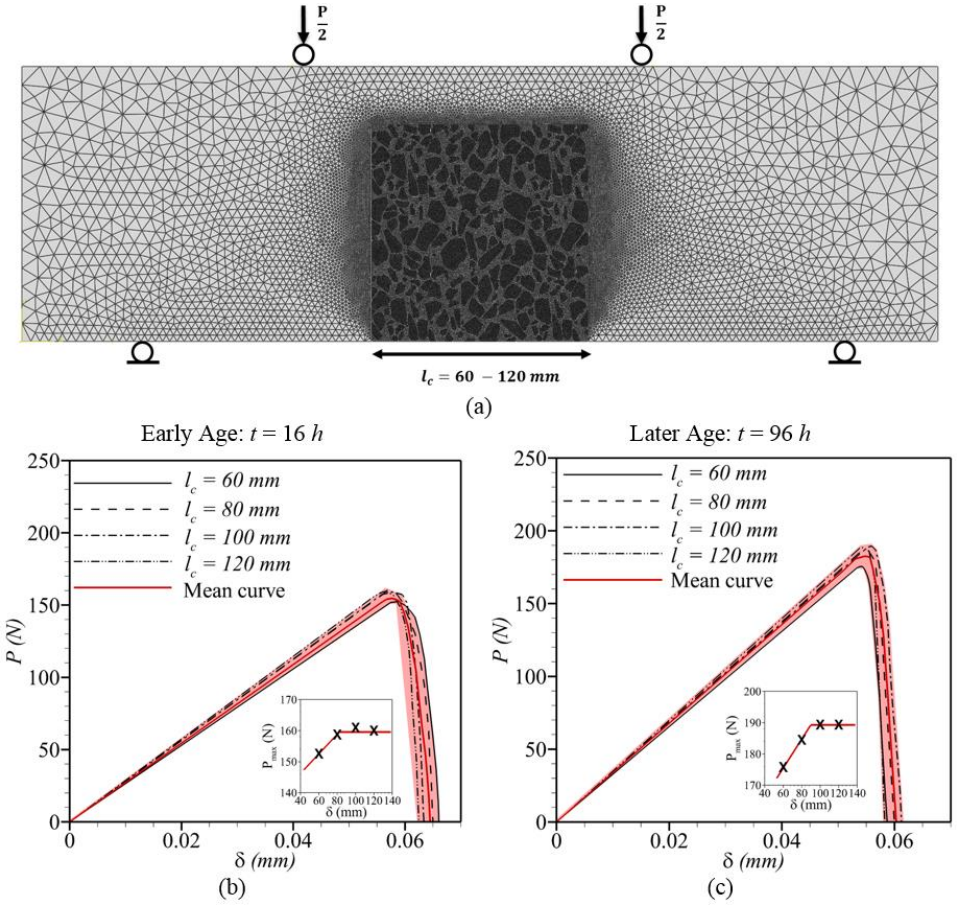


Figure 4-14. Force-displacement curves of (a) concrete beams containing four sizes of RVE under four-point flexural loading (b) at an early age of $t$ = 16 $h$, and (c) at a later age of $t$ = 96 $h$. Sequential macro-crack pattern evolution of concrete RVE at (d, e, f) $t$ = 16 $h$; and (g, h, i) $t$ = 96 $h$.

Figure 4-14 continued

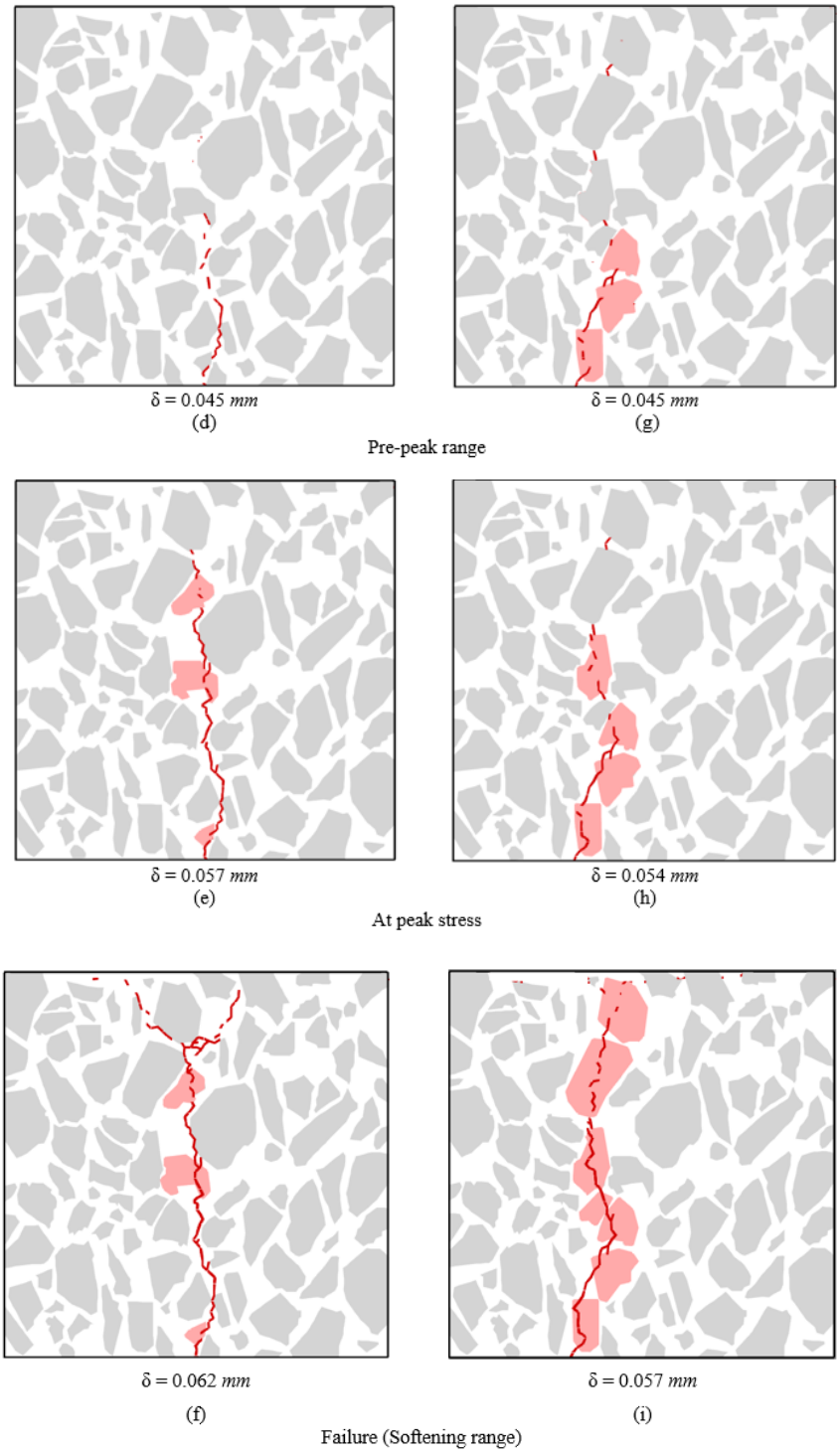


A mesh size range from 0.5 *mm* to 2 *mm* is analyzed to investigate the effect of mesh size on the mechanical response of concrete at $t$ = 16 *h*. The analyzed range indicates that the error in

$E^c$ is less than 7% and in $T^c_{max}$ is less than 4%. For this range of mesh sizes, we observe no changes in the crack pattern and number of fractured aggregates. To achieve a balance between the accuracy of results and computational cost, we selected a mesh size of 1 *mm* for all the simulations of Level III concrete. The current model has 36427 nodes with two degrees of freedom per node. For an explicit scheme, the time step is chosen to be $10^{-6}$ *secs*. The computations are carried out to a total of 0.0629 *mm* in displacement (until loads drop due to failure) with a total number of time steps of 656,000.

The detailed pictures of two typical macro-crack patterns with only one dominant crack are illustrated at various loading stages in Figure 4-14: (1) At early ages (i.e., before 25 *h*), the numerical modeling suggests that the damage mechanism is dominated by mortar fracture, where the number of damaged aggregate particles is three highlighted in pink color, as sketched in Figure 4-14(d-f). In the initial loading stages, a significant number of micro-cracks are observed to form at $ITZ^c$ (Figure 4-14(d)). As loading progresses, several micro-cracks coalescence into one predominant macro-crack, whereas redistribution causes the other micro-cracks to arrest (Figure 4-14(e)). The single dominant crack progressively propagates through $ITZ^c$ and mortar elements indicating a rapid softening behavior (Figure 4-14(f)); (2) At later ages (i.e., after 25 *h*), the numerical modeling illustrates an alteration in fracture behavior of concrete as the damage mechanism is dominated by aggregate fracture, where a single dominant crack propagates across seven aggregate particles, as sketched in Figure 4-14(g-i). Looking at the details of mesostructural cracking, one can see how micro-cracks start developing in a distributed manner all over the specimen, especially at the aggregate interfaces. At a certain stage of the loading, some micro-cracks initiate at $ITZ^c$ and aggregate phases which continue opening and getting interconnected as the loading increases, as sketched in Figure 4-14(g) and (h). At the softening region, the localization process is spontaneously triggered, and the process leads finally to only one dominant crack cutting through the RVE into two big pieces. The results also exhibit other realistic features such as crack branching at an early age. It clearly shows that as $T^{ca}_{max} > T^m_{max}(t)$ at early ages, cracks have more tendency to propagate across the mortar phase and do not deflect through aggregates that leads to a branching mechanism. This mechanism occurs even within small mortar regions between adjacent aggregate particles or corners.

Here, we quantify the early-age tensile stiffness and strength at discrete ages using continuous homogenization scheme, and compare them with experimental observations, shown in

Figure 4-15(a), and Figure 4-15(b), respectively. The comparisons presented in Figure 4-15 also include the range of experimental values of $E^{ca}$ and $T^{ca}_{max}$ (highlighted in pink) obtained from (Hadi Shagerdi Esmaeeli, 2015). Figure 4-15(a) shows the relationship between $E^c$ and the age of concrete. The numerical results show that the development of $E^c$ is similar to the development of $E^m$. This similar trend of tensile stiffness development for early-age mortar and concrete specimens as the concrete has not developed significant damage. Therefore, the aggregates have not fractured, and as such, do not influence the tensile stiffness development. Comparing the numerical solution and experimental observation, it is seen that the percentage difference becomes less than 10% calculated at discrete ages, except at two ages of 19 *h* (32%) and 37 *h* (26%), which implies a promising agreement. Next, given the tensile strength of concrete constituents, the development of strength in mode-I as a function of age for concrete material obtained from numerical solution and experimental observations is shown in Figure 4-15(b). It can be observed that the slope between the strength and age significantly alters once the strength of the mortar (ITZ) phase exceeds the strength of the aggregate phase. The comparison between numerical and experimental results shows that the variation is less than 6%, which indicates an excellent agreement.

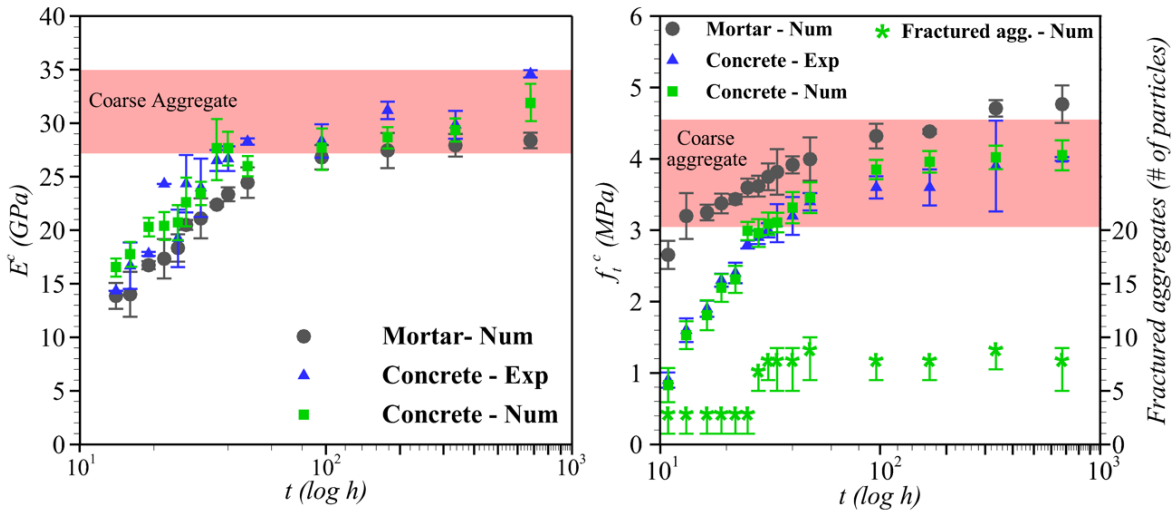


Figure 4-15. (a) Numerical and experimental results for mechanical properties development of early age concrete in terms of (a) tensile stiffness $E^c$, and (b) tensile strength $f_t^c$ and number of fractured aggregate particles in concrete RVE.

It is crucial to understand the competing mechanisms associated with the energy dissipation in heterogeneous mesostructure of cementitious composites to address their remarkable early-age

mechanical properties development. Our study indicates that two competing mechanisms exist between energy dissipation through the failure of mortar and ITZ$^{c}$ phases at an early age, and the energy dissipated at the aggregate phase at later ages. To verify the hypothesis considered in the experiment, this behavior is currently considered to be attributed to (1) weak interfaces of mortar relative to coarse aggregate interfaces which become the preferred crack paths at early ages, when the development of tensile strength of mortar due to aging effect leads to a similar strength gain for concrete; and (2) weak interfaces for aggregate relative mortar interfaces leads to alteration in the preferred crack path which leads to a considerable increase of the number of fractured aggregates and therefore limiting the strength development governed by the aggregate strength. The numerical framework developed in this work could be used to predict the correct tensile (or flexural) strength development for cementitious composites at an early age, where the presence of aggregates is considered to modify the maturity-strength gain relationship.

## 4.4 Conclusion

This paper investigated the early-age tensile stiffness and strength development of cementitious composites such as mortar and concrete through the finite element model, which were compared with experimental measurements. Following the work performed by Barde (Barde et al., 2005), the flexural results indicated that a linear relationship existed between the strength and degree of hydration for paste specimens. However, a bilinear relationship is observed as the aggregate was added to the paste (i.e., mortar and concrete). The rate of development of tensile stiffness contrasts with that of strength, as the fracture of aggregates does not affect the stiffness as a function of the degree of hydration. A two-step homogenization model multiscale method consisted of continuous and discontinuous homogenization schemes for multiscale modeling of failure of quasi-brittle mortar (Level II) and concrete (Level III) having heterogeneous mesostructures were used.

- Level II mortar: Mesostructure of mortar contains fine aggregates dispersed in cement paste, equipped with intra-phase (fine aggregate/fine aggregate and cement paste/cement paste) and inter-phase (fine aggregate/cement paste) cohesive elements. While the geometry for mortar is not explicitly considered, the mechanical properties of mortar constituents strongly affect the mechanical response and crack propagation in mortar. The continuous homogenization scheme has been used for quantification of pre-peak and peak

stress response of mortar. At the same time, the behavior of a macroscopic cohesive crack is defined upon microscopic localization using the discontinuous homogenization scheme. The comparison between numerical solutions and experimental observations obtained for tensile stiffness and strength development at discrete early ages showed that the variations are less than 5%. With discontinuous homogenization scheme, the fracture energy associated with the amount of energy dissipation over the localized band has been estimated to be approximately $G_{IC}^{m}$ = 15.7 ± 3.4 (J/m$^2$). Comparing the elastic and cohesive properties quantified with the numerical model and experimental data, it is concluded that the employed continuous and discontinuous homogenization schemes can perfectly predict the mechanical properties of mesoscopic mortar. We also observed that the pre-peak response of mortar is strongly sensitive to the tensile stiffness of their constituents. In contrast, the differences between constituents' strengths lead to govern the micro-crack coalescence and macro-crack pattern. We validated the hypothesis of this work by showing the influence of aggregate fracture on the knee point is primarily controlled by the competition between the energy dissipation mechanism of the cement paste at very early ages and the energy dissipation mechanism of the aggregate phase at later ages.

- Level III concrete: Mesostructure of concrete contains coarse aggregates embedded in mortar, equipped with intra-phase cohesive elements (coarse aggregate/coarse aggregate and mortar/mortar), as well as and inter-phase cohesive element (coarse aggregate/mortar). An efficient algorithm for generating three-dimensional mesostructures with the known volume fraction of aggregate ($f_{ca}$ = 38% used in (Barde et al., 2005)) of spherical shapes were developed to perform a statistical analysis to determine a representative area fraction of aggregate ($f_{ca}$ = 45%) for two-dimensional mesostructures of concrete. Afterward, a three-dimensional mesostructure of concrete containing realistic polyhedral aggregates with $f_{ca}$ = 38% is generated, where four two-dimensional mesostructures with $f_{ca}$ = 38% and 45% are extracted to compare their pre-peak response and peak stress with analytical and experimental observations at an early age of t = 16 h. We observed that an increase in area fraction of aggregate in two-dimensional specimen alleviates the 2D effect, as the variation between predicted numerical results and experimental data decreased to less than 5%. Hence, the images from the cross-section of the concrete beam tested in the experiment are used to obtain the real 2D RVE of concrete using a computed tomography approach.

With a continuous homogenization scheme, the uncertainty of results obtained from the predictive model for early-age tensile stiffness and tensile strength development was less than 10% and 6%, respectively, that indicates an outstanding agreement. Similar to mortar, we observed that by understanding the composite nature of early age concrete, tensile stiffness and strength development were captured. It was observed that the tensile stiffness of mortar and concrete increases at a very similar rate, while the presence of coarse aggregates influences the rate of strength development. It was shown that the hydration of the paste phase describes the strength gain at an early age; however, it is primarily governed by aggregates after a certain degree of hydration is reached. Aggregates do not influence the tensile stiffness development similar to how they influence the flexural strength development.

# 5. TOWARDS FABRICATION OF ENHANCED DAMAGE TOLERANT ARCHITECTURED CEMENT-BASED MATERIAL

This chapter contains experimental data and numerical simulations collected by Hadi S. Esmaeeli. Data conceptualization was a collaborative effort with Pablo D. Zavattieri. The manuscript was written by Hadi S. Esmaeeli and edited by Pablo D. Zavattieri.

## 5.1 Problem definition

A recent development in additive manufacturing (AM) of cementitious composites have demonstrated that this technology has the potential to address some key challenges such as fabrication of multifunctional structures with enhanced controllability over architecture, composition, and incorporation of components (e.g., reinforcement, sensors, and nanomaterials) in the construction industry compared with those resulting from conventional casting techniques. This technology also opens new avenues for overcoming durability issues by fabricating a carefully tailored heterogeneous structure at an architectural scale. A primary source of premature cracking of cementitious composites is restrained shrinkage with early-onset, due to temperature variation, self-desiccation, and non-uniform drying. In this chapter, we assess the mechanical performance of 3D-printed cementitious composites along with the role and characteristics of processing-induced heterogeneous interfaces in controlling and mitigating shrinkage cracking. Particularly, this work focuses on utilizing weak interfaces between filaments to promote a unique *damage localization mechanism*, where the damage propagation to neighboring layers is inhibited. For further performance improvement, we employ a novel architecture inspired by Bouligand design to promote a *damage delocalization mechanism* at unrestrained layers. This novel integration of two damage mechanisms leads to enhancing the damage tolerant and fracture characteristics, which allows the cementitious composites with early-age autogenous and drying shrinkage behavior to accommodate the damage evolution, without sacrificing the inherent early-age strength development.

## 5.2 Literature review

Ceramic-based materials, such as traditionally cast cementitious materials, fall into the category of material classes with the highest strength and stiffness (Ashby & Cebon, 1993). A

desirable requirement for the majority of structural materials is that they exhibit attainment of high strength and toughness properties simultaneously (generally, these two specific material properties are mutually exclusive (Robert O Ritchie, 2011)). The strength of material represents its invariable resistance characteristic when a material undergoes non-recoverable (inelastic or plastic) deformation, and toughness represents the invariable energy required to cause fracture the material. Owing to strong and directional bonding between constitutive phases at atom-level in ceramics, these materials are unable to locally dissipate high stresses developed when they undergo limited unrecoverable deformation. Conversely, materials with lower strength exhibit higher deformation and tend to be tougher (shown in Figure 5-1).

While it has been generally thought that ceramics with iono-covalent atomic bonding is unlikely to undergo plasticity corresponding to the dislocation movements in crystalline materials, prior research has discovered numerous types of damage-tolerant biological materials, such as glass sponges, tooth enamel, and nacreous part of seashells, which their primary constituents (hydroxyapatite, aragonite, silica glass) inherent brittle behavior surprisingly (Dunlop & Fratzl, 2010; Y. F. Gao & Bower, 2004; Ji & Gao, 2010; Launey et al., 2010). This counter-intuitive behavior has led to many investigations performed on biomaterials (Francois Barthelat et al., 2016; Chen et al., 2018; Eder et al., 2018; Faber et al., 2018; Fratzl & Weinkamer, 2007; Grunenfelder et al., 2018; Kokkinis et al., 2015; S. Ling et al., 2018; Zengqian Liu et al., 2017; Meyers et al., 2013; Naleway et al., 2016; C. Ortiz & Boyce, 2008; Su et al., 2016; Weaver et al., 2012; W. Yang et al., 2019; Yaraghi & Kisailus, 2018; Z. Yin et al., 2019), where the dissipating mechanisms fall into two distinct categories: 1) the increase of crack growth resistance occurs at the traveling crack tip occurring within the fracture process zone (an inherent material property) due to inelastic deformation of soft constituents, micro-cracking, and fiber bridging and pullout (F Barthelat & Espinosa, 2007; Espinosa et al., 2009; Launey & Ritchie, 2009; Rabiei et al., 2010); 2) crack growth resistance increases by extending the crack size due to fracture process zone lengthening, or microcrack deflection through weak interface network (Launey et al., 2010; Launey & Ritchie, 2009; R O Ritchie, 1988).

For most of the anisotropic bioinspired designs, the key properties of interfacial materials are different than of constituents which is common among various biological systems: 1) interfacial regions are exhibit more compliant behavior and therefore are more likely to deform than the constituent, and 2) interfaces are typically weaker and attain lower flaw-resistant

properties (Zengqian Liu et al., 2020; Moini et al., 2018). These physical characteristics are solid foundations for promoting a unique toughness mechanism by deflecting and twisting the crack through the complexity of (micro-)structural orientations (Currey & Kohn, 1976; Kamat et al., 2000; Mayer, 2005; Suksangpanya et al., 2018). Therefore, there is a dramatic rise of interest in utilizing additive manufacturing (AM) and multiscale hierarchal design of multifunctional and multilayered composites with unique flaw-tolerant and damage-resistant properties (Compton & Lewis, 2014; Duoss et al., 2014; Gosselin et al., 2016; Khoshnevis et al., 2001; Wegst et al., 2015). Given the flexibility of AM technique on combining arbitrary hierarchal structural orientation and interfacial materials of distinct properties, current research on adaptation of AM technology to the production of cement-based materials focus on eliminating the weak interfacial regions to improve their resulting mechanical properties and durability performance (Khan et al., 2020; Nerella et al., 2020; Panda et al., 2017; Zareiyan & Khoshnevis, 2017). Unlike the approach of elimination of AM-induced interfacial regions in cement-based materials, we surmise that the fabrication of weaker interfaces combined with an optimized structural orientation (inspired by nature) encompassing anisotropy leads to desirable damage-resistant properties under intrinsic shrinkage loading. We hypothesize that harnessing the unique physical properties of heterogeneous interfaces (more compliant and weaker when compared to filaments) introduces the easy propagation of cracks along with interfaces and crack growth inhibition into unrestrained neighboring layers for promoting the flaw-resistance properties, without sacrificing the strength of the cementitious composite.

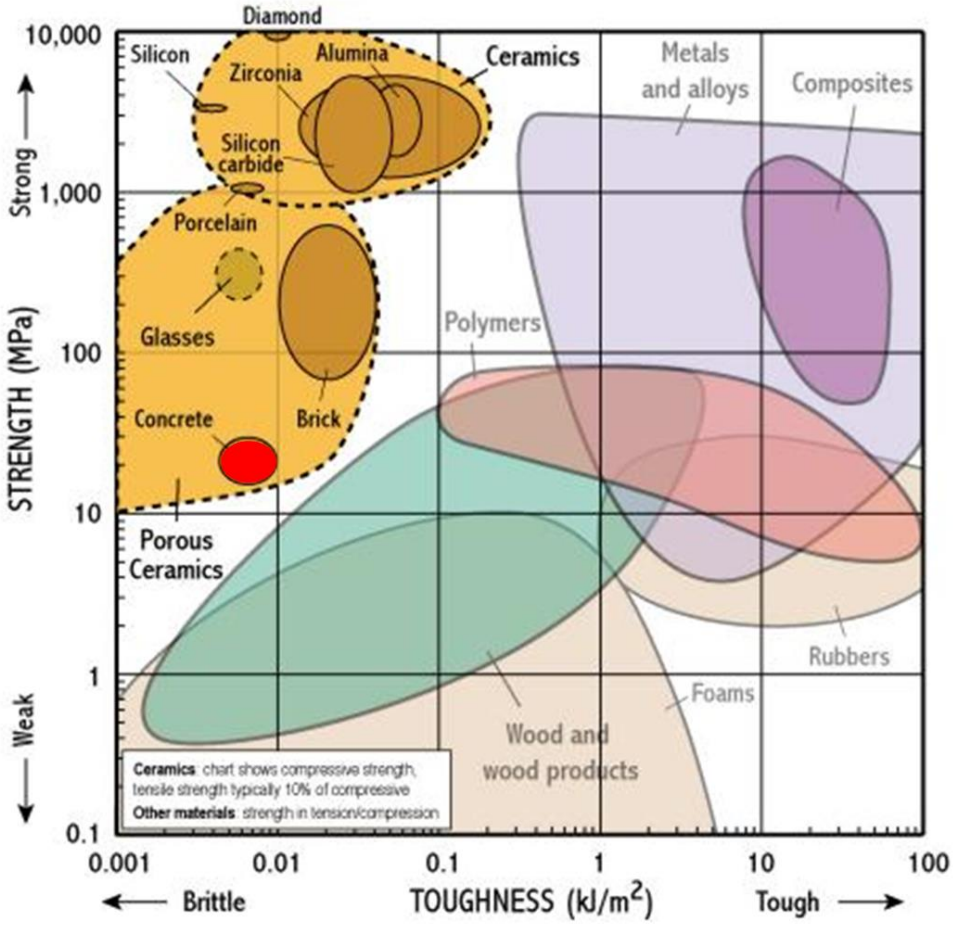


Figure 5-1. Fracture toughness-strength relation of engineering materials developed by Ashby(Ashby & Cebon, 1993).

The present study investigates the effect of filament orientation and AM-induced heterogeneous anisotropic behavior of 3D-printed structures on their performance under intrinsic shrinkage loading for 7 days determined by quantifying their physical characteristics (e.g., strength, fracture toughness) subject to quasi-static three-point flexural test, and compare them with of their cast counterparts. To assess how 3D-printed structure harness the heterogeneous interfaces to deflect the crack penetration through them, leading to damage localization at the restrained layer, X-ray microtomography (X-ray $\mu CT$) technique (i.e., no need of synchrotron facility) was used at two magnifications to analyze the microstructural characteristics of intact (i.e., not tested) damage-free and shrinkage-induced damaged 3d-printed and cast structures. In parallel, the digital image correlation (DIC) technique was employed to speculate the data from X-ray $\mu CT$ on the evolution

of fracture zone size and microcrack opening associated with the shrinkage microcracking. Another goal of this study is to discern whether bioinspired Bouligand structural design as the second layer of resistance to bending can contribute to promoting a distinct mechanism by delocalizing the microcrack evolution in 3D-printed brittle hcp structures. A numerical framework is developed to assess the contribution of carefully designed structural orientations (found in biological systems) in offering a second layer of protection, thus enhancing shrinkage cracking resistance of the hcp element.

## 5.3 Materials and methods

### 5.3.1 3D Printing Setup

Filament-based direct ink wiring (DIW) allows for the fabrication of ceramics utilized with a prudently designed hierarchal structure at multiple length scales based on extruding the pressurized ink without any heat application(Lewis, 2006). The filament-based approach to direct ink writing of 3D cement paste structure is based on extrusion freeform fabrication (EFF), where the ink is continuously extruded through a fine cylindrical nozzle to fabricate the filamentary structure. Figure 5-2 shows the integration of a stepper motor-driven ink delivery system (Structur3d Discov3ry Paste Extruder) and a gantry-based 3D printer (Ultimaker 2 Extended+) assembly to extrude the ink (henceforth, fresh cement paste) as a single continuous array of filament. The filament diameter (size) mainly depends on three printing factors of nozzle diameter, ink rheology, and printing speed. Given the favorable high yield stress and viscosity of printing paste, the DIW technique fabricates the structure of filaments that is capable of holding their designed shape. For further details on experimental configuration, the readers are referred to the conference paper by Moini et al. (Moini et al., 2019).


Figure 5-2. Filament-based extrusion system: (a) a stepper motor-driven extrusion system (Discov3ry) and a gantry-based 3D printer ; (b) constant-displacement extrusion through a syringe with lever pressure force at a uniform volumetric flow rate (adapted from Moini et al. (Moini et al., 2019)).

### 5.3.2 Mixture Proportions, Mixing Procedure, and Curing Conditions

For two purposes of structural integrity, including printability (i.e., extrudability) and buildability (i.e., shape-holding), an iterative ink design process is established to introduce two favorable fresh properties of viscosity and yield stress. To this end, a sequential combination of viscosity modifying admixture (VMA) and superplasticizer additives are utilized to increase the resistance to segregation and facilitating the flowability of ink of 0.275 w/c, associated with a solid fraction of 53%. The final ink is composed of commercially available Type-I Portland cement powder, deionized water, HRWRA, and VMA. For every 250.0 grams of cement, 65.3, 1.84, and 2.38 grams of deionized water, HRWRA and VMA are used, respectively.

A Twister Evolution Venturi vacuum mixer is utilized to achieve a homogenous ink of air void-free, thus inhibiting the degradation of the hcp structural element. After a sequential

combination of water with HRWRA and VMA, the fluid-type mixture is added on the cement powder, and then the cement paste is mixed at a pre-mixing mode (of slow speed) for the duration of 25 s. Afterward, a torque of 400 rpm at a 70% vacuum level is applied to the paste for a duration of 90 s, which is followed by a final mixing process of applied torque of 400 rpm at a 100 % vacuum level for the duration of 90 s. Upon mixing, the final ink is loaded into the syringe, which is equipped with the plunger and assembled on the stepper-motor extruder.

Extrusion of the 3D-printed specimen and placing cast specimens in the forms are carried out in a lab environment at 20 ± 3 °C and 60 ± 3 % RH. To apply restraint to these specimens while hindering any possible moisture exchange between the fresh specimen and the substrate (on which specimens are placed), we have utilized a novel approach of sanding Teflon rectangular prism of 50 mm thickness with a sandpaper grit of 80 to create a superhydrophobic surface possessing an RMS roughness of 14.5 μm and a high advancing contact angle of 146$^{o}$ (Nilsson et al., 2010). Sanding is performed in an arbitrary manner for 20 s in any specific direction, followed by cleaning the sanded surface with acetone, rinsing the residues with deionized water, and cleaning with pressurized air. Figure 5-3 outlines the scanning electron microscopy (SEM) scans from untreated Teflon surface and Teflon surface sanded with 80-grit sandpaper, highlighting an introduction of surface roughness in sanded Teflon surface. Conversely, a thin Teflon sheet of a thickness (of 2 mm thickness) adhered to an acrylic rectangular prism of 10 mm thickness was built to fabricate a perfect superhydrophobic substrate with no roughness (i.e., unrestraint substrate). The former method of substrate fabrication is used to exert shrinkage-associated local tensile stress at the specimen-substrate interface and induce shrinkage microcracking along with the depth of "damaged" specimen. In contrast, the latter method is used to obstruct any tensile stress development at the specimen-substrate interface which leads to making a perfect "undamaged" specimen. Upon the end of specimen fabrication, the specimens are placed in a curing chamber of 20 ± 3 °C and 33 ± 2 % RH (using a saturated solution of Magnesium Chloride ($MgCl_2$)). Cast specimens are demolded at the age of 24 h and placed back in the chamber for the remainder of the experiment.

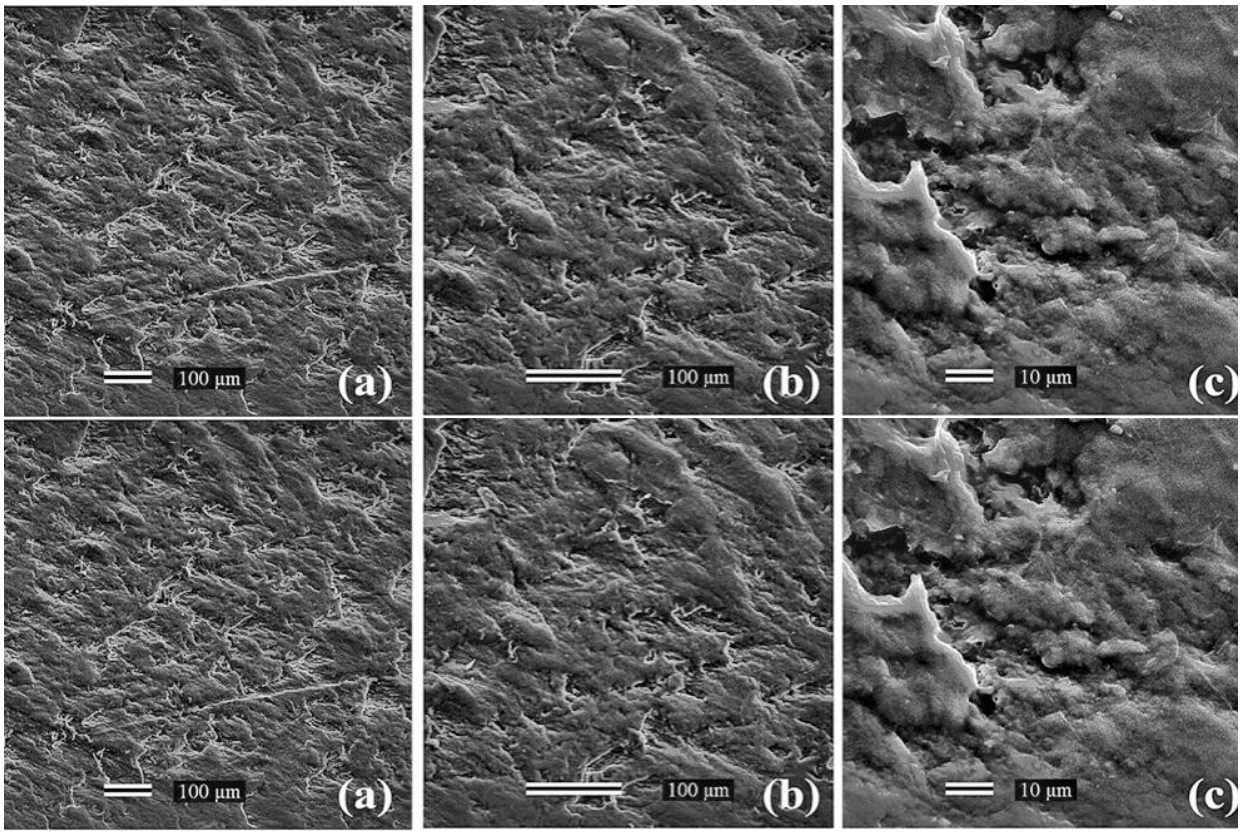


Figure 5-3. SEM images of Teflon surfaces sanded with 80-grit sandpaper: (a) smooth at 100×, (b) smooth at 200×, (c) smooth at 1000×, (d) 80-grit at 100×, (e) 80-grit at 200×, (f) 80-grit at 1000×.

### 5.3.3 Slicing and Design Parameters

Simplify3D is the commercially available slicer that has provided detailed information on converting digital 3D models to 3d-printable parts, required amount of ink, printing time, and creating optimized printing toolpath. All processed information is generated in g-code which includes: Point cloud coordinates (X, Y, Z axes) of the toolpath to govern the travels of the nozzle and the bed; Extrusion to govern the quantity of extrusion with regards to the movement of the nozzle; Printing speed to control the speed of the movement of the nozzle. Simplify3D controls the E and F axes using an extrusion rate multiplier and printing speed in the slicer interface. Additional motions of the print head for moving the nozzle to 'home' coordinates without running into the printed objects are also programmed into the g-code command.

The mere dimensions of the structure of the hcp element of this study is a rectangular prism of 50 *mm* × 12 *mm* × 12 *mm*. To achieve the desired lamellar and Bouligand architectured elements,

the geometrical characteristics of filament height, filament width, and structural orientation at each layer, combined with the processing parameters of printing speed, extrusion multiplier, and infill percentage are programmed in the slicer. Each filament layer is composed a continuous printing toolpath with two structural orientation characteristics of $\theta$ and $\gamma$, as shown in Figure 5-4; $\theta$ defines the orientation of printed filaments in the first layer concerning the X-axis, while $\gamma$ identifies the re-orientation of printed filaments concerning their neighboring bottom layer along Z-axis. Figure 5-4 (a1-a3) depicts the sequential printing toolpath of the hcp element with the lamellar architecture of $\theta = 0^o$ and $\gamma = 0^o$, where Figure 5-4 (a4) highlights the arrangement of filaments which are prone to cracking under three-point flexural loading along the X-Z plane. Figure 5-4 (b1-b3) depicts the sequential printing toolpath of an hcp element with the lamellar architecture of $\theta = 90^o$ and $\gamma = 0^o$, where Figure 5-4 (b4) highlights the arrangement of filaments which represents the susceptibility of the interface region between filaments to cracking under three-point flexural loading along the X-Z plane. Figure 5-4 (c1-c3) depicts the sequential printing toolpath of an hcp element with Bouligand architecture of $\theta = 90^o$ and $\gamma = 7^o$, where Figure 5-4 (b4) highlights the arrangement of filaments which represents the susceptibility of twisting interface region between filaments to cracking under three-point flexural loading along the X-Z plane. A layer height (i.e., filament height) of 1.0 *mm* and the extrusion width of 1.63 *mm* are programmed. The speed of printing is 750 mm/min.

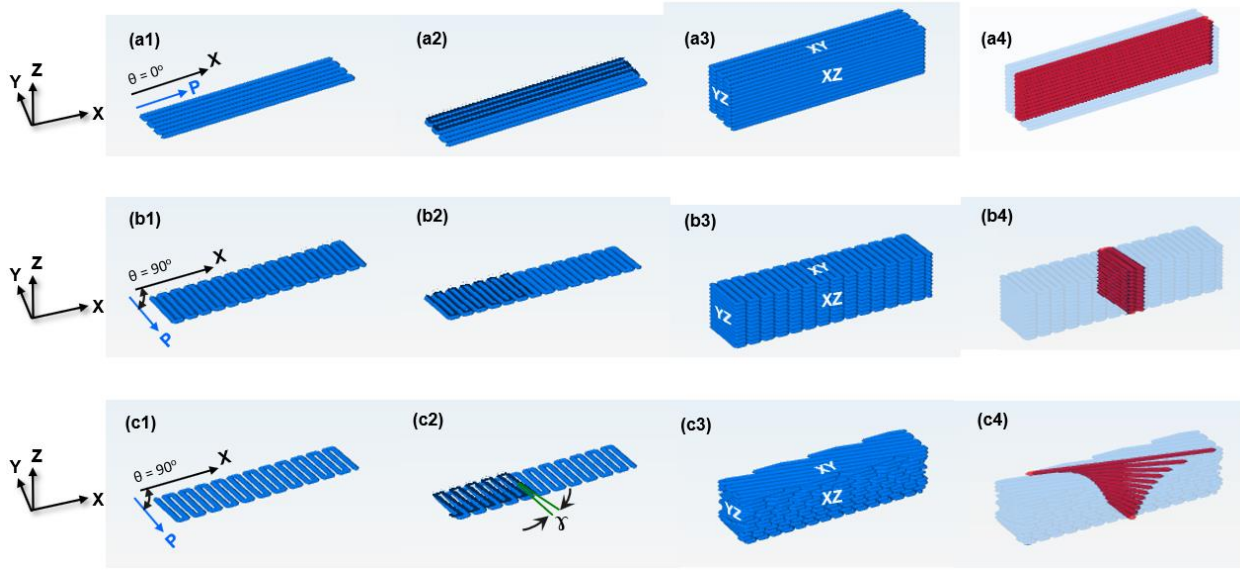


Figure 5-4. Schematics of printing path and structural orientation of (a1-a4) lamellar architectured structure, (b1-b4) lamellar architectured structure, and (c1-c4) bio-inspired Bouligand architectured structure : (a1,b1,c1) Printing path of the first layer of filament highlighting the individual filament orientation concerning primary printing direction (along X-axis), $\theta = 0^{o}$; (a2,b2,c2) Printing path of the sequential second layer of filaments highlighting the individual filament reorientation respect to of first layer filaments; (a3,b3,c3) resulting 3D-printed structures; and (a4,b4,c4) arrangement of filaments in the lamellar and Bouligand architectured hcp elements showing potential cracking paths under mechanical loading.

### 5.3.4 X-ray µCT Imaging

Because the interior microcracking development associated with inherently shrinkage behavior of cementitious material is unsightly on the surface of the element, the level of stress is significantly dissimilar inside the element experiencing inelastic deformation than that on the surface. Therefore, it is vital to observe the damage gradient along with the depth of 3D-printed and cast hcp elements. To this end, we employ X-ray µCT (micro-computed tomography) imaging technique to incorporate the logging of sequences of 2D radiographs recorded at numerous viewpoints around a revolving element. The entire volume (3D appearance of the interior and exterior) of the element is digitally rendered via mathematical reconstruction of re-configured spatial maps. Subsequent 3D renderings are characteristically displayed as a sequence of sliced radiographs with intensities associated with X-ray absorption and specific mass of material at a certain voxel (Landis & Keane, 2010). The subsequent disparities in intensity enable documentation of different phases and features of the intact and damaged structure at micro-level (e.g., microcracking) and their associated 3D distributions. Traditionally, X-ray microscopes

utilized for the μCT characterization tool utilize a flat panel detector and then depend on single-step (i.e., geometric) intensification, which implies the degradation of imaging resolution as the size of the specimen and the working distance increase.

In this study, an X-ray microscope (XRM), Zeiss Xradia 510 Versa, is used to characterize the microstructural feature of both undamaged and damaged elements, including bulk elements and microcracks, which permits for a rise in the resolving power of X-rays via dual-stage intensification procedure. Therefore, a favorable field of view (FOV) is determined to examine the middle volume of the specimen through the intensification procedure, which includes maintaining spaces between the source, detector, and element (similar to traditional μCT technique). Using a detector equipped with a scintillator and objective lens allows us to achieve the highest resolution of the region, which is hypothesized to contain a high density of microcracks, resulting in degradation of the overall strength of the element under 3-point flexural loading.

### 5.3.5 Multi-cutting compliance tests

To quantitatively measure the length and nature of the microcrack growth behind the crack tip, a multi-cutting compliance technique, similar to that of Wittmann and Hu(Hu & Wittmann, 1990), was employed for undamaged and damaged 3D printed and cast elements. Particularly, a thin diamond saw blade was used to extend the cut length consecutively and therefore incrementally abolish the crack wake (steps of ~0.6 - 1 mm), while two specimen compliances obtained from slopes of load-line displacement vs. load curve and crack mouth opening displacement (CMOD) vs. load curve were quantified (via the digital image correlation cut width (~ 100 μm) exerts an insignificant effect on the compliance. As part of the crack wake, which is abolished, is free of traction, no alteration in compliance is observed after cutting (i.e., the cut region is free of shrinkage-induced microcracks). Though, when effective microcrack bridges are abolished from the crack wake by the diamond blade, there is a rise in compliance. Through the employment of this approach, the length of shrinkage cracking advancement along the specimen height is assessed by logging the length of the notch when the specimen compliance with active shrinkage cracking occurs to raise until it becomes identical to that of undamaged specimen compliance.

#### 5.3.5.1 **Load-line displacement vs. load compliance measurement on notched beams**

A quasi-static three-point bending test is carried out by MTS Universal Testing Instrument to measure the applied displacement and corresponding load. Before the specimens were notched on the diamond saw, load-displacement tests are performed to calculate the "un-notched" compliance, $C_0$. The loading rate is justly fast enough (a displacement-controlled loading rate of 2 $\mu m/s$) to reduce the creep effect.

The value of critical fracture toughness, $K_{Ic}$ can be calculated from the dimensions of the beam, the peak load, and the notch depth. Several equations are obtained by different stress-analysis technique but all effectively equivalent, appear in the literature; this work uses the one deduced by ASTM E-1820 (*Standard Test Method for Measurement of Fracture Toughness: ASTM E1820 - 06*, n.d.) as shown in equations 5-1 and 5-2:

$$K_{Ic} = \left[\frac{P_{max}S}{(BB_N)^{1/2}h^{3/2}}\right] f(a/w) \tag{5-1}$$

where:

$$f(a/w) = \frac{3\left(\frac{a}{h}\right)^{1/2}\left[1.99 - \left(\frac{a}{h}\right)\left(1-\frac{a}{h}\right)\left(2.15 - 3.93\left(\frac{a}{h}\right) + 2.7\left(\frac{a}{h}\right)^2\right)\right]}{2\left(1+2\frac{a}{h}\right)\left(1-\frac{a}{h}\right)^{3/2}} \tag{5-2}$$

In equation 5-1, $P_{max}$ indicates the peak load, $S$ is the span length, $B$ is the average thickness, $B_N$ is the net thickness, $h$ is the beam height. In equation 5-2, $a$ is the notch depth.

The change of compliance with notch depth can be derived by making use of a general relationship between the critical strain energy release rate, $G_{Ic}$, and the specimen compliance(Kenny & Campbell, 1968), shown in equation 5-3:

$$G_{Ic} = \frac{1}{2}(P_{max}/B)^2(dC/da) \tag{5-3}$$

The stress analysis in an hcp element is analyzed based on the linear elastic fracture mechanics (LEFM) approach. Under linear elastic behavior before catastrophic failure assumption, the energy flowing through the fracture process zone (FPZ) per new crack surface growth is equivalent to Griffith's energy release rate. Given $G_{Ic} = \frac{K_{Ic}^2(1-\nu^2)}{E}$, equations 5-1 and 5-3 are combined to obtain a relationship between $C$ and $a$. To make the relationship generally applicable,

the elastic modulus must be eliminated from the equation; this is accomplished by calculating the ratio $C_0/C$ rather than $C$. Eliminating $K_{Ic}$ and $G_{Ic}$ and considering $B = B_N$ leads to equation 5-4:

$$\frac{dC}{da} = \frac{2(1-\nu^2)}{E}\frac{S^2}{h^3}[f(a/h)]^2 \qquad 5\text{-}4$$

Hence

$$C = \frac{2(1-\nu^2)S^2}{E}\int \frac{[f(a/h)]^2}{h^3}da \qquad 5\text{-}5$$

Now, from elementary beam theory,

$$E = \frac{1}{C_0}\frac{L^3}{4bh^3} \qquad 5\text{-}6$$

where $C_0$ is the compliance of the beam when $a = 0$. The substitution of equation 5-6 into equation 5-5 leads to equation 5-7:

$$\frac{C_0}{C} = A\int \frac{[f(a/h)]^2}{h}da \qquad 5\text{-}7$$

Where $A = \frac{8(1-\nu^2)S^2h}{L^3}$. For the geometry of the present experiment, specimen, $A = 1.296$ if $\nu = 0.2$.

Now, $\int \frac{[f(a/h)]^2}{h}da = \left[\frac{k_1}{2}\left(\frac{a}{h}\right)^2 + \cdots + \frac{k_9}{10}\left(\frac{a}{h}\right)^{10}\right] + \text{constant} = f(a/h) + \text{constant}$. Since $C/C_0 = 1$ when $a = 0$, $C/C_0 = Af(a/h) + 1$.

### 5.3.5.2 **CMOD vs. load compliance measurement**

The compliance method is a primary technique to determine the length of propagated crack; nevertheless, it is known that the presence of microcracks ahead of clearly cut notch influences the accuracy of the method significantly. Therefore, the effect of microcrack zone extension on overall compliance of specimens should be examined using a compliance calibration curve. This curve is constructed with cut specimens within their linear-elastic region. It is sensible to consider that the calibration curve is constructed for undamaged specimens, where no micro-damage associated with shrinkage ahead of clearly cut notch exists. Figure 5-5 shows a qualitative representation of measurements of loading compliance of the undamaged and damaged specimens ($C_L$ and $C_U$) to examine the existence of crack bridging along with the clear-cut notch. Figure 5-5(a) outlines the experimental configuration of a three-point bending test applied to cement paste specimens of undamaged and damaged associated with shrinkage. A diamond saw is used to consecutively cut

out the specimen (and potential microdamage ahead of notch tip) at a specific increment to quantitively determine the extent of the microcracking zone behind the notch tip, given that a damaged material can be considered as a component constituted of materials of two elastic moduli of undamaged material ($E$) and material with microcracks ($E^*$). Consequently, there is a difference in compliance due to the elastic modulus reduction shown in Figure 5-5(b) where $P$ is the load, and $CMOD$ is the crack mouth opening displacement. Figure 5-5(c) depicts the compliance calibration curve that is constructed with a notched specimen within their linear-elastic region. This figure illustrates how the length of microcrack bridging can be determined with the compliance method in conjunction with multi-cutting, where $C$ specifies the compliance calibration curve (solid line), and $C_p$ represents the compliance of a damaged specimen acquired from the multi-cutting tests. The x-axis in Figure 5-5(c) shows the increase of notch length with the origin at the initial notch length of ~0.6 mm. With the incremental cutting, the existence of bridging crack can be separated from the bridge-free region. When the part of the crack wake that is abolished contains bridging cracks, the compliance will be increased by cutting. When the cutting is through the entire crack wake region, the compliance of damage specimen and calibration curve will merge. $a_s$ represents the initial notch size in this study, and $a_f$ is the total propagation, including the extension of the active bridge zone.

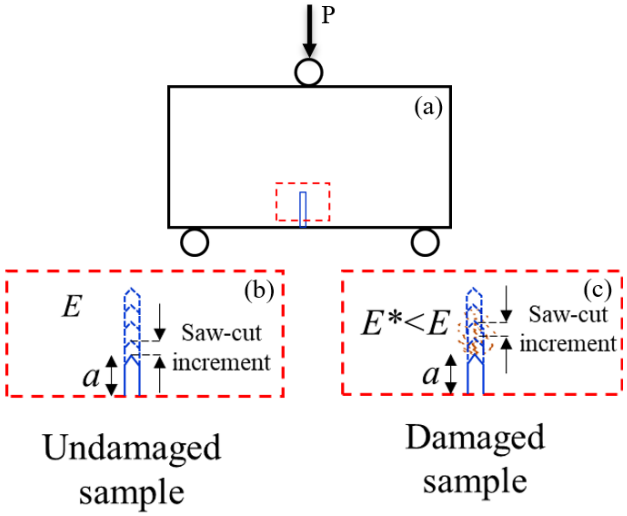


Figure 5-5. Schematics of multi-cutting compliance experiment (a) investigation the effect of notch size extension on the mechanical response of undamaged and damaged cement paste elements under three-point bending test, (b) a loading and subsequent unloading response within linear-elastic region where microcrack zone length to be quantified, (c) evaluation of compliance curves from multi cutting of undamaged and damaged specimens.

## 5.4 Results

As noted above, the interfaces between filaments in biological materials with the hierarchal pattern are one of the important structural features that determine the anisotropic behavior governed by the preferred alignment of filaments. Here, we emphasize the key role of interfaces in deflection and arrest of microcrack development associated with restrained shrinkage, which contributes to the promotion of a damage localization mechanism. This hypothesis is derived based on the fact that the interfaces are characteristically weaker than filaments in biological materials (W. Yang et al., 2019). In other words, the easy crack growth across the interfacial region is serious for rendering the toughening effect via the complexity of filament orientation. Besides, a carefully designed structural orientation of filaments plays a key role in allowing for developing an additional number of delocalized microcracks distributed throughout the domain subject to external loading before the catastrophic failure of the damaged hcp element.

### 5.4.1 Mechanical performance of 3D printed hcp elements with lamellar architecture and cast hcp elements

Here we examine the effect of shrinkage-induced internal micro-cracks on the mechanical performance of 3D printed hcp elements with two structural orientations. To characterize the strength of two main constituents of filament and interface in 3D printed elements, the values of modulus of rupture (MOR) of printed elements with two structural orientations of $\theta = 0^o$ and $\gamma = 0^o$ and $\theta = 90^o$ and $\gamma = 0^o$ are quantified under three-point bending test. A comparison of the mean value of five MOR measurements for damaged 3D printed specimen (i.e., 3DP (D)) and damage-free 3D printed specimen (i.e., 3DP (UD)) highlights a reduction of 11.6%. In contrast, the value of MOR for damaged cast specimen (i.e., cast (D)) is reduced by 30.6% when compared to that for damage-free cast specimen (i.e., cast (UD)). The higher decrease of MOR in cast specimen leads to the idea that microcracks associated with shrinkage are easily distributed through its mesoscopic homogenous structure along with the specimen depth, effectively compromising the resistance of the material to damage. On the other hand, the lower decrease of MOR in 3DP specimens promotes a novel damage mechanism where the heterogeneous interface region contributes to trapping the microcrack development at the restrained filament layer. Owing to the weakness of interface by 25% when compared to the filament, promotes the hypothetical idea that these interfaces can deflect and channel the propagating microcracks from the restrained layer

along these predefined paths. To this end, we surmise that the fabrication of weaker interfaces increases the ability of 3DP elements in guiding and deflecting cracks to introduce a novel toughening mechanism through damage localization. The motivation of this work is inspired by biological systems where nature leverages from strong and brittle filaments delimited by weaker interfaces architectured in careful designs to induce the crack propagation along with the well-designed interface, effectively promoting damage and flaw resistance properties.

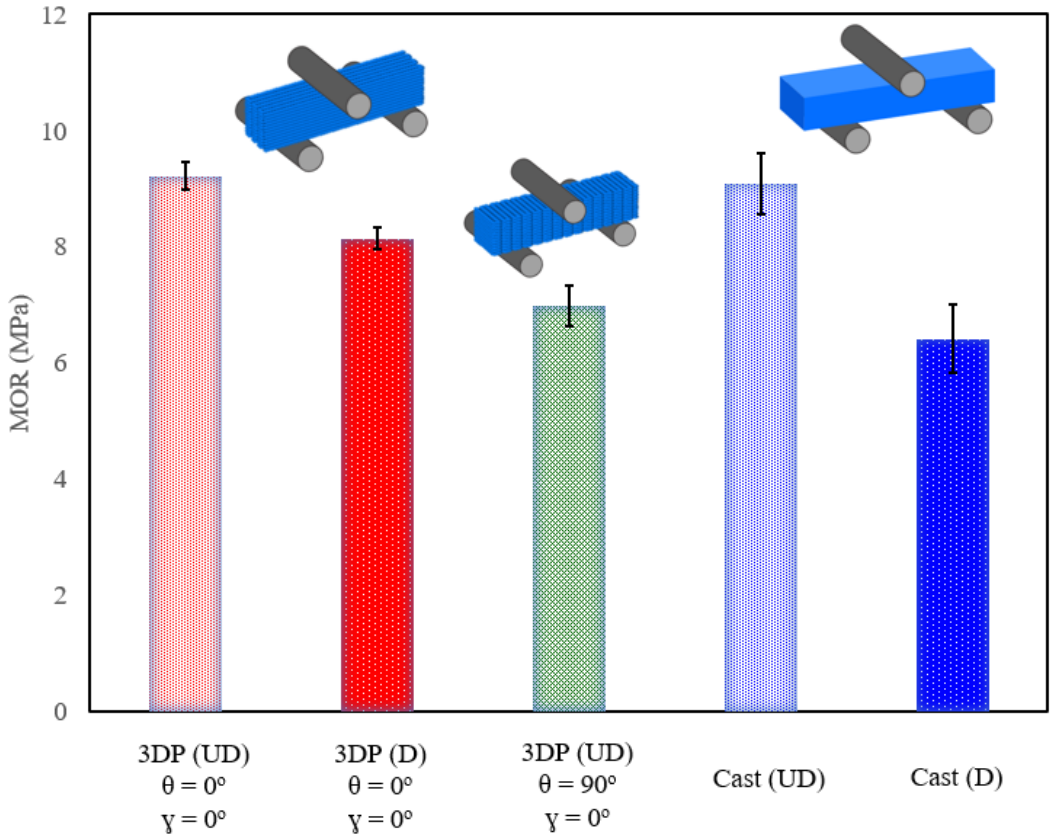


Figure 5-6. Mechanical response of damaged (D) and damage-free (UD) 3D printed (3DP) and cast hcp elements tested in three-point bending.

### 5.4.2 Multi-cutting fracture toughness and compliance experiments

#### 5.4.2.1 **5.4.2.1 Fracture toughness measurement**

The toughness represents the materials' resistance to cracking, particularly by resisting the increase of clearly cut specimens. A prime source of reduction in fracture toughness is the development of inherent cracks formed at hierarchical length scales and distributed behind a crack

tip in brittle hcp material. When there are bridged or unbridged microcracks distributed at or behind the crack tip in damaged hcp elements (3DP or cast), the elements at the crack wake require lower energy to fracture when compared to their undamaged counterparts. Here, we present experimental results that a more quantitative description of how far shrinkage-induced microcracks propagate from the interface between specimen and substrate (i.e., the bottom of the specimen). Figure 5-7 outlines the $K_{Ic}$ measurements of two 3D printed specimens of 3DP (UD) and 3DP (D) along with two cast specimens of the cast (UD) and cast (D) concerning various notch length, demonstrated by a/h ratio. The initial a/h ratio is 0.05 (0.05 × 12 = 0.6 mm), highlighted as Zone I. A comparison of findings from cast specimens indicates the presence of region with significant weakness behind the crack tip that is impacted by shrinkage microcracks. It is observed a reduction in $K_{Ic}$ by 33% between a/h ratio of 0.05 and 0.163, whereas no significant deviation is observed at higher a/h ratios. Therefore, it is clear that the length of crack growth in cast specimens is extended to *2 mm* (= 0.163 × 12 mm) during 7 days of exposure to the dry environment. A similar comparison of the $K_{Ic}$ trend in 3D printed specimens highlights the limitation of the length of crack growth to *0.6 mm* (= 0.05 × 12 mm), where a considerable deviation of 16.7% is observed. This implies that the crack propagation tends to propagate along with weak interfaces, requiring little energy, and inhibited to penetrate the neighboring top layer of filaments. The carefully designed interfaces are introduced within the element to alter its mechanical response to inherent shrinkage behavior entirely. On propagation a/h increases (> 0.05), no significant deviation of $K_{Ic}$ is observed due to the ability of (porous) weak interfaces for stabilizing cracks, effectively alleviating the strength compromise of the 3D-printed elements when compared to their cast counterparts.

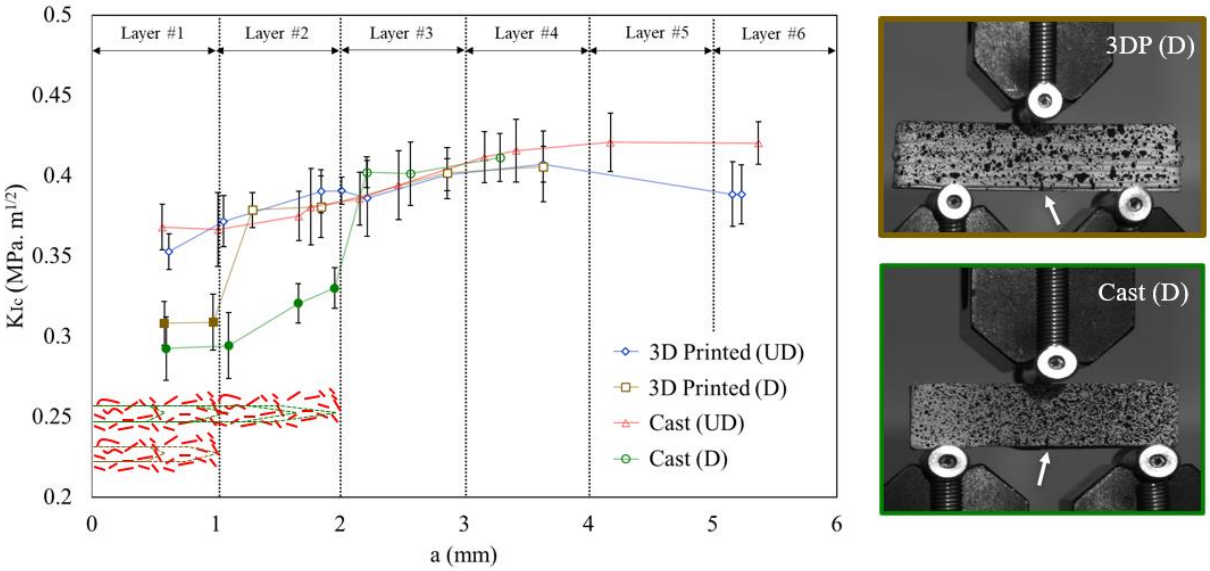


Figure 5-7. $K_{Ic}$ evolution of damaged and damage-free 3D-printed and cast hcp elements tested under three-point bending in the multi-cutting experiment.

### 5.4.2.2 **Compliance measurement**

The relationship between notch depth and load-line compliance, defined as beam displacement at the loading point divided by the load, of multi-cutting experiments for four specimen types of the cast (UD), cast (D), 3DP (UD), and 3DP (D) are shown in Figure 5-8. The theoretical relationship between $C_0/C$ and the notch depth is superimposed on the experimental results. The comparison of experimental results of each specimen type with the theoretical line indicates an insignificant deviation between the theoretical line and damage-free specimens (cast (UD) and 3DP(UD)), which implies that the theoretical line adequately represents the change in compliance with notch depth for all shallow notches. Conversely, the experimentally measured compliance values for damaged specimens (cast (D) and 3DP (D)) are lower than that for the ideal, undamaged specimen, providing direct evidence to the notion of microcrack extension at and behind the notch tip. Furthermore, Figure 5-8 shows that an essentially significant increase in the cast (D) and 3DP (D) is observed at the notch length of smaller than ~0.6 mm, highlighted in dark red color (Zone I). As the saw-cut notch length (i.e., microcrack wake region) is reached within ~2mm (Zone II), highlighted in light red color, no increase in 3DP (D) specimen compliance is observed. In contrast, a significant variation is shown for cast (D) specimen compliance. This indicates that the microcrack extension length is on the order of 0.6 mm for 3DP (D) specimens,

while a greater value of 2 mm is found for cast (D) specimens. This experimental finding of load-line vs. load compliance obtained from the multi-cutting approach is in a strong agreement with that of fracture toughness measurement as they promote the effectiveness of interfaces in trapping the microcrack growth associated with shrinkage, and channeling the microcracks into stable well-designed configurations in the first "restrained" layer of filaments. The cast specimens are, however, deprived of this structural feature for controlling crack growth, which leads to being more likely susceptible to undergo excessive damage associated with shrinkage.

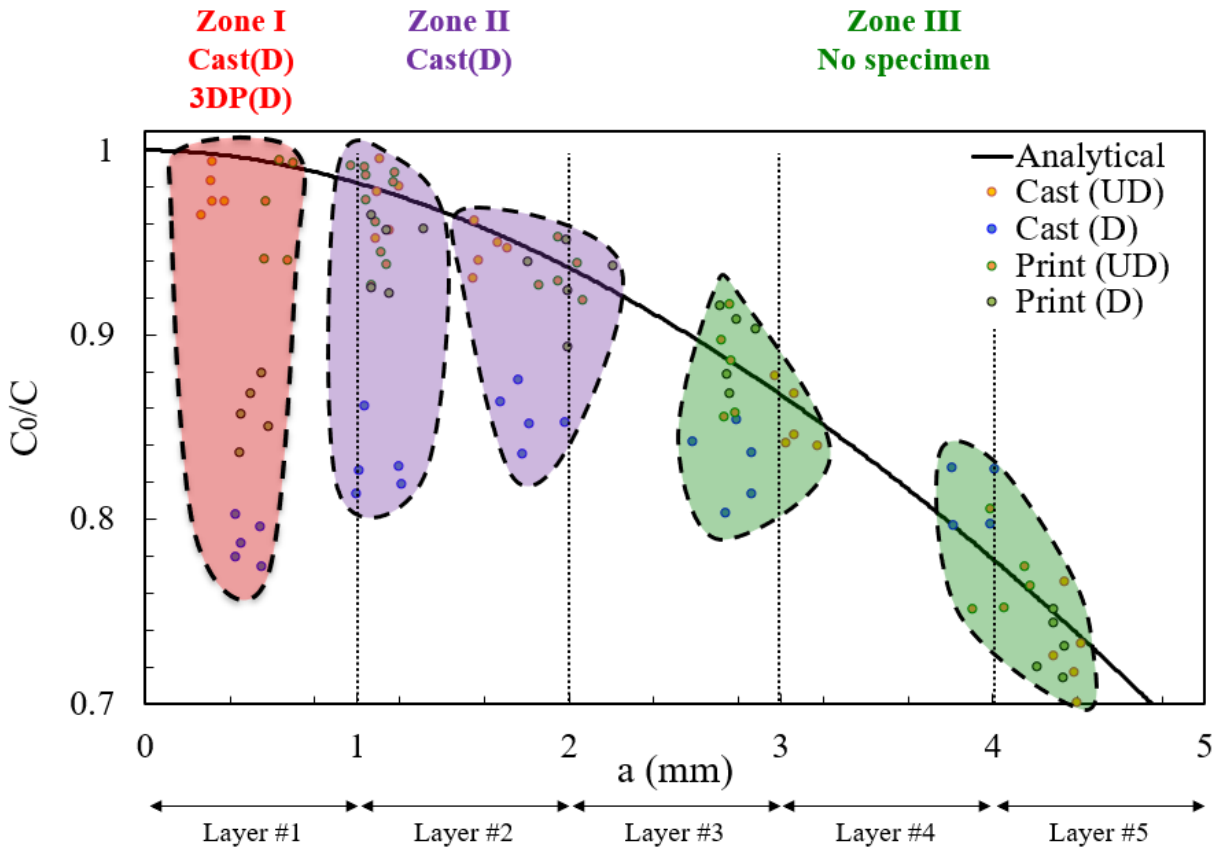


Figure 5-8. Relationship between compliance ratio and notch depth. $C$ = compliance, $C_0$ = compliance for zero notch.

As has been noted in this work, the present results affirm the notion that the shrinkage-induced crack localization is a major competitive mechanism in 3D-printed specimens. New results on mechanical performance characteristics of 3d-printed and cast specimens confirm how 3D configuration of interface regions provide ideal crack propagation sites, effectively inhibiting crack growth into the neighboring layers. The load-line vs. load compliance measurement using

multi-cutting compliance experiments showed how the greater extension of microcracks along with the specimen height leads to a significant increase in the global compliance of the damaged specimen when compared to its undamaged counterpart. Here, we perform a compliance-based measurement of crack mouth opening displacement (CMOD) of clearly saw-cut notch regarding the applied load to analyze the effect of microcrack length extension on local compliance of specimen. To determine the CMOD in a non-contact optical mode, digital image correlation (DIC) is used to extract the real-time full-contour displacement on a specimen surface(Yates et al., 2010). For more information on specimen preparation and image recording method, readers are referred to an article by Sutton et al. (Sutton et al., 2007) examining the capability of the DIC method for quantification of deformation and CMOD in ductile aluminum subjected to mixed-mode loading.

Representative CMOD-load responses are shown in Figure 5-9 for the undamaged and damaged cast specimens, which demonstrated the local compliance alteration about sequential notch length extension ranging from a = ~0.6 mm to ~4 mm. The line fitted to the data points suggests a best-fit linear function to determine the compliance value approximately. Shown for comparison at a specific notch length, it is apparent that the experimentally acquired compliance values of damaged specimens (in Figure 5-9(b)) are greater than those for the ideal, undamaged specimens (in Figure 5-9(a)) at notch sizes as long as roughly 2 mm. When further extending the notch length size to larger values (i.e., 3 mm and 4 mm), the difference of compliance values of damaged and undamaged cast specimens appears to be negligible, which implies a microcrack-free zone at these notch length sizes.

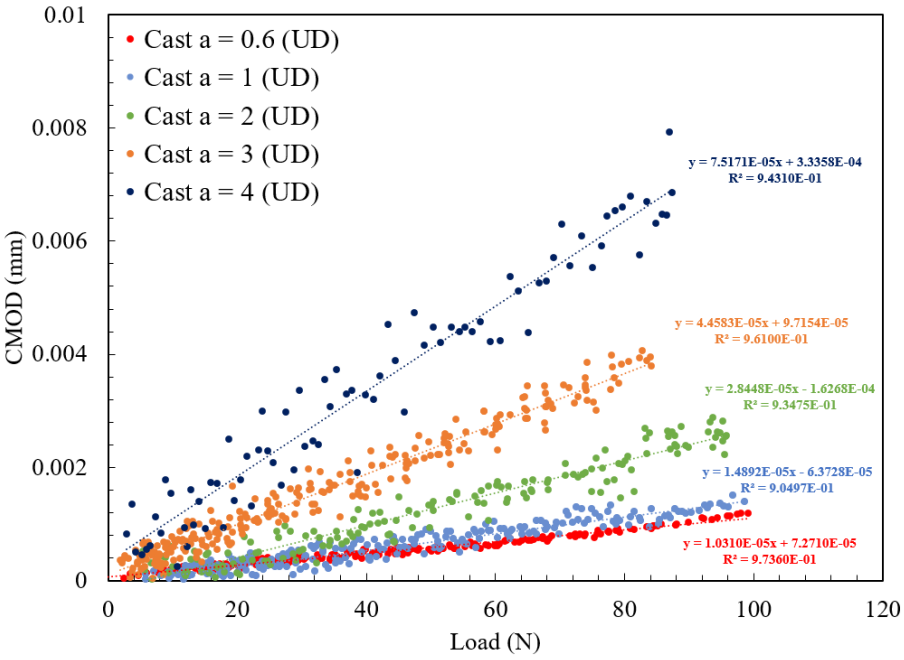


(a)

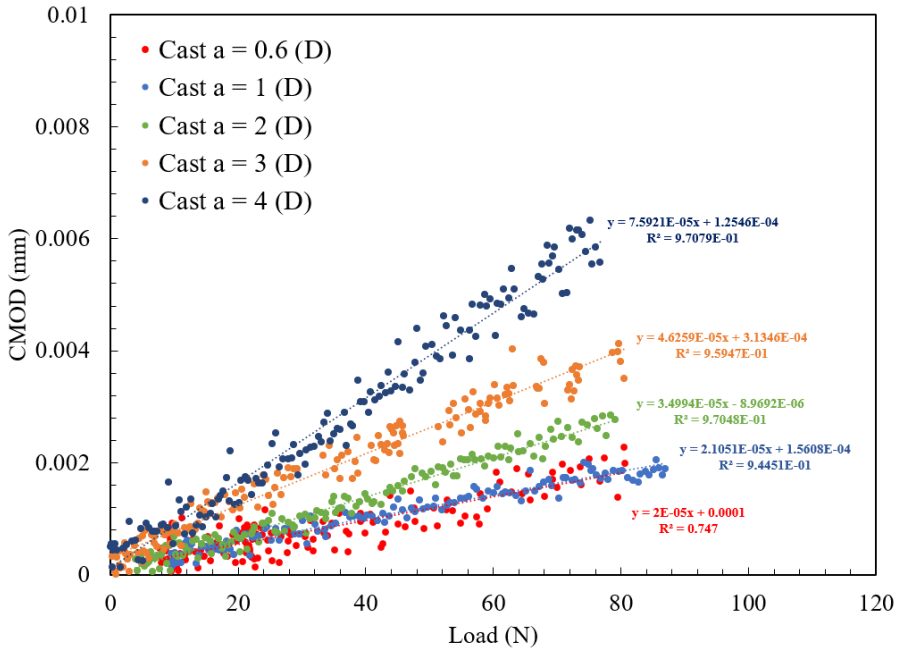


(b)

Figure 5-9. Quantitative representation of pre-failure CMOD-Load curves for (a) undamaged cast specimens with notch length range between a = 0.6 mm and a = 4 mm, and (b) damaged cast specimens with notch length range between a = 0.6 mm and a = 4 mm.

Similar multi-cutting experiments and analysis are performed on undamaged and damaged 3DP specimens, shown in Figure 5-10. A comparison of compliance values of undamaged and damaged specimens at a specific notch length indicates that microcrack extension zone for 3DP specimen is significantly smaller than that for cast specimen; indeed, the zone length is on the order of 0.6 mm long in damaged 3DP specimens when compared to their undamaged counterparts. It is concluded that the microcrack zone is extended to a length on the order of ~ 2 mm, which is much larger than those inferred for cast specimens that yielded a steady state "plateau" compliance after ~ 0.6 mm. This difference is seemingly due to the fabrication of weaker interfaces within the bulk material to induce the crack propagation along these interfacial regions, *thereby providing a layer of protection against detrimental shrinkage cracking*.

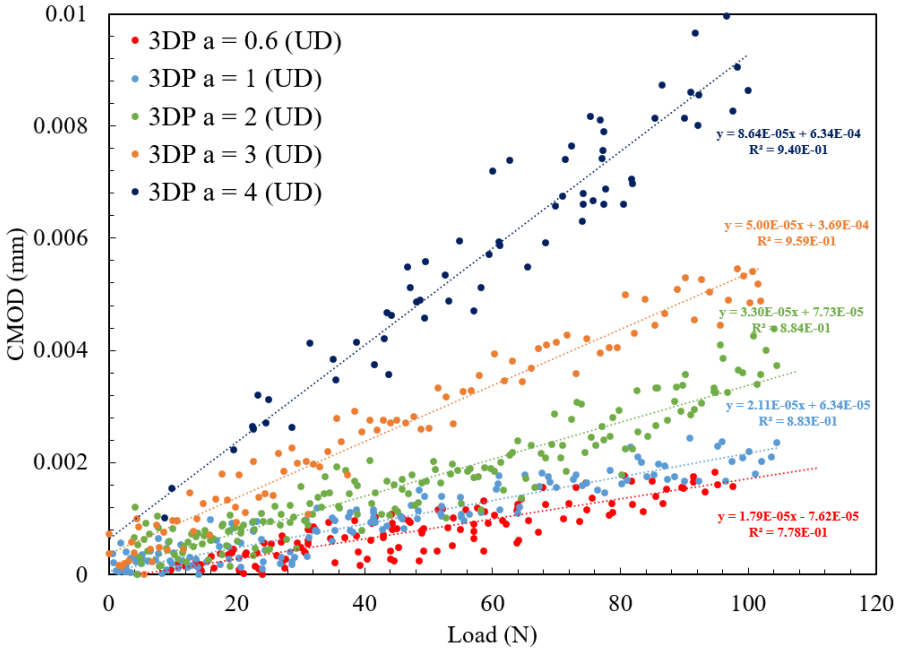


(a)

Figure 5-10. Quantitative representation of pre-failure CMOD-Load curves for (a) undamaged 3DP specimens with notch length range between a = 0.6 mm and a = 4 mm, and (b) damaged 3DP specimens with notch length range between a = 0.6 mm and a = 4 mm.

Figure 5-10 continued

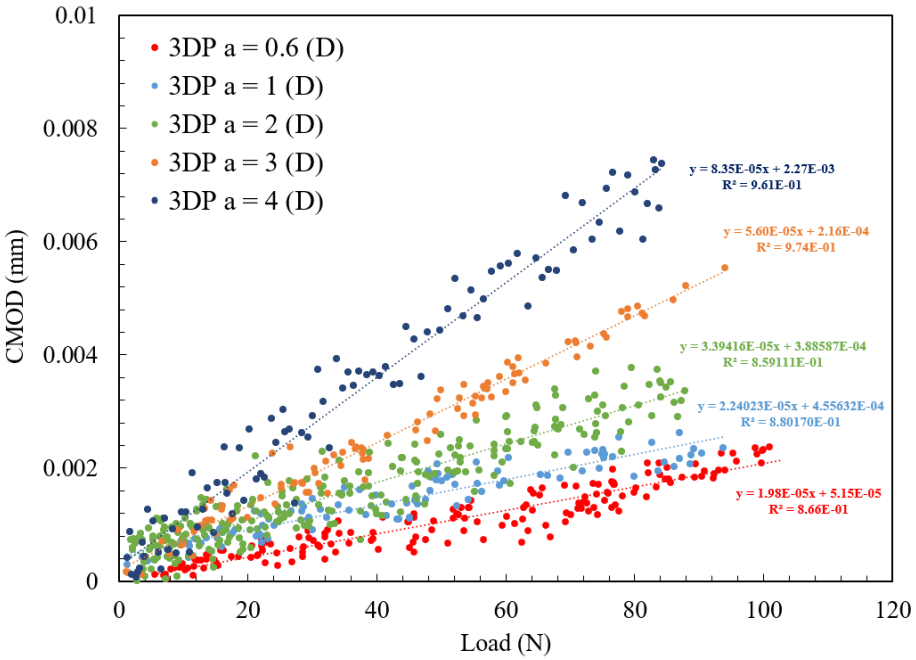


(b)

The efficient microcrack advancement determined from the compliance-calibration curve is used. The associated compliance curve for both cast and 3DP specimens obtained from multi cutting and highlighted with black color is presented in Figure 5-11(a) and (b), respectively. Each data point represents the mean value of five measurements for the associated notch size, while the curve fitted to the data points specifies a best-fit sixth-order polynomial function to the data. It is seen that the variation of the compliance through the notch length increase in damaged specimens is less than that of the compliance-calibration curve (i.e., compliance variation of the undamaged specimen) since the bridging stress transported within the zone with shrinkage-induced microcracks is less than what is likely to be transported within the zone with intact material. Through the curve fitting, it is discovered that the lengths of the microcrack zone extended along the specimen height are on the orders of 2.57 *mm* and 1.23 *mm*, which is in agreeable compliance with previous findings.

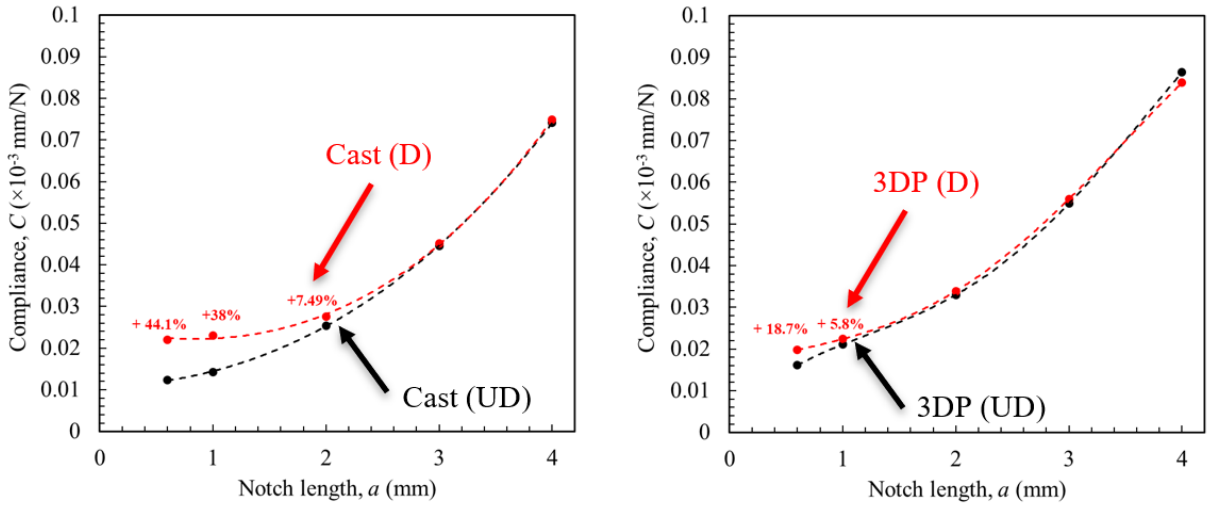


(a) (b)

Figure 5-11. Results from multi-cutting compliance experiments on (a) an undamaged and a damaged cast specimen, and (b) an undamaged and a damaged 3D-printed specimen. The indicated location of the crack tip is measured by multi-cutting methods, while each plotted data point corresponds to the mean of five compliance measurements.

### 5.4.3 Micro-imaging of crack growth

This work investigates the effect of interface characteristics on alleviating the growth of shrinkage-induced damage within the cast and 3D printed lamellar elements using the X-ray μCT scanning method. Traditionally, laboratory-based X-ray radiographs (i.e., images) are produced from an X-ray source bombarding high-speed electrons to the target region of interest (ROI) of an element (Landis & Keane, 2010). The resulting alteration in distributed intensities depending on the X-ray absorption and material density allows for the identification of various phases and their geometrical properties.

In this study, an X-ray microscope (XRM), Zeiss Xradia 510 Versa, is used, which allows for scanning resolution enhancement through a dual-stage magnification technique. Figure 5-12 depicts an overview of the X-ray μCT scanning procedure. Given the internal crack opening size associated with the shrinkage is on the order of microns, the microstructure of elements is characterized using 4X magnification with a resolution size of ~15 μm. The desirable region of interest (ROI) is selected to enable us to visualize the randomly distributed microcracks within a cylinder of 12 mm in diameter and 12 mm in height located in the center of elements. A beam energy of 150 KeV, a power of 10 W, exposure time of 4 seconds, and full 360$^{o}$ rotation are used

for 4X scans of elements. For the post-processing of the images, Dragonfly software is used. One intact cast, one intact 3D printed, one damaged cast, and one damaged 3D printed prismatic hcp elements (50 mm × 12 mm × 12 mm ± 1 mm) are used in this experiment.

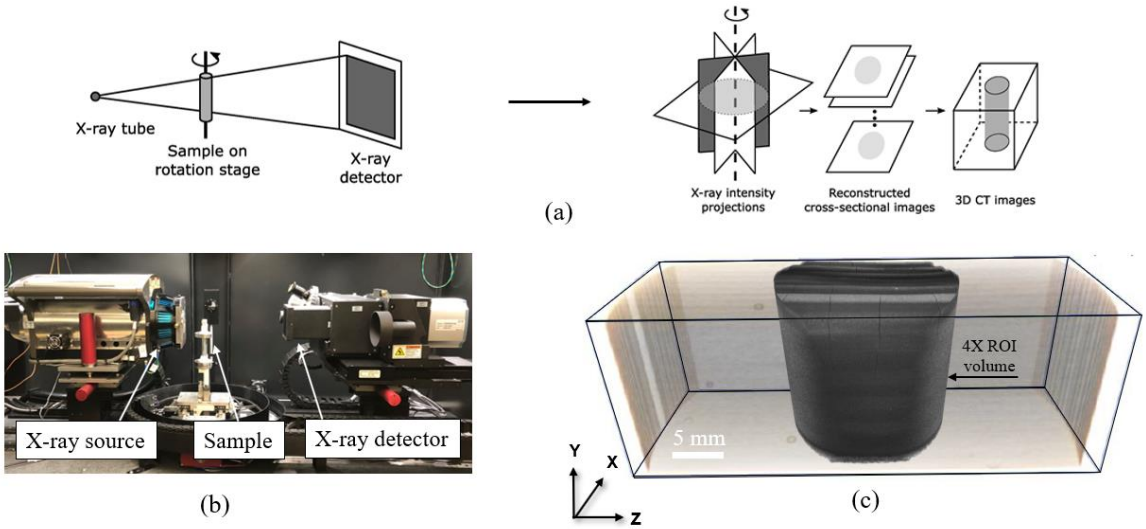


Figure 5-12. Schematic illustration of procedure of X-ray μCT scan: (a) a laboratory-based X-ray technique generating and reconstructing cross-sectional images, (b) experimental configuration of specimen scanning using an X-ray microscope (XRM), (c) 3d rendering of the volume of the region of interest in 4X scan mode.

#### 5.4.3.1 **Restrained and unrestrained shrinkage in 3D printed specimens with lamellar architecture**

To investigate the characteristics of the interface and its role in trapping the microcrack growth, the microstructure of 3D printed hcp element with $\theta = 0^o$ is characterized, and the microcrack distribution at carefully-selected cross-sections is studied, as shown in Figure 5-13-Figure 5-15. In μCT images of hcp, darker intensities represent both pores filled with air or water and microcrack openings, with greyscale intensities associated with hydrated cement paste particles.

Three horizontal slices ($F_1$, $F_{11}$, $F_{12}$) and three horizontal slices ($I_1$, $I_{10}$, $I_{11}$) shown in cross-sectional view in Figure 5-13(a), corresponds to the 'core' (i.e., through the interface) and 'interfacial regions' between the filaments. It is necessary to note that the numbering starts from the bottom of the specimen. Moreover, the horizontal slice (S) and two vertical slices ($H_1$, $H_2$) corresponds to the 'exterior' cross-sectional views of the specimen that are exposed to exterior boundary conditions (i.e., slice S corresponds to the bottom surface of the filament in the first layer

deposited on the substrate with no roughness, whereas slice $H_1$ and $H_2$ represents the stack of 12 layered filaments exposed to severe low humidity). Analysis of Figure 5-13(b1-b7) indicates no significant microcrack onset or growth within the filaments at the bottom layer. In contrast, observable microcrack distribution is observed within the filaments located at the two top layers ($F_{11}$ and $F_{12}$ cross-sectional views) and the interface between them ($I_{11}$ cross-sectional view) owing to the drying shrinkage mechanism exacerbated by the severe dry ambient environment. Furthermore, observable microcrack growth in an arbitrary pattern on two lateral sides of the element (displayed in Figure 5-13(b8-b9)) provides further direct evidence of the deleterious effect of drying shrinkage on generating damage within filament microstructure. While a previous study has suggested for appropriate curing for alleviating the excessive degree of shrinkage cracking in 3D printed elements, the comparison of MOR of two unrestrained cast and 3D printed hcp elements indicates 'zero' contribution of these developed micro-cracks on the mechanical performance of 3D printed elements.

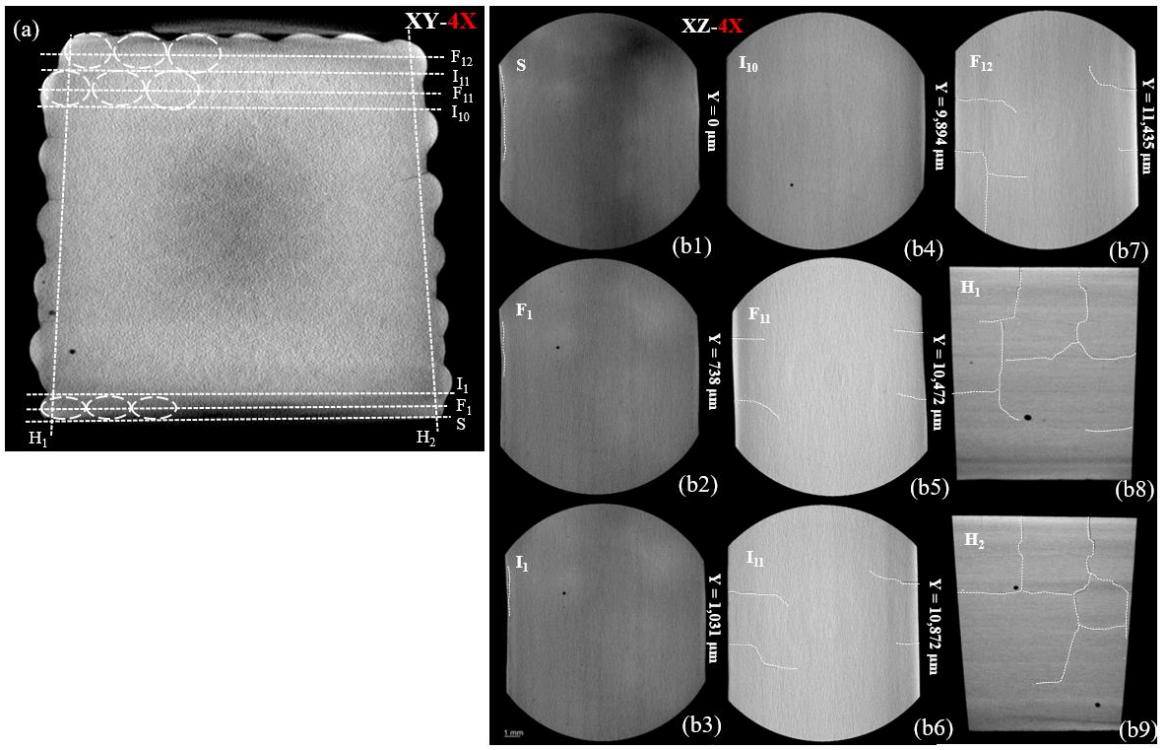


Figure 5-13. X-ray μCT images of the microstructure of 3D-printed solid prism ($\theta = 0^o$) specimen containing shrinkage-induced microcracks collected during 4X scan: a) 2D image of the cross-section in XY plane, b1-b10) 2D images of the cross-section, highlighted in (a), in XZ plane, screening the shrinkage-induced microcrack propagation along with the specimen height.

Here, the cracking behavior and associated damage mechanism in restrained 3D printed hcp elements are investigated to highlight the role of the interface in governing the damage mechanism using μCT images at 4X magnification. Figure 5-14 depicts the microstructural characteristics of the element at nine critical cross-sectional views in X-Z plane (slice S corresponds to the bottom surface of the filament in the first layer deposited on the substrate with a specific roughness; five slices $F_1$, $F_2$, $F_3$, $F_{11}$, $F_{12}$ corresponds to the 'core' (i.e., through the interface); and, four slices $I_1$, $I_2$, $I_{10}$, $I_{11}$ are associated with the 'interfacial regions' between the filaments). These slices are intentionally selected to monitor the guiding capability of interfaces along their predefined surface (i.e., path). When the five bottom horizontal cross-sectional views are examined, a gradient of microcrack population and distribution is observed along the filaments of the first layer, with a maximum degree of cracking screened on slice S (i.e., Y = 0 mm) and a minimum degree of cracking screened on slice $I_1$ (i.e., Y = 839 mm). When the second layer of filaments are examined microscopely, 'zero' cracking population and distribution is observed

which reveals the channeling of cracks into weaker heterogeneous interfaces and inhibiting the damaging of stronger filaments at the neighboring upper layers (slices $F_2$, $F_3$) and the interface between them (slice $I_2$). Similar to unrestrained 3D printed hcp element, the microcrack advancement within filaments of the top two layers (slices $F_{11}$, $I_{11}$, $F_{12}$) is observed owing to the excessive degree of drying shrinkage. Following the influence of these pronounced interfaces on deflecting the overall crack paths, no crack population or distribution been observed on cross-sectional $I_{11}$ view, highlighting the microcrack channeling along with the interface between two filaments.

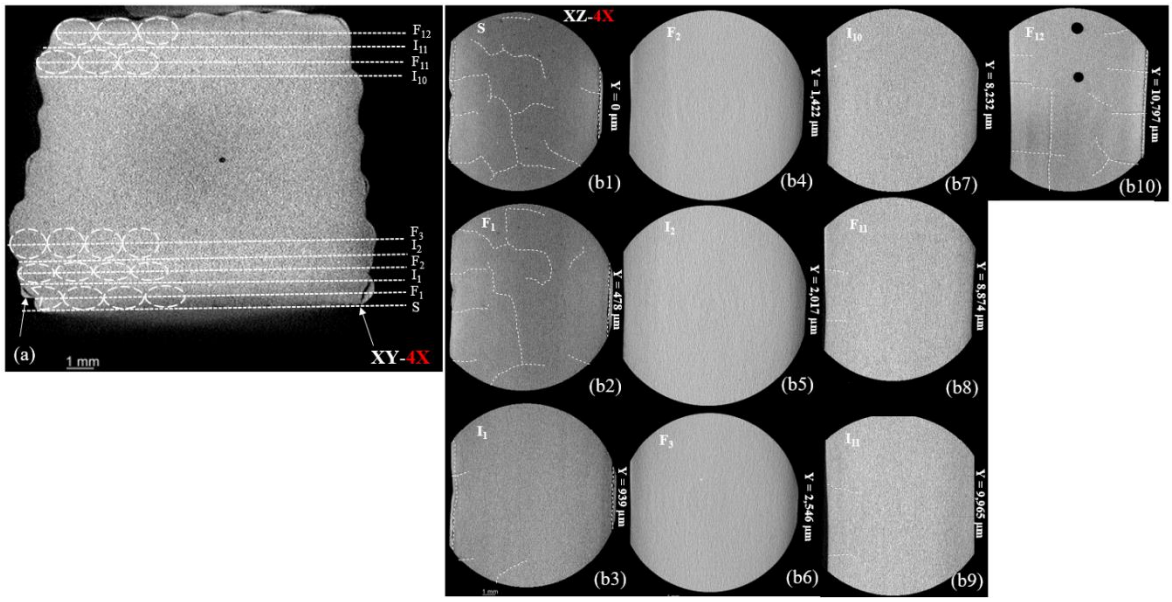


Figure 5-14. X-ray μCT images of the microstructure of 3D-printed solid prism ($\theta = 0^o$) specimen containing shrinkage-induced microcracks collected during 4X scan: a) 2D image of the cross-section in XY plane, b1-b10) 2D images of the cross-section, highlighted in (a), in XZ plane, screening the shrinkage-induced microcrack propagation along with the specimen height.

Furthermore, μCT characterization of restrained 3D printed hcp element along the Y-Z plane (i.e., third plane) is necessary to monitor the realistic three-dimensionality of the microcrack growth gradient along with the specimen height and associated damage mechanism. The μCT analysis is performed as a mean to improve further our understanding the central role of the interface, as shown in Figure 5-15. Figure 5-15 depicts the microstructural characteristics of the element at nine critical vertical cross-sectional views in Y-Z plane (two slices $H_1$ and $H_2$

corresponds to the cross-sectional views of lateral filament layers directly exposed to the dry ambient environment, and seven slices $H_3$-$H_9$ correspond to 'interior' filament layers). Similar to unrestrained 3D printed hcp element, a significant degree of microcracking distribution is observed along the specimen height shown in slices $H_1$ and $H_2$ (Figure 5-15(b1-b2)), where its onset occurs within the filaments located at the top layer propagating toward to the bottom layers. Figure 5-15(b3-b9) depicts the examination of microcrack propagation within the stacked filaments in the Y-Z plane. The observational microcracking on each slice reveals the development of microcracks, initiating from the (restrained) bottom of element extended towards the interface between the filaments of the first and second layers with an associated maximum height of 919 μm. According to μCT images in Figure 5-14, this microcracking zone length is approximately identical to the height of the first filament layer (~939 μm), highlighting the influence of weak interfaces in hindering the crack propagation into the second layer of filaments. This finding complements our earlier observations that the mechanical response analysis that local and global compliances of damaged 3D printed hcp elements cut with a notch length up to 1 mm are higher than those of for undamaged 3D printed hcp elements. In other words, the fabrication of stiff and hard filaments delimited by weaker interfaces arranged in specific architectures can promote a unique damage mechanism that enhances the mechanical response of hcp elements without sacrificing their overall strength.

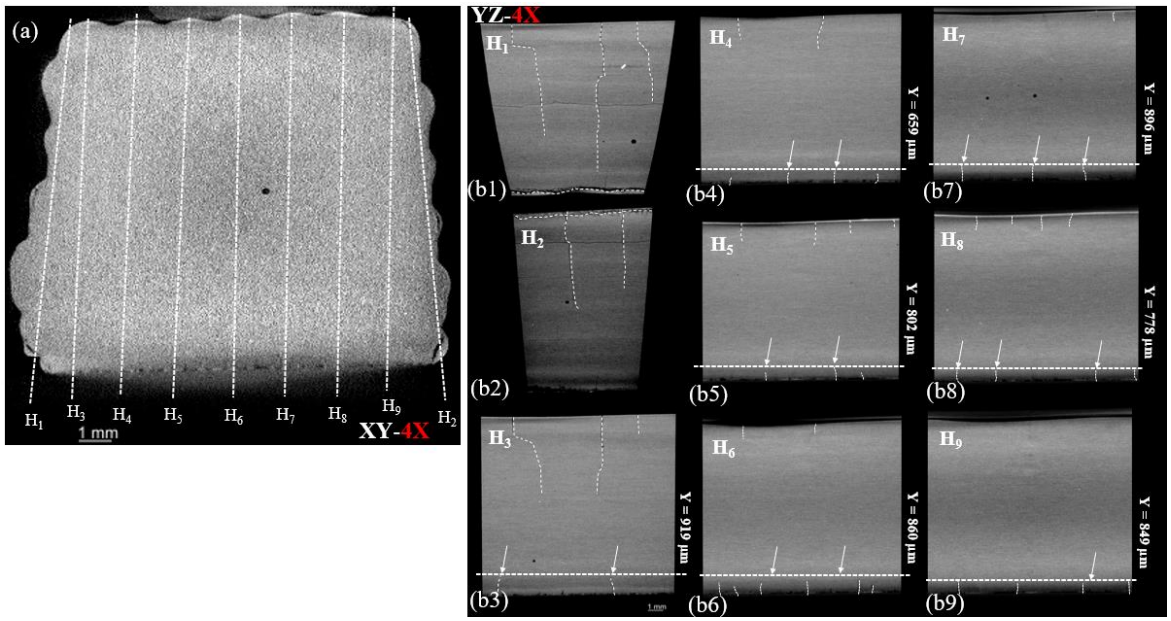


Figure 5-15. X-ray μCT images of the microstructure of 3D-printed solid prism ($\theta = 0^o$) specimen containing shrinkage-induced microcracks collected during 4X scan: a) 2D image of the cross-section in XY plane, b1-b10) 2D images of the cross-section, highlighted in (a), in XZ plane, screening the shrinkage-induced microcrack propagation along with the specimen height.

### 5.4.3.2 **Restrained and unrestrained shrinkage in cast hcp elements**

To highlight the importance of interface fabrication in enhancing the flaw-tolerance properties of 3D printed hcp element, the microstructure of its cast counterpart is characterized, and the microcrack distribution is studied at favorable cross-sections, as shown in Figure 5-16-Figure 5-18.

Six horizontal slices (S, $L_1$, $L_2$, $L_3$, $L_4$, $L_5$) shown in cross-sectional view in Figure 5-16 (a), corresponds to the mapping of microcracking population and distribution evolution along with the specimen height, while the two vertical slice ($H_1$, $H_2$) corresponds to the 'exterior' cross-sectional views of the specimen that are exposed to the external boundary conditions. Analysis of Figure 5-16 (b1-b6) indicates the only significant microcrack pattern occurs at the top surface of the specimen (i.e., Y = 11,740 μm), where the lateral and top surfaces of the element is subject to an excessive degree of drying shrinkage. When compared to its 3D printed counterpart, it is observed that less microcracking takes place in cast hcp elements deposited on unrestrained substrate since the formwork essentially plays a central role in decreasing the degree of drying shrinkage by limiting the exposure of the element to top surface. Similar to its 3D printed element,

observable microcrack growth in an arbitrary pattern is observed on two lateral surfaces of the element (displayed in Figure 5-16 (b7-b8)), which provides direct evidence of the deleterious effect of drying shrinkage on generating damage within filament microstructure. It should be noted that these microcracks have a less pronounced influence on the overall MOR of the hcp element.

Six horizontal slices (S, $L_1$, $L_2$, $L_3$, $L_4$, $L_5$) shown in cross-sectional view in Figure 5-16 (a), corresponds to the mapping of microcracking population and distribution evolution along with the specimen height, while the two vertical slice ($H_1$, $H_2$) corresponds to the 'exterior' cross-sectional views of the specimen that are exposed to the external boundary conditions. Analysis of Figure 5-16(b1-b6) indicates the only significant microcrack pattern occurs at the top surface of the specimen (i.e., Y = 11,740 μm), where the lateral and top surfaces of the element is subject to an excessive degree of drying shrinkage. When compared to its 3D-printed counterpart, it is observed that less microcracking takes place in cast hcp elements deposited on unrestrained substrate since the formwork essentially plays a central role in decreasing the degree of drying shrinkage by limiting the exposure of the element to top surface. Similar to its 3D-printed element, observable microcrack growth in an arbitrary pattern is observed on two lateral surfaces of the element (displayed in Figure 5-16(b7-b8)), which provides direct evidence of the deleterious effect of drying shrinkage on generating damage within filament microstructure. It should be noted that these microcracks have a less pronounced influence on the overall MOR of the hcp element.

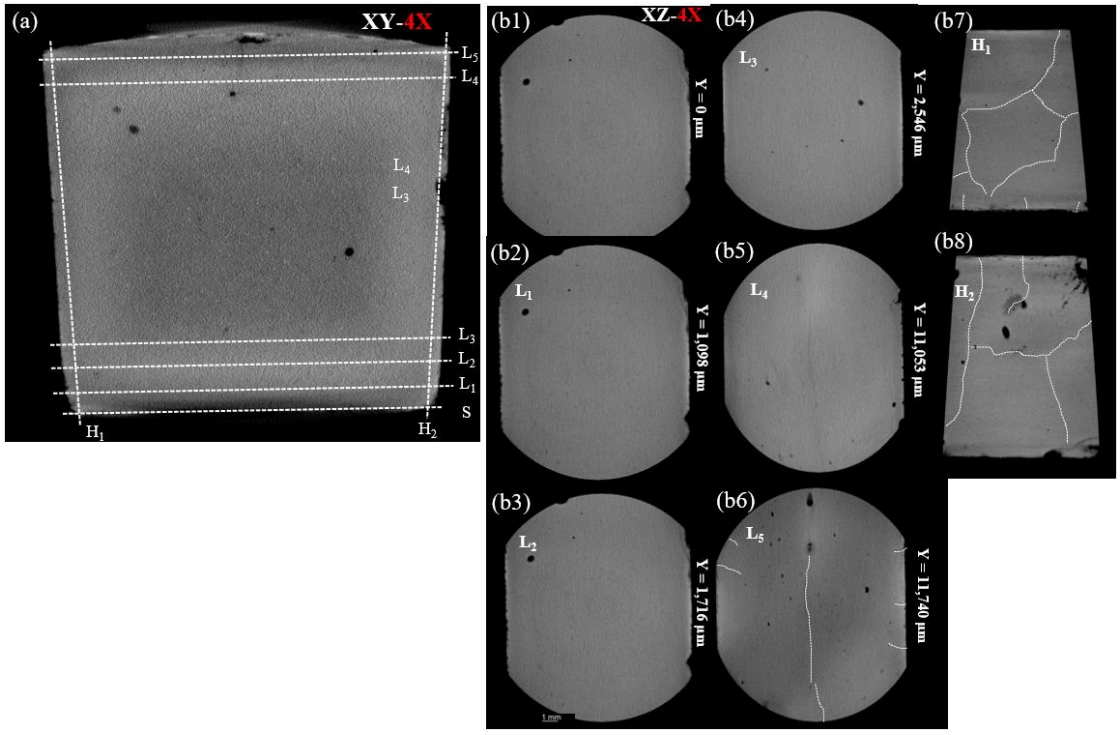


Figure 5-16. X-ray µCT images of the microstructure of unrestrained cast prism specimen collected during the 4X scan: a) 2D image of the cross-section in the XY plane, b1-b8) 2D images of the cross-section along the XZ plane.

Next, the cracking behavior and associated damage mechanism in restrained cast hcp elements are investigated to understand the governing damage mechanism using µCT images at 4X magnification. Figure 5-17 depicts the microstructural characteristics of the element at eight critical cross-sectional views in X-Z plane (slice S corresponds to the bottom surface of the filament in the first layer deposited on the substrate with a specific roughness; eight slices $L_1$, $L_2$, $L_3$, $L_4$ represent the microstructural details of the element adjacent to the restrained bottom surface; and, three slices $L_5$, $L_6$, $L_7$ represent the microstructural details of the element adjacent to the to surface subject to the excessive degree of drying). These slices are intentionally selected to monitor how damage-tolerant the hcp element is when exposed to an extreme drying environment, guiding the capability of interfaces along their predefined surface (i.e., path). When the five bottom horizontal cross-sectional views are examined, a gradient of microcrack population and distribution is observed along with the specimen height, with the highest degree of microcracking screened on slices S and $L_1$ and $L_2$ (i.e., $Y \leq 762$ mm). As the slice location moves away from the bottom of the specimen (i.e., slices $L_3$ and $L_4$), the degree of microcracking reduces significantly due to the less pronounced tensile stress development. Similar to unrestrained cast hcp element,

the microcrack advancement within the portion of the element located adjacent to the top surface (on three slices $L_5$, $L_6$, $L_7$) is observed owing to the excessive degree of drying shrinkage. In overall, a more pronounced degree of microcracking with regards to microcrack population and distribution along with a higher microcrack propagation depth is observed in restrained cast hcp elements when compared to the 3D printed counterparts. This microcracking pattern eventually leads to a significant reduction of resulting mechanical response (e.g., MOR) of cast element, which suitably promotes our earlier findings in section 5.4.1.

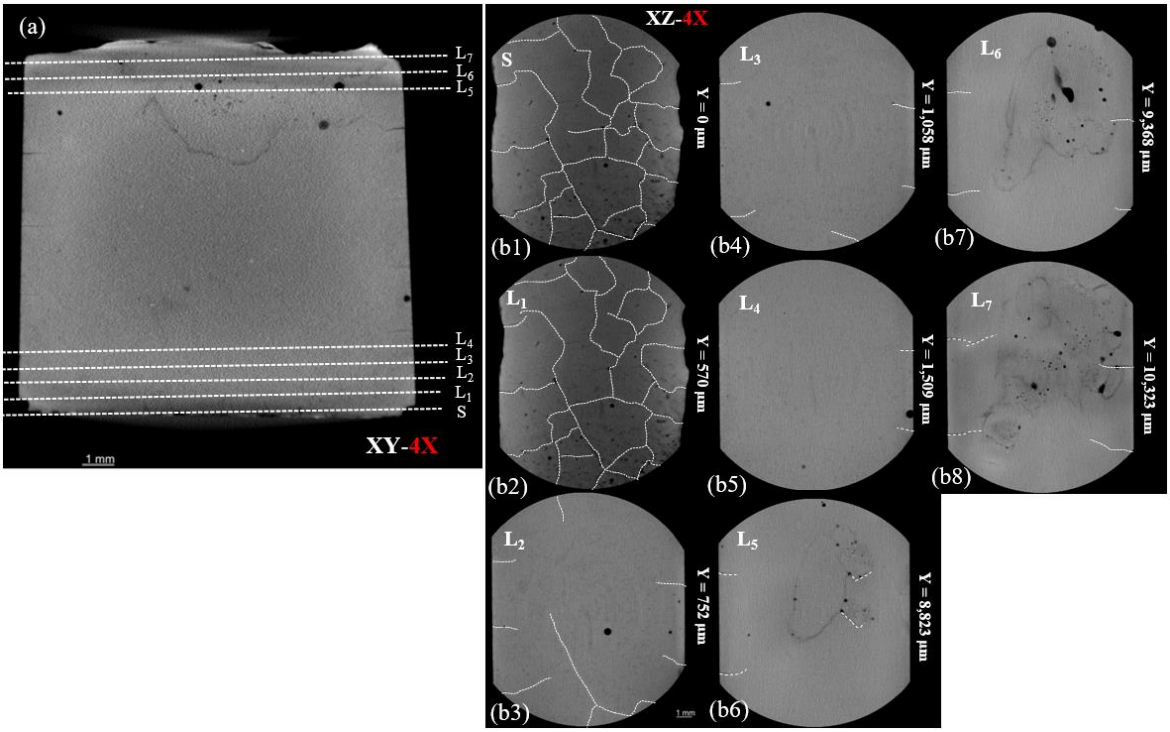


Figure 5-17. X-ray µCT images of the microstructure of restrained cast prism specimen collected during 4X scan: a) 2D image of the cross-section in XY plane, b1-b8) 2D images of the cross-section along the XZ plane.

Furthermore, µCT characterization of restrained cast hcp element along the Y-Z plane (i.e., third plane) is essential to monitor the third dimension microcrack pattern gradient along with the specimen height. The µCT analysis is performed as a means to improve further our understanding of how the hcp element with no structural design of interfaces delimiting the bulk material is susceptible to the inherent damage associated with shrinkage, as shown in Figure 5-18. Figure 5-18 depicts the microstructural characteristics of the element at eleven critical vertical cross-sectional views in Y-Z plane (two slices $H_1$ and $H_{11}$ corresponds to the cross-sectional views of filament

layers neighboring exterior surfaces of the element directly exposed to the dry ambient environment, and nine slices $H_2$-$H_{10}$ correspond to 'interior' filament layers). Similar to unrestrained cast hcp element, a significant degree of microcracking distribution is observed along the specimen height shown in slices $H_1$ and $H_{11}$ (Figure 5-18 (b1, b11)). In converse to its 3D printed counterpart, the microcracking pattern is observed to be distributed and extended across the entire microstructure. When examining the microcrack propagation height along nine interior slices shown in Figure 5-18 (b2-b10), it is revealed that the development of microcracks, initiating from the (restrained) bottom of element extended towards the specimen height reaches to a maximum length 1,580 μm. When compared to μCT images of its 3D printed counterpart, this microcracking zone length is approximately ~ 1.7 times larger in restrained cast hcp elements, which contributes to sacrificing the resulting MOR of the element. This finding complements our earlier observations with regards to the mechanical response analysis that local and global compliances of damaged 3D printed hcp elements cut with a notch length up to 2 mm are higher than those of for undamaged 3D printed hcp elements. In other words, the absence of weaker interface fabrication leads to worsening of overall mechanical performance and damage tolerance properties of the hcp element.

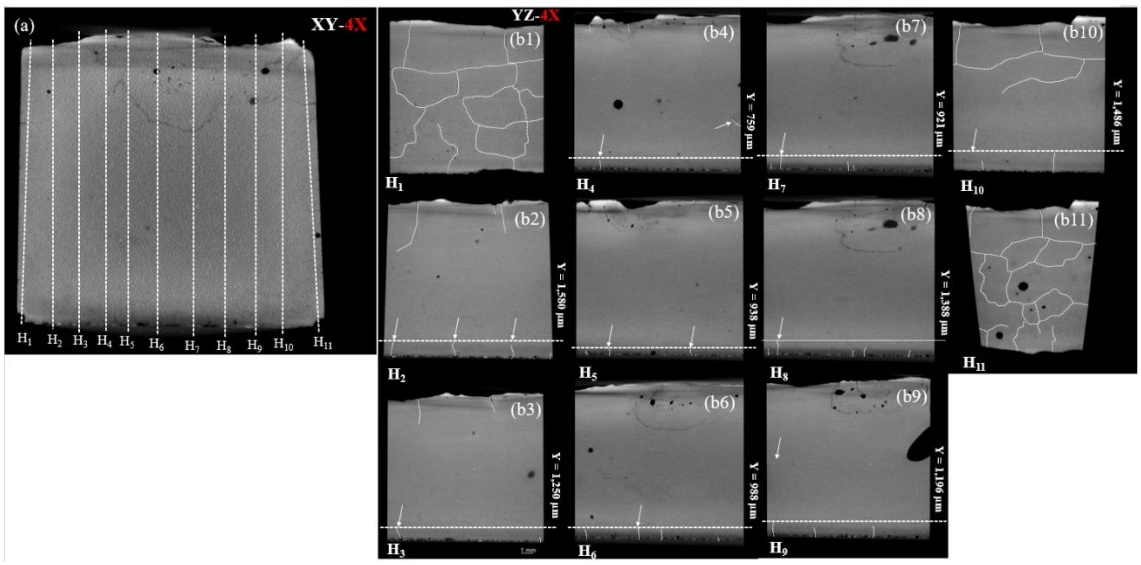


Figure 5-18. X-ray μCT images of the microstructure of restrained cast prism specimen collected during 4X scan: a) 2D image of the cross-section in XY plane, b1-b11) 2D images of the cross-section along the XZ plane.

### 5.4.4 Finite element modeling and analysis: Bio-inspired architecture effect

In this section, the mechanical response of restrained 3D printed cement paste elements with specific architectures subject to shrinkage loading, along with the associated damage mechanisms, have been investigated by examining and comparing the behavior of these elements with their unrestrained counterparts under flexural loading. Here, we focus on the *Bouligand* architecture inspired by the light-weight appendages of mantis shrimp (Figure 5-19 (a)) (Weaver et al., 2012). The last segment of this appendage is the dactyl club (Figure 5-19 (b)), which is composed of three main regions of impact (I), periodic (II), and striated (III). The architecture of the periodic region is found to follow a helicoidal arrangement of stacked layers of unidirectional chitin fibrils (Figure 5-19 (c)). A schematic illustration of an idealized Bouligand structure is shown in Figure 5-19 (d-e), where a pitch angle (ɣ) is used for structural characterization. It is noteworthy that this architecture produces many crack deflection pathways during loading (Moini et al., 2018; Suksangpanya et al., 2017).

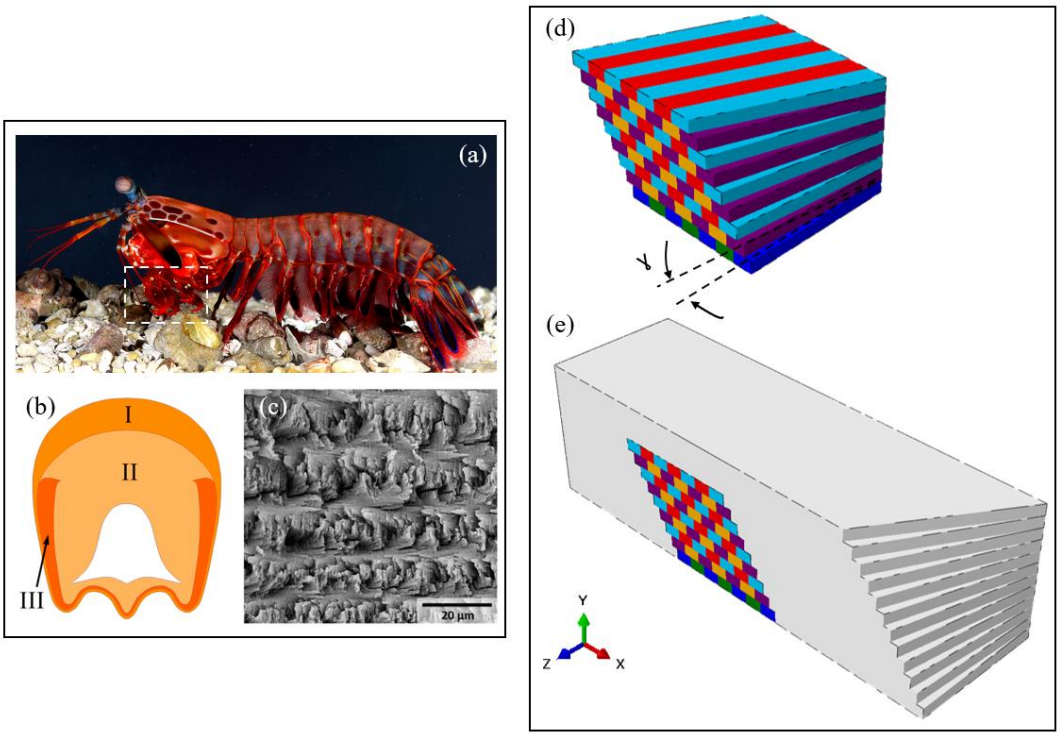


Figure 5-19. (a) Photograph of *Mantis Shrimp*. (b) Schematic image of the transverse section of the dactyl club (highlighted in Figure 5-19(a)) where I, II, and III display the impact, periodic, and striated regions, respectively. (c) SEM micrograph of a fractured surface of the periodic region. (d-e) Representative prism creation: the multilayer section highlighted in multiple colors is built from the orientation of each layer with a pitch angle ɣ.

To characterize the mechanical response of 3D printed hcp elements, we present a combination of simulation (3D finite element model), additive manufacturing, and flexural testing of Bouligand architecture to expound the role of multiscale architectures in hcp elements' enhanced shrinkage-induced crack resistance. This work addresses the modeling of the behavior of 3D printed hcp elements through a two-step multiscale approach that first starts at the lower length scale, where the configuration of four semi-rectangular filaments. The second step considers the modeling of the entire 3-D printed prism hcp element composed of consecutive layers of filaments stacked on one another. Moini et al. (Moini et al., 2019) reported the self-drifting of filaments from their programmed toolpath, which leads to the creation of both diamond- and triangular-shaped gaps between neighboring filaments. In the first step, this work develops a three-dimensional finite element model- (FEM-) based model that accounts for the influence of this characteristic of printed microstructure on the overall tensile mechanical response of interface, as shown in Figure 5-20. The goal of this step is to homogenize the fracture response for a free-of-gap interface element in terms of cohesive properties ($T_n^{int,num}$ and $G_{Ic}^{int,num}$) to significantly minimize the computational cost required to discretize the curves generated during the filament deposition. To test the validity of fracture behavior of interface in this new configuration, a comparison between the overall mechanical responses of (i) four-filament configuration with a diamond-shaped gap and known tensile mechanical properties of both filament and interface phases (Figure 5-20(a)), and (ii) four-filament configuration free-of-gap with known tensile mechanical properties of filament and homogenized tensile mechanical properties of the interface (Figure 5-20(b)) are performed subject to a mode-I loading condition.

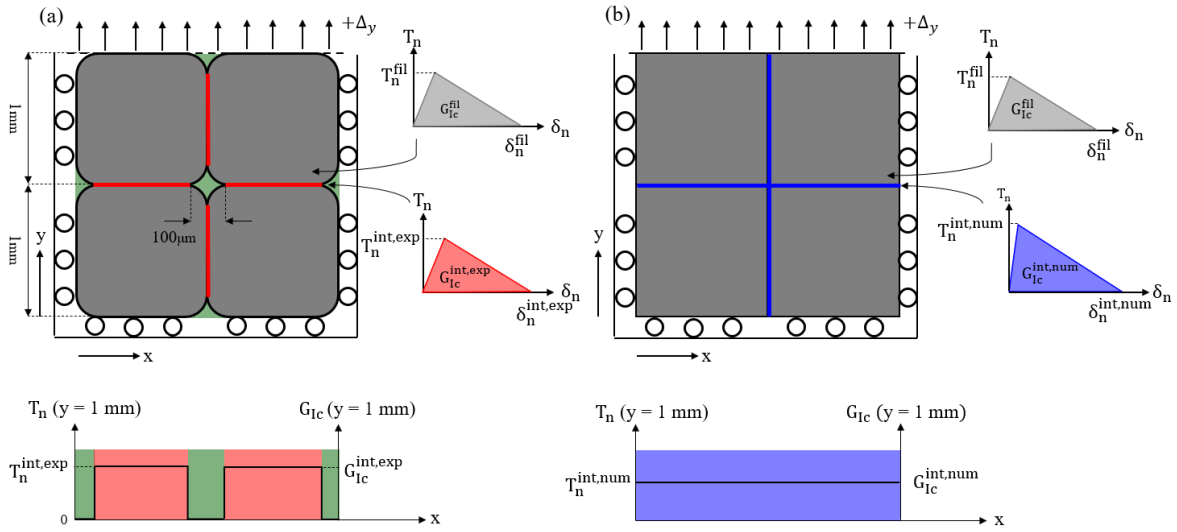


Figure 5-20. Numerical framework representing the first step of multiscale modeling of the mechanical response of (a) a four-filament configuration with semi-rectangular shape in the filament axis, knowing the tensile strength of filament and interface ($T_n^{fil}$ and $T_n^{int,exp}$) and fracture energy of filament and interface ($G_{Ic}^{fil}$ and $G_{Ic}^{int,exp}$) obtained from experiment; (b) a four-filament configuration with rectangular-shape in the filament axis, knowing the tensile strength and fracture energy of filament ($T_n^{fil}$ and $G_{Ic}^{fil}$) obtained from experiment and tensile strength and fracture energy of the new interface ($T_n^{int,num}$ and $G_{Ic}^{int,num}$) calculated from numerical modeling.

The elastic and cohesive properties of two phases of filament, as well as an interface in the four-filament configuration with the diamond-shaped gap (labeled as 'int, exp') obtained from the earlier experimental analysis, are outlined in Table 5-1. Given these properties along with the structural characteristics of two configurations, a trial-and-error process is employed until desirable cohesive properties for the free-of-gap interface (labeled as 'int, num') are obtained to calculate the homogenized stress-displacement ($\sigma_n$-$\delta_n$) along with loading axis. This process includes first calculating the resulting peak stress obtained from the mechanical response of four-filament with diamond-shaped configuration and then calculating a desirable value for $\delta_n$ by calibrating the resulting $\sigma_n$-$\delta_n$ of four-filament free of gap configuration to match with of that for its counterpart containing diamond-shaped gap, shown in Figure 5-21. Then, the desirable values for cohesive properties of the free-of-gap interface are measured and outlined in Table 5-1. Note that the intrinsic cohesive properties of filament and interface in pure mode-I are identical to those in pure mode-II.

Table 5-1. Material parameters of filament and interfaces in two various configurations.

| Mechanical property | Unit | Filament (fil) | Interface (int, exp) | Interface (int, num) |
|---|---|---|---|---|
| $E$ | GPa | 6000 | - | - |
| $v$ | - | 0.2 | - | - |
| $G_{Ic}$ | MPa.mm | 0.00816 | 0.003 | 0.00267 |
| $T_{max}$ | MPa | 10.5 | 8.81 | 6.57 |
| $\delta_n$ | mm | 0.001556 | 0.000681 | 0.000812 |
| $l_{cz}$ | mm | 0.45 | 0.115 | 0.186 |

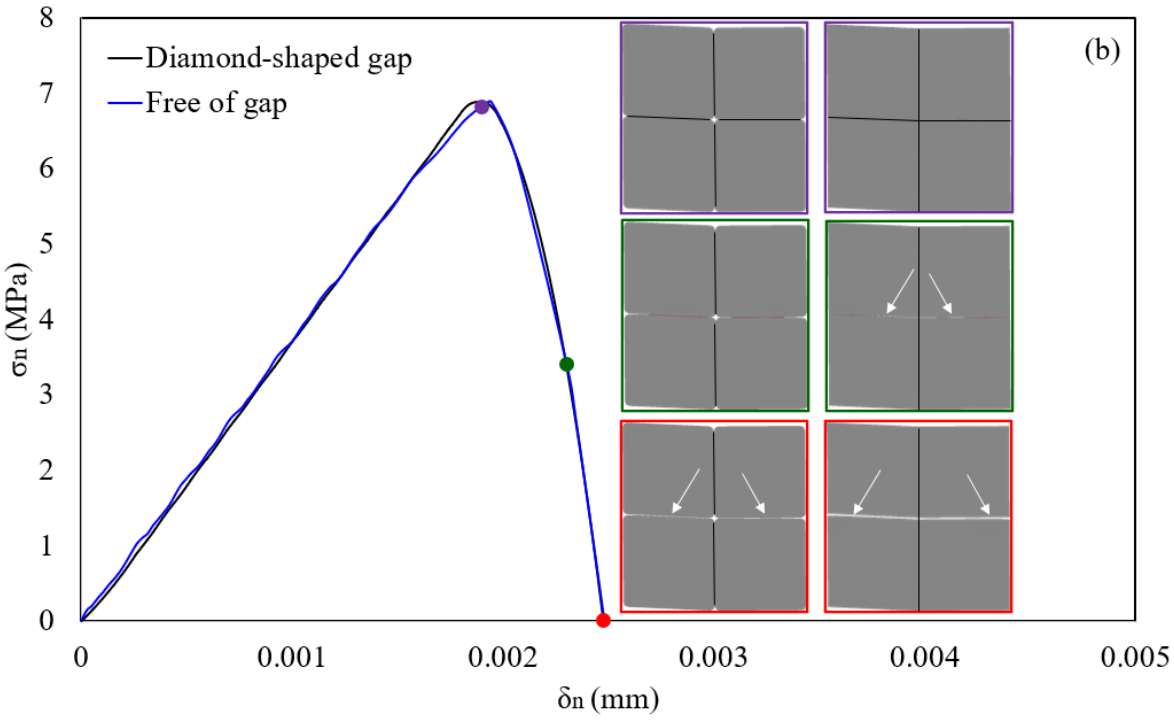


Figure 5-21. Validation of cohesive properties of four-filament free of gap configuration with of those for four-filament configuration with diamond-shaped gaps in terms of averaged stress-displacement response. The insets represent the evolution of the cracking of interface at corresponding loading applied to the configuration.

While experiments are useful to quantify the mechanical properties, including strength and fracture toughness of hcp elements, they provide no knowledge of the competing damage mechanism in elements of complex (micro-)structures. To this end, we employ a FEM-based numerical approach to look at how the cracking onset and propagation takes place in anisotropic

heterogeneous composites which cannot be explicitly described by theoretical or experimental approaches. First, to verify the validity of the numerical model, the mechanical responses of printed hcp prisms with lamellar architecture are quantified using numerical analysis and then contrasted with earlier experimental observations. Following the experimental protocol, the three-point flexural loading in simulated using three rigid rollers having frictionless contact between the roller and the hcp prism (40 mm × 12 mm × 12 mm). The elastic properties of continuum elements are obtained from performing separate hcp prisms with no interface elements tested under identical loading conditions and then compared with the experimental data of unrestrained hcp elements. As a result, the values of elastic modulus $E$ and Poisson's ratio $v$ are determined to be roughly about ~ 6000 *MPa* and ~ 0.2, respectively.

Here, we quantify the $\sigma_r$-$\delta$ response of unrestrained hcp element with two different characteristic angles $\theta = 0^o$ and $\gamma = 0^o$ where loading plane is perpendicular to the filament axis (i.e., testing the mechanical response of the filament layers explicitly) as well $\theta = 90^o$ and $\gamma = 0^o$ where loading plane is parallel with the interface axis (i.e., testing the mechanical response of the interface layers clearly), and compare them with experimental observations, as shown in Figure 5-22. Comparing the numerical solution and experimental observation, it is seen that the percentage difference for calculation of peak stress becomes less than 4%, which implies a promising agreement. The next step is to predict the mechanical response of restrained hcp element with characteristic angles $\theta = 0^o$ and $\gamma = 0^o$, where it accounts for the contribution of shrinkage-induced microcracks propagated across the filaments of the first layer and neighboring interfacial region. Given the mechanical properties of intact and free-of-damage filaments in the above layers (i.e., layers 2-12), a trial-and-error process is employed until desirable cohesive properties for the filaments in the first layer are obtained to match with the mechanical response obtained from experimental data. After several trials and errors, the most desirable values of $E$, $T_{max}$, $G_{Ic}$, and $\delta_n$ are determined to be 3000 *MPa*, 5.1 *MPa*, 0.004 *MPa.mm*, and 0.00081 *mm*, which yield to a percentage difference of less than ~ 2% for peak stress value. Correspondingly, the favorable values of $E$, $T_{max}$, $G_{Ic}$, and $\delta_n$ for the damaged interface in the first layer are determined to be 3000 *MPa*, 3.38 *MPa*, 0.0013 *MPa.mm*, and 0.00081 *mm*.

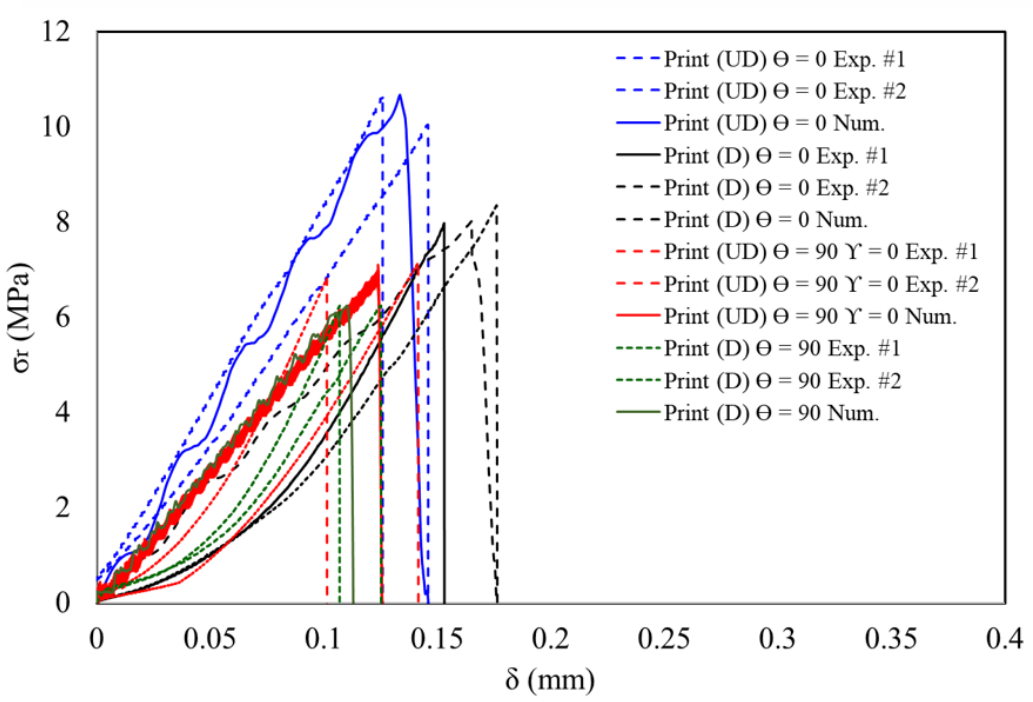


Figure 5-22. Mechanical response of lamellar architecture using the three-point flexural test: a) flexural stress-displacement ($\sigma_r$-$\delta$) for unrestrained (undamaged) and restrained (damaged) printed prisms with characteristic angles of $\theta = 0$ and $\gamma = 0$, as well as unrestrained printed, prisms with characteristic angles of $\theta = 90$ and $\gamma = 0$. The insets represent the evolution of cracking at corresponding loading applied to the hcp element.

In bio-inspired fibrous Bouligand architectures, a competing damage mechanism between solid failure, representing fiber fracture, and interfacial failure, representing the separation between fibers, is expected to control the trade-off between large and small pitch angles (Suksangpanya et al., 2017; Weaver et al., 2012). While small pitch angle allows the crack to deflect into the interface, the activation of this interfacial failure can be achieved by designing a crack path that facilitates the crack twisting. This provides delocalization damage mechanisms and the spread of damage to the neighboring interfacial regions. Therefore, this study focuses on the examination of the hcp elements with small pitch angles (e.g., $\gamma = 1^o$, $3^{o,}$ and $5^o$). This section aims to assess the use of Bouligand architecture as the second layer of protection for hcp elements when subject to damage associated with shrinkage. Three-point flexural testing is performed on these elements for the determination of resulting $\sigma_r$-$\delta$ behavior and specific strength (MOR).

The results presented in Figure 5-23 (a) illustrate that peak stress values consistently increases with the increase of pitch angle in unrestrained hcp elements (UD). At the same time,

independent of the architecture and structural orientation of filaments, a catastrophic failure of specimen takes place after reaching to the peak stress. Specifically, the observed increases in the peak stress are ~ 11% and 21% for architectures with $\gamma = 3^o$ and $\gamma = 5^o$, respectively, when compared to their counterpart with $\gamma = 1^o$. While there is no available data on the effect of restrained shrinkage cracking on the mechanical performance of hcp elements with Bouligand architecture, we utilize the numerical tool to predict the resulting mechanical behavior and an integrated localization-delocalization damage mechanism through trapping the microcracking associated with shrinkage at the first layer of filaments, followed by guiding the cracks induced by mechanical loading through interfaces with stable configurations. When a comparison of $\sigma_r$-$\delta$ responses of Bouligand architecture specimen with $\gamma = 3^o$ obtained from numerical analysis and experimental data, a similar peak stress value is observed with a percentage difference of less than ~ 6%. Afterward, the cohesive properties of damaged filaments and interfaces produced in the first layer and interfaces between the filaments in the first layer and consecutive top layer (i.e., second layer) obtained from earlier numerical results are incorporated into the first layer of printed Bouligand architecture to mimic the microcracking associated with shrinkage. A similar $\sigma_r$-$\delta$ response between unrestrained (UD) and restrained (D) Bouligand architecture specimen with $\gamma = 3^o$ is observed, except an insignificant increase in the specimen compliance and an insignificant decrease in the peak stress value are depicted.

In terms of strength, the effect of structural anisotropy fabricated by additive manufacturing on alleviating the effect of restrained shrinkage cracking is quantified in three distinct hcp elements of the cast, printed lamellar architecture, and printed Bouligand architecture, as shown in Figure 5-23 (b). The decrease in the MOR values of 3D printed element with $\theta = 0^o$ and $\gamma = 0^o$, 3D printed element with $\theta = 90^o$ and $\gamma = 0^o$, 3D printed element with $\theta = 90^o$ and $\gamma = 3^o$, and cast element are 11.66%, 9.8%, 5.76% and 29.51%, respectively, highlighting the important influence of structural orientation of filaments on solving a primary durability issue. Furthermore, it is observed that the unrestrained printed Bouligand architecture with $\gamma = 5^o$ and unrestrained printed lamellar architecture hcp elements are statistically identical, emphasizing on the role of crack deflection at the interface as the primary source of enhanced damage and flaw tolerance.

The detailed images of typical crack propagation in a stepwise pattern, crack reorientation, and branching offering enhanced fracture properties for unrestrained and restrained printed hcp elements with $\gamma = 3^o$ are illustrated at various loading stages in Figure 5-23 (c–n): 1) At the pre-

peak response before peak stress (highlighted in green color), the numerical modeling suggests that a particular primarily unidirectional crack propagates along with the vertical interfaces of first two layers in the Y-Z plane (shown in Figure 5-23 (c)). In Figure 5-23 (d) and (e), the crack path is detected to be redirected to the weak interface along the filaments (i.e., it is parallel to X-direction). This stepwise crack pattern promotes the idea of using Bouligand architectures in which they tend to allow the cracks propagate in twisted designs following the path of the interfaces. These twisting patterns have been explored to be responsible for increasing damage resistance and promoting the spread of damage (i.e., delocalization damage mechanism). As loading progresses passing the peak stress (highlighted in yellow color), the crack propagation is systematically deflected into interface channels rather than deflecting straight into the filaments, where maximum concurrent tensile and principal shear stresses are most likely to be exerted (shown in Figure 5-23 (f), (g), and (h)). At certain stages of loading before ultimate failure (highlighted in purple color), it is observed that these weak interfaces are exploited to deflect and branch the cracks into the design where growth becomes more energy-consuming, which is the strategy observed in biological systems (shown in Figure 5-23 (i), (j), and (k)). Ultimately, the principle crack advancement appears to grow along the interfaces located until reaching the top layer. In contrast, a second crack pattern tends to branch from broken interfaces of middle layers, leading to shearing a few filaments (shown in Figure 5-23 (l), (m), and (n)). The boundary effect on the fracture process is likely the primary source of filament cracking and, thus, this secondary crack pattern is not considered to be a part of the damage mechanism.

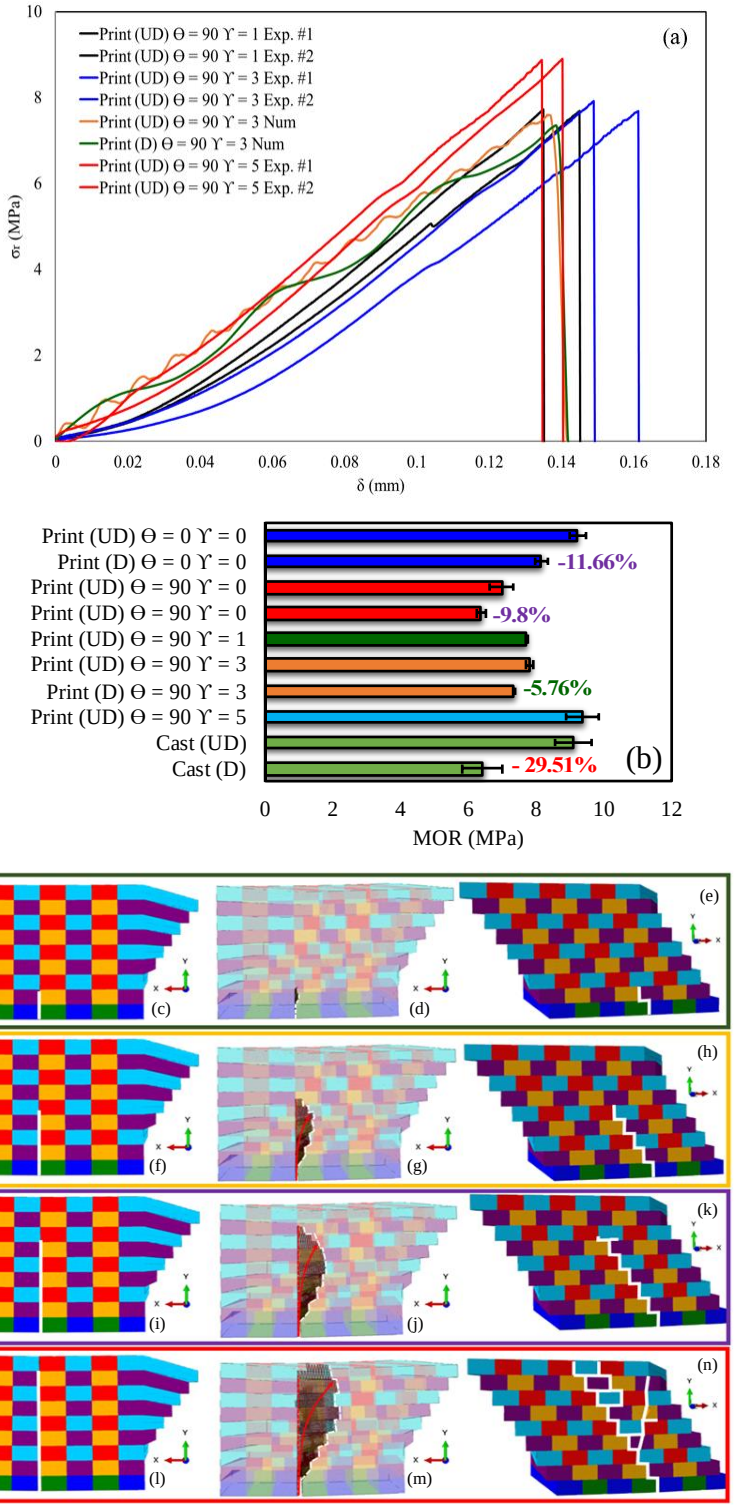


Figure 5-23. Mechanical response of Bouligand architecture using the three-point flexural test: a) stress-displacement for unrestrained and restrained printed specimens; b) specific modulus of rupture (MOR); c) schematic visualization of twisting crack pattern evolution in unrestrained and restrained Bouligand architecture with pitch angle ɣ = 3º.

### 5.4.5 Concluding remarks

In summary, the results presented demonstrate two novel damage mechanisms that can allow hcp elements to attain damage-resistant properties when they are subject to restrained shrinkage loading. These damage mechanisms are two folds: 1) damage localization mechanism as the first layer of protection of hcp elements where the microcracks propagated across the filaments of the first layer (i.e., restrained filaments) deflect into the weak interfacial region fabricated between the first and second layers rather than deflecting straight into the filaments of the second layer; 2) damage delocalization mechanism as the second layer of filaments where an interplay between weak interface properties and bio-inspired Bouligand architecture leads to a crack twisting mechanism and delocalizes damage spread throughout the specimen. For analysis of the former damage mechanism, the length of microcracking advancement along the specimen height is measured using three mechanical testing approaches and a non-destructive X-ray μCT imaging technique. It is found that the presence of heterogeneous interface in 3D printed hcp elements improves the reduction of MOR for restrained specimens by ~ 15% when compared to their cast counterparts. The measurement of maximum crack propagation length yields to values of 1 *mm* and 2 *mm* obtained from the global and local compliance analysis of notched restrained 3D printed and cast hcp elements, respectively. The analysis of microstructure characteristics of hcp elements reveals that the maximum length of crack propagated along the specimen height is 939 μm and 1,580 μm (with a resolution of 15 μm) for restrained 3D printed and cast hcp elements, complementing the results revealed by mechanical tests. The latter damage mechanism shows a further improvement of MOR of Bouligand architectures by ~ 25% when compared to their cast counterparts., exhibiting the controlled spread of damage without compromising the strength.

# 6. SUMMARY, CONCLUSION

The main goal of this study is to understand the underlying physical mechanisms of three common durability-related issues of internal frost damage, restrained shrinkage damage, and aggregate susceptibility to fracture. We thoroughly invested several topics that are important to understand the damage mechanisms, including the role of curvature in governing the freezing of pore solution and green phase change materials, the source of competing fracture mechanism in heterogeneous mortar and concrete, and anisotropic behavior of 3D printed hcp elements dictated by the structural orientation of filaments and the interfacial regions between them on alleviating the damage associated with shrinkage cracking.

First, a thermodynamic-based computational heat transfer model was developed to thoroughly investigate the mechanisms that are responsible for macroscopic freeze-thaw behavior of air-entrained mortar specimens. The computational results were compared to the experimental ones obtained for mortar specimens saturated with pore solution using a low-temperature LGCC. Effective medium theory and rule mixture homogenization techniques were utilized to estimate the effective thermal properties of composite mortar, where the phase transition of in-pore solution at nano and micro levels were considered. The role of curvature, owing to a broad range of pore sizes, was considered in calculating the volume fraction of freezable pore solution exposed to freezing/thawing cycles using measured absorption–desorption isotherms. Our analysis of the synergetic effect between the role of curvature and undercooling before ice nucleation onset revealed that the consideration of pore size distribution could reasonably be neglected during the freezing process due to undercooling. Conversely, the melting of formed ice indicated a gradual process as the temperature increases in both the experimental data and the model with a continuous pore size distribution.

Next, the effect of paraffin oil (sustainable phase change material) incorporation as a TES agent on enhancing the macroscopic freeze-thaw behavior of cementitious composites is studied. The computational results were compared to the experimental data for mortar specimen tested in the LGCC (small-scale) test with a temperature range of −40 °C to +24 °C and concrete slabs (large-scale) tested with a temperature range of −10 °C to +10 °C. The numerical model was validated by measured data from LGCC experimental data, where we leveraged our understanding of the role of curvature combined with the in-pore solution solidification in porous composites. It

was concluded that the consideration of a gradual phase transition of PCM with a narrow range of transition temperature better predicted the thermal response (temperature profile and associated heat flow) of the specimen, while the LWA pore sizes had a negligible effect. Analysis of the slab test also showed that the time of freezing at which temperature reduced below 0 °C was decreased roughly by 9 h when compared to a slab without PCM, which implied the improvement in the freeze-thaw performance of slab. The numerical model was also used to investigate the PCM effectiveness on reducing the impact of freeze-thaw cycling within concrete pavements located in different regions of the United States. It was observed that the transition temperatures of PCM during freezing and melting events are important properties that govern the effectiveness of PCM at reducing the impact of freeze-thaw cycles. In other words, they help control how quickly the temperature of the pavement drops below the freezing point of pore solution within concrete pores. In 122 out of 210 cities investigated, a dose of 170 (kg/m3) of FT0-MT1 PCM would reduce the freezing time and depth of concrete pavement by at least 10%, primarily throughout the East, the Central, and Pacific Northwest regions. The model results also showed that low transition temperatures were more effective, where pavements located in an additional 13 and 44 experienced a reduction in freezing time and depth of pavements by at least 10%. These preliminary results suggested that the use of PCM-LWA composites as a thermal energy storage system shows promise in improving the freeze-thaw performance of concrete pavements and merits further, more detailed investigations.

We, then, studied the key mesostructure morphological and mechanical properties of three-phase heterogeneous mortar and concrete to understand better the early-age tensile stiffness and strength development, and evolution of competing fracture mechanism in cementitious composites. Experimental results indicated that a linear relationship existed between the strength and degree of hydration for paste specimens. However, a bilinear relationship is observed as the aggregate was added to the paste (i.e., mortar and concrete). The rate of development of tensile stiffness contrasts with that of strength, as the fracture of aggregates does not affect the stiffness as a function of the degree of hydration. A two-step homogenization model multiscale method consisted of continuous and discontinuous homogenization schemes for multiscale modeling of failure of quasi-brittle mortar (Level II) and concrete (Level III) having heterogeneous mesostructures were used. For Level II mortar, the continuous homogenization scheme has been used for quantification of pre-peak and peak stress response of mortar. At the same time, the

behavior of a macroscopic cohesive crack is defined upon microscopic localization using the discontinuous homogenization scheme. The comparison between numerical solutions and experimental observations obtained for tensile stiffness and strength development at discrete early ages showed that the variations are less than 5%. With a discontinuous homogenization scheme, the fracture energy associated with the amount of energy dissipation over the localized band has been estimated to be approximately $15.7 \pm 3.4$ ($J/m^2$). We observed that the pre-peak response of mortar is strongly sensitive to the tensile stiffness of their constituents. In contrast, the differences between constituents' strengths lead to govern the micro-crack coalescence and macro-crack pattern. We validated the hypothesis of this work by showing that the influence of aggregate fracture on the knee point is primarily controlled by the competition between the energy dissipation mechanism of the cement paste at very early ages and the energy dissipation mechanism of the aggregate phase at later ages. For Level III concrete, we observed that an increase in area fraction of aggregate in two-dimensional samples alleviates the 2D effect, as the variation between predicted numerical results and experimental data decreased to less than 5%. Hence, the images from the cross-section of the concrete beam tested in the experiment are used to obtain the real 2D RVE of concrete using a computed tomography approach. With a continuous homogenization scheme, the uncertainty of results obtained from the predictive model for early-age tensile stiffness and tensile strength development was less than 10% and 6%, respectively, that indicates an outstanding agreement. Similar to mortar, we observed that by understanding the composite nature of early age concrete, tensile stiffness and strength development were captured. It was observed that the tensile stiffness of mortar and concrete increases at a very similar rate, while the presence of coarse aggregates influences the rate of strength development. It was shown that the hydration of the paste phase describes the strength gain at an early age; however, it is primarily governed by aggregates after a certain degree of hydration is reached. Aggregates do not influence the tensile stiffness development similar to how they influence the flexural strength development.

Finally, we studied the synergetic effect between the weak interface and strong filament orientation on enhancing the shrinkage-induced damage tolerant properties of 3D printed cementitious systems. As a first step, we elucidated a novel approach detailing the progress in creating damage-resistant hardened cement paste (hcp) elements, using additive manufacturing (AM). The elements can achieve on-demand strength enhancement when subject to restrained shrinkage loading, which is a primary source of the durability-related issue. We incorporate two

levels of the structural feature as the two levels of protection into our design. We show that adding both first and second levels can greatly enhance mechanical performance (MOR) by 7% compared to the design with only the first level of protection and 25% compared to the stiff bulk material. Moreover, a detailed FEM analysis for the mechanical response of printed hcp elements with lamellar and Bouligand architectures are presented to reveal the damage delocalization mechanism evidenced at the layered interfaces. These results and analyses demonstrate proof of concept that fabrication of AM-induced weak interfacial regions in conjunction with carefully designed structural orientation of bulk filaments offers an unmatched solution for the design of damage-tolerant infrastructure elements. Although this study examined the roles of interface and architecture in damage resistance of hcp elements under restrained shrinkage loading specifically, the methodology presented in this work can be tailored and adapted to gain understanding and insight on damage resistance characteristics of other biological materials. Integrating additive manufacturing into computational modeling can open a wide new avenue of unprecedented application not possible before.

# REFERENCES


Andersson, K., Allard, B., Bengtsson, M., & Magnusson, B. (1989). Chemical composition of cement pore solutions. *Cement and Concrete Research*, *19*(3), 327–332.

Antaki, P. J. (1997). Analysis of hyperbolic heat conduction in a semi-infinite slab with surface convection. *International Journal of Heat and Mass Transfer*, *40*(13), 3247–3250.

Antico, F., Esmaeeli, H., De la Varga, I., Jones, W., Barrett, T., Zavattieri, P., & Weiss, W. J. (2015). *Removing Obstacles for Pavement Cost Reduction by Examining Early Age Opening Requirements: Material Properties*.

Ashby, M. F., & Cebon, D. (1993). Materials selection in mechanical design. *Le Journal de Physique IV*, *3*(C7), C7-1.

Askeland, D. R., & Pradeep, P. P. (2003). The science and engineering of materials. In 6th (Ed.), *ZAMM - Zeitschrift für Angewandte Mathematik und Mechanik*. Cengage Learning.

Baetens, R., Jelle, B. P., & Gustavsen, A. (2010). Phase change materials for building applications: A state-of-the-art review. *Energy and Buildings*, *42*(9), 1361–1368.

Balapour, M., & Farnam, Y. (2018). The potential use of micro-capsulated phase change materials for thermal energy saving in concrete. *ACI Conference*, 1–8.

Barde, A., Mazzotta, G., & Weiss, J. (2005). Early Age Flexural Strength: The Role of Aggregates and Their Influence on Maturity Predictions. In *Materials science of concrete VII* (pp. 247–264).

Barthelat, F, & Espinosa, H. D. (2007). An experimental investigation of deformation and fracture of nacre–mother of pearl. *Experimental Mechanics*, *47*(3), 311–324.

Barthelat, Francois, Yin, Z., & Buehler, M. J. (2016). Structure and mechanics of interfaces in biological materials. *Nature Reviews Materials*, *1*(4), 1–16.

Bazant, Z., & Oh, B. (1983). Crack band theory of concrete. *Materials and Structures*, *16*, 155–177.

Bažant, Z. P. (1997). Scaling of quasibrittle fracture: asymptotic analysis. *International Journal of Fracture*, *83*(1), 19.

Bazant, Z. P., & Planas, J. (1997). Fracture and size effect in concrete and other quasi-brittle materials. In *CRC press* (1st ed.). CRC Press.

Beddoe, R., & Setzer, M. (1988). A low-temperature DSC investigation of hardened cement paste subjected to chloride action. *Cement and Concrete Research*, *18*(2), 249–256.

Benedetto, M. F., Caggiano, A., & Etse, G. (2018). Virtual elements and zero thickness interface-based approach for fracture analysis of heterogeneous materials. *Computer Methods in Applied Mechanics and Engineering*, *338*, 41–67.

Bentz, D. (2000). *A computer model to predict the surface temperature and time-of-wetness of concrete pavements and bridge decks*. US Department of Commerce, Technology Administration, National Institute of Standards and Technology.

Bentz, D. P., & Jensen, O. M. (2004). Mitigation strategies for autogenous shrinkage cracking. *Cement and Concrete Composites*, *26*(6), 677–685.

Bentz, Dale P., & Turpin, R. (2007). Potential applications of phase change materials in concrete technology. *Cement and Concrete Composites*, *29*(7), 527–532.

Bentz, Dale P, Garboczi, E. J., & Quenard, D. A. (1998). Modelling drying shrinkage in reconstructed porous materials: application to porous Vycor glass. *Modelling and Simulation in Materials Science and Engineering*, *6*(1998), 211–236.

Bernard, O., Ulm, F. J., & Lemarchand, E. (2003). A multiscale micromechanics-hydration model for the early-age elastic properties of cement-based materials. *Cement and Concrete Research*, *33*(9), 1293–1309.

Biernacki, J. J., Bullard, J. W., Sant, G., Brown, K., Glasser, F. P., Jones, S., Ley, T., Livingston, R., Nicoleau, L., Olek, J., Sanchez, F., Shahsavari, R., Stutzman, P. E., Sobolev, K., & Prater, T. (2017). Cements in the 21 st century: Challenges, perspectives, and opportunities. *Journal of the American Ceramic Society*, *100*(7), 2746–2773.

Brun, M., Lallemand, A., Quinson, J.-F., & Eyraud, C. (1977). A new method for the simultaneous determination of the size and shape of pores: the thermoporometry. In *Thermochimica Acta* (Vol. 21, Issue 1, pp. 59–88).

Buswell, R. A., Leal de Silva, W. R., Jones, S. Z., & Dirrenberger, J. (2018). 3D printing using concrete extrusion: A roadmap for research. *Cement and Concrete Research*, *October 2017*, 0–1.

Byfors, J. (1980). *Plain concrete at early ages*. Cement-och betonginst.

Cabeza, L. F., Castell, A., Barreneche, C., De Gracia, A., & Fernández, A. I. (2011). Materials used as PCM in thermal energy storage in buildings: A review. In *Renewable and Sustainable Energy Reviews* (Vol. 15, Issue 3, pp. 1675–1695).

Cai, H., & Liu, X. (1998). Freeze-thaw durability of concrete: ice formation process in pores. In *Cement and Concrete Research* (Vol. 28, Issue 9, pp. 1281–1287).

Callister, W. D., & Rethwisch, D. (2009). *Materials science and engineering: An introduction* (8th ed.).

Camacho, G. T., & Ortiz, M. (1996). Computational modelling of impact damage in brittle materials. *International Journal of Solids and Structures*, *33*(20–22), 2899–2938.

Carino, N. (1991). The maturity method. In *CRC Handbook on Nondestructive Testing of Concrete. Edited by V. M. Malhotra and N. J. Carino*. CRC Handbook on Nondestructive Testing of Concrete. Edited by V. M. Malhotra and N. J. Carino, pp. 101-144 CRC Press, USA.

Carpinteri, A. (1986). *Mechanical damage and crack growth in concrete*. Springer Netherlands.

Castellón, C., Günther, E., Mehling, H., Hiebler, S., & Cabeza, L. F. (2008). Determination of the enthalpy of PCM as a function of temperature using a heat-flux DSC-A study of different measurement procedures and their accuracy. *International Journal of Energy Research*, *32*(13), 1258–1265.

Castro, J., Bentz, D., & Weiss, J. (2011). Effect of sample conditioning on the water absorption of concrete. *Cement and Concrete Composites*, *33*(8), 805–813.

Castro, J., Keiser, L., Golias, M., & Weiss, J. (2011). Absorption and desorption properties of fine lightweight aggregate for application to internally cured concrete mixtures. *Cement and Concrete Composites*, *33*(10), 1001–1008.

Chen, S.-M., Gao, H.-L., Zhu, Y.-B., Yao, H.-B., Mao, L.-B., Song, Q.-Y., Xia, J., Pan, Z., He, Z., & Wu, H.-A. (2018). Biomimetic twisted plywood structural materials. *National Science Review*, *5*(5), 703–714.

Christensen, R. M. (1990). A critical evaluation for a class of micro-mechanics models. *Journal of the Mechanics and Physics of Solids*, *38*(3), 379–404.

Christensen, R., Schantz, H., & Shapiro, J. (1992). On the range of validity of the Mori-Tanaka method. *Journal of the Mechanics and Physics of Solids*, *40*(1), 69–73.

Cohen, M. D., Olek, J., & Dolch, W. L. (1990). Mechanism of plastic shrinkage cracking in portland cement and portland cement-silica fume paste and mortar. *Cement and Concrete Research*, *20*(1), 103–119.

Compton, B. G., & Lewis, J. A. (2014). 3D-Printing of Lightweight Cellular Composites. *Advanced Materials*, *26*(34), 5930–5935.

Constantinides, G., & Ulm, F. J. (2004). The effect of two types of C-S-H on the elasticity of cement-based materials: Results from nanoindentation and micromechanical modeling. *Cement and Concrete Research*, *34*(1), 67–80.

Costa, M., Buddhi, D., & Oliva, A. (1998). Numerical simulation of a latent heat thermal energy storage system with enhanced heat conduction. *Energy Conversion and Management*, *39*(3–4), 319–330.

Coussy, O., & Monteiro, P. J. M. (2008). Poroelastic model for concrete exposed to freezing temperatures. *Cement and Concrete Research*, *38*(1), 40–48.

Currey, J. D., & Kohn, A. J. (1976). Fracture in the crossed-lamellar structure ofConus shells. *Journal of Materials Science*, *11*(9), 1615–1623.

Davies, J. T. (2012). *Interfacial phenomena*. Elsevier.

De Borst, R. (2008). Challenges in computational materials science: Multiple scales, multi-physics and evolving discontinuities. *Computational Materials Science*, *43*(1), 1–15.

De Schutter, G., Lesage, K., Mechtcherine, V., Nerella, V. N., Habert, G., & Agusti-Juan, I. (2018). Vision of 3D printing with concrete — Technical, economic and environmental potentials. In *Cement and Concrete Research* (Vol. 112, pp. 25–36).

Debenedetti, P. (2003). Supercooled and glassy water. *Journal of Physics: Condensed Matter 15.45*, *1669*.

Du, X., & Jin, L. (2014). Meso-scale numerical investigation on cracking of cover concrete induced by corrosion of reinforcing steel. *Engineering Failure Analysis*, *39*, 21–33.

Dunlop, J. W. C., & Fratzl, P. (2010). Biological composites. *Annual Review of Materials Research*, *40*, 1–24.

Duoss, E. B., Weisgraber, T. H., Hearon, K., Zhu, C., Small, W., Metz, T. R., Vericella, J. J., Barth, H. D., Kuntz, J. D., Maxwell, R. S., Spadaccini, C. M., & Wilson, T. S. (2014). Three-Dimensional Printing of Elastomeric, Cellular Architectures with Negative Stiffness. *Advanced Functional Materials*, *24*(31), 4905–4913.

Dutta, S., & Chandra Kishen, J. M. (2018). Progressive damage through interface microcracking in cementitious composites: A micromechanics based approach. *International Journal of Solids and Structures*, *150*, 230–240.

Eder, M., Amini, S., & Fratzl, P. (2018). Biological composites—Complex structures for functional diversity. *Science*, *362*(6414), 543–547.

Eldin, N. N., & Senouci, A. B. (1993). Rubber-tire particles as concrete aggregate. *Journal of Materials in Civil Engineering*, *5*(4), 478–496.

Eliáš, J., Vořechovský, M., Skoček, J., & Bažant, Z. P. (2015). Stochastic discrete meso-scale simulations of concrete fracture: Comparison to experimental data. *Engineering Fracture Mechanics*, *135*, 1–16.

Esmaeeli, Hadi S., Farnam, Y., Bentz, D. P., Zavattieri, P. D., & Weiss, W. J. J. (2017). Numerical simulation of the freeze–thaw behavior of mortar containing deicing salt solution. *Materials and Structures*, *50*(1), 96.

Esmaeeli, Hadi S., Farnam, Y., Haddock, J. E., Zavattieri, P. D., & Weiss, W. J. (2018). Numerical analysis of the freeze-thaw performance of cementitious composites that contain phase change material (PCM). *Materials & Design*, *145*, 74–87.

Esmaeeli, Hadi S, Shishehbor, M., Weiss, W. J., & Zavattieri, P. D. (2019). A two-step multiscale model to predict early age strength development of cementitious composites considering competing fracture mechanisms. *Construction and Building Materials*, *208*, 577–600.

Esmaeeli, Hadi Shagerdi. (2015). *Numerical simulation of freeze-thaw behavior and fracture behavior of cementitious systems*. Purdue University.

Espinosa, H. D., Rim, J. E., Barthelat, F., & Buehler, M. J. (2009). Merger of structure and material in nacre and bone–Perspectives on de novo biomimetic materials. *Progress in Materials Science*, *54*(8), 1059–1100.

Faber, J. A., Arrieta, A. F., & Studart, A. R. (2018). Bioinspired spring origami. *Science*, *359*(6382), 1386–1391.

Farnam, Y., Liston, L., Krafcik, M., Tao, B., Erk, K., & Weiss, J. (2015). *Evaluation of Phase Change Materials to Store Energy in Concrete Pavements*.

Farnam, Yaghoob, Bentz, D., Hampton, A., & Weiss, W. (2014). Acoustic emission and low-temperature calorimetry study of freeze and thaw behavior in cementitious materials exposed to sodium chloride salt. *Transportation Research Record: Journal of the Transportation Research Board*, *2441*, 81–90.

Farnam, Yaghoob, Bentz, D., Sakulich, A., Flynn, D., & Weiss, J. (2014). Measuring Freeze and Thaw Damage in Mortars Containing Deicing Salt Using a Low-Temperature Longitudinal Guarded Comparative Calorimeter and Acoustic Emission. *Advances in Civil Engineering Materials*, *3*(1), 20130095.

Farnam, Yaghoob, Dick, S., Wiese, A., Davis, J., Bentz, D., & Weiss, J. (2015). The influence of calcium chloride deicing salt on phase changes and damage development in cementitious materials. *Cement and Concrete Composites*, *64*, 1–15.

Farnam, Yaghoob, Esmaeeli, H. S., Bentz, D., Zavattieri, P., & Weiss, J. (2015). Experimental and Numerical Investigation on the Effect of Cooling/Heating Rate on the Freeze-Thaw Behavior of Mortar Containing Deicing Salt Solution. *International Conference on the Regeneration and Conservation of Concrete Structures (RCCS)*.

Farnam, Yaghoob, Esmaeeli, H. S., Zavattieri, P. D. P. D., Haddock, J., & Weiss, J. (2017). Incorporating phase change materials in concrete pavement to melt snow and ice. *Cement and Concrete Composites*, *84*, 134–145.

Farnam, Yaghoob, Krafcik, M., Liston, L., Washington, T., Erk, K., Tao, B., & Weiss, J. (2015). Evaluating the Use of Phase Change Materials in Concrete Pavement to Melt Ice and Snow. *Journal of Materials in Civil Engineering*, *28*(4), 04015161.

Farnam, Yaghoob, Todak, H., Spragg, R., & Weiss, J. (2015). Electrical response of mortar with different degrees of saturation and deicing salt solutions during freezing and thawing. *Cement and Concrete Composites*, *59*, 49–59.

Farnam, Yaghoob, Wiese, A., Bentz, D., Davis, J., & Weiss, J. (2015). Damage Development in Cementitious Materials Exposed to Magnesium Chloride Deicing Salt. *Construction and Building Materials*, *93*, 384–392.

Feng, D. C., & Wu, J. Y. (2018). Phase-field regularized cohesive zone model (CZM) and size effect of concrete. *Engineering Fracture Mechanics*, *197*, 66–79.

Fernandes, F., Manari, S., Aguayo, M., Santos, K., Oey, T., Wei, Z., Falzone, G., Neithalath, N., & Sant, G. (2014). On the feasibility of using phase change materials (PCMs) to mitigate thermal cracking in cementitious materials. *Cement and Concrete Composites*, *51*, 14–26.

Fratzl, P., & Weinkamer, R. (2007). Nature's hierarchical materials. *Progress in Materials Science*, *52*(8), 1263–1334.

Fukai, J., Hamada, Y., Morozumi, Y., & Miyatake, O. (2003). Improvement of thermal characteristics of latent heat thermal energy storage units using carbon-fiber brushes: experiments and modeling. *International Journal of Heat and Mass Transfer*, *46*(23), 4513–4525.

Gao, W., Zhang, Y., Ramanujan, D., Ramani, K., Chen, Y., Williams, C. B., Wang, C. C. L., Shin, Y. C., Zhang, S., & Zavattieri, P. D. (2015). The status, challenges, and future of additive manufacturing in engineering. *Computer-Aided Design*, *69*, 65–89.

Gao, Y. F., & Bower, A. F. (2004). A simple technique for avoiding convergence problems in finite element simulations of crack nucleation and growth on cohesive interfaces. *Modelling and Simulation in Materials Science and Engineering*, *12*(3), 453–463.

Garboczi, E. J. (1993). Computational materials science of cement-based materials. *Materials and Structures*, *26*(4), 191–195.

Geers, M. G. D., Kouznetsova, V. G., & Brekelmans, W. A. M. (2010). Multi-scale computational homogenization: Trends and challenges. *Journal of Computational and Applied Mathematics*, *234*(7), 2175–2182.

Ghourchian, S., Wyrzykowski, M., Baquerizo, L., & Lura, P. (2018a). Performance of passive methods in plastic shrinkage cracking mitigation. *Cement and Concrete Composites*, *91*(February), 148–155.

Ghourchian, S., Wyrzykowski, M., Baquerizo, L., & Lura, P. (2018b). Susceptibility of Portland cement and blended cement concretes to plastic shrinkage cracking. *Cement and Concrete Composites*, *85*, 44–55.

Ghourchian, S., Wyrzykowski, M., Plamondon, M., & Lura, P. (2019). On the mechanism of plastic shrinkage cracking in fresh cementitious materials. *Cement and Concrete Research*, *115*(October 2018), 251–263.

Gitman, I. M., Askes, H., & Sluys, L. J. (2007). Representative volume: Existence and size determination. *Engineering Fracture Mechanics*, *74*(16), 2518–2534.

Gong, Z.-X., & Mujumdar, A. S. (1997). Finite-element analysis of cyclic heat transfer in a shell-and-tube latent heat energy storage exchanger. *Applied Thermal Engineering*, *17*(6), 583–591.

Gosselin, C., Duballet, R., Roux, P., Gaudillière, N., Dirrenberger, J., & Morel, P. (2016). Large-scale 3D printing of ultra-high performance concrete - a new processing route for architects and builders. *Materials and Design*, *100*, 102–109.

Grunenfelder, L. K., Milliron, G., Herrera, S., Gallana, I., Yaraghi, N., Hughes, N., Evans-Lutterodt, K., Zavattieri, P., & Kisailus, D. (2018). Ecologically driven ultrastructural and hydrodynamic designs in stomatopod cuticles. *Advanced Materials*, *30*(9), 1705295.

Hamada, Y., Ohtsu, W., & Fukai, J. (2003). Thermal response in thermal energy storage material around heat transfer tubes: effect of additives on heat transfer rates. *Solar Energy*, *75*(4), 317–328.

Han, B., Choi, J. H., Dantzig, J. a, & Bischof, J. C. (2006). A quantitative analysis on latent heat of an aqueous binary mixture. *Cryobiology*, *52*(1), 146–151.

He, B., Martin, V., & Setterwall, F. (2004). Phase transition temperature ranges and storage density of paraffin wax phase change materials. *Energy*, *29*(11), 1785–1804.

Henkensiefken, R., Bentz, D., Nantung, T., & Weiss, J. (2009). Volume change and cracking in internally cured mixtures made with saturated lightweight aggregate under sealed and unsealed conditions. *Cement and Concrete Composites*, *31*(7), 427–437.

Herrmann, A. W. (2013). *2013 Report Card for America's Infrastructure*. American Society of Civil Engineers.

Hibbert, S. E., Markatos, N. C., & Voller, V. R. (1988). Computer simulation of moving-interface, convective, phase-change processes. *International Journal of Heat and Mass Transfer*, *31*(9), 1785–1795.

Holt, E., & Leivo, M. (2004). Cracking risks associated with early age shrinkage. *Cement and Concrete Composites*, *26*(5), 521–530.

Hoover, C. G., & Ulm, F.-J. (2015). Experimental chemo-mechanics of early-age fracture properties of cement paste. *Cement and Concrete Research*, *75*, 42–52.

Hori, M., & Nemat-Nasser, S. (1994). Double-Inclusion Model and Overall Moduli of Multi-Phase Composites. *Journal of Engineering Materials and Technology*, *116*(3), 305.

*https://www.wunderground.com/*. (n.d.). https://www.wunderground.com/

Hu, X., & Wittmann, F. H. (1990). Experimental method to determine extension of fracture-process zone. *Journal of Materials in Civil Engineering*, *2*(1), 15–23.

Huang, Y., Yang, Z., Ren, W., Liu, G., & Zhang, C. (2015). 3D meso-scale fracture modelling and validation of concrete based on in-situ X-ray Computed Tomography images using damage plasticity model. *International Journal of Solids and Structures*, *67–68*, 340–352.

Huggins, L. H. (1941). Densities and Refractive Indices of Liquid Paraffin Hydrocarbons. *Journal of the American Chemical Society*, *63*(1), 116–120.

Incropera, F. P., DeWitt, D. P., Bergman, T. L., & Lavine, A. S. (2007). Fundamentals of heat and mass transfer. In F. P. Incropera, F. P. F. O. H. Incropera, & M. Transfer (Eds.), *Water* (Vol. 6th). John Wiley & Sons.

Ismail, K. A. R., & Abugderah, M. M. (2000). Performance of a thermal storage system of the vertical tube type. *Energy Conversion and Management*, *41*(11), 1165–1190.

Ismail, K. A. R., & Da Silva, M. das G. E. (2003). Numerical solution of the phase change problem around a horizontal cylinder in the presence of natural convection in the melt region. *International Journal of Heat and Mass Transfer*, *46*(10), 1791–1799.

Jackson, C. L., & McKenna, G. B. (1990). The melting behavior of organic materials confined in porous solids. *The Journal of Chemical Physics*, *93*(12), 9002–9011.

Ji, B., & Gao, H. (2010). Mechanical principles of biological nanocomposites. *Annual Review of Materials Research*, *40*, 77–100.

Kamat, S., Su, X., Ballarini, R., & Heuer, A. H. (2000). Structural basis for the fracture toughness of the shell of the conch Strombus gigas. *Nature*, *405*(6790), 1036–1040.

Kan, L., Hui-Sheng, S., Sakulich, A. R., & Li, V. C. (2010). Self-Healing Characterization of Engineered Cementitious Composite Materials. *ACI Materials Journal*, *107*, 617–624.

Kaufmann, J. (2000). Experimental identification of damage mechanisms in cementitious porous materials on phase transition of pore solution under frost deicing salt attack. Ph.D. Thesis. In *Ecole Polytechnique Fe´de´rale de Lausanne, Switzerland*.

Kazemian, A., Yuan, X., Cochran, E., & Khoshnevis, B. (2017). Cementitious materials for construction-scale 3D printing: Laboratory testing of fresh printing mixture. *Construction and Building Materials*, *145*, 639–647.

Kenny, P., & Campbell, J. D. (1968). Fracture toughness an examination of the concept in predicting the failure of materials. *Progress in Materials Science*, *13*, 135–181.

Khan, M. S., Sanchez, F., & Zhou, H. (2020). 3-D printing of concrete: Beyond horizons. *Cement and Concrete Research*, *133*, 106070.

Khoshnevis, B., Bukkapatnam, S., Kwon, H., & Saito, J. (2001). Experimental investigation of contour crafting using ceramics materials. *Rapid Prototyping Journal*, *7*(1), 32–42.

Kim, S.-M., & Abu Al-Rub, R. K. (2011). Meso-scale computational modeling of the plastic-damage response of cementitious composites. *Cement and Concrete Research*, *41*(3), 339–358.

Kokkinis, D., Schaffner, M., & Studart, A. R. (2015). Multimaterial magnetically assisted 3D printing of composite materials. *Nature Communications*, *6*(1), 1–10.

Kumar, R., & Bhattacharjee, B. (2003). Porosity, pore size distribution and in situ strength of concrete. *Cement and Concrete Research*, *33*(1), 155–164.

Kupfer, H., & Hilsdorf, H. K. (1969). Behavior of Concrete Under Biaxial Stresses. *ACI Journal Proceedings*, *66*(8).

Landis, E. N., & Keane, D. T. (2010). *X-ray microtomography*. *61*(12), 1305–1316.

Launey, M. E., Buehler, M. J., & Ritchie, R. O. (2010). On the mechanistic origins of toughness in bone. *Annual Review of Materials Research*, *40*, 25–53.

Launey, M. E., & Ritchie, R. O. (2009). On the fracture toughness of advanced materials. *Advanced Materials*, *21*(20), 2103–2110.

Lavergne, F., Sab, K., Sanahuja, J., Bornert, M., & Toulemonde, C. (2015). Investigation of the effect of aggregates' morphology on concrete creep properties by numerical simulations. *Cement and Concrete Research*, *71*, 14–28.

Lecomte, D., & Mayer, D. (1985). Design method for sizing a latent heat store/heat exchanger in a thermal system. *Applied Energy*, *21*(1), 55–78.

Levy, O., & Stroud, D. (1997). Maxwell Garnett theory for mixtures of anisotropic inclusions: Application to conducting polymers. *Physical Review B*, *56*(13), 8035–8046.

Lewis, J. A. (2006). Direct Ink Writing of 3D Functional Materials. *Advanced Functional Materials*, *16*(17), 2193–2204.

Li, G., Zhao, Y., Pang, S.-S., & Li, Y. (1999). Effective Young's modulus estimation of concrete. *Cement and Concrete Research*, *29*(9), 1455–1462.

Li, W., Ling, C., Jiang, Z., & Yu, Q. qian. (2019). Evaluation of the potential use of form-stable phase change materials to improve the freeze-thaw resistance of concrete. *Construction and Building Materials*, *203*, 621–632.

Li, W., Pour-Ghaz, M., Castro, J., & Weiss, J. (2012). Water Absorption and Critical Degree of Saturation Relating to Freeze-Thaw Damage in Concrete Pavement Joints. *Journal of Materials in Civil Engineering*, *24*(March), 299–307.

Li, W., Sun, W., & Jiang, J. (2011). Damage of concrete experiencing flexural fatigue load and closed freeze/thaw cycles simultaneously. *Construction and Building Materials*, *25*(5), 2604–2610.

Lim, S., Buswell, R. A., Le, T. T., Austin, S. A., Gibb, A. G. F., & Thorpe, T. (2012). Developments in construction-scale additive manufacturing processes. *Automation in Construction*, *21*, 262–268.

Ling, S., Kaplan, D. L., & Buehler, M. J. (2018). Nanofibrils in nature and materials engineering. *Nature Reviews Materials*, *3*(4), 1–15.

Ling, T.-C., & Poon, C.-S. (2013). Use of phase change materials for thermal energy storage in concrete: An overview. *Construction and Building Materials*, *46*, 55–62.

Litvan, G. (1972). Phase transitions of adsorbates: IV, mechanism of frost action in hardened cement paste. *Journal of the American Ceramic Society*, *55*(1), 38–42.

Litvan, G. (1976). Frost action in cement in the presence of De-Icers. *Cement and Concrete Research*, *6*(3), 351–356.

Liu, C., Li, F., Ma, L.-P., & Cheng, H.-M. (2010). Advanced Materials for Energy Storage. *Advanced Materials*, *22*(8), E28–E62.

Liu, L., Wang, X., Chen, H., & Wan, C. (2016). Microstructure-based modelling of drying shrinkage and microcracking of cement paste at high relative humidity. *Construction and Building Materials*, *126*, 410–425.

Liu, L., Ye, G., Schlangen, E., Chen, H., Qian, Z., Sun, W., & Van Breugel, K. (2011). Modeling of the internal damage of saturated cement paste due to ice crystallization pressure during freezing. *Cement and Concrete Composites*, *33*(5), 562–571.

Liu, Zengqian, Meyers, M. A., Zhang, Z., & Ritchie, R. O. (2017). Functional gradients and heterogeneities in biological materials: Design principles, functions, and bioinspired applications. *Progress in Materials Science*, *88*, 467–498.

Liu, Zengqian, Zhang, Z., & Ritchie, R. O. (2020). Structural Orientation and Anisotropy in Biological Materials: Functional Designs and Mechanics. *Advanced Functional Materials*, 1908121.

Liu, Zhichao, & Hansen, W. (2016). Freeze-thaw durability of high strength concrete under deicer salt exposure. *Construction and Building Materials*, *102*, 478–485.

López, C. M., Carol, I., & Aguado, A. (2008a). Meso-structural study of concrete fracture using interface elements. I: Numerical model and tensile behavior. *Materials and Structures/Materiaux et Constructions*, *41*(3), 583–599.

López, C. M., Carol, I., & Aguado, A. (2008b). Meso-structural study of concrete fracture using interface elements. II: Compression, biaxial and Brazilian test. *Materials and Structures/Materiaux et Constructions*, *41*(3), 601–620.

Lura, P., Jensen, O. M., & van Breugel, K. (2003). Autogenous shrinkage in high-performance cement paste: An evaluation of basic mechanisms. *Cement and Concrete Research*, *33*(2), 223–232.

Mammeri, A., Ulmet, L., Petit, C., & Mokhtari, A. M. (2015). Temperature modelling in pavements: the effect of long- and short-wave radiation. *International Journal of Pavement Engineering*, *16*(3), 198–213.

Marchon, D., Kawashima, S., Bessaies-Bey, H., Mantellato, S., & Ng, S. (2018). Hydration and rheology control of concrete for digital fabrication: Potential admixtures and cement chemistry. *Cement and Concrete Research*, *May*, 0–1.

Mayer, G. (2005). Rigid biological systems as models for synthetic composites. *Science*, *310*(5751), 1144–1147.

Mehta, P. K. and Monteiro, P. J. (2006). *Concrete microstructure, properties and materials*. McGraw-Hill.

Meyers, M. A., McKittrick, J., & Chen, P.-Y. (2013). Structural biological materials: critical mechanics-materials connections. *Science*, *339*(6121), 773–779.

Mirzabozorg, H., & Ghaemian, M. (2005). Non-linear behavior of mass concrete in three-dimensional problems using a smeared crack approach. *Earthquake Engineering & Structural Dynamics*, *34*(3), 247–269.

Moini, M., Olek, J., Magee, B., Zavattieri, P., & Youngblood, J. (2019). Additive Manufacturing and Characterization of Architectured Cement-Based Materials via X-ray Micro-computed Tomography. In *RILEM Bookseries* (Vol. 19, pp. 176–189).

Moini, M., Olek, J., Youngblood, J. P., Magee, B., Zavattieri, P. D., & Zavattieri, D. (2018). Additive Manufacturing and Performance of Architectured Cement-Based Materials. *Under Review*, *1802123*(43), 1–11.

Naleway, S. E., Taylor, J. R. A., Porter, M. M., Meyers, M. A., & McKittrick, J. (2016). Structure and mechanical properties of selected protective systems in marine organisms. *Materials Science and Engineering: C*, *59*, 1143–1167.

Nerella, V. N., Krause, M., & Mechtcherine, V. (2020). Direct printing test for buildability of 3D-printable concrete considering economic viability. *Automation in Construction*, *109*, 102986.

Neubauer, C. M., Jennings, H. M., & Garboczi, E. J. (1996). Three-phase model of the elastic and shrinkage properties of mortar. *Advanced Cement Based Materials*, *4*(1), 6–20.

Ng, K., & Dai, Q. (2011). Investigation of Fracture Behavior of Heterogeneous Infrastructure Materials with Extended-Finite-Element Method and Image Analysis. *Journal of Materials in Civil Engineering*, *23*(12), 1662–1671.

Nguyen, V. P., Lloberas-Valls, O., Stroeven, M., & Sluys, L. J. (2011). Homogenization-based multiscale crack modelling: From micro-diffusive damage to macro-cracks. *Computer Methods in Applied Mechanics and Engineering*, *200*(9–12), 1220–1236.

Nguyen, V. P., Stroeven, M., & Sluys, L. J. (2011). Multiscale continuous and discontinuous Multiscale Continuous and Discontinuous Modeling of Heterogeneous Materials: a Review on Recent Developments. J Multiscale Model. *Journal of Multiscale Modelling*, *03*(04), 229–270.

Nguyen, V. P., Stroeven, M., & Sluys, L. J. (2012a). Multiscale failure modeling of concrete: Micromechanical modeling, discontinuous homogenization and parallel computations. *Computer Methods in Applied Mechanics and Engineering*, *201–204*, 139–156.

Nguyen, V. P., Stroeven, M., & Sluys, L. J. (2012b). An enhanced continuous–discontinuous multiscale method for modeling mode-I cohesive failure in random heterogeneous quasi-brittle materials. *Engineering Fracture Mechanics*, *79*, 78–102.

Nilsson, M. A., Daniello, R. J., & Rothstein, J. P. (2010). A novel and inexpensive technique for creating superhydrophobic surfaces using Teflon and sandpaper. *Journal of Physics D: Applied Physics*, *43*(4).

Ortiz, C., & Boyce, M. C. (2008). Bioinspired structural materials. *Science*, *319*(5866), 1053–1054.

Ortiz, M., & Pandolfi, A. (1999). Finite-deformation irreversible cohesive elements for three-dimensional crack-propagation analysis. *International Journal for Numerical Methods in Engineering*, *44*(9), 1267–1282.

Panda, B., Chandra Paul, S., & Jen Tan, M. (2017). Anisotropic mechanical performance of 3D printed fiber reinforced sustainable construction material. *Materials Letters*, *209*, 146–149.

Parks, G. S., & Todd, S. S. (1929). Heats of Fusion of Some Paraffin Hydrocarbons. *Industrial & Engineering Chemistry*, *21*(12), 1235–1237.

Perrot, A., & Amziane, S. (2019). 3D Printing in Concrete: General Considerations and Technologies. In *3D Printing of Concrete* (pp. 1–40). John Wiley & Sons, Inc.

Phu Nguyen, V., Lloberas-Valls, O., Stroeven, M., & Johannes Sluys, L. (2010). On the existence of representative volumes for softening quasi-brittle materials – A failure zone averaging scheme. *Computer Methods in Applied Mechanics and Engineering*, *199*(45–48), 3028–3038.

Pigeon, M., & Pleau, R. (2010). *Durability of concrete in cold climates*. CRC Press.

Powers, T. C. (1945). A working hypothesis for further studies of frost resistance of concrete. *American Concrete Cement, Portland Cement Association*, *41*(4), 245–272.

Powers, T. C. (1949). The air requirement of frost-resistant concrete. *Highway Research Board*, *29*, 184–211.

Powers, T. C., Helmuth, R. A., & Helmuth., R. A. (1953). THEORY OF VOLUME CHANGES IN HARDENED PORTLAND-CEMENT PASTE DURING FREEZING. *Highway Research Board Proceedings*, *32*.

Qian, Y., Farnam, Y., & Weiss, J. (2014). Using acoustic emission to quantify freeze–thaw Damage of mortar saturated with naCl solutions. *Proceedings of the 4th International Conference on the Durability of Concrete Structures*, 32–37.

Rabiei, R., Bekah, S., & Barthelat, F. (2010). Failure mode transition in nacre and bone-like materials. *Acta Biomaterialia*, *6*(10), 4081–4089.

Radjy, F. (1968). *A thermodynamic study of the system hardened cement paste and water and its dynamic mechanical response as a function of temperature*.

Radlinska, A., Rajabipour, F., Bucher, B., Henkensiefken, R., Sant, G., & Weiss, J. (2008). Shrinkage mitigation strategies in cementitious systems: A closer look at differences in sealed and unsealed behavior. *Transportation Research Record: Journal of the Transportation Research Board*, *2070*(1), 59–67.

Ren, W., Yang, Z., Sharma, R., Zhang, C., & Withers, P. J. (2015). Two-dimensional X-ray CT image based meso-scale fracture modelling of concrete. *Engineering Fracture Mechanics*, *133*, 24–39.

Rimoli, J. J., & Rojas, J. J. (2015). Meshing strategies for the alleviation of mesh-induced effects in cohesive element models. *International Journal of Fracture*, *193*(1), 29–42.

Ritchie, R O. (1988). Mechanisms of fatigue crack propagation in metals, ceramics and composites: role of crack tip shielding. *Materials Science and Engineering: A*, *103*(1), 15–28.

Ritchie, Robert O. (2011). The conflicts between strength and toughness. *Nature Materials*, *10*(11), 817–822.

Riyazi, S., Kevern, J. T., & Mulheron, M. (2017). Super absorbent polymers (SAPs) as physical air entrainment in cement mortars. *Construction and Building Materials*, *147*, 669–676.

Rohsenow, W. M., Hartnett, J. P., & Cho, Y. (1998). *Handbook of heat transfer*. McGraw-Hill.

Rubinsky, B., & Cravahlo, E. G. (1981). A finite element method for the solution of one-dimensional phase change problems. *International Journal of Heat and Mass Transfer*, *24*(12), 1987–1989.

Sakulich, A.R., & Bentz, D. P. (2012). Incorporation of phase change materials in cementitious systems via fine lightweight aggregate. *Construction and Building Materials*, *35*, 483–490.

Sakulich, Aaron R., & Bentz, D. P. (2012). Increasing the Service Life of Bridge Decks by Incorporating Phase-Change Materials to Reduce Freeze-Thaw Cycles. *Journal of Materials in Civil Engineering*, *24*(8), 1034–1042.

Sanjayan, J. G., & Nematollahi, B. (2019). 3D Concrete Printing for Construction Applications. In *3D Concrete Printing Technology* (pp. 1–11). Elsevier.

Scherer, G. (1999). Crystallization in pores. *Cement and Concrete Research*, *29*(December 1998), 1347–1358.

Scherer, G. W., & Valenza, J. (2005). Mechanisms of Frost Damage. *Materials Science of Concrete VII*, *i*, 209–246.

Scrivener, K. L., Crumbie, A. K., & Laugesen, P. (2004). The interfacial transition zone (ITZ) between cement paste and aggregate in concrete. *Interface Science*, *12*(4), 411–421.

Sears, F. W., Young, H. D., & Zemansky, M. W. (1982). *University physics*. Reading, MA : Addison-Wesley.

Shah, S. S. P. S., Swartz, S. S. E., & Ouyang, C. (1995). *Fracture mechanics of concrete: applications of fracture mechanics to concrete, rock and other quasi-brittle materials*. John Wiley & Sons.

Shah, S., Weiss, W. J., & Yang, W. (1998). Shrinkage Cracking - Can It Be Prevented? *Concrete International*, *20*(4), 51–55.

Shamsundar, N., & Sparrow, E. M. (1975). Analysis of multidimensional conduction phase change via the enthalpy model. *Journal of Heat Transfer*, *97*(3), 333.

Simeonov, P., & Ahmad, S. (1995). Effect of transition zone on the elastic behavior of cement-based composites. *Cement and Concrete Research*, *25*(1), 165–176.

Simonova, H., Vyhlídal, M., Kucharczyková, B., Bayer, P., Kersner, Z., Malíková, L., & Klusák, J. (2017). Modelling of interfacial transition zone effect on resistance to crack propagation in fine-grained cement-based composites. *Frattura Ed Integrità Strutturale*, *11*(41), 211–219.

Skrikerud, P. E., & Bachmann, H. (1986). Discrete crack modelling for dynamically loaded, unreinforced concrete structures. *Earthquake Engineering & Structural Dynamics*, *14*(2), 297–315.

Slavcheva, G. S. (2019). Drying and shrinkage of cement paste for 3D printable concrete. *IOP Conference Series: Materials Science and Engineering*, *481*(1), 12043.

Smit, R. J. M., Brekelmans, W. A. M., & Meijer, H. E. H. (1998). Prediction of the mechanical behavior of nonlinear heterogeneous systems by multi-level finite element modeling. *Computer Methods in Applied Mechanics and Engineering*, *155*(1–2), 181–192.

Smith, W. F., & Hashemi, J. (2006). *Foundations of materials science and engineering* (4th ed.). McGraw-Hill.

*Standard Test Method for Measurement of Fracture Toughness: ASTM E1820 - 06*. (n.d.).

Stutzman, P. E. (2000). Scanning electron microscopy in concrete petrography. *Materials Science of Concrete*.

Su, B., Tian, Y., & Jiang, L. (2016). Bioinspired interfaces with superwettability: from materials to chemistry. *Journal of the American Chemical Society*, *138*(6), 1727–1748.

Suksangpanya, N., Yaraghi, N. A., Kisailus, D., & Zavattieri, P. (2017). Twisting cracks in Bouligand structures. *Journal of the Mechanical Behavior of Biomedical Materials*, *76*, 38–57.

Suksangpanya, N., Yaraghi, N. A., Pipes, R. B., Kisailus, D., & Zavattieri, P. (2018). Crack twisting and toughening strategies in Bouligand architectures. *International Journal of Solids and Structures*, *150*, 83–106.

Sukumar, N., Moës, N., Moran, B., & Belytschko, T. (2000). Extended finite element method for three-dimensional crack modelling. *International Journal for Numerical Methods in Engineering*, *48*(11), 1549–1570.

Sun, B., Wang, X., & Li, Z. (2015). Meso-scale image-based modeling of reinforced concrete and adaptive multi-scale analyses on damage evolution in concrete structures. *Computational Materials Science*, *110*, 39–53.

Sun, Z., & Scherer, G. W. (2010a). Effect of air voids on salt scaling and internal freezing. *Cement and Concrete Research*, *40*(2), 260–270.

Sun, Z., & Scherer, G. W. (2010b). Pore size and shape in mortar by thermoporometry. *Cement and Concrete Research*, *40*(5), 740–751.

Sun, Z., & Scherer, G. W. (2010c). Measurement and simulation of dendritic growth of ice in cement paste. *Cement and Concrete Research*, *40*(9), 1393–1402.

Sutton, M. A., Yan, J. H., Deng, X., Cheng, C.-S., & Zavattieri, P. (2007). Three-dimensional digital image correlation to quantify deformation and crack-opening displacement in ductile aluminum under mixed-mode I/III loading. *Optical Engineering*, *46*(5), 51003.

Tang, S. B., Wang, S. Y., Ma, T. H., Tang, C. A., Bao, C. Y., Huang, X., & Zhang, H. (2016). Numerical study of shrinkage cracking in concrete and concrete repair systems. *International Journal of Fracture*, *199*(2), 229–244.

Tang, S. B., Yu, Q. L., Li, H., Yu, C. Y., Bao, C. Y., & Tang, C. A. (2013). Mesomechanical model of moisture diffusion and shrinkage cracking in building material – Model development. *Construction and Building Materials*, *47*, 511–529.

Taylor, R. (2008). FEAP—A Finite Element Analysis Program. User Manual, Version 8.2. *University of California at Berkeley*, *March*.

Thomas, J. J., & Jennings, H. M. (2006). A colloidal interpretation of chemical aging of the C-S-H gel and its effects on the properties of cement paste. *Cement and Concrete Research*, *36*(1), 30–38.

Thomas, L. C. (n.d.). *Heat transfer*. Englewood Cliffs, N.J. : Prentice Hall.

Toyama, H., Kishida, H., & Yonezu, A. (2018). Characterization of fatigue crack growth of concrete mortar under cyclic indentation loading. *Engineering Failure Analysis*, *83*, 156–166.

Urgessa, G., Yun, K. K., Yeon, J., & Yeon, J. H. (2019). Thermal responses of concrete slabs containing microencapsulated low-transition temperature phase change materials exposed to realistic climate conditions. *Cement and Concrete Composites*, *104*, 103391.

Velraj, R., Seeniraj, R. V., Hafner, B., Faber, C., & Schwarzer, K. (1999). Heat transfer enhancement in a latent heat storage system. *Solar Energy*, *65*(3), 171–180.

Verhoosel, C. V., Remmers, J. J. C., Gutiérrez, M. A., & de Borst, R. (2010). Computational homogenization for adhesive and cohesive failure in quasi-brittle solids. *International Journal for Numerical Methods in Engineering*, *83*(8–9), 1155–1179.

Villani, C., Farnam, Y., Washington, T., Jain, J., & Weiss, J. (2015). Performance of conventional portland cement and calcium silicate based carbonated cementitious dystems furing freezing and thawing in the presence of calcium chloride deicing salts. *Transportation Research Board*.

Voller, V. R., & Swaminathan, C. R. (1993). Treatment of discontinuous thermal conductivity in control-volume solutions of phase-change problems. *Numerical Heat Transfer, Part B: Fundamentals*, *24*(2), 161–180.

Walker, C. L., & Anderson, M. R. (2016). Cloud Impacts on Pavement Temperature and Shortwave Radiation. *Journal of Applied Meteorology and Climatology*, *55*(11), 2329–2347.

Wang, D., & Roesler, J. R. (2012). One-Dimensional Rigid Pavement Temperature Prediction Using Laplace Transformation. *Journal of Transportation Engineering*, *138*(9), 1171–1177.

Wang, X. F., Yang, Z. J., Yates, J. R., Jivkov, A. P., & Zhang, C. (2015). Monte Carlo simulations of mesoscale fracture modelling of concrete with random aggregates and pores. *Construction and Building Materials*, *75*, 35–45.

Wang, X., Zhang, M., & Jivkov, A. P. (2015). Computational technology for analysis of 3D meso-structure effects on damage and failure of concrete. *International Journal of Solids and Structures*, *80*, 310–333.

Watson, E. S., O'Neil, M. J., Justin, J., & Brenner, N. (1988). A Differential Scanning Calorimeter for Quantitative Differential Thermal Analysis. *Analytical Chemistry*, *36*(7), 1233–1238.

Weaver, J. C., Milliron, G. W., Miserez, A., Evans-Lutterodt, K., Herrera, S., Gallana, I., Mershon, W. J., Swanson, B., Zavattieri, P., DiMasi, E., & Kisailus, D. (2012). The stomatopod dactyl club: A formidable damage-tolerant biological hammer. *Science*, *336*(6086), 1275–1280.

Wegst, U. G. K., Bai, H., Saiz, E., Tomsia, A. P., & Ritchie, R. O. (2015). Bioinspired structural materials. *Nature Materials*, *14*(1), 23–36.

Weiss, W. J., & Shah, S. P. (2002). Restrained shrinkage cracking: the role of shrinkage reducing admixtures and specimen geometry. *Materials and Structures*, *35*(2), 85–91.

Weiss, W. J., Yang, W., & P., S. S. (2000). Factors Influencing Durability and Early-Age Cracking in High-Strength Concrete Structures. *ACI*, *189*, 387–410.

Weiss, William Jason. (1999). *Prediction of Eatly-Age Shrinkage Cracking in Concrete Elements*.

Whiting, D. A., & Nagi, M. A. (1998). Manual on control of air content in concrete. In *Bulletin EB116, Portland Cement Association, Skokie*.

Wilding, C. R. (1992). The performance of cement based systems. *Cement and Concrete Research*, *22*(2–3), 299–310.

Williams, R. J. J., & Aldao, C. M. (1983). Thermal conductivity of plastic foams. *Polymer Engineering and Science*, *23*(6), 293–298.

Wittmann, F. H., Rokugo, K., Brühwiler, E., Mihashi, H., & Simonin, P. (1988). Fracture energy and strain softening of concrete as determined by means of compact tension specimens. *Materials and Structures*, *21*(1), 21–32.

Wittmann, Folker H. (1983). *Fracture mechanics of concrete* (Folker H. Wittmann (Ed.); Vol. 7). Elsevier.

Wriggers, P., & Moftah, S. O. (2006). Mesoscale models for concrete: Homogenisation and damage behaviour. *Finite Elements in Analysis and Design*, *42*(7), 623–636.

Xu, X.-P., & Needleman, A. (1996). Numerical simulations of dynamic interfacial crack growth allowing for crack growth away from the bond line. *International Journal of Fracture*, *74*(3), 253–275.

Xu, X., & Needleman, A. (1995). Numerical simulations of dynamic crack growth along an interface. *International Journal of Fracture*, 289–324.

Yang, W., Meyers, M. A., & Ritchie, R. O. (2019). Structural architectures with toughening mechanisms in Nature: A review of the materials science of Type-I collagenous materials. *Progress in Materials Science*, *103*, 425–483.

Yang, Z., Weiss, W. J., & Olek, J. (2006). Water transport in concrete famaged by tensile loading and freeze–thaw cycling. *Journal of Materials in Civil Engineering*, *18*(3), 424–434.

Yaraghi, N. A., & Kisailus, D. (2018). Biomimetic structural materials: inspiration from design and assembly. *Annual Review of Physical Chemistry*, *69*, 23–57.

Yates, J. R., Zanganeh, M., & Tai, Y. H. (2010). Quantifying crack tip displacement fields with DIC. *Engineering Fracture Mechanics*, *77*(11), 2063–2076.

Yeon, J. H., & Kim, K. K. (2018). Potential applications of phase change materials to mitigate freeze-thaw deteriorations in concrete pavement. *Construction and Building Materials*, *177*, 202–209.

Yin, A., Yang, X., Zhang, C., Zeng, G., & Yang, Z. (2015). Three-dimensional heterogeneous fracture simulation of asphalt mixture under uniaxial tension with cohesive crack model. *Construction and Building Materials*, *76*, 103–117.

Yin, Z., Hannard, F., & Barthelat, F. (2019). Impact-resistant nacre-like transparent materials. *Science*, *364*(6447), 1260–1263.

Yoo, J., & Rubinsky, B. (2007). Numercial computation using finite elements for the moving interface in heat transfer problems with phase transformation. *Numerical Heat Transfer*, *6*(2), 209–222.

Yoshitake, I., Rajabipour, F., Mimura, Y., & Scanlon, A. (2012). A prediction method of Tensile young's modulus of concrete at early age. *Advances in Civil Engineering*, *2012*.

Young, J. F. (1988). *A review of the pore structure of cement paste and concrete and its influence on permeability*. *108*, 1–18.

Zareiyan, B., & Khoshnevis, B. (2017). Effects of interlocking on interlayer adhesion and strength of structures in 3D printing of concrete. *Automation in Construction*, *83*, 212–221.

Zhang, Jieying, Cusson, D., Monteiro, P., & Harvey, J. (2008). New perspectives on maturity method and approach for high performance concrete applications. *Cement and Concrete Research*, *38*(12), 1438–1446.

Zhang, Jun, Gao, Y., Han, Y., & Sun, W. (2012). Shrinkage and Interior Humidity of Concrete under Dry–Wet Cycles. *Drying Technology*, *30*(6), 583–596.

Zhao, H., Huang, D., Wang, X., & Chen, X. (2014). Dynamic elastic modulus of cement paste at early age based on nondestructive test and multiscale prediction model. *Journal Wuhan University of Technology, Materials Science Edition*, *29*(2), 321–328.

Zhou, F., & Molinari, J. F. (2004). Dynamic crack propagation with cohesive elements: a methodolgy to address mesh dependence. *International Journal for Numerical Methods in Engineering*, *59*(1), 1–24.

Zhou, L.-P., Wang, B.-X., Peng, X.-F., Du, X.-Z., & Yang, Y.-P. (2010). On the Specific Heat Capacity of CuO Nanofluid. *Advances in Mechanical Engineering*, *2010*, 1–4.

Zhou, R., & Lu, Y. (2018). A mesoscale interface approach to modelling fractures in concrete for material investigation. *Construction and Building Materials*, *165*, 608–620.

Zhou, T., Ioannidou, K., Ulm, F.-J., Bazant, M. Z., & Pellenq, R.-M. (2019). Multiscale poromechanics of wet cement paste. *Proceedings of the National Academy of Sciences*, *116*(22), 10652–10657.

Zivkovic, B., & Fujii, I. (2001). An analysis of isothermal phase change of phase change material within rectangular and cylindrical containers. *Solar Energy*, *70*(1), 51–61.

Zohdi, T. I., & Wriggers, P. (2008). *An introduction to computational micromechanics*. Springer Science & Business Media.